eXPRESS Polymer Letters Vol.7, No.3 (2013) 211
Available online at www.expresspolymlett.com
DOI: 10.3144/expresspolymlett.2013.19

Editorial corner – a personal view
Carbon nanodot – a new rising fluorescence star

*Z. Sun**

State Key Laboratory of Luminescence and Applications, Changchun Institute of Optics, Fine Mechanics and Physics, Changchun, Jilin 130033, P. R. China

Since carbon nanodots (CDs) were accidently found in 2004 (DOI: 10.1021/ja040082h), they rapidly attracted great research interest due to their unique properties and potential applications. They show excellent bio-compatibility and tunable light emitting and two-photon adsorption properties, which can be potentially used in bio-imaging, light-emitting devices, and for photocatalysis.

Currently, researchers mainly focus on the synthesis of CDs. The synthesis methods can be divided two categories: top-down and bottom-up routes. So called, top-down routes consist in delaminating bulk graphite or carbon materials into nanosize graphite particles via physical or chemical methods. These include arc discharge, laser ablation, electrochemical oxidation and chemical oxidation, and so on. However, there is no fluorescence from these nanosize graphite particles. Another passivation step is necessary to produce light emission, which is associated with defects in the grapheme structures. Bottom-up methods are approaches, which convert non-graphite carbon sources into nanosize graphite particles via chemical reactions, for examples, combustion, pyrolysis, microwave, ultrasonic, hydrothermal methods. In the recent half decade the bottom-up methods have attracted more and more attention due to the simple preparation route and cheap carbon sources. Luminescent carbon nanodots can also be obtained from the following biocompatible sources, such as, citric acid, glucose, coffee grounds, grass, egg yolk, and orange juice via a simple heat treatment.

The most attractive properties of carbon nanodots are excellent biocompatibility and luminescence. Although the carbon nanodots are prepared by different methods, they all show good biocompatiblity with cells, tissues of animals and plants. Their luminescence exhibits interesting wavelength dependence. That means that carbon nanodots show a tunable light-emitting range from blue to red under different exciting wavelength irradiations. Two-photon adsorption phenomenon is also observed for the carbon nanodots, which emit visible light under excitation by near infrared or infrared light. Based on the above properties, carbon nanodots may exert a huge impact in both health- and bio-related applications because of their potential to serve as non-toxic replacements of traditional heavy metal-based quantum dots.

On the other hand, carbon nanodots may also serve as a fluorescent sensor for detection of metal ions and DNA, as emitting materials for light-emitting devices (LED) and photocatalysis for degradation dye molecules. Within a decade, the researchers have made a huge progress in the development of new synthesis strategies and potential applications of CDs. So, a bright future of carbon nanodots is facing us.

Dr. Zaicheng Sun
Member of International Advisory Board

*Corresponding author, e-mail: sunzc@ciomp.ac.cn

eXPRESS Polymer Letters Vol.7, No.3 (2013) 212–223
Available online at www.expresspolymlett.com
DOI: 10.3144/expresspolymlett.2013.20

Microwave absorption behaviour of MWCNT based nanocomposites in X-band region

*P. Bhattacharya, S. Sahoo, C. K. Das**

Materials Science centre, Indian Institute of technology, 721302 Kharagpur, West Bengal, India

Received 26 July 2012; accepted in revised form 19 October 2012

Abstract. Multiwall carbon nanotube (MWCNT) based nanocomposites were prepared by a two-step process. Firstly, titanium dioxide (TiO_2) coated MWCNT was prepared via sol-gel technique. In the second step, the acid modified MWCNTs were dispersed in the thermoplastic polyurethane matrix by solution blending process. Characterizations of the nanocomposites were done by X-ray diffraction analysis, X-ray photoelectron spectroscopy, Scanning Electron Microscopy, Transmission Electron Microscopy and Energy-dispersive X-ray spectroscopy. Microwave absorption studies of the nanocomposites were carried out in X-band region. The microwave absorption result was discussed with the help of complex permittivity and permeability of the prepared radar absorbing material (RAM). The result showed superior microwave absorption property of the composite containing both TiO_2 coated MWCNT and magnetite (Fe_3O_4). This result is due to the effective absorption of both electrical and magnetic components of the microwave. RAM-MW, RAM-Ti, RAM-Ti@MW and RAM-Ti@MW/Fe and showed the maximum reflection loss of –16.03 dB at 10.99 GHz, –8.4 dB at 12.4 GHz, –36.44 dB at 12.05 GHz and –42.53 dB at 10.98 GHz respectively. Incorporation of MWCNT enhanced the thermal stability of the composite which has been confirmed by thermogravimetric analysis.

Keywords: *nanocomposites, carbon nanotube, permittivity, permeability, microwave absorption*

1. Introduction

In this modern era, designing and manufacturing of electronic device, which functions in higher frequency range, is a great challenge for the engineers because of the electromagnetic interference (EMI) problems. In defense, use of radar absorbing material (RAM), a material which absorbs microwave radiation in X band region only, is must to stealth the object by reducing the radar cross section. Therefore, the demand for light weight and effective radar absorbing material, in both commercial and military application, is increasing day to day [1–3]. Scientists are interested in X band region particularly, because most of the Radio Detection and Ranging (RADAR) applications are involved in this region. Many composites based on graphene, graphene oxide, carbon nanotube (CNT) have already been reported on this particular topic due to their great thermal stability, reluctance toward chemical agent, high aspect ratio and excellent electrical conductivity [4–7]. Sometimes, graphene [8] and graphene oxide [9] showed their potentiality as a radar absorbing material over CNT, but the problem is that they are very much uneconomical, and their synthetic approach is not very much fruitful. Hence, CNT and its composite materials are very much attractive for the preparation of RAMs. Yang *et al*. [10] reported a composite material, made of CNT and polystyrene, which showed maximum reflection loss (*RL*) of –19 dB. Qi *et al*. [11] reported a CNT-paraffin composite that showed –20 dB *RL* at 10.5 GHz. The composite prepared with the addition of 20 wt% of the Fe filled CNTs showed reflection loss of –11.2 dB [12]. From past few years, the composite containing

*Corresponding author, e-mail: chapal12@yahoo.co.in

both dielectric and magnetic component is a well-considered topic in the field of EMI shielding and RAMs [13–18]. As the electromagnetic radiation has both dielectric and magnetic component, so it is obvious that both dielectric and magnetic material is effective for the absorption of microwave radiation. X. Liu *et al*. [19] reported the hybrid microsphere, Fe-phthalocyanine oligomer/Fe_3O_4 that showed the maximum reflection loss of –31.1 dB at 8.6 GHz. Murugan *et al*. [20] reported the microwave absorbing property of nanosized $CaTiO_3$/epoxy resin composites where the maximum reflection loss is –30 dB at 8.5 GHz. X. Zhou *et al*. [21] also reported the maximum reflection loss of –18 dB at 9 GHz for CNT-$CoFe_2O_4$ nanocomposite, whereas, the maximum reflection loss for CNT and $CoFe_2O_4$ is –6 dB and –8.3 dB respectively. Hence, the composite material, in combination with dielectric or magnetic component or both, is always a better microwave absorber than their individual component. In this paper, we have prepared four different nanocomposites and investigated their microwave absorption property in X band (8.2–12.4 GHz) region. To prepare those nanocomposites, we have used MWCNT, a dielectric material (TiO_2) and magnetite (Fe_3O_4) as a magnetic component. Here TiO_2 was taken because of its high thermal stability and moderate dielectric constant of 100 [22]. Fe_3O_4, a member of spinel family, was taken due to its low toxicity and great stability at high temperature [23–24]. TiO_2 coated MWCNT is well known for multipurpose applications [25–29]. But to best of our knowledge it has not been reported yet for microwave application. HereTiO_2 coated MWCNT has been prepared by sol-gel process and then both uncoated and TiO_2 coated MWCNT was dispersed in a matrix. Thermoplastic polyurethane (TPU) was taken as a polymer matrix for all RAMs due to its flexibility [30].

2. Experimental work

2.1. Materials

MWCNTs (Guangzhou Jiechuang Trading Co. Ltd., China) having the outer diameter of 20–30 nm and length of 3–15 μm were used as a component for the preparation of nanocomposites. Titanium (IV) n-butoxide was utilised for coating on MWCNT and iso-propanol (Sigma Aldrich, India) was used as a solvent. Tetrahydrofuran (C_4H_8O, E. Merck Ltd., India) was used as a solvent for the preparation of RAM. Titanium dioxide (TiO_2, Loba Chemie Private Limited, India) and magnetite (Fe_3O_4, Loba Chemie Private Limited, India) used as a nanofiller. Cetyltrimethylammonium bromide (CTAB) has played the role of a surfactant [$(C_{16}H_{33})N(CH_3)_3Br$), Loba Chemie Private Limited, India]. All the chemicals and materials were used as purchased without any purification unless specified. The TPU (Lubrizol Advanced Materials, Thermedics TM Inc. Polymer Products, USA) used for developing RAMs belong with commercial medical grade aliphatic, polyether (TecoflexVR EG 80A injection grade). Tecoflex EG 80A (around 35% of hard segments) has shore hardness of 72A, specific gravity of 1.04, and its constituent formulation contains methylene bis (cyclohexyl) diisocyanate (HMDI) as hard segment, and polytetramethylene oxide (PTMO) as soft segment (molecular weight =1000 g/mol), and chain extender 1, 4-butane di-ol (BD).

2.2. Preparation of TiO_2 coated MWCNT

The pristine MWCNT has lower dispersibility in solvent and remained unfunctionalised, which is not suitable for further reaction with chemical substance. Hence, to make effective reactant and highly dispersible in solvent, MWCNT was modified by the mixture of HNO_3 and H_2SO_4 (3:1) according to the procedure described in [31]. Acid modification generates many oxygenated functional group on the surface of MWCNT. This functionalization assists the interaction between MWCNT and TiO_2 particle [32]. *In situ* coating of acid modified MWCNT was done by titanium(IV) n-butoxide via the sol-gel technique. The process of coating followed the procedure reported by Yuen S. M. *et al*. [33]. At first, acid modified MWCNT was dispersed in iso-propanol through sonication in presence of a cationic surfactant cetyltrimethylammonium bromide. After that the titanium (IV) n-butoxide was added to this solution and sonicated for 20 min. Then distilled H_2O was added to it slowly and kept under stirring at room temperature. The stirring was continued for next two days. In presence of H_2O, titanium (IV) n-butoxide converted to its hydrolysed product titanium (IV) hydroxide which may add to the MWCNT surface by forming H–bonds [34]. Finally, the solution was dried at 100°C and then it was further annealed at 450°C. One schematic presentation has been shown in Figure 1 to understand the formation of TiO_2 coated MWCNT nanocomposite.

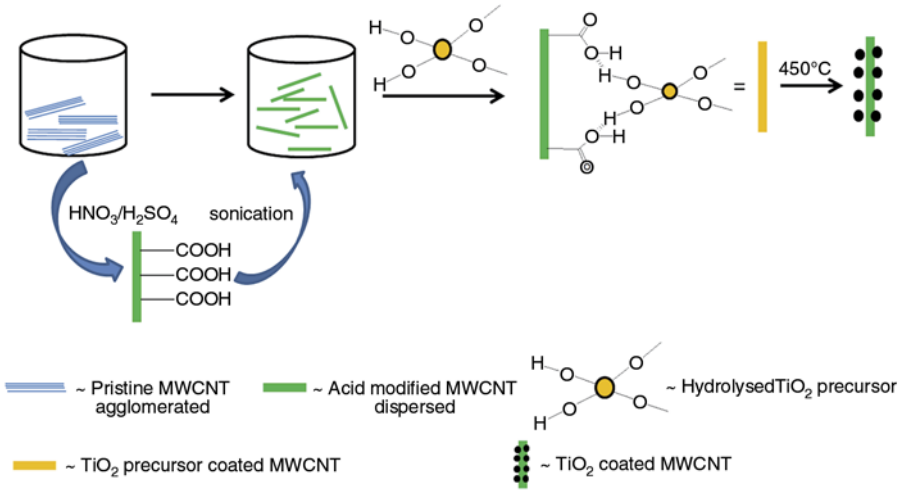

Figure 1. Schematic presentation for the formation of TiO_2 coated MWCNT nanocomposite

2.3. Preparation of nanocomposites

Four different TPU based nanocomposites were prepared with various combinations of fillers. The composition details for all RAMs were given in Table 1. To prepare the nanocomposites, TPU was dissolved in 200 mL THF at 60°C by stirring it for overnight and then required filler was added to it in desired ratios. After the addition of fillers, the stirring was continued by a mechanical stirrer till the filler becomes fully dispersed in the matrix. After that the mixture was dried at 70°C to evaporate the solvent and make the mixture highly concentrated. Then this highly concentrated mixture was poured on a petri dish and heating was continued at 70°C for complete drying. After complete drying, the product was treated by compression molding technique at 5 MPa pressure and 170°C temperature. Four samples were prepared with 30% loading of MWCNT, TiO_2, TiO_2 coated MWCNT and TiO_2 coated MWCNT (15%) + Fe_3O_4 (15%). For the preparation of RAM-Ti@MW/Fe, ball milling technique was used to mix TiO_2 coated MWCNT and Fe_3O_4. Thickness of the RAM was maintained at 2 mm. All the four samples were cut into desired rectangular shape of size 0.4 inch × 0.9 inch to fit into X-band waveguide for microwave measurements.

Table1. Composition used for RAMs preparation

Sample code	Components
RAM-MW	MWCNT (30%)
RAM-Ti	TiO_2 (30%)
RAM-Ti@MW	TiO_2 coated MWCNT (30%)
RAM-Ti@MW/Fe	TiO_2 coated MWCNT (15%) + Fe_3O_4 (15%)

3. Characterization

The samples were characterized by X-ray diffraction (XRD), which was conducted on a Rigaku X-ray diffracrometer, ULTIMA III with Cu K_α radiation (λ = 1.5418 Å) at a scanning rate of 1°/min. The TiO_2 coated MWCNTs were analyzed by X-ray photoelectron spectroscopy (XPS) with a PHI ESCA spectrometer (Perkin–Elmer 5400), using Mg K_α radiation (1253.6 eV) to reveal the change in surface characteristics of MWCNTs. The surface morphology and filler distribution of nanocomposites was analysed by scanning electron microscopy (SEM) which is governed by VEGA LSU, TESCAN instrument. For the SEM analysis to be done, the specimens were coated by a thin layer of gold for electrical conductivity. Transmission electron microscopy (TEM) analysis was carried out by a JEOL JEM-2100 microscope, to analyse the dispersion state of the fillers in TPU matrix. Energy-dispersive X-ray spectroscopy (EDX) attached to TEM, while EDX analysis was performed to understand their chemical constituents. Microwave absorption study was done by using a two port vector network analyzer (ENA E5071C). Microwave absorption property of the prepared RAMs was measured by using Transmission Line method where, the material was placed inside an enclosed rectangular waveguide transmission line. Relative complex permittivity (ε_r) and permeability (μ_r) was computed from the measurement of the reflected signal (S11) and transmitted signal (S21). Total filler percentage was maintained at 30% and the thicknesses of the RAMs were

2 mm. Thermogravimetric analysis (TGA) was performed by using Dupont 2100 Thermogravimetric analyzer. The TGA measurements were conducted at a heating rate of 10°C/min under Nitrogen atmosphere from 30 to 800°C.

4. Results and discussion

4.1. XRD analysis

The XRD patterns of MWCNT, TiO_2 coated MWCNT and Fe_3O_4 are shown in Figure 2a and 2b respectively. MWCNT showed its characteristic peak (002) at $2\theta = 25.69$ whereas TiO_2 coated MWCNT showed multiple peaks. Comparing with the standards it was found that the TiO_2 formed was in anatase form. The most intense peak (101) for TiO_2 coated MWCNT appeared at $2\theta = 25.38$. This XRD patterns were confirmed from the previously reported literature [34–35]. Hence, appearance of peaks corresponding to anatase TiO_2 confirmed the formation of TiO_2 during the sol gel coating process. The XRD pattern of Fe_3O_4 showed the characteristic peaks of Fe_3O_4 which are perfectly matched with

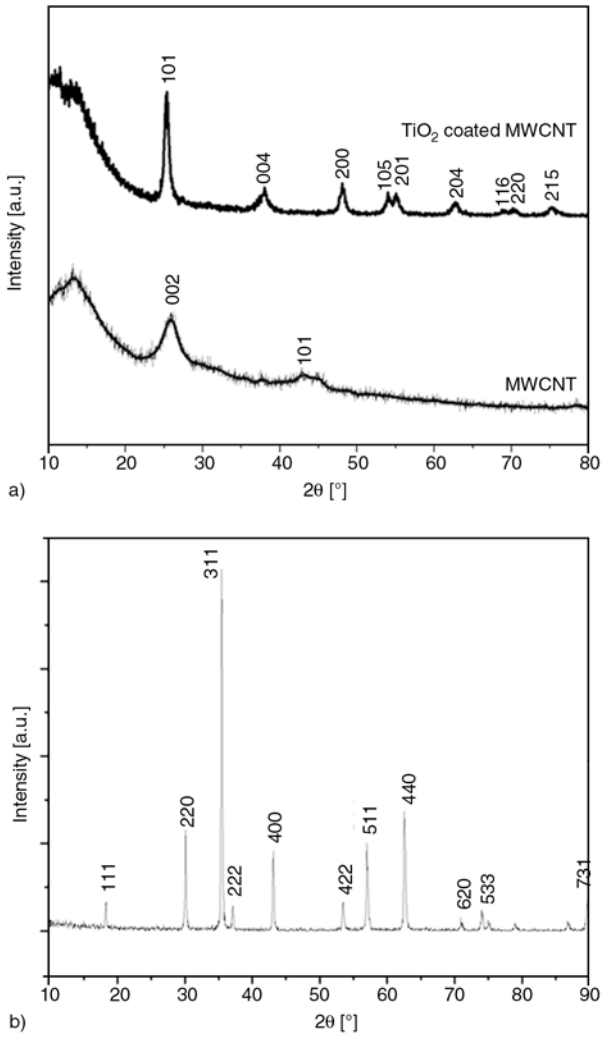

Figure 2. XRD analysis of (a) MWCNT and TiO_2 coated MWCNT, (b) Fe_3O_4

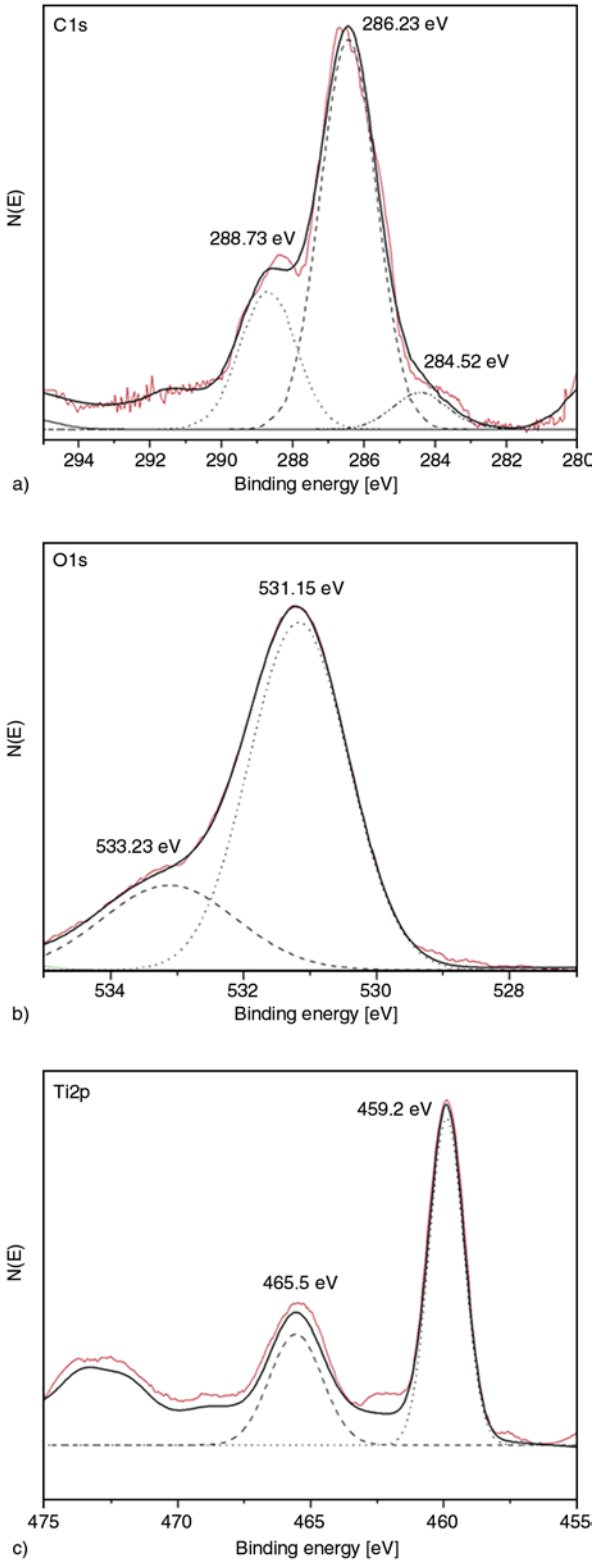

Figure 3. XPS Spectra of (a) C1s core level of modified MWCNTs, (b) O1s core level of modified MWCNTs and (c) Ti2p core level of modified MWCNTs

JCPDS analysis (No-75-1610). Crystalline facets of Fe_3O_4 are (111), (220), (311), (222), (400), (422), (511), (440), (620), (533) and (731) respectively.

4.2. XPS analysis

XPS analysis was carried out to investigate the interaction between MWCNTs and TiO_2. XPS spectrum of C, O and Ti core levels of TiO_2 coated MWCNT are shown in Figure 3a–c. The C1s XPS spectrum of TiO_2 coated MWCNT showed two peaks at 284.52 and 286.23 eV corresponding to –C–C and –C–O bonds respectively. The presence of peak at 284.52 indicated that there may be some uncoated MWCNTs or some part of the long MWCNTs remained uncoated. The presence of uncoated MWCNT in TiO_2 coated MWCNT was also supported by TEM analysis (discussed later). Another peak was found at 288.73 eV which corresponds to the C–O–Ti bond [34, 36]. The peaks at 530.6 and 532.7 eV of standard anatase TiO_2 corresponding to the lattice and surface oxygen, were shifted to 531.16 and 533.23 eV, respectively, in the O1s XPS spectrum of TiO_2 coated MWCNT. This shift may be due to the bonding between oxygen and carbon present in MWCNT. The peaks present in the XPS spectrum of Ti (in TiO_2 coated MWCNT) corresponds to 459.2 and 465.5 eV for $Ti2p_{1/2}$ and $Ti2p_{3/2}$ respectively, which were shifted from the standard anatase TiO_2 peaks (458.4 and 464.2 eV). Absence of C–Ti direct bonding in the C1s spectra (281.3 eV) and the shifting in the XPS spectrum of Ti, O and C core levels confirmed the formation of C–O–Ti bond in TiO_2 coated MWCNT.

4.3. Morphological study

SEM images of the nanocomposites are shown in Figure 4. Figure 4a demonstrated the dispersion of MWCNTs in TPU matrix of RAM-MW whereas; Figure 4b shows the dispersion of TiO_2 particles in TPU matrix (RAM-Ti). In both cases the fillers

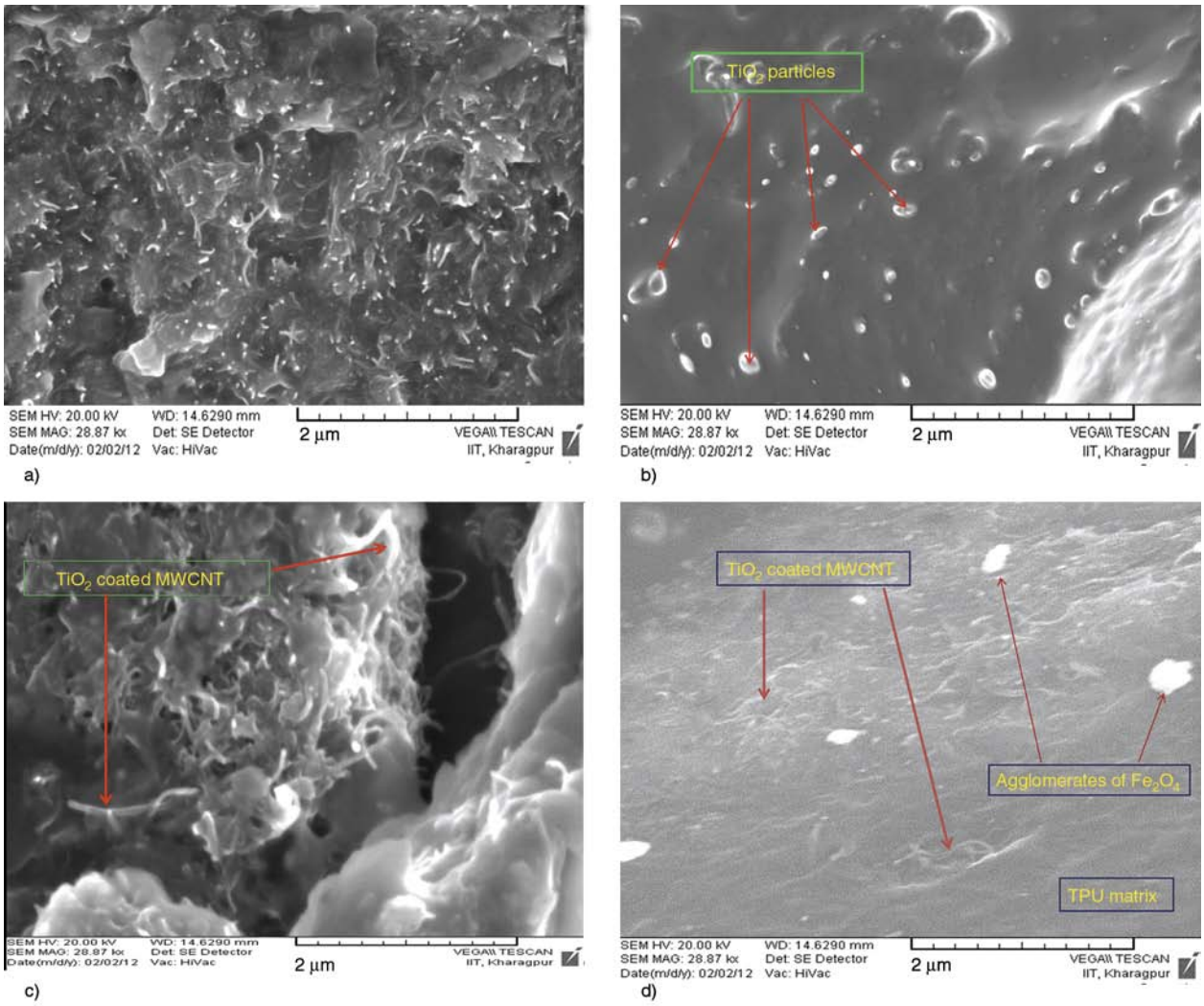

Figure 4. SEM images of (a) RAM-MW, (b) RAM-Ti, (c) TiO_2 coated MWCNT and (d) RAM-Ti@MW/Fe

were dispersed quite uniformly in the TPU matrix. Figure 4c shows the dispersion of TiO_2 coated MWCNTs in TPU matrix and the adhesion between the modified MWCNTs and TPU matrix was

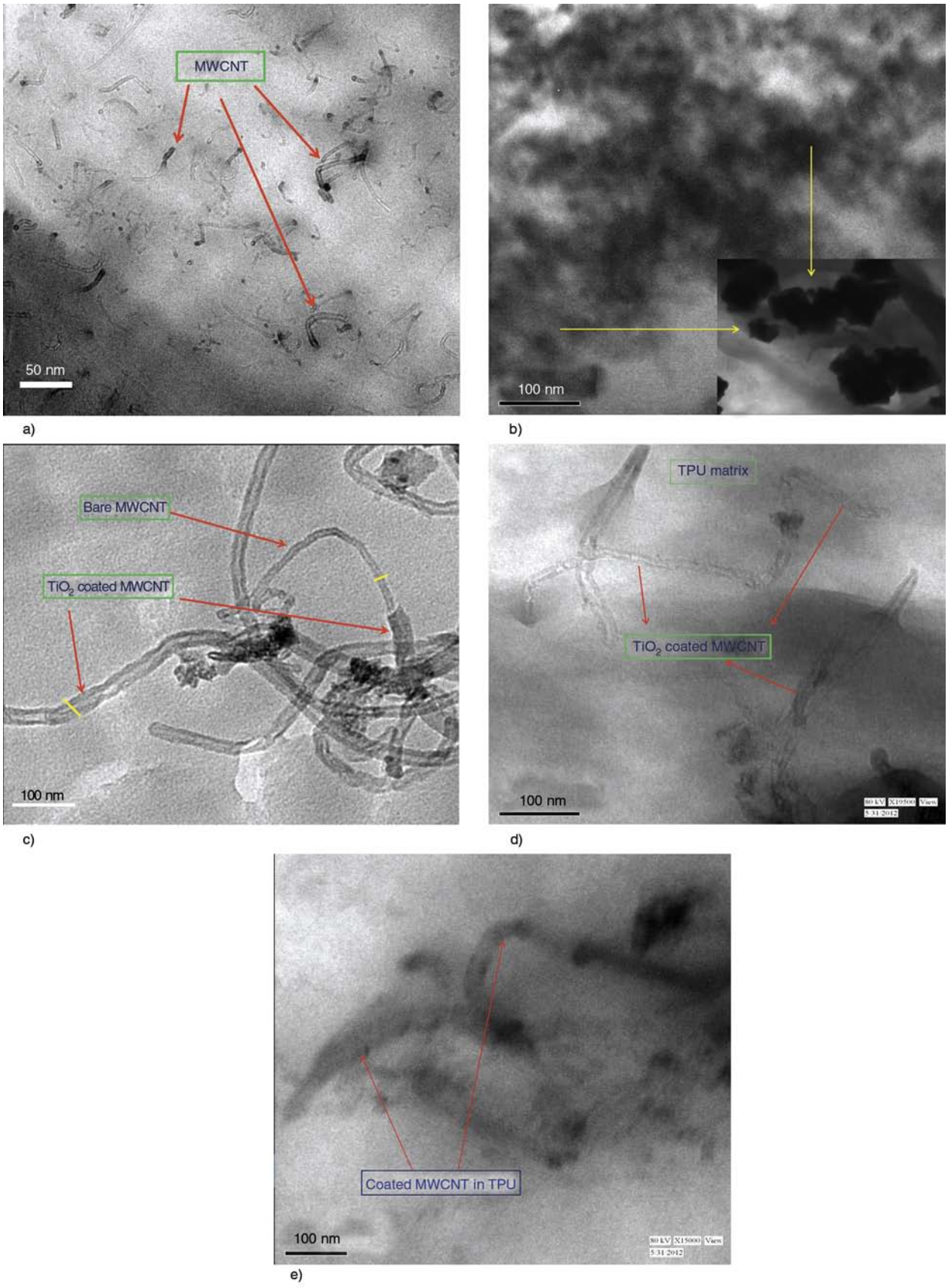

Figure 5. TEM images of (a) RAM-MW, (b) RAM-Ti, (c) TiO_2 coated MWCNT, (d) RAM-Ti@MW and (e) RAM-Ti@MW/Fe

observed to be better than the unmodified MWCNTs. Figure 4d shows the dispersion of TiO_2 coated MWCNTs and ferrite particles in TPU matrix. To further confirm the dispersion of nanofillers in TPU matrix, TEM analysis was done and discussed below.

Figure 5a–e, shows the TEM images for all nanocomposites. Figure 5a and 5b shows the dispersion of unmodified MWCNTs and TiO_2, respectively, and further confirms the uniform dispersion of nanofillers in TPU matrix. Figure 5c shows the TEM image of TiO_2 coated MWCNTs. It was observed that certain section of MWCNTs remain uncoated during the sol-gel coating process. It was also observed that the coated section (~ 40–45 nm) has larger diameter as compared to uncoated portion (~20–30 nm) which confirmed the coating of MWCNTs. Figure 5d showed the dispersion of TiO_2 coated MWCNT in TPU matrix to confirm the formation of RAM-Ti@MW. Figure 5e refers the formation of RAM-Ti@MW/Fe. Development of RAM-Ti@MW and RAM-Ti@MW/Fe was further confirmed by EDX analysis which proved the presence of different element in the composite and shown in Figure 6. The presence of Ti and Fe peaks in the EDX analysis of RAM-Ti@MW and RAM-Ti@MW/Fe was due to the presence of TiO_2 and Fe_3O_4, respectively.

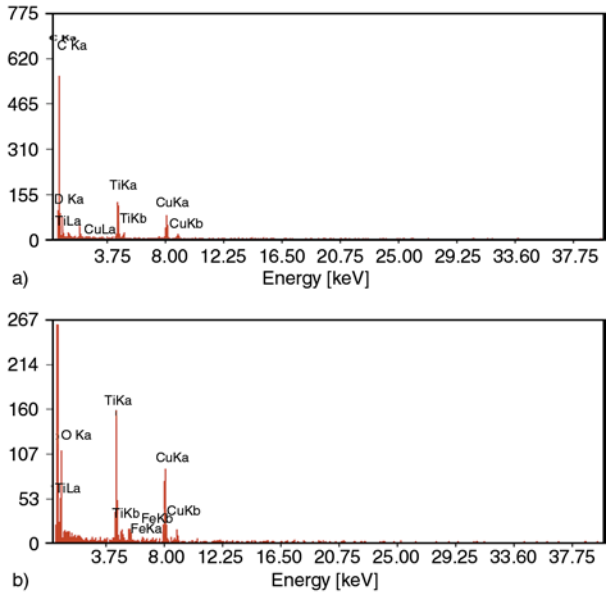

Figure 6. EDX study of (a) RAM-Ti@MW and, (b) RAM-Ti@MW/Fe

4.4. Microwave absorbing properties

The microwave absorbing properties of the prepared RAMs were explained with the help of the characteristic electromagnetic parameters by using the Equation (1) and (2) [37], are related in this manner:

$$Z = \sqrt{\frac{\mu_r}{\varepsilon_r}} \tanh\left[-j\left(\frac{2\pi}{c}\right)(\sqrt{\mu_r \varepsilon_r})fd \right] \quad (1)$$

$$\text{Reflection loss (in dB)} \quad -20\log\left[\left|\frac{z-1}{z+1}\right|\right] \quad (2)$$

where Z is the normalized input impedance with respect to the impedance in free space and reflection loss (RL) is in decibels [dB], μ_r and ε_r are the relative complex permeability and permittivity of the absorber medium, f and c are the frequency of microwave in free space and the velocity of light, respectively and d is the sample thickness. Figure 7 represents the reflection loss V_s frequency plot for all the four RAMs. The prepared RAMs showed the absorbing properties in a wide frequency range in the X-band region. RAM-MW, RAM-Ti, RAM-

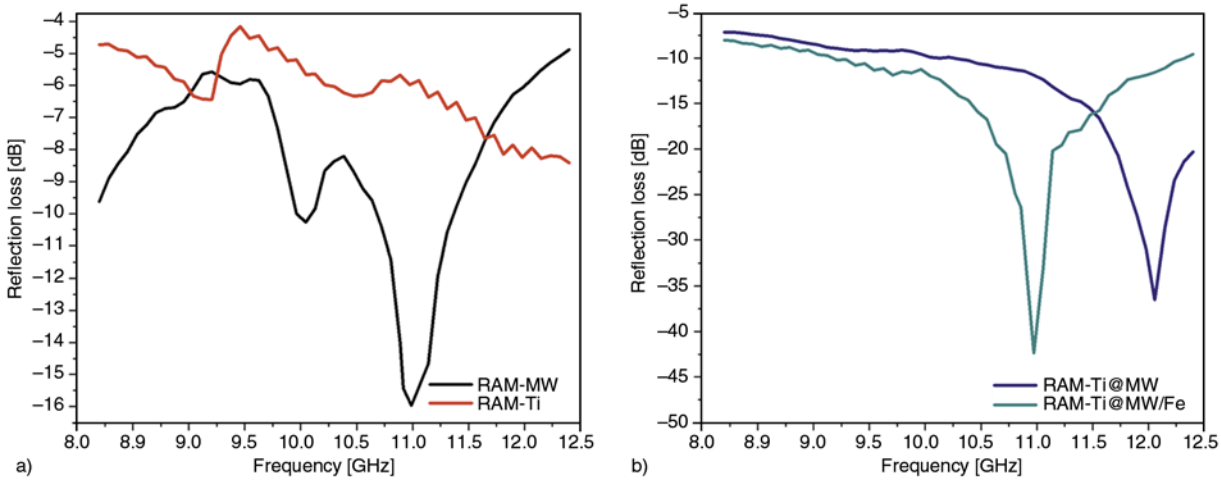

Figure 7. Reflection loss V_s frequency plot of (a) RAM-MW and RAM-Ti, (b) RAM-Ti@MW and RAM-Ti@MW/Fe

Ti@MW and RAM-Ti@MW/Fe displayed the maximum reflection loss of –16.03 dB at 10.99 GHz, –8.4 dB at 12.4 GHz, –36.44 dB at 12.05 GHz and –42.53 dB at 10.98 GHz respectively. Hence, from Figure 7a, it was observed that the MWCNT based nanocomposite possessed superior microwave absorption property as compared to TiO_2 based nanocomposite. RAM-Ti@MW and RAM-Ti@MW/Fe are most promising for RADAR application compared to other two. TiO_2 coated MWCNT composite showed improved microwave absorbing properties than its individual components. Addition of magnetite (Fe_3O_4) evidently enhanced the microwave absorbing properties of TiO_2 coated MWCNT composite. RAM-Ti@MW showed the reflection loss of –10 dB or more (absorption about 90% and above) by covering a frequency range from 10.01 GHz to 12.4 GHz. RAM-Ti@MW/Fe also covered a long frequency range of 9.15–12.4 GHz in the X-band region, where the reflection loss value is –10 dB or greater. According to the transmission line theory, [38] permittivity, permeability, sample thickness, and electromagnetic wave frequency can influence the reflectivity of electromagnetic wave which transmits through a medium. In this particular case, the frequency of radiation and thickness of the sample remained same for all the RAMs. So, to explain the variation in reflectivity, we studied the permittivity and permeability characteristics of the RAMs. The microwave absorption result of RAM-MW and RAM-Ti can be explained by considering their qualitative nature of conductivity. MWCNT is conducting whereas TiO_2 is insulating. For good microwave absorption optimum conductivity of material is needed. Material with low conductivity may cause partial absorption of the microwave and highly conducting material transmits or reflects the wave without any absorption [39]. Since, the MWCNT has free electrons in its skeleton, so it can absorb energy and helps in attenuating as well [40]. Further the high surface area of MWCNT also may be a reason for its good microwave absorption behaviour. Now, if MWCNT and TiO_2 involved in making a composite then it showed far better result than the individual component. This is may be due to the good combination between a conducting and an insulating material. TiO_2 is a semiconducting material with low band gap energy of 3.23 eV, which also can assist the microwave absorption [41]. The addition of Fe_3O_4 in TiO_2 coated MWCNT further helps in absorption and increases the reflection loss due to the loss initiated by a magnetic component. That is why RAM-Ti@MW/Fe becomes the superior microwave absorbing material among all. RAM-Ti@MW is only responsible for dielectric loss but RAM-Ti@MW/Fe showed its microwave absorption ability due to both dielectric and magnetic loss.

4.5. Relative complex permittivity and permeability

The possible mechanism of microwave absorption was investigated with the help of the real and imaginary part of complex permittivity (ε', ε'') and permeability (μ', μ''), where the real and imaginary part infers to the storage and loss part of the energy of a material respectively. Figure 8a and 8b showed the real and imaginary parts of complex relative permittivity spectra for all four RAMs respectively. Figure 8c showed the real and imaginary parts of complex relative permeability for RAM-Ti@MW/Fe which contain a magnetic component. The values of real part of permittivity (ε') for RAM-MW, RAM-Ti, RAM-Ti@MW and RAM-Ti@MW/Fe are 14.95–15.71, 3.68–3.84, 5.11–5.03 and 6.78– 6.56 respectively. The values of imaginary part of permittivity (ε'') for RAM-MW, RAM-Ti, RAM-Ti@MW and RAM-Ti@MW/Fe are 2.86–2.93, 0, 1.02–1.03 and 1.51–1.47 respectively. The lines for both real and imaginary part of permittivity remain almost constant throughout the whole frequency range in X-band region. The extent of polarization happening in the material is related to the real part of permittivity (ε') and the imaginary part (ε'') of permittivity is associated with the energy dissipated [42]. The different possible polarization mechanisms, which are helpful to describe the dielectric performance of the material, are ionic, electronic, orientational, and space charge polarization. In the microwave frequency range the active contribution can only be expected from orientational, and space charge polarization. The heterogeneity exists in the material is responsible for space charge polarization and the bound charges (dipoles) present in the material is answerable to the orientational polarization [43]. Hence, only orientational polarization may happen in RAM-Ti whereas, for other RAMs both orientational and space charge polarization can play a major role towards their dielectric performances. The values of real (μ') and imaginary part (μ'') of permeability for RAM-Ti@MW/Fe was determined

and lie from 1.18 to 1.02 and 0.006 to 0.002 respectively. The real part of permeability decreases with increase in frequency whereas, the imaginary part of permeability (μ'') is almost zero and independent on frequency. To understand the particular loss mechanism for each RAM, we have showed the loss tangent vs frequency plot in Figure 8d and 8e.The dielectric and magnetic loss tangents can be

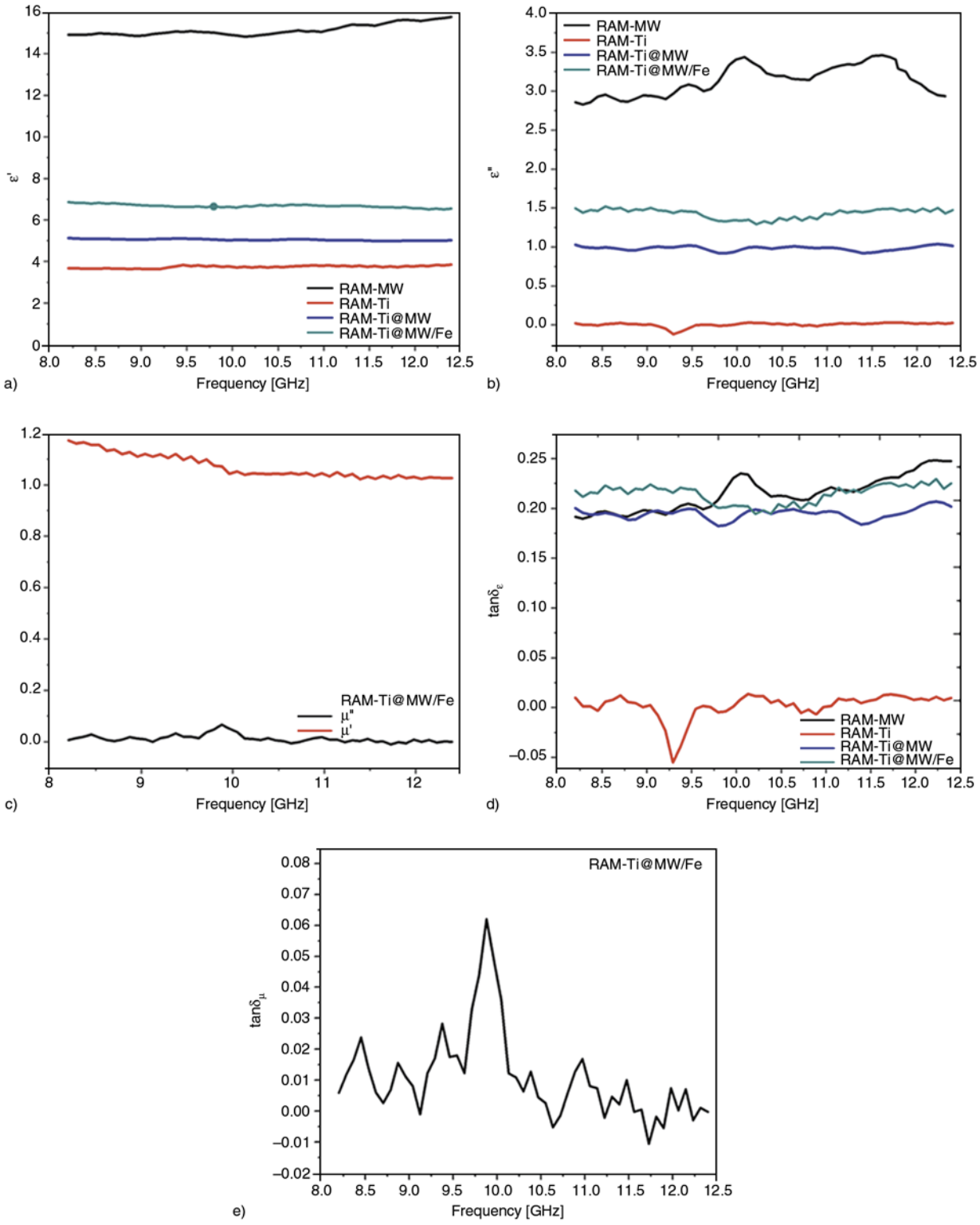

Figure 8. (a) Real (ε') and (b) imaginary (ε'') parts of relative complex permittivity of prepared RAMs, (c) real (μ') and imaginary (μ'') parts of relative complex permeability of RAM-Ti@MW/Fe, (d) loss tangent of relative complex permittivity ($\tan\delta_\varepsilon$) of the prepared RAMs and (e) loss tangent of relative complex permeability ($\tan\delta_\mu$) of RAM-Ti@MW/Fe

expressed as $\tan\delta_\varepsilon = \varepsilon''/\varepsilon'$ and $\tan\delta_\mu = \mu''/\mu'$, respectively. Figure 8d showed the dielectric loss and Figure 8e showed the magnetic loss as a function of frequency. The plot showed that RAM-Ti@MW/Fe has both dielectric and magnetic loss part but the other RAMs showed mainly dielectric loss. This plots showed some negative values at different portion which might be due to the noise [44]. Addition of Fe_3O_4 particle may cause the hysteresis loss and eddy current loss which is responsible for magnetic loss [45]. Hence, the permittivity and permeability data supported the microwave absorption results of the prepared RAMs.

4.6.Thermo gravimetric analysis (TGA)

The thermal stability of the RAMs namely RAM-MW, RAM-Ti, RAM-Ti@MW and RAM-Ti@MW/Fe were analysed by TGA instrument, in nitrogenous atmosphere and shown in Figure 9. Thermally stable RAMs are required for its application in stealth technology. All the four RAMs showed similar behaviour in their TGA analysis but their thermal stabilities were found to be different. RAM-Ti@MW/Fe is comparatively most thermally stable material among all. The TGA analysis was performed from 30 to 800°C. The thermal degradation was started after 330°C for all four RAMs and before 330°C, the loss is insignificant. Up to 430°C the residual weight loss is only 15%. After 430°C, the loss becomes noticeable for all RAMs and at 500°C the loss reached to the maxima. From 500 to 800°C, all showed a constant line but the extent of loss is different. Maximum weight loss for RAM-MW, RAM-Ti, RAM-Ti@MW and RAM-Ti@MW/Fe is 81, 79, 77 and 74% respectively i.e. a decreasing trend which may be due to the increase in multiple bonding sites provided by different fillers present in the composite. Hence, all RAMs can be used up to 330°C effectively but RAM-Ti@MW/Fe is most thermally stable material. The highest thermal stability for RAM-Ti@MW/Fe was may be due to the better interaction between the components of the composite.

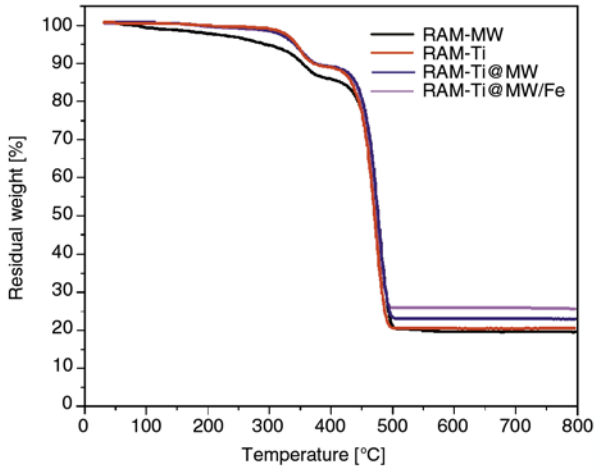

Figure 9. TGA plot of RAM-MW, RAM-Ti, RAM-Ti@MW and RAM-Ti@MW/Fe

5. Conclusions

MWCNT based nanocomposites were prepared and characterized by different techniques to confirm their formation and then microwave absorption behaviour was discussed systematically. The maximum reflection loss achieved by RAM-Ti@MW/Fe was –42.53 dB which was the result of optimal combination of both dielectric loss and magnetic loss. Dielectric loss mainly comes from dielectric material TiO_2 and MWCNT, whereas magnetic loss was mainly due to the Fe_3O_4. Other RAMs were also attractive but RAM-Ti@MW/Fe was the most promising candidate in 8.2–12.4 GHz region. TGA measurement showed that RAM-Ti@MW/Fe was thermally more stable among all nanocomposites. Hence, TiO_2 coated MWCNT and its nanocomposites were encouraging candidate as radar absorbing materials with usability in a wide frequency range maintaining strong absorption.

Acknowledgements

The authors are thankful to IIT Kharagpur. P.B. and S.S. are also thankful to Council of Scientific and Industrial Research (CSIR), New Delhi, India for providing the fellowship.

References

[1] Kakirde A., Sinha B., Sinha S. N.: Development and characterization of nickel-zinc spinel ferrite for microwave absorption at 2·4 GHz. Bulletin of Materials Science, **31**, 767–770 (2008).
DOI: 10.1007/s12034-008-0121-2

[2] Guo J., Wu H., Liao X., Shi B.: Facile synthesis of size-controlled silver nanoparticles using plant tannin grafted collagen fiber as reductant and stabilizer for microwave absorption application in the whole Ku band. Journal of Physical Chemistry C, **115**, 23688–23694 (2011).
DOI: 10.1021/jp207194a

[3] Liu Z., Bai G., Huang Y., Li F., Ma Y., Guo T., He X., Lin X., Gao H., Chen Y.: Microwave absorption of single-walled carbon nanotubes/soluble cross-linked polyurethane composites. Journal of Physical Chemistry C, **111**, 13696–13700 (2007).
DOI: 10.1021/jp0731396

[4] Zhan Y., Meng F., Yang X., Zhao R., Liu X.: Solvothermal synthesis and characterization of functionalized graphene sheets (FGSs)/magnetite hybrids. Materials Science and Engineering: B, **176**, 1333–1339 (2011).
DOI: 10.1016/j.mseb.2011.07.023

[5] Nanni F., Travaglia P., Valentini M.: Effect of carbon nanofibres dispersion on the microwave absorbing properties of CNF/epoxy composites. Composites Science and Technology, **69**, 485–490 (2009).
DOI: 10.1016/j.compscitech.2008.11.026

[6] Lv X., Yang S. L., Jin J. H., Zhang L., Li G., Jiang J. M.: Microwave absorbing characteristics of epoxy composites containing carbon black and carbon fibers (in Korean). Polymer-Korea, **33**, 420–428 (2009).

[7] Wang Y. T., Wang C. S., Yin H. Y., Wang L. L., Xie H. F., Cheng R. S.: Carboxyl-terminated butadiene-acrylonitrile-toughened epoxy/carboxyl-modified carbon nanotube nanocomposites: Thermal and mechanical properties. Express Polymer Letters, **6**, 719–728 (2012).
DOI: 10.3144/expresspolymlett.2012.77

[8] Das C. K., Bhattacharya P., Karla S. S.: Graphene and MWCNT: Potential candidate for microwave absorbing materials. Journal of Materials Science Research, **1**, 126–132 (2012).
DOI: 10.5539/jmsr.v1n2p126

[9] Singh V. K., Shukla A., Patra M. K., Saini L., Jani R. K., Vadera S. R., Kumar N.: Microwave absorbing properties of a thermally reduced graphene oxide/nitrile butadiene rubber composite. Carbon, **50**, 2202–2208 (2012).
DOI: 10.1016/j.carbon.2012.01.033

[10] Yang Y. L., Gupta M. C., Dudley K. L., Lawrence R. W.: Novel carbon nanotube–polystyrene foam composites for electromagnetic interference shielding. Nano Letters, **5**, 2131–2134 (2005).
DOI: 10.1021/nl051375r

[11] Qi X., Yang Y., Zhong W., Deng Y., Au C., Du Y.: Large-scale synthesis, characterization and microwave absorption properties of carbon nanotubes of different helicities. Journal of Solid State Chemistry, **182**, 2691–2697 (2009).
DOI: 10.1016/j.jssc.2009.07.036

[12] Zhu H., Lin H., Guo H., Yu L.: Microwave absorbing property of Fe-filled carbon nanotubes synthesized by a practical route. Materials Science and Engineering: B, **138**, 101–104 (2007).
DOI: 10.1016/j.mseb.2006.12.018

[13] Liu X. G., Li B., Geng D. Y., Cui W. B., Yang F., Xie Z. G., Kang D. J., Zhang Z. D.: (Fe, Ni)/C nanocapsules for electromagnetic-wave-absorber in the whole Ku-band. Carbon, **47**, 470–474 (2009).
DOI: 10.1016/j.carbon.2008.10.028

[14] Kim J-H., Kim S-S.: Microwave absorbing properties of Ag-coated Ni–Zn ferrite microspheres prepared by electroless plating. Journal of Alloys Compounds, **509**, 4399–4403 (2011).
DOI: 10.1016/j.jallcom.2011.01.050

[15] Shi G. M., Zhang J. B., Yu D. W., Chen L. S.: Synthesis and microwave-absorbing properties of Al_2O_3 coated polyhedral Fe nanocapsules prepared by arc-discharge method. Advanced Materials Research, **299–300**, 739–742 (2011).
DOI: 10.4028/www.scientific.net/AMR.299-300.739

[16] Kavanloui M., Hashemi B.: Effect of B_2O_3 on the densification and magnetic properties of Li–Zn ferrite. Materials and Design, **32**, 4257–4261 (2011).
DOI: 10.1016/j.matdes.2011.04.019

[17] Liu Z., Bai G., Huang Y., Ma Y., Du F., Li F., Guo T., Chen Y.: Reflection and absorption contributions to the electromagnetic interference shielding of single-walled carbon nanotube/polyurethane composites. Carbon, **45**, 821–827 (2007).
DOI: 10.1016/j.carbon.2006.11.020

[18] Li N., Huang Y., Du F., He X., Lin X., Gao H., Ma Y., Li F., Chen Y., Eklund P. C.: Electromagnetic interference (EMI) shielding of single-walled carbon nanotube epoxy composites. Nano Letters, **6**, 1141–1145 (2006).
DOI: 10.1021/nl0602589

[19] Meng F., Zhao R., Zhan Y., Lei Y., Zhong J., Liu X.: Preparation and microwave absorption properties of Fe-phthalocyanine oligomer/Fe_3O_4 hybrid microspheres. Applied Surface Science, **257**, 5000–5006 (2011).
DOI: 10.1016/j.apsusc.2011.01.010

[20] Murugan M., Kokate V. K., Bapat M. S.: Synthesis, characterization and evaluation of reflectivity of nano-sized $CaTiO_3$/epoxy resin composites in microwave bands. Bulletin of Materials Science, **34**, 699–704 (2011).
DOI: 10.1007/s12034-011-0184-3

[21] Che R. C., Zhi C. Y., Liang C. Y., Zhou X. G.: Fabrication and microwave absorption of carbon nanotubes/$CoFe_2O_4$ spinel nanocomposite. Applied Physics Letters, **88**, 033105/1–033105/3 (2006).
DOI: 10.1063/1.2165276

[22] Kim S. K., Kim W-D., Kim K-M., Hwang C. S., Jeong J.: High dielectric constant TiO_2 thin films on a Ru electrode grown at 250°C by atomic-layer deposition. Applied Physics Letters, **85**, 4112–4114 (2004).
DOI: 10.1063/1.1812832

[23] Zhou W., Hu X., Bai X., Zhou S., Sun C., Yan J., Chen P.: Synthesis and electromagnetic, microwave absorbing properties of core–shell Fe_3O_4–poly(3, 4-ethylenedioxythiophene) microspheres. ACS Applied Materials and Interfaces, **3**, 3839–3845 (2011).
DOI: 10.1021/am2004812

[24] Ni S., Wang X., Zhou G., Yang F., Wang J., He D. J.: Designed synthesis of wide range microwave absorption Fe_3O_4–carbon sphere composite. Journal of Alloys and Compounds, **489**, 252–256 (2010). DOI: 10.1016/j.jallcom.2009.09.065

[25] Hudec B., Husekova K., Dobrocka E., Lalinsky T., Aarik J., Aidla A., Frohlich K.: High-permittivity metal-insulator-metal capacitors with TiO_2 rutile dielectric and RuO_2 bottom electrode. Materials Science and Engineering, **8**, 012024/1–012024/4 (2010). DOI: 10.1088/1757-899X/8/1/012024

[26] Li C., Wang J., Wang X., Su W., Chen H., Zhuang D.: Nonlinear electrical properties of TiO_2–Y_2O_3–Nb_2O_5 capacitor-varistor ceramics. Materials Science and Engineering: B, **85**, 6–10 (2001). DOI: 10.1016/S0921-5107(01)00563-3

[27] Grätzel M.: Solar energy conversion by dye-sensitized photovoltaic cells. Inorganic Chemistry, **44**, 6841–6851 (2005). DOI: 10.1021/ic0508371

[28] Waser R.: Nanoelectronics and information technology. Wiley-VCH Weinhein (2003).

[29] Lee C-S., Kim J., Son J. Y., Choi W., Kim H.: Photocatalytic functional coatings of TiO_2 thin films on polymer substrate by plasma enhanced atomic layer deposition. Applied Catalysis B: Environmental, **91**, 628–633 (2009). DOI: 10.1016/j.apcatb.2009.06.037

[30] Jia Y., Jiang Z. M., Gong X. L., Zhang Z.: Creep of thermoplastic polyurethane reinforced with ozone functionalized carbon nanotubes. Express Polymer Letters, **6**, 750–758 (2012). DOI: 10.3144/expresspolymlett.2012.80

[31] Yuen S-M., Ma C-C. M., Lin Y-Y., Kuan H-C.: Preparation, morphology and properties of acid and amine modified multiwalled carbon nanotube/polyimide composite. Composites Science and Technology, **67**, 2564–2573 (2007). DOI: 10.1016/j.compscitech.2006.12.006

[32] Vatanpour V., Madaeni S. S., Moradian R., Zinadini S., Astinchap B.: Novel antibifouling nanofiltration polyethersulfone membrane fabricated from embedding TiO_2 coated multiwalled carbon nanotubes. Separation and Purification Technology, **90**, 69–82 (2012). DOI: 10.1016/j.seppur.2012.02.014

[33] Yuen S-M., Ma C-M., Chuang C-Y., Hsiao Y-H., Chiang C-L., Yu A.: Preparation, morphology, mechanical and electrical properties of TiO_2 coated multiwalled carbon nanotube/epoxy composites. Composites Part A: Applied Science and Manufacturing, **39**, 119–125 (2008). DOI: 10.1016/j.compositesa.2007.08.021

[34] Nayak G. C., Sahoo S., Rajasekar R., Das C. K.: Novel approach for the selective dispersion of MWCNTs in the Nylon/SAN blend system. Composites Part A: Applied Science and Manufacturing, **43**, 1242–1251 (2012). DOI: 10.1016/j.compositesa.2012.03.008

[35] Lee T. Y., Alegaonkar P. S., Yoo J-B.: Fabrication of dye sensitized solar cell using TiO_2 coated carbon nanotubes. Thin Solid Films, **515**, 5131–5135 (2007). DOI: 10.1016/j.tsf.2006.10.056

[36] Okpalugo T. I. T., Papakonstantinou P., Murphy H., McLaughlin J., Brown N. M. D.: High resolution XPS characterization of chemical functionalised MWCNTs and SWCNTs. Carbon, **43**, 153–161 (2005). DOI: 10.1016/j.carbon.2004.08.033

[37] Gang Y-R.: Electromagnetic properties and microwave absorption properties of $BaTiO_3$–carbonyl iron composite in S and C bands. Journal of Magnetism and Magnetic Materials, **323**, 1805–1810 (2011). DOI: 10.1016/j.jmmm.2011.02.013

[38] Michielssen E., Sajer J-M., Ranjithan S., Mittra R.: Design of lightweight, broad-band microwave absorbers using genetic algorithms. IEEE Transactions on Microwave Theory, **41**, 1024–1031 (1993). DOI: 10.1109/22.238519

[39] Li G., Xie T., Yang S., Jin J., Jiang J.: Microwave absorption enhancement of porous carbon fibers compared with carbon nanofibers. Journal of Physical Chemistry C, **116**, 9196–9201 (2012). DOI: 10.1021/jp300050u

[40] Wu J., Kong L.: High microwave permittivity of multiwalled carbon nanotube composites. Applied Physics Letters, **84**, 4956–4958 (2004). DOI: 10.1063/1.1762693

[41] Xiao H-M., Liu X-M., Fu S-Y.: Synthesis, magnetic and microwave absorbing properties of core-shell structured $MnFe_2O_4/TiO_2$ nanocomposites. Composites Science and Technology, **66**, 2003–2008 (2006). DOI: 10.1016/j.compscitech.2006.01.001

[42] Ohlan A., Singh K., Chandra A., Dhawan S. K.: Microwave absorption behavior of core–shell structured poly (3,4-ethylenedioxy thiophene)–barium ferrite nanocomposites. ACS Applied Materials and Interfaces, **2**, 927–933 (2010). DOI: 10.1021/am900893d

[43] Zhang Q., Li C., Chen Y., Han Z., Wang H., Wang Z., Geng D., Liu W., Zhang Z.: Effect of metal grain size on multiple microwave resonances of Fe/TiO_2 metal-semiconductor composite. Applied Physics Letters, **97**, 133115/1–133115/3 (2010). DOI: 10.1063/1.3496393

[44] Chiu S-C., Yu H-C., Li Y-Y.: High electromagnetic wave absorption performance of silicon carbide nanowires in the gigahertz range. Journal of Physical Chemistry C, **114**, 1947–1952 (2010). DOI: 10.1021/jp905127t

[45] Zhua Y-F., Zhang L., Natsuki T., Fu Y-Q., Ni Q-Q.: Synthesis of hollow poly(aniline-*co*-pyrrole)–Fe_3O_4 composite nanospheres and their microwave absorption behavior. Synthetic Metals, **162**, 337–343 (2012). DOI: 10.1016/j.synthmet.2011.12.015

eXPRESS Polymer Letters Vol.7, No.3 (2013) 224–237
Available online at www.expresspolymlett.com
DOI: 10.3144/expresspolymlett.2013.21

Characterization of the morphology of iPP/sPP blends with various compositions

S. Bourbigot[1*], *L. Garnier*[1], *B. Revel*[2], *S. Duquesne*[1]

[1]ISP/UMET – UMR/CNRS 8207, Ecole Nationale Supérieure de Chimie de Lille (ENSCL), Avenue Dimitri Mendeleïev – Bât. C7a, BP 90108, 59652 Villeneuve d'Ascq Cedex, France
[2]Centre Commun de Mesures RMN, Université des Sciences et Technologies de Lille, 59650 Villeneuve d'Ascq, France

Received 26 August 2012; accepted in revised form 8 November 2012

Abstract. The paper investigates the morphology and the structural properties of blends of isotactic polypropylene (iPP) and syndiotactic polypropylene (sPP) having different compositions using different techniques. Solid-state nuclear magnetic resonance (NMR) permits via appropriate sequence to measure the composition, conformation and dynamics, and intimacy of mixing of polymeric materials. Measurement of relaxation times gives information on local structure of phases with different mobility. The morphology is directly related to the structural organization of the blends. The crystallization rate decreases as a function of the sPP content. The minor component is dispersed as a nodule in the main component of the blend and it plays the role of nucleating agent on it. Besides, morphology changes occur for the composition 50/50 (wt/wt) of the blend iPP/sPP. Different phases are identified, namely free amorphous, constrained amorphous and crystalline regions which exhibit different molecular mobilities. It is also shown at the interphase matrix-nodules, the nodules create a constrained amorphous zone.

Keywords: *polymer blends, syndiotactic polypropylene, isotactic polypropylene, morphology*

1. Introduction

Syndiotactic polypropylene (sPP) was first synthesized in the early 1960s with a Ziegler Natta catalyst [1]. Unfortunately, this new stereoregular polypropylene exhibited low syndiotacticity and had poor mechanical and thermal properties which prevented it for many applications. The use of new metallocene catalysts allowed Ewen *et al*. [2] to synthesize a sPP with high tacticity in 1988. This new sPP exhibits superior properties including toughness and excellent elastic behavior [3]. The excellent elastic properties of sPP are based upon a phase transition occurring in the crystalline regions during stretching (four crystalline forms have been found for sPP). In the most stable forms (form I and form II), chains are in a helical conformation while they are in a trans-planar conformation in the metastable forms III and IV. Previous investigations found that stretching of sPP blends and fibers induce a transition from the stable form I or II to form III. This transition is reversible because form I or II is again obtained when the applied stress is removed [4]. However, besides its excellent elastic properties sPP exhibits many disadvantages such as poor mechanical properties, very complicated polymorphism and slow crystallization rate [5, 6].

Blending sPP with another material having better mechanical properties and a faster crystallization rate can be an alternative for improving processing of sPP. So, investigations have been performed on sPP blends with isotactic polypropylene (iPP). Thomman *et al.* [7] found that iPP/sPP blends are

*Corresponding author, e-mail: serge.bourbigot@ensc-lille.fr

phase separated. They showed that crystallization of iPP and sPP occurs separately and that crystallization of iPP/sPP blend is dependent on the crystallization nature of the neat components. An iPP matrix with a dispersed sPP phase or a sPP matrix with an iPP dispersed phase can be obtained as a function of the blend composition. A co-continuous morphology was also found for nearly equi-mass compositions. Those results were then confirmed by Clancy *et al*. [8] by numerical simulation. Using the method of equilibrium melting points, Woo *et al.* [9] assessed the Flory-Huggins interaction parameter of the sPP/iPP blend and they found it was nearly zero indicating that the interactions in the blend are weak. They suggest a state of mixture bordering on phase separation or in other words, the blend iPP/sPP is immiscible. It is also confirmed by Phillips [10] and by Wang *et al.* [11] on iPP/sPP blend of composition 50/50 (wt/wt). Zou *et al.* [12] also examined this composition and its behavior during injection-molding. They found a dispersed structure in the skin layer and a co-continuous structure in the core layer. It was explained by the difference of crystallization temperature of iPP and sPP inducing a migration phenomenon and creating then composition inhomogeneity in the blend. Zhang *et al.* [5] report similar conclusions for different compositions of iPP/sPP investigating morphology and mechanical behavior of iPP/sPP blends and fibers. However, they suggest that the amorphous phases of iPP and sPP might be partially interconnected. This interconnection is also suggested by Gorrasi *et al.* [13] examining mechanical properties of iPP/sPP fibers. Finally, the miscibility of the iPP/sPP blends was investigated by NMR and rheology by Zheng *et al.* [14]. They confirmed the immiscibility of the blends for a wide range of composition but they found for compositions containing a low amount of sPP (iPP/sPP 90/10 (wt/wt)) that no phase separation was observed. They explained this miscibility by the existence of intermolecular chain interactions between sPP and iPP components in the solid state.

Although many investigations have been done on morphology of iPP/sPP blends, questions remain and it is the goal of this paper to investigate the structure and the morphology of iPP/sPP blends of various compositions. Solid-state nuclear magnetic resonance (NMR) is a powerful method for measuring the composition, conformation and dynamics, and intimacy of mixing of solid materials. In particular in the case of polymeric blends, NMR permits to analyze the miscibility, phase structure, and heterogeneity of polymer mixtures on a molecular scale [15, 16]. It is especially useful in polymeric blend systems containing complex phase structures that may exist beyond the resolution limits of traditional microscopic or thermal analyses. Many different NMR parameters can be used to study molecular motions like relaxation times. The relaxation times of ^{1}H nucleus contain a large amount of information on the dynamics. It can be expected measuring relaxation times to get information on local structure of phases with different mobilities. In particular, spin-lattice relaxation times are very sensitive to the short spatial proximity of interacting dipole moments of the protons. Wide-line ^{1}H NMR permits the determination of different phases, interphases and the measurement of the crystallinity in polymers [17–19]. High-resolution solid-state ^{13}C NMR is a selective method that permits following the motional behavior of each carbon of the repeat unit independently [20, 21]. From those measurements, two useful proton spin-relaxation times can be obtained: the spin lattice relaxation times in the laboratory frame, T_1, and in the rotating frame, $T_{1\rho}$. The length scale of heterogeneity – from a few nanometers to tens of nanometers – can be evaluated approximately from their values to allow measurements of compositional heterogeneity on length scales limited by spin diffusion [22].

This paper is organized in three parts. The first part will examine the morphology of blends iPP/sPP of different composition by electronic microscopy. Structural analyses of the blends will be then done using different techniques like scanning differential calorimetry (DSC), high resolution solid state NMR and wide-angle X-ray diffraction (WAXD). The third part is devoted to the investigations of the molecular dynamic in the blends iPP/sPP by solid state NMR.

2. Experimental

2.1. Materials

Commercial grades of isotactic polypropylene and syndiotactic polypropylene were used in this study. iPP (PPH9069) and sPP (Finaplas 1751) were supplied by Total petrochemicals (Feluy, Belgium). PPH9069 has a melt flow rate (MFR) for a load of 2.16 g at 230°C of 25 g/10 min whereas MFR of Finaplas 1751 is 20 g/10 min. Blends of iPP/sPP

(75/25, 50/50, 40/60, 30/70, 25/75 wt/wt) were prepared in a Brabender mixer at 190°C for 12 minutes with a shear rate of 50 rpm. Homopolymers of iPP and sPP were identically prepared in order to have blends and homopolymers with the same thermal history. Virgin polypropylenes and blends were ground to powder using a cryogenic crushing unit. All analyses (except electron microscopy) were performed with the prepared powder.

2.2. Electron microscopy

Scanning electron microscopy (SEM) was performed using a Hitachi S4700 microscope (Verrières-le-Buisson, France). All samples (piece of material got after melt-mixing) were cryo-fractured in liquid nitrogen before analysis. The fractured surface was observed with secondary electrons at 6 kV, 10 μA to get SEM images of the blends.

For transmission electron microscopy (TEM), all samples (piece of material got after melt-mixing) were ultra microtomed with a diamond knife on a Leica ultracut UCT microtome, at room temperature to give sections with a nominal thickness of 70 nm. Surface of the samples was then stained with RuO_4. Sections were transferred to Cu grids of 400 meshes. Bright-field TEM images of nanocomposites were obtained at 200 kV under low dose conditions with a Philips CM30 electron microscope (Zaventem, Belgium), using a Gatan CCD camera. Low magnification images were taken at 17 000× and high-magnification images were taken at 100 000×.

2.3. Differential scanning calorimetry (DSC)

Non isothermal crystallization kinetics of iPP/sPP blends were investigated by DSC using a TA Instruments Q100 Calorimeter (Guyancourt, France). All measurements were performed in nitrogen (nitrogen flow = 50 mL/min) to avoid degradation of the iPP/sPP blend upon heating. 8.3±0.1 mg of each sample were put in a sealed aluminum pan. Samples were first heated up from 25 to 200°C at a rate of 10°C/min and held for 10 minutes to erase thermal history of the blend. Samples were then cooled down at 10°C/min. Calculation of the degree of crystallinity of iPP ($\chi_{c,\,iPP}$) and sPP ($\chi_{c,\,sPP}$) has been done as Equations (1) and (2):

$$\chi_{c,\,PP} = \frac{\Delta H_{f,\,iPP}}{\Delta H^0_{f,\,iPP} \cdot wt\%_{iPP}} \tag{1}$$

$$\chi_{c,\,sPP} = \frac{\Delta H_{f,\,sPP}}{\Delta H^0_{f,\,sPP} \cdot wt\%_{sPP}} \tag{2}$$

where $\Delta H_{f,\,iPP}$ is the melting enthalpy of iPP (area of the melting endotherm of iPP), $\Delta H_{f,\,sPP}$ is the melting enthalpy of sPP (area of the melting endotherm of sPP). $\Delta H^0_{f,\,iPP}$ et $\Delta H^0_{f,\,sPP}$ are the melting enthalpies of iPP and sPP exhibiting 100% crystallinity and equaling 209 and 196 J/g respectively [5, 23–25]. 'wt% iPP' and 'wt% sPP' are the mass composition of the mixture. The degree of crystallinity of the blends has been calculated as follows (Equation (3)):

$$\chi_{c,\,mixture} = \chi_{c,\,iPP} \cdot wt\%_{iPP} + \chi_{c,\,sPP} \cdot wt\%_{sPP} \tag{3}$$

2.4. Wide-angle X-ray diffraction (WAXD)

WAXD spectra were recorded in the 10–80° 2θ range using a Bruker AXS D8 diffractometer (Champs-sur-Marne, France) ($\lambda_{(Cu\ K\alpha)}$ = 1.5418 Å, 40 keV, 25 mA) in configuration $2\theta/\theta$. The acquisition parameters were as follows: a step of 0.02°, a step time of 2 s. The data are analyzed using the diffraction patterns of inorganic crystal structure database (ICSD).

2.5. Solid state nuclear magnetic resonance (NMR)

High-resolution solid-state ^{13}C NMR spectra were recorded at 100.63 MHz using a Bruker Avance 400 spectrometer (9.4 T) (Wissembourg, France). A variable temperature 4 mm magic angle spinning (MAS) probe head was used. Samples were packed in zirconium dioxide rotors closed with boron nitride caps and spun at 10 kHz unless otherwise specified. The inner spinner volume was approximately 0.1 cm^3. All spectra were obtained by cross-polarization (CP) from the spin-locked protons, followed by high-power proton dipolar decoupling (DD). The matched spin-locked cross-polarization transfers were carried out with ^1H magnetic field strength of 55 kHz, corresponding to $\pi/2$ pulse duration of 3.5 μs. The Hartmann-Hahn condition was matched using glycine. Chemical shift calibrations were performed using the glycine (α-form) carbonyl carbon resonance at 176.03 ppm. Contact time and repetition time were 1 ms and 5 s, respectively. About 1024 scans were needed to obtain a suitable signal-to-noise ratio. Rotating frame spin–lattice relax-

ation times $T_{1\rho}$ (C) were also measured at different temperatures (25, 50, 80 and 100°C). A spin locking experiment was performed under CP and MAS conditions and the spin-lock pulse was up to 50 ms. ^{13}C spins were locked with the field of 64 kHz.

Low-resolution ^{1}H NMR experiments were carried out on the same spectrometer as above using a 4 mm static Bruker probe, with a ^{1}H $\pi/2$ pulse length of 2.5 μs corresponding to magnetic field strength of 100 kHz. Spin-lattice relaxation times in the laboratory frame, T_1 (^{1}H), were measured using the saturation-recovery pulse sequence with direct proton observation. Three closely spaced 90° pulses accomplished the saturation. Spin-lattice relaxation times, $T_{1\rho}$ (^{1}H), in the rotating frame were determined with a $\pi/2$ spin-lock experiment with a spin-locking field corresponding to 50 kHz for 4.8 μs. Measurements of all relaxation times were also performed at various temperatures (25, 50, 80 and 100°C).

3. Results and discussion

3.1. Morphology of the blends iPP/sPP

SEM images of virgin iPP and sPP are similar and no significant difference of morphology is revealed between the two samples (not shown). The morphologies of the blends 75/25 and 50/50 show the presence of two phases (Figure 1). The blend 75/25 exhibits a continuous phase (polymeric matrix) in which an additional phase is dispersed with a circular shape of different sizes (nodules are shown by circles on Figure 1a). In this blend, iPP is the main component and the continuous phase is assigned to it and the nodules are assigned to sPP. It is worth to note a different surface aspect between the two phases: the nodules exhibit rough surface while the continuous phase looks smooth. The blend 50/50 shows a different morphology compared to the blend 75/25 (Figure 1b). The nodules are larger in size (4–5 μm in average compared to 1–2 μm for the blend 75/25) and they are more ovoid than spherical. It indicates the general morphology turns into two co-continuous phases which is characteristic of immiscible blends having equal mass compositions.

The morphologies of the blends 40/60 and 30/70 are almost similar to those of the blend 75/25. The presence of continuous phase containing a dispersed phase with nodules having spherical shapes of different sizes is observed (Figure 2). Taking into account the blends' compositions, the continuous phase is assigned to sPP while the dispersed phase (nodules) is assigned to iPP. This assignment is confirmed noticing the nodules exhibit a smooth aspect while the continuous phase exhibits a rough surface. The opposite (in terms of aspect) was observed in the case of the blend 75/25. The nodules of the blend 40/70 are of 1 to 4 μm in size which are similar to those measured for the blend 50/50 (Figure 2a). The nodules of the blend 30/70 are smaller in size (1–2 μm in size) which is similar to those of the blend 75/25. These results indicate therefore the size of the nodules increases as a function of the concentration of the dispersed phase.

In order to confirm the assignments done from the SEM images, the morphologies have been then examined by TEM on samples stained by RuO_4. It permits to highlight the amorphous zones since it appears as dark zones on TEM images. Remarking that sPP exhibits low crystallinity, it should appear mainly in the dark zones permitting to distinguish between iPP and sPP (Figure 3–5).

As already observed by SEM, TEM images reveal that the blends iPP/sPP exhibit morphology consti-

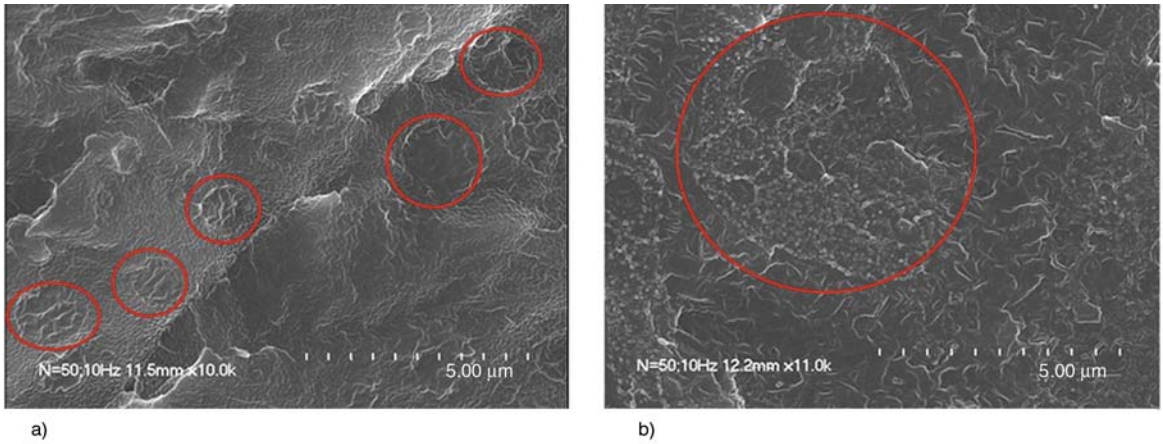

Figure 1. SEM images of cryo-fracturated surfaces of the blends iPP/sPP at (a) 75/25 and (b) 50/50 (nodules are in circles)

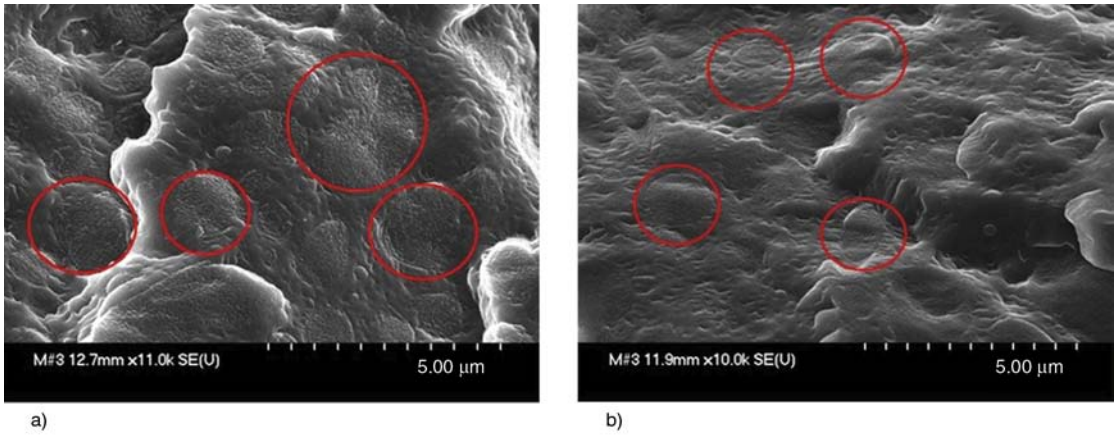

Figure 2. SEM images of cryo-fracturated surfaces of the blends iPP/sPP at (a) 40/60 and (b) 30/70 (nodules are in circles)

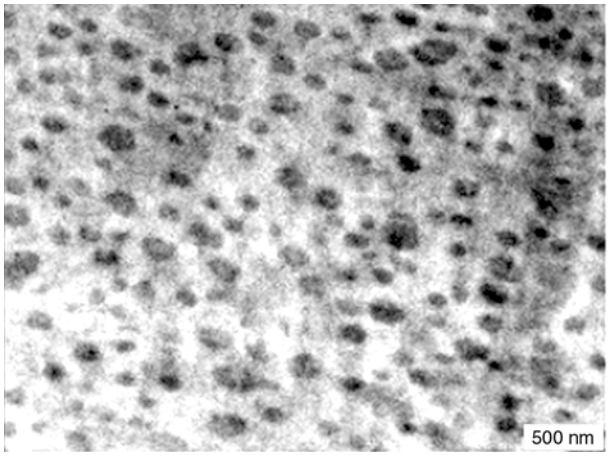

Figure 3. TEM image of the blend iPP/sPP 75/25 (×5000)

tuted by a continuous phase in which there is a dispersed phase (dispersed nodules). In the case of the blend 75/25, the nodules are elliptic in shape (Figure 3). The black color confirms that the dispersed phase is constituted by sPP. It is noteworthy that some zones in the continuous phase are darker suggesting iPP is not highly crystalline (this aspect will be discussed in the following). On the contrary, the dark zones of the blends 40/60 and 30/70 correspond to the continuous phase while the nodules are the bright zones (Figure 4). Hence it is confirmed that the blends 40/60 and 30/70 are constituted by a continuous phase of sPP in which nodules of iPP are dispersed. The nodules in the blend 40/60 exhibit various shapes and sizes. Finally in the blend 50/50, the continuous phase is constituted by iPP and the dispersed phase is sPP (Figure 5). The nodules exhibit various shapes and their sizes are larger compared to those of the other blends. Coalescence phenomenon is clearly shown on Figure 5 evidencing that the blend turns into two co-continuous phases as suggested by SEM. According to this TEM study, the co-continuous structure should be obtained for composition lying between 50/50 and 40/60.

3.2. Structural analysis of the blends iPP/sPP

SEM and TEM analyses have shown that the morphology of the blends iPP/sPP is bi-phasic. It can be then expected that structural changes can be induced by the different morphologies of the blends and it is

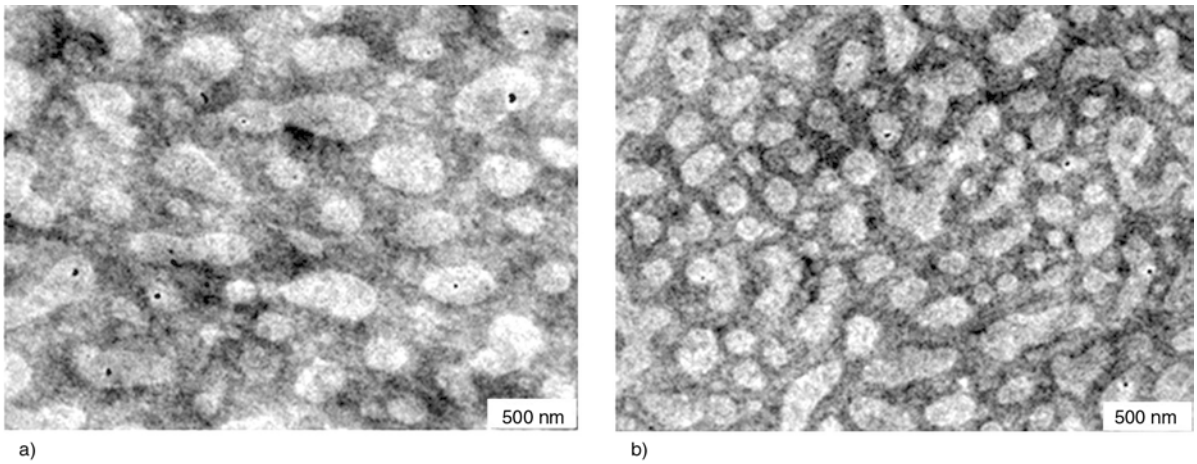

Figure 4. TEM images of the blends iPP/sPP at (a) 30/70 and (b) 40/60 (×5000)

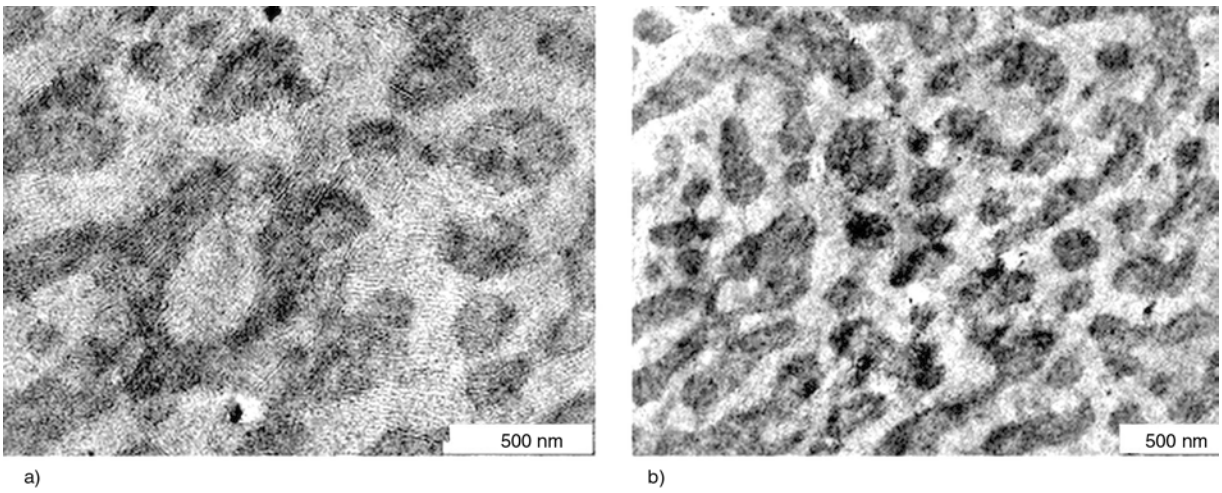

Figure 5. TEM images of the blends iPP/sPP at 50/50 at (a) ×10 000 and (b) ×5000

the purpose of this section to investigate this using DSC, WAXD and high resolution solid state 13C NMR.

3.2.1. DSC analysis

The temperatures of crystallization of the blends iPP/sPP have been determined by DSC during the cooling of the samples (Table 1). The DSC thermograms (not shown) exhibit two distinct exotherms corresponding to the crystallization of the two components of the blend. It shows therefore that iPP and sPP does not co-crystallize but on the contrary they crystallize separately. iPP crystallizes in the temperature range of 110–120°C while sPP crystallizes in the temperature range of 85–95°C. A shift in the crystallization temperatures of iPP and sPP in the blends is observed compared to the virgin polypropylenes. The incorporation of iPP in the blend up to the composition 50/50 increases $T_{c,\,sPP}$ and it favors the crystallization of sPP. In our previous work [26] on the crystallization kinetics of iPP/sPP blends, it was suggested that the incorporation of sPP in iPP promotes the formation of crystallization defaults which can act as nucleating sites. The crystallization is enhanced while sPP is in the dispersed phase and hence sPP exhibits higher crystallization temperatures until the composition reaches 50/50. It is also true in the case of incorporating sPP in iPP since a shift of $T_{c,\,iPP}$ is observed towards higher temperatures. Nevertheless from the blend 40/60, $T_{c,\,iPP}$ is lower than that of virgin iPP. These results evidence the immiscibility of the crystalline phases of iPP and sPP in the blends iPP/sPP but the shifts of the crystallization temperatures indicates intermolecular interactions between the two components.

Table 1. Crystallization temperatures measured by DSC of the blends iPP/sPP where $T_{c,\,iPP}$ and $T_{c,\,sPP}$ are the temperatures of crystallization of iPP and sPP respectively

Blend	$T_{c,\,iPP}$ [°C]	$T_{c,\,sPP}$ [°C]
100/0 (virgin iPP)	117.2	–
75/25	121.9	90.1
50/50	120.5	95.7
40/60	114.4	88.4
30/70	112.1	88.8
0/100 (virgin sPP)	–	85.9

Figure 6 shows DSC thermograms of the blends iPP/sPP during heating (melting cycle). Two distinct melting zones can be distinguished corresponding to the melting of the two components of the blend: (i) an endotherm at about 160°C assigned to the melting of iPP and (ii) a double endotherm at about 120–130°C assigned to the melting of sPP. The presence of these distinct two melting zones

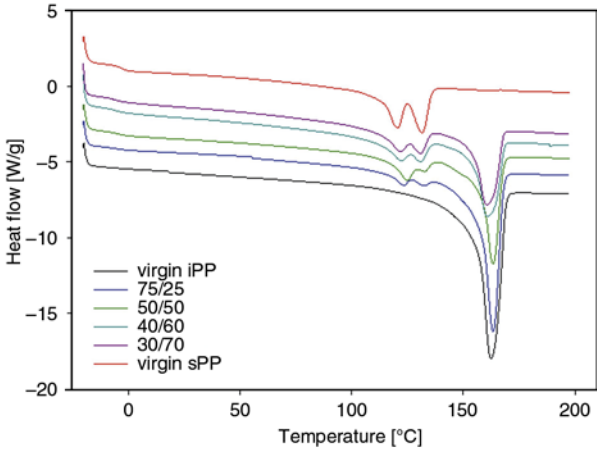

Figure 6. DSC thermograms of the blends iPP/sPP compared to virgin iPP and sPP during heating

confirms the conclusions made from the crystallization of the blends. The double endotherm is assigned to the characteristic behavior of the melting of the polymeric sPP chains in helical conformation (form I and/or II). It is indeed very rare under classical crystallization conditions to get stable crystalline forms (forms I or II) without defects. So, the first endotherm (at about 120°C) corresponds to the melting of defects and the second one (at about 130°C) is assigned to the melting of the polymeric chains without defects [5].

The degrees of crystallinity, χ_c, have been calculated from the melting endotherms and they are listed in Table 2. It is observed that whatever the composition of the blend, the degree of crystallinity of iPP is always higher than that of sPP. It was expected because sPP exhibits usually low degree of crystallinity especially compared to iPP. Besides, the degree of crystallinity of iPP decreases when the concentration of sPP increases up to 50/50 in the blend. The trend is inversed at low concentration of iPP in the blend iPP/sPP (blends at 40/60 and 30/70), the degree of crystallinity of iPP increases and it is even higher for the blend 30/70 than that of virgin iPP. In the case of sPP, its degree of crystallinity decreases with the incorporation of iPP in the blend but the influence of the composition is less than in the case of iPP.

Glass transition temperatures, T_g, of the blends iPP/sPP determined on the DSC thermograms (graphs not shown) are listed in Table 3. It is noteworthy that only one T_g is observed for all samples. It is recognized that immiscible blends like iPP/sPP should exhibit two distinct Tg. The miscibility of the two amorphous phases of iPP/sPP could explain it but no evidence is given for this (it is discussed in the following). The signal corresponding to the T_g of iPP is of very low intensity and it is reasonable to assume it is not detectable in the blend.

Table 3. Glass transition temperature measured by DSC of the blends iPP/sPP compared to virgin polypropylenes

Blend	Glass transition temperature (T_g) [°C]
Virgin iPP	–10.1
75/25	–4.2
50/50	–4.2
40/60	–2.8
30/70	–2.8
Virgin sPP	–3.1

3.2.2. High resolution solid state ^{13}C NMR

In order to characterize further the crystalline forms of the blends, CP-DD MAS ^{13}C NMR have been performed (Figure 7).

The NMR spectrum of virgin iPP exhibit three bands located at 44.5, 26.5 and 22.5 ppm which are assigned to CH_2, CH and CH_3 groups. The bands assigned to methylene and methyl group show splits which are characteristic of α crystalline form of iPP. Those splits have a theoretical ratio of 2 to 1

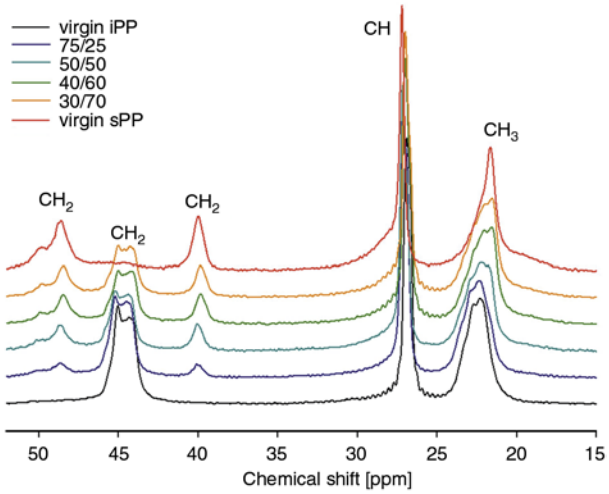

Figure 7. CP-DD MAS ^{13}C NMR spectra of the blends iPP/sPP compared to virgin iPP and sPP

Table 2. Crystallization rates and crystallization enthalpies measured by DSC of the blends iPP/sPP compared to virgin polypropylenes where ΔH_c is the crystallization enthalpy (with the subscript iPP and sPP corresponding to iPP and sPP respectively) and χ_c is the crystallization rate (with the subscript iPP and sPP corresponding to iPP and sPP respectively)

Blend	$\Delta H_{c,iPP}$ [J/g]	$\chi_{c,iPP}$ [%]	$\Delta H_{c,sPP}$ [J/g]	$\chi_{c,sPP}$ [%]	$\chi_{c,total}$ [%]
Virgin iPP	100.8	48.2±0.7	–	–	48.2±0.7
75/25	62.9	40.1±1.6	4.5	9.2±0.8	32.4±0.1
50/50	43.0	41.1±0.2	13.0	13.3±0.5	27.2±0.2
40/60	37.8	45.2±0.7	14.5	12.3±0.6	25.5±0.5
30/70	35.3	56.3±1.8	15.8	11.5±1.6	24.9±1.1
Virgin sPP	–	–	34.6	17.6±0.4	17.6±0.4

corresponding to the presence of two sites in the α crystalline form of iPP [27]. This crystalline form was expected since it is that obtained in usual crystallization conditions.

The NMR spectrum of virgin sPP exhibit four bands located at 48.5, 39.8, 26.1 and 22.1 ppm. The bands at 26.1 and 22.1 ppm are assigned to resonances of CH and CH_3 groups and those at 48.5 and 39.8 ppm correspond to C resonances in CH_2 groups in helical 4_1 conformation (crystalline form I and/or II). The explanation of having two bands is all carbons of CH_2 are not conformationally equivalent. According to the literature [4, 28], the two signals correspond to CH_2 in conformations *tggt* and *gttg*. The shift of 8.7 ppm between those two bands are characteristic of two γ-gauche effects [28]. It evidences therefore that the crystalline chains of sPP are mainly in helical conformation. It is noteworthy that shoulders are located at 50.1 and 40.5 ppm and the broadening of bands of methene and methyl groups and low intense and broad band around 44.5 ppm. From previous works [4], those broad bands are assigned to the contribution of polymeric chains in amorphous phases.

On the MAS ^{13}C NMR spectra of the blends iPP/sPP, characteristic bands of iPP and sPP are observed: bands assigned to CH_2, CH and CH_3 groups of iPP located at 44.5, 26.5 and 22.5 ppm and also bands' splitting at 44.5 and 22.5 ppm characteristic of the α form of iPP. Bands of sPP are detected at 48.5, 39.8, 26.1 and 22 ppm assigned to polymeric chains of sPP in helical conformation. It is noteworthy that bands assigned to CH and CH_3 belonging to iPP and to sPP overlaps in the blends iPP/sPP. A shoulder is also observed on the spectra at 50.1 ppm together with the broadening of bands of CH and CH_3 corresponding to the contributions of amorphous chains.

In the blends iPP/sPP and virgin iPP, iPP crystallizes in α form while crystalline sPP chains are mainly in conformations of type helical 4_1. The amorphous chains of sPP are in various conformations as indicated by broad bands detected by MAS ^{13}C NMR. The mixing of iPP with sPP does not influence the crystalline forms obtained. Nevertheless, it is very difficult to distinguish between the crystalline form I and II from MAS ^{13}C NMR because the chains are in helical conformations in the two cases. To get additional information, investigations by X-ray diffraction will be performed in the next section.

3.2.3. Wide-angle X-ray diffraction

X-ray patterns of iPP and sPP (not shown) exhibit in the two cases, diffraction peaks superimposed on a broad band. The broad band is assigned to the scattering of the iPP and sPP amorphous phases and the diffraction peaks are assigned to the diffraction of the crystallites of iPP and sPP. The diffraction peaks detected on the X-ray pattern of iPP are characteristic of the crystalline α form of iPP and those detected on the X-ray pattern of sPP are characteristic of the crystalline form I of sPP. It is noteworthy that the X-ray pattern of sPP does not reveal the diffraction peak at $2\theta = 18.8°$ (211). Its absence is assigned to the presence of defects in the chains' packing in the orthorhombic phase characteristic of form I [4]. This is consistent with DSC results showing a double melting endotherm assigned to the melting of defects in the crystalline form I.

X-ray patterns of the different blends (not shown) reveal the contributions of each component. The intensities of the peaks vary as function of the composition of the blend. It is shown that iPP crystallizes under the α form and that sPP crystallizes under the form I whatever the blend iPP/sPP considered. It indicates that the blending of iPP and sPP does not seem to have a significant influence on their respective crystalline structures. These results are consistent with the conclusions drawn from MAS ^{13}C NMR and DSC.

3.3. Molecular dynamics of the blends iPP/sPP by solid state NMR

Solid state NMR is a powerful tool for characterising and studying the structural and dynamic properties of polymers including blends of them. The possibility of performing selective experiments renders this spectroscopy particularly interesting for analysing the structure and the dynamic of polymers. The measurement of relaxation times should get information on local structure in the blend iPP/sPP isolating phases with different mobilities.

Relaxation times of solid polymers are not only determined by dynamic phenomena. There exists a contribution from the static mechanism of spin diffusion [18]. When two proton populations have different spin temperatures at a given time, they will tend to a common spin temperature by spin diffusion. Such a situation occurs during $T_1(^1H)$ and $T_{1\rho}(^1H)$ determinations in systems which may contain heterogeneities. According to these considera-

tions, it has been estimated that for polymeric systems, spin diffusion will be efficient at length scales of the order of 10 and 1 nm during $T_1(^1H)$ and $T_{1\rho}(^1H)$ measurements respectively. These measurements are therefore interesting to characterize localized motion in the materials.

3.3.1. Broad line ^{1}H NMR: spin-lattice relaxation time in the laboratory frame of proton ($T_1(^1H)$)

$T_1(^1H)$ has been determined at 25°C for the blends iPP/sPP and its evolution as a function of the composition of the blend is shown in Table 4. For each blend, only one $T_1(^1H)$ has been found meaning that there is no heterogeneity of mobility having diffusion length higher than 10 nm. It can be explained by the spin diffusion phenomenon and because of the close value of T_g with the room temperature. Indeed T_g lies between –10 and 0°C for iPP and sPP and the mobility difference between the polymeric chains of the blends are similar leading to only one value of $T_1(^1H)$.

As shown in Table 4, sPP exhibits the highest value of $T_1(^1H)$. An increase of $T_1(^1H)$ corresponds to the reduction of the molecular mobility and sPP is the material having the lowest molecular mobility among the analyzed materials. The blends 75/25, 50/50 and 30/70 exhibit similar $T_1(^1H)$ values closed to that of virgin iPP. On the contrary, the blend 40/60 exhibit a $T_1(^1H)$ value intermediate between those of virgin polypropylenes. It indicates that the molecular mobility is less with this composition of blend because of the particular the morphology of the blend exhibiting co-continuous phases.

Table 4. $T_1(^1H)$ of the blend iPP/sPP at 25°C as a function of the composition

Material	$T_1(^1H)$ [s]
Virgin iPP	0.95
iPP/sPP (75/25)	0.86
iPP/sPP (50/50)	0.88
iPP/sPP (40/60)	1.10
iPP/sPP (30/70)	0.93
Virgin sPP	1.19

3.3.2. Broad line ^{1}H NMR: spin-lattice relaxation time in the rotating frame of proton ($T_{1\rho}(^1H)$)

In order to limit the number of measurement, only the blend iPP/sPP 30/70 compared to the virgin polypropylenes was examined. For each material, three distinct $T_{1\rho}(^1H)$ values have been found (Table 5). $T_{1\rho}(^1H)$) is sensitive at shorter scale than $T_1(^1H)$ and different zones of mobility can be detected. Recognizing that shorter $T_{1\rho}(^1H)$ is associated to the decrease of molecular mobility, longer $T_{1\rho}(^1H)$, $T_{1\rho long}(^1H)$, is assigned to crystalline regions, the shortest $T_{1\rho}(^1H)$, $T_{1\rho short}(^1H)$, is assigned to free amorphous regions, and the intermediate $T_{1\rho}(^1H)$, $T_{1\rho inter}(^1H)$, is assigned to constrained amorphous regions. In semi-crystalline materials, the constrained amorphous zones correspond to amorphous zones at the interface amorphous phase – crystalline phase between the crystalline lamellae [18]. Nevertheless, the immiscibility character and the morphology of the blends iPP/sPP also suggest that the constrained amorphous zone could incorporate amorphous polymeric chains located at the interface matrix – nodule. This assumption will be further considered and discussed when investigating the measurements of $T_{1\rho}(C)$.

From Table 5, it is observed that the $T_{1\rho}(^1H)$ values of the components 'long' and 'intermediate' decrease when increasing the concentration of sPP. It indicates the mobilities of the crystalline regions and the constrained amorphous regions increase when incorporating sPP in the blends iPP/sPP. In the case of the short component, the $T_{1\rho short}(^1H)$ value of the blend iPP/sPP 30/70 is smaller than those of virgin polypropylenes with the highest number of associated protons. It shows a higher molecular mobility of the free amorphous regions in the blend than in iPP and sPP. It shows that interactions take place between the amorphous phases of iPP and sPP in

Table 5. $T_{1\rho}(^1H)$ of the blend iPP/sPP (30/70) compared to virgin polypropylenes

Material	Component 'long'		Component 'intermediate'		Component 'short'	
	$T_{1\rho long}(^1H)$ [ms]	$\%\ ^1H_{long}$	$T_{1\rho inter}(^1H)$ [ms]	$\%\ ^1H_{inter}$	$T_{1\rho short}(^1H)$ [ms]	$\%\ ^1H_{short}$
Virgin iPP	51	42	7	22	0.8	36
iPP/sPP (30/70)	38	31	4	23	0.5	46
Virgin sPP	18	30	2	18	0.6	52

the blend enhancing the molecular mobility of the amorphous polymeric chains.

3.3.3. High resolution ^{13}C NMR: Spin-lattice relaxation time in the rotating frame of carbon ($T_{1\rho}$(C))

$T_{1\rho}$(C) measurement via high resolution ^{13}C NMR experiment has the advantage to be selective since the measurement is done via selected carbons. It permits to get localized information and in particular about protons in the vicinity of the carbons. Hence evolution curve of $T_{1\rho}$(C) gives the molecular dynamic associated to each carbon of the polymeric chain.

$T_{1\rho}$(C) as a function of the composition. Three components of $T_{1\rho}$(C) have been determined for the methylene carbons of iPP and sPP (see Figure 7). The short, intermediate and long components are assigned to amorphous, constrained amorphous and crystalline regions. Table 6 shows the evolutions of each component of $T_{1\rho}$(C) as a function of methylene carbons and of the concentration of sPP in the blend. Note that CH_2 (a) of sPP corresponds to CH_2 located on the periphery of the 4_1 helix while CH_2 (b) of sPP corresponds to CH_2 located on the main axis of the helix.

The evolution of $T_{1\rho}$(C) of the methylene carbons of sPP depends on the composition of the blends which shows different dynamics as a function of the location of CH_2 in the helical 4_1 conformation. In the blend iPP/sPP 75/25, the CH_2 groups of iPP and the CH_2 (a) and CH_2 (b) groups of sPP exhibit similar values of $T_{1\rho short}$(C) and they have values between that of CH_2 of iPP and that of CH_2 (a) of sPP. This result evidences the miscibility of the free amorphous zones in the vicinity of the CH_2 groups of the blend [18, 28, 29]. The intermediate components are also similar and the $T_{1\rho inter}$(C) values are between the values of CH_2 of iPP and of CH_2 (b) of sPP which means also the miscibility of the constrained amorphous zones. On the contrary, the $T_{1\rho long}$(C) values of the different CH_2 of the blend are not similar which confirms as discussed in the previous sections the immiscibility of the crystalline zones. In addition to this, the $T_{1\rho short}$(C) values of CH_2 (iPP) and CH_2 (a) (sPP) are very close to those of virgin iPP and virgin sPP: it indicates that the presence of a second component in the blend does not modify significantly the molecular mobility of the crystalline zones of iPP and sPP in the vicinity of the methylene carbons. It evidences therefore there is no interaction between the crystalline regions in the blend iPP/sPP 75/25.

In the blend iPP/sPP 30/70, the $T_{1\rho short}$(C) values of CH_2 of iPP and of CH_2 (b) of sPP are higher than those of the virgin polypropylenes. It shows the presence of strong interactions between the free amorphous regions. Nevertheless, there is no miscibility between the free amorphous phases since the $T_{1\rho short}$(C) of CH_2 of iPP and of CH_2 (b) are different. The $T_{1\rho short}$(C) of CH_2 (a) of sPP (in the blend) is lower than that of virgin sPP. This increase of the molecular mobility is probably due to interactions enhancing the mobility of the amorphous zones located around CH_2 (a). Concerning the $T_{1\rho inter}$(C) values, they are similar to those of the virgin polypropylenes and no conclusion can be drawn for the constrained amorphous zones. The $T_{1\rho long}$(C) values of CH_2 (iPP) and CH_2 (b) are similar and there is no interaction between the crystalline regions.

In the blend iPP/sPP 50/50, the three methylene groups exhibit $T_{1\rho short}$(C), $T_{1\rho inter}$(C) and $T_{1\rho long}$(C) values different of the virgin polypropylenes which indicates the immiscibility between the free amorphous, constrained amorphous and crystalline regions. The $T_{1\rho short}$(C) values for the CH_2 of iPP and CH_2 (a) of sPP are higher and less respectively than those determined for the virgin polypropylenes suggesting interactions between the free amorphous zones. The $T_{1\rho inter}$(C) values of the methylene car-

Table 6. $T_{1\rho}$(C) of the methylene carbons of iPP and sPP in the blend iPP/sPP 30/70 as a function of composition

Composition iPP/sPP	CH_2 (iPP)			CH_2 (a) (sPP)			CH_2 (b) (sPP)		
	Component								
	$T_{1\rho short}$(C) [ms]	$T_{1\rho intermediate}$(C) [ms]	$T_{1\rho long}$(C) [ms]	$T_{1\rho short}$(C) [ms]	$T_{1\rho intermediate}$(C) [ms]	$T_{1\rho long}$(C) [ms]	$T_{1\rho short}$(C) ms]	$T_{1\rho intermediate}$(C) [ms]	$T_{1\rho long}$(C) [ms]
100/0	0.51	2.5	7.1	N/A	N/A	N/A	N/A	N/A	N/A
75/25	0.80	2.9	8.2	0.80	1.8	7.5	0.8	1.9	4.0
50/50	0.78	3.5	9.8	0.45	1.6	5.1	0.40	1.7	7.1
30/70	0.78	2.0	6.8	0.48	2.0	4.2	0.85	1.7	6.8
0/100	N/A	N/A	N/A	0.60	2.1	6.8	0.51	2.2	6.5

bons of iPP are higher than that in the virgin iPP while the values for the two types of CH_2 of sPP are less than those measured for the virgin sPP. It indicates therefore interactions between the constrained zones of iPP and sPP.

The measurements of $T_{1\rho}$(C) values show that there are large interactions between free amorphous regions and constrained amorphous regions in the blends iPP/sPP 75/25 and 30/70. These blends exhibit morphologies consisting in a matrix in which nodules of the minor component are dispersed. In addition to this, the results show a partial miscibility between the amorphous regions of iPP and sPP in the blend iPP/sPP 75/25. On the other hand, the miscibility of the amorphous regions of the blend iPP/sPP 50/50 remains questionable. It was shown there are interactions in the free amorphous regions and in the constrained zones: the specific morphology of the blend (co-continuous phases) can be an explanation of this.

Table 7. $T_{1\rho}$(C) of the methylene carbons of iPP as a function of temperature

Temperature °C]	CH_2 (iPP)		
	Component		
	$T_{1\rho short}$(C) [ms]	$T_{1\rho intermediate}$(C) [ms]	$T_{1\rho long}$(C) [ms]
25	0.2	2.7	7.2
50	0.2	3.1	15.1
80	0.7	–	7.9
100	9.0	–	11.1

$T_{1\rho}$(C) as a function of the temperature. The reason of measuring $T_{1\rho}$(C) as a function of temperature is to get better understanding on the organization of the blend iPP/sPP in the solid state. The evolution of the methylene carbons as function of temperature is listed in Table 7 for virgin iPP, in Table 8 for virgin sPP and Table 9 for the blend iPP/sPP 30/70.

The temperature rise modifies the number of components in the calculation of $T_{1\rho}$(C). The intermediate component associated to a constrained amorphous region disappears at temperature higher than 50°C. It is explained by the relaxation α* ($T_{\alpha*}$ is about 80–90°C) leading to higher mobility between the crystalline chains (motion of the crystalline lamellae in which are the amorphous chains). Hence, the constrained amorphous zones appear as free in terms of $T_{1\rho}$(C). In the case of virgin sPP, three components of $T_{1\rho}$(C) are detected at room temperature but with the temperature rise, the intermediate component of CH_2 (b) also disappears from 80°C. This disappearance of the constrained amorphous zone in the vicinity of CH_2 (b) is linked to the low melting temperature of sPP (130°C) which leads to the decrease of crystalline zones and therefore of the constrained amorphous zones.

In the case of the blend iPP/sPP 30/70, temperature changes do not modify the number of components of $T_{1\rho}$(C). According to our previous discussion on the disappearance of the intermediate component, it suggests that the intermediate carbons are assigned to constrained amorphous zones located in the

Table 8. $T_{1\rho}$(C) of the methylene carbons of sPP as a function of temperature

Temperature [°C]	CH (a) (sPP)			CH (b) (sPP)		
	Component					
	$T_{1\rho short}$(C) [ms]	$T_{1\rho intermediate}$(C) [ms]	$T_{1\rho long}$(C) [ms]	$T_{1\rho short}$(C) [ms]	$T_{1\rho intermediate}$(C) [ms]	$T_{1\rho long}$(C) [ms]
25	0.3	3.0	7.1	0.2	1.6	7.6
50	0.2	2.9	21.7	0.2	4.3	21.0
80	0.8	3.5	7.1	0.2	3.9	20.9
100	0.2	6.0	23.7	3.3	–	38.4

Table 9. $T_{1\rho}$(C) of the methylene carbons of iPP and sPP in the blend iPP/sPP 30/70 as a function of temperature

Temperature [°C]	CH_2 (iPP)			CH_2 (a) (sPP)			CH_2 (b) (sPP)		
	Component								
	$T_{1\rho short}$(C) [ms]	$T_{1\rho intermediate}$(C) [ms]	$T_{1\rho long}$(C) [ms]	$T_{1\rho short}$(C) [ms]	$T_{1\rho intermediate}$(C) [ms]	$T_{1\rho long}$(C) [ms]	$T_{1\rho short}$(C) [ms]	$T_{1\rho intermediate}$(C) [ms]	$T_{1\rho long}$(C) [ms]
25	0.3	4.5	16.2	0.20	2.8	37.2	0.15	4.6	7.3
50	0.2	3.5	17.1	0,20	3.6	8.2	0.20	4.5	15.1
80	0.5	4.8	19.6	0.08	2.3	12.5	0.15	3.5	12.2
100	0.3	5.5	20.4	0.50	4.2	13.8	0,20	4.6	27.4

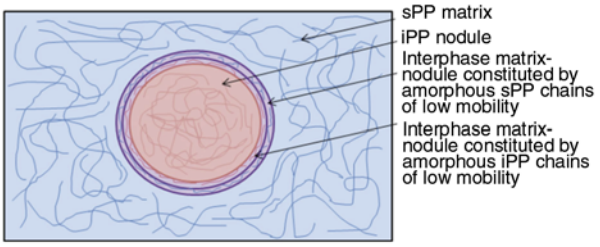

Figure 8. Scheme of the amorphous zones located at the interface matrix-nodule in the blend iPP/sPP 30/70

blend at the interface matrix-nodule in which the amorphous chains of iPP and sPP are involved (Figure 8).

In the blend iPP/sPP 30/70, the $T_{1\rho short}$(C) values of the methylene protons are almost constant from 80°C. It shows that the mobility of the amorphous zones of the blend is less sensitive than those of the virgin polypropylenes where the variations are more significant. On the other hand, the molecular mobility of the crystalline regions associated to CH_2 of iPP and to CH_2 (b) of sPP decreases slightly with the temperature rise. The mobility of CH_2 (a) of sPP (periphery of the helix) remains constant at temperatures higher than 50°C while a strong increase of the mobility is observed from 25 to 50°C.

The amorphous regions in the blend iPP/sPP 30/70 shows different changes as a function of the temperature. In the vicinity of CH_2 of iPP, they exhibit the highest mobility at 50°C and the lowest one at 100°C. The mobility of the constrained amorphous zones in the vicinity of CH_2 (b) remain almost constant over the examined temperature range. Finally, the constrained amorphous zones in the vicinity of CH_2 (a) exhibit minimum mobility at 50 and 100°C while it is maximum at 25 and 80°C. The highest mobility is observed for the methylene carbons of sPP at 80°C.

3.4. Discussion

The different analyses done in this paper have characterized the morphology and the structure of the blends iPP/sPP as a function of their composition. DSC has revealed that crystallization of iPP and sPP occurs separately in the blends iPP/sPP. The apparent immiscibility of the two components of the blends is confirmed by electronic microscopy (SEM and TEM). It is shown that the blends iPP/sPP exhibit biphasic structures constituted by a polymeric matrix (the main component) in which are dispersed nodules (minor component). Nevertheless, the compositions 50/50 and 40/60 are similar as a structure constituted of co-continuous phases which are characteristic of equi-mass concentration blends of immiscible polymers. This observation suggests that a co-continuous structure should be obtained for a composition lying between 50/50 and 40/60.

The separation of the crystalline phases of each component of the blends has been evidenced by WAXD and by MAS ^{13}C NMR. WAXD of the different blends shows the crystalline forms of each component of the blend as they are in the pure polypropylenes. iPP and sPP in the blends crystallize under the most stable forms, namely the α form for iPP and the form I for sPP (in this last case, defects in the chain packing are detected). Same conclusions are done from MAS 13C NMR and DSC analyses.

Relaxation times' measurements $T_{1\rho}$(^{1}H) and $T_{1\rho}$(C) have evidenced there are strong interactions between the amorphous phases of iPP and sPP in the blends which modify significantly the molecular mobility in the phases. These measurements have shown the partial miscibility of the amorphous zones in the blend iPP/sPP 75/25 but it remains unclear for the composition 30/70 in which the continuous phase is sPP instead of iPP. The miscibility of the amorphous phases disappears in the blend iPP/sPP 50/50 because of the specific morphology of the blend. Those results show the dependence of the morphology (and therefore the composition of the blend) on the miscibility of the amorphous phases of iPP and sPP. The component related to constrained amorphous phases in the virgin polypropylenes disappear when increasing temperature because of the α* relaxation in iPP (80°C) and of the proximity of the melting temperature of sPP (130°C). On the other hand, this component does not disappear as a function of the temperature in the blends and it suggests the formation of specific zone containing constrained amorphous polymeric chains at the interphase matrix-nodule.

4. Conclusions

In this paper, the morphology and the structural properties of blends iPP/sPP have been investigated by different techniques. It has been shown the influence of the composition of the blends on the morphology of the materials. The morphology is then directly related to the structural organization of the blends. The crystallization rate decreases as a function of

the sPP content. The minor component is dispersed as a nodule in the main component of the blend and it plays the role of nucleating agent on it. Besides, morphology changes occur for the composition 50/50 of the blend iPP/sPP. Different phases have been identified, namely free amorphous, constrained amorphous and crystalline regions which exhibit different molecular mobilities. It is also shown an additional constrained amorphous zone due to nodules at the interphase matrix-nodule.

Acknowledgements

The present work was part of the MEMOTI project which was financially supported by the Ministère de l'Economie, de l'industrie et de l'emploi and in particular the Direction Générale des Entreprises. The UpTex competitive cluster is also acknowledged for administrative assistance in this project.

References

[1] Natta G., Pasquon I., Zambelli A.: Stereospecific catalysts for the head-to-tail polymerization of propylene to a crystalline syndiotactic polymer. Journal of the American Chemical Society, **84**, 1488–1490 (1962). DOI: 10.1021/ja00867a029

[2] Ewen J. A., Jones R. L., Razavi A., Ferrara J. D.: Syndiospecific propylene polymerizations with Group IVB metallocenes. Journal of the American Chemical Society, **110**, 6255–6256 (1988). DOI: 10.1021/ja00226a056

[3] De Rosa C., De Ballesteros O. R., Auriemma F.: Mechanical properties of helical and mesomorphic forms of syndiotactic polypropylene at different temperatures. Macromolecules, **37**, 7724–7735 (2004). DOI: 10.1021/ma049214h

[4] De Rosa C., Auriemma F.: Structure and physical properties of syndiotactic polypropylene: A highly crystalline thermoplastic elastomer. Progress in Polymer Science, **31**, 145–237 (2006). DOI: 10.1016/j.progpolymsci.2005.11.002

[5] Zhang X., Zhao Y., Wang Z., Zheng C., Dong X., Su Z., Sun P., Wang D., Han C. C., Xu D.: Morphology and mechanical behavior of isotactic polypropylene (iPP)/syndiotactic polypropylene (sPP) blends and fibers. Polymer, **46**, 5956–5965 (2005). DOI: 10.1016/j.polymer.2005.05.004

[6] Supaphol P., Spruiell J. E.: Isothermal melt- and cold-crystallization kinetics and subsequent melting behavior in syndiotactic polypropylene: A differential scanning calorimetry study. Polymer, **42**, 699–712 (2001). DOI: 10.1016/S0032-3861(00)00399-2

[7] Thomann R., Kressler J., Setz S., Wang C., Mülhaupt R.: Morphology and phase behaviour of blends of syndiotactic and isotactic polypropylene: 1. X-ray scattering, light microscopy, atomic force microscopy, and scanning electron microscopy. Polymer, **37**, 2627–2634 (1996). DOI: 10.1016/0032-3861(96)87621-X

[8] Clancy T. C., Pütz M., Weinhold J. D., Curro J. G., Mattice W. L.: Mixing of isotactic and syndiotactic polypropylenes in the melt. Macromolecules, **33**, 9452–9463 (2000). DOI: 10.1021/ma0011035

[9] Woo E. M., Cheng K. Y., Chen Y-F., Su C. C.: Experimental verification on UCST phase diagrams and miscibility in binary blends of isotactic, syndiotactic, and atactic polypropylenes. Polymer, **48**, 5753–5766 (2007). DOI: 10.1016/j.polymer.2007.07.015

[10] Phillips R. A.: Macromorphology of polypropylene homopolymer tacticity mixtures. Journal of Polymer Science Part B: Polymer Physics, **38**, 1947–1964 (2000). DOI: 10.1002/1099-0488(20000801)38:15<1947::aid-polb10>3.0.co;2-m

[11] Wang Z-G., Phillips R. A., Hsiao B. S.: Morphology development during isothermal crystallization. II. isotactic and syndiotactic polypropylene blends. Journal of Polymer Science Part B: Polymer Physics, **39**, 1876–1888 (2001). DOI: 10.1002/polb.1162

[12] Zou X-X., Yang W., Zheng G-Q., Xie B-H., Yang M-B.: Crystallization and phase morphology of injection-molded isotactic polypropylene (iPP)/syndiotactic polypropylene (sPP) blends. Journal of Polymer Science Part B: Polymer Physics, **45**, 2948–2955 (2007). DOI: 10.1002/polb.21237

[13] Gorrasi G., Vittoria V., Longo P.: Transport and mechanical properties of iPP–sPP fibers. Journal of Applied Polymer Science, **80**, 539–545 (2001). DOI: 10.1002/1097-4628(20010425)80:4<539::aid-app1128>3.0.co;2-3

[14] Zheng C-X., Zhang X-Q., Rottstegge J., Dong X., Zhao Y., Wang D-J., Zhu S-N., Wang Z-G., Han C. C., Xu D-F.: Preliminary investigation on the miscibility of isotactic polypropylene (iPP) and syndiotactic polypropylene (sPP) blends. Chinese Journal of Polymer Science, **24**, 569–573 (2006). DOI: 10.1142/s0256767906001655

[15] da Silva N. M., Tavares M. I. B., Stejskal E. O.: ^{13}C-detected ^{1}H spin diffusion and ^{1}H relaxation study of multicomponent polymer blends. Macromolecules, **33**, 115–119 (2000). DOI: 10.1021/ma980798v

[16] White J. L., Wachowicz M.: Polymer blend miscibility. in 'Annual reports on NMR spectroscopy' (ed.: Webb G. A.) Vol 64, 189–209 (2008).

[17] McBrierty V. J.: Heterogeneity in polymers as studied by nuclear magnetic resonance. Faraday Discussions of the Chemical Society, **68**, 78–86 (1979). DOI: 10.1039/dc9796800078

[18] McBrierty V. J., Douglass D. C.: Recent advances in the NMR of solid polymers. Journal of Polymer Science: Macromolecular Reviews, **16**, 295–366 (1981). DOI: 10.1002/pol.1981.230160105

[19] McBrierty V. J., Ward I. M.: Investigation of the orientation distribution functions in drawn polyethylene by broad line nuclear magnetic resonance. Journal of Physics D: Applied Physics, **1**, 1529–1542 (1968). DOI: 10.1088/0022-3727/1/11/319

[20] Chu C. W., Dickinson L. C., Chien J. C. W.: Study of critical phenomena of polystyrene–poly(vinyl methyl ether) blends by solid state NMR. Journal of Applied Polymer Science, **41**, 2311–2325 (1990). DOI: 10.1002/app.1990.070410933

[21] Hjertberg T., Hargitai T., Reinholdsson P.: Carbon-13 CP-MAS NMR study on content and mobility of double bonds in poly(trimethylolpropane trimethacrylate). Macromolecules, **23**, 3080–3087 (1990). DOI: 10.1021/ma00214a009

[22] Le Menestrel C., Kenwright A. M., Sergot P., Lauprêtre F., Monnerie L.: Carbon-13 NMR investigation of local dynamics in compatible polymer blends. Macromolecules, **25**, 3020–3026 (1992). DOI: 10.1021/ma00038a003

[23] Thomann R., Kressler J., Rudolf B., Mülhaupt R.: Morphology and phase behaviour of blends of syndiotactic and isotactic polypropylene: 2. Differential scanning calorimetry, light transmission measurements, and PVT measurements. Polymer, **37**, 2635–2640 (1996). DOI: 10.1016/0032-3861(96)87622-1

[24] Spaleck W., Antberg M., Rohrmann J., Winter A., Bachmann B., Kiprof P., Behm J., Herrmann W. A.: High molecular weight polypropylene through specifically designezirconocene catalysts. Angewandte Chemie International Edition in English, **31**, 1347–1350 (1992). DOI: 10.1002/anie.199213471

[25] Galambos A., Wolkowicz M., Zeigler R.: Structure and morphology of highly stereoregular syndiotactic polypropylene produced by homogeneous catalysts. in 'Polymeric Materials Science and Engineering' (eds.: Vandenberg E. J., Salamone J. C.) ACS Symposium Series, Vol 496, 104–120 (1992). DOI: 10.1021/bk-1992-0496.ch008

[26] Garnier L., Duquesne S., Bourbigot S., Delobel R.: Non-isothermal crystallization kinetics of iPP/sPP blends. Thermochimica Acta, **481**, 32–45 (2009). DOI: 10.1016/j.tca.2008.10.006

[27] Fričová O., Uhrínová M., Hronský V., Koval'aková M., Olčák D., Chodák I., Spěváček J.: High-resolution solid-state NMR study of isotactic polypropylenes. Express Polymer Letters, **6**, 204–212 (2012). DOI: 10.3144/expresspolymlett.2012.23

[28] Sozzani P., Simonutti R., Galimberti M.: MAS NMR characterization of syndiotactic polypropylene: Crystal structure and amorphous phase conformation. Macromolecules, **26**, 5782–5789 (1993). DOI: 10.1021/ma00073a036

[29] Dadayli D., Harris R. K., Kenwright A. M., Say B. J., Sünnetçioğlu M. M.: Solid-state ^{1}H n.m.r. studies of polypropylene. Polymer, **35**, 4083–4087 (1994). DOI: 10.1016/0032-3861(94)90579-7

eXPRESS Polymer Letters Vol.7, No.3 (2013) 238–248
Available online at www.expresspolymlett.com
DOI: 10.3144/expresspolymlett.2013.22

Centrifugal spun ultrafine fibrous web as a potential drug delivery vehicle

L. Amalorpava Mary[1], *T. Senthilram*[1], *S. Suganya*[1], *L. Nagarajan*[1] *J. Venugopal*[2], *S. Ramakrishna*[2], *V. R. Giri Dev*[1*]

[1]Department of Textile Technology, Anna University, Chennai-25, India
[2]Nanoscience and Nanotechnology Initiative, Faculty of Engineering, National University of Singapore, Singapore

Received 1 September 2012; accepted in revised form 10 November 2012

Abstract. Centrifugal spinning (C-spin) is one of the emerging techniques for the production of ultrafine fibrous web which mimics Extracellular matrix (ECM). Due to its unique characteristic features it is widely used in bio-medical applications such as tissue engineered scaffolds, wound dressing materials and drug delivery vehicles. In the present study tetracycline loaded polycaprolactone (PCL) blended polyvinyl pyrrolidone (PVP) fibers were fabricated using in-house built C-spin system. The developed ultrafine fibers were morphologically characterized by Scanning Electron Microscope (SEM) before and after drug release and the results showed that the developed webs were highly porous and the pores were evenly distributed. Fourier Transform Infrared (FTIR) spectroscopy results confirmed that the drug was incorporated on the fibers. The antibacterial activity and drug releasing strategy were examined and the results showed that the developed webs can effectively act as a drug delivery vehicle.

Keywords: *nanomaterials, centrifugal spinning, drug delivery, wound dressing, PCL/PVP/Tetracycline scaffolds*

1. Introduction

Over the last few decades, ultrafine fibers webs have engrossed the interest of the researchers for its innovative applications. Due to its captivating characteristics features such as large surface area-to-volume ratio, high porosity, and fully interconnected pore network it has been widely used in applications like drug delivery, wound dressings, tissue engineered scaffolds, protective clothing, filtration systems, sanitary goods, and sensor assemblies [1, 2]. At present ultrafine fibers are produced by phase separation, template synthesis, self-assembly, electrospinning [3–5]. Among these, electrospinning is the most promising and versatile technique for the production of ultrafine fibers. But the utilization of electrospinning is limited by the major disadvantages like low production rate, low safety features and getting aligned fibers. Research attempts are being made to replace electrospinning with alternative techniques around the globe. Forced spinning and rotary jet spinning techniques are now being attempted to produce aligned fibers without application of high voltage. This facile method of centrifugal spinning can be able to replace the limitations of electro spinning and the process is highly scalable.

Centrifugal spinning system is developed based on cotton candy machine working principle. Polymers are drawn into fibers by applying high centrifugal force. Centrifugal spinning process offers several appealing features such as the obtained fibrous web shows high surface area to volume ratio (the diameter of the fibers varies from several micrometers down to nano meters range), webs with higher

*Corresponding author, e-mail: vrgiridev@yahoo.com

degree of alignment and interconnected fibers offers good mechanical strength, highly porous, well interconnected pores, facile and low cost effective process. Because of these cynosural characteristics of ultrafine fibers produced by this process can be used as a tissue engineering scaffolds (especially those needing aligned architecture such as nerve, muscle, tendons), drug delivery vehicles and wound dressing materials [6]. An ideal wound dressing material should possess moderately hydrophilic surface, dimensional un-shrinkage, suitable microstructure, porosity, controllable biodegradability, suitable mechanical property and should support initial cell adhesion and proliferation [7–9].

PCL is Food and Drug administration (FDA) approved semi crystalline aliphatic polyester having an excellent biocompatibility and degradability. When compared to other biocompatible polymers such as poly(lactic-co-glycolic acid) (PLGA), it does not create an acidic environment on degradation [10, 11]. Even though it possesses an excellent processability and mechanical properties, utilization of PCL in wound dressings is limited because of its hydrophobicity. Hydrophobic polymers provide a structure or back bone and degrade over a long period whereas the more hydrophilic polymers degrade rapidly. The choice of polymer and polymer blends plays an important role where it is aimed as a vehicle for controlled release. PVP is one of the important hydrophilic polymers that can be blended homogeneously with PCL. Due to its good complexion, adhesion properties, excellent physiological compatibility, low chemical toxicity, and reasonable solubility it has been widely used in many industries such as pharmaceuticals, cosmetics, beverages, adhesives, detergents, paints, electronics, and biological engineering materials [12, 13].

Some trail works have been done with electrospun PCL nanofibrous web as a drug releasing vehicle. Metronidazole benzoate loaded PCL fibrous web was prepared for targeting periodontal disorder by electrospinning and drug releasing behaviors has been studied [14]. Controlled release of diclofenac sodium and teracyclin hydrochloride from electrospun PCL, polyvinyl alcohol, PVA-SA (Sodium alginate) has also been reported [15]. Release of tetracycline from electrospun mats of Poly (ethylene- co- vinyl acetate) (PEVA), PLA 50/50 blend was studied and was found that electrospun PEVA and 50/50 PLA/PEVA mats gave relatively smooth release of drug electrospun fibers after release over about 5 days [16].

To the best of our knowledge, no attempt has been made with centrifugal spun fibrous web as a drug carrier. Still no report has been found for centrifugal spinning of PCL/PVP blends. Hence, studying the release pattern of drug from the centrifugal spun mat will provide insight to the usage of material as the drug delivery vehicle. In the present study PCL/PVP ultrafine fiber mats were prepared by in-house developed centrifugal spinning setup. Drug was loaded on the mat and its releasing profiles were studied, the efficiency of the mat against skin pathogens are also examined and discussed for wound healing.

2. Experimental

2.1. Materials

Polycaprolactone (M_n 70 000–90 000), polyvinyl pyrrolidone (M_w 1300 KD) and tetracycline were obtained from Sigma Aldrich India. Chloroform and Methanol (RANKEM, India) used in this study were analytical grade and used without further purification.

2.2. Preparation of ultrafine fibrous web by centrifugal spinning

Centrifugal spinning was carried out using 12% w/v solutions of PCL/PVP in the ratio of 100:0, 70:30, 50:50, 30:70, 0:100 in chloroform. Drug loaded samples were prepared by dissolving 0.2% w/v of tetracycline with respect to polymer concentration in 10:90 methanol:chloroform mixture. Prior to centrifugal spinning the solutions were stirred for an hour. Both drug free and drug loaded samples were carefully injected into the pot type rotating spinneret head with the help of syringe. Centrifugal spinning was carefully carried out under a constant 2000 rpm. The formed ultrafine fibers were collected on a round bottom collector. The obtained aligned fibrous web was kept under vacuum to remove the excess solvent. Schematic diagram of the in-house developed centrifugal spinning system is given in Figure 1. The actual drug loaded in the samples was found out by the procedure cited in literature with chloroform as solvent and it was found be 96-99% of the initial loading of drug in the samples [17].

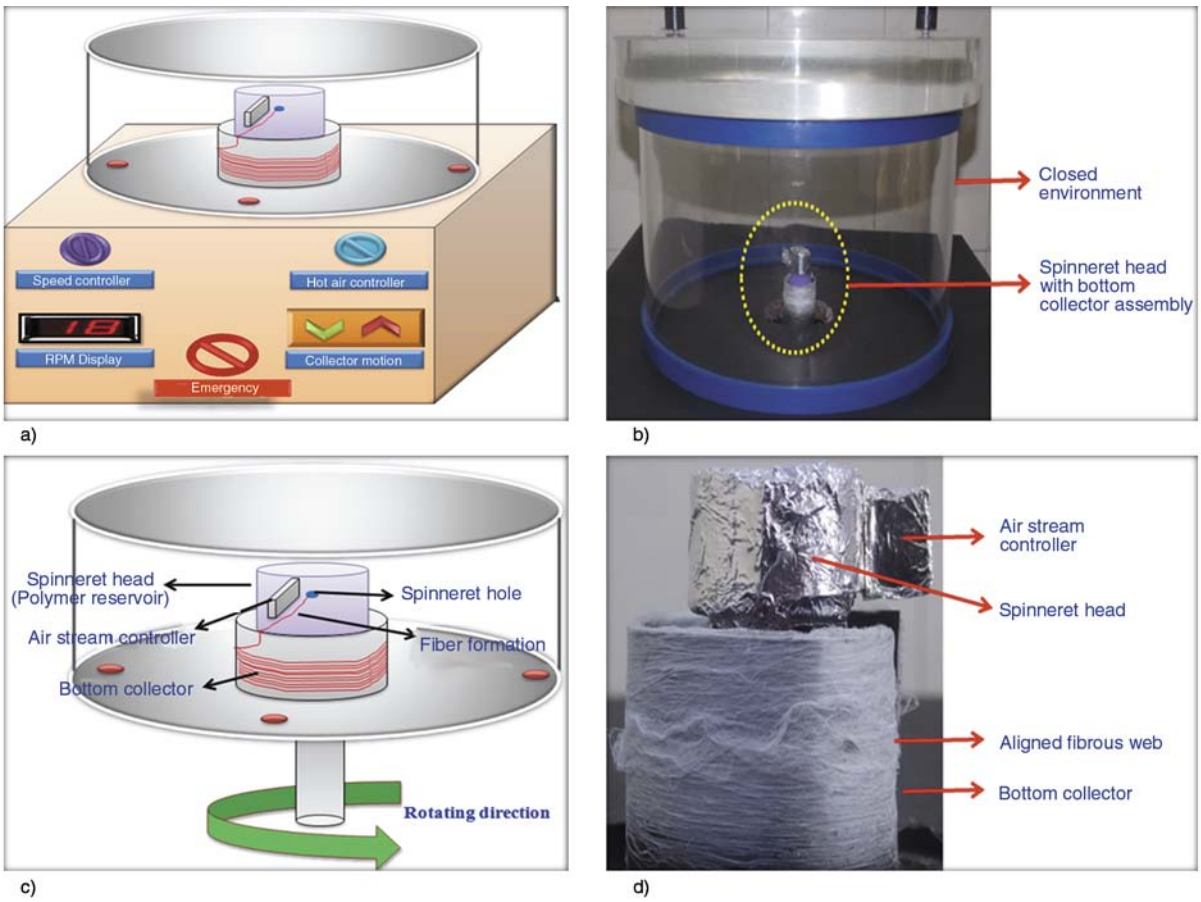

Figure 1. Schematic diagram of the in-house developed centrifugal spinning system, (a) centrifugal spinning set up (b) fiber production (c) rotating pot type spinneret head (d) aligned fibers on bottom collector

2.3. Characterization of drug loaded fibers

The morphology of the ultrafine fibrous web was observed using scanning electron microscope (SEM) (S3400NSEM, HITACHI, Japan). The spun fibers were sputtered with thin layer of gold prior to SEM observation. On the basis of SEM images, the diameter of the fibers was calculated with the help of image analyzing software Digimizer. ATR-FTIR spectroscopic analysis of centrifugal spun ultrafine fibrous web was made using Spectrum One (Perkin-Elmer, USA model). The thermal behavior of centrifugal spun fibrous web samples (PCL, PCL/PVP, PCL/PVP/Tetracycline and PVP) was examined by TA Q50 series Thermo Gravimetric Analyzer (TGA, USA). Measurements were conducted over a temperature range of 0 to 700°C at a heating rate of 20°C/min under nitrogen purge.

2.4. Swelling and degradation studies

The degree of swelling and weight loss of the drug loaded ultrafine fibrous mats were calculated by using Equations (1) and (2) respectively:

$$\text{Degree of swelling [\%]} = \frac{M - M_d}{M_d} \cdot 100 \quad (1)$$

$$\text{Weight loss [\%]} = \frac{M_i - M_d}{M_i} \cdot 100 \quad (2)$$

where M is weight of each sample submersion in the buffer solution which is wiped dry with filter paper, M_d is the dry weight of immersed sample which is dried at 40°C and M_i is the initial weight of the sample in its dry state [18]. Both tests were carried out in the acetate buffer of pH 5.5 at 37°C for 2, 4, 12 and 24 hours.

2.5. Antimicrobial activity

The antibacterial activity of the centrifugal spun fibrous web against four pathogenic bacteria commonly found on burn wounds: *P.aeruginosa* (Gram-negative) *S.epidermidis* (Gram-positive), *B.magaterium* (Gram-positive) and *E.coli* (Gram-negative) were investigated. The assessment was conducted based on the disc agar diffusion method. A 100 µL

aliquot of bacteria reconstituted in nutrient broth and previously subcultured was spread onto an agar plate. Both the drug-free and drug-containing PCL/PVP fiber mats were cut into circular discs (10 mm in diameter) and placed on the top of the agar plate. The plates were incubated at 37°C for 24 h. If inhibitory concentrations were reached, there would be no growth of the microbes, which could be seen as a clear zone around the disc specimens. The zone was then recorded as an indication of inhibition against the microbial species.

2.6. In vitro drug release studies

A drug-containing fiber mat (0.5 g) was first placed in a vial filled with 20 ml of release medium acetate buffer. Drug release studies were carried out at 37°C and 100 rotation/min [rpm] in a thermostated shaking incubator. The releasing medium acetate buffer with pH 5.5 was prepared by dissolving 1.5 g of sodium acetate in 1.5 mL of glacial acetic acid and then the final solution was made up to 100 mL by adding distilled water. In this case, 4 mL of sample was taken from the medium after appropriate intervals for about 24 h and then the same volume of fresh release medium was added as replacement. A calibration curve was obtained for the tetracycline hydrochloride concentration at a peak absorption wavelength of 360 nm, and a linear equation was derived by a curve-fitting method. In the assessment of drug release behavior, a cumulated amount of the released drug was calculated. The percentages of drug released from the fibrous web were plotted against time. The drug release studies were carried out on PCL and PCL/PVP blended fibrous mat alone and the kinetics studies were carried out on the drug release from the mat using the Zero order, First order, Higuchi, Hixson-crowell and Peppas model as suggested in the literature [19–23].

3. Results and discussion

3.1. Scanning electron microscope analysis

Wound care products are likely to be sophisticated formulations that incorporate antimicrobial components and optimize the wound environment to promote healing. Since evolution is faster in microbial species than in other species, there will be a continual need to search for novel wound dressing materials for tropical skin infection treatments. Morphologies of C-spun fibrous webs are given in the Figure 2. The average diameter of the fibers calculated using Digimizer software is given in Table 1. The diameter of the fibers produced from C-spun fiber ranges from 300 to 927 nm. It can be inferred from the table that the addition of PVP to PCL increases the diameter of the fiber. The increase in diameter of the fiber due to the addition of PVP can be attributed to the hydrophilic nature of PVP. It can absorb the moisture present in air and can coalesce with other fibers leading to increase in diameter. The addition of drug to PCL/PVP (50/50) blended samples further increases the diameter as the drug occupies matrices of the polymer structure. However the changes in diameter of the PCL fibers loaded with drugs were not substantial when compared to that of the blends. The surface of C-spun fibers are rough and lack luster where as with corporation of PVP, the samples look lustrous due to the presence of homogeneity in diameter of the fibers. The photograph of the sample is given in the Figure 3. Another interesting observation is that the obtained fibers are highly aligned and the fiber alignment is mainly due to the presence of air stream controller which is placed near to the fine orifice. When the polymers are ejected from the narrow orifice with high centrifugal force, the air stream controller push the fibers down wards and paving a path for collecting at the bottom with higher degree of alignment. It has been reported in literature that the high degree of alignment has a significant influence on the drug release behavior after the initial burst release due to enhanced density of packing of fibers and limited pore size in aligned mats. It has also been reported in the literature that alignment of fibers supplements the proliferation rate of fibroblasts cells apart from providing good mechanical properties [24, 25].

Table 1. Measurements of average fibre diameter of C-spun ultrafine fibres

PCL/ PVP Blend ratio [%]	Average fiber diameter [nm]
100/0	311
70/30	352
50/50	619
50/50/Tetracycline	927
30/70	726
0/100	823

3.2. Fourier transform infrared spectroscopic analysis

The FTIR spectrum of PCL is shown in the Figure 4a. The spectrum showed characteristic peaks

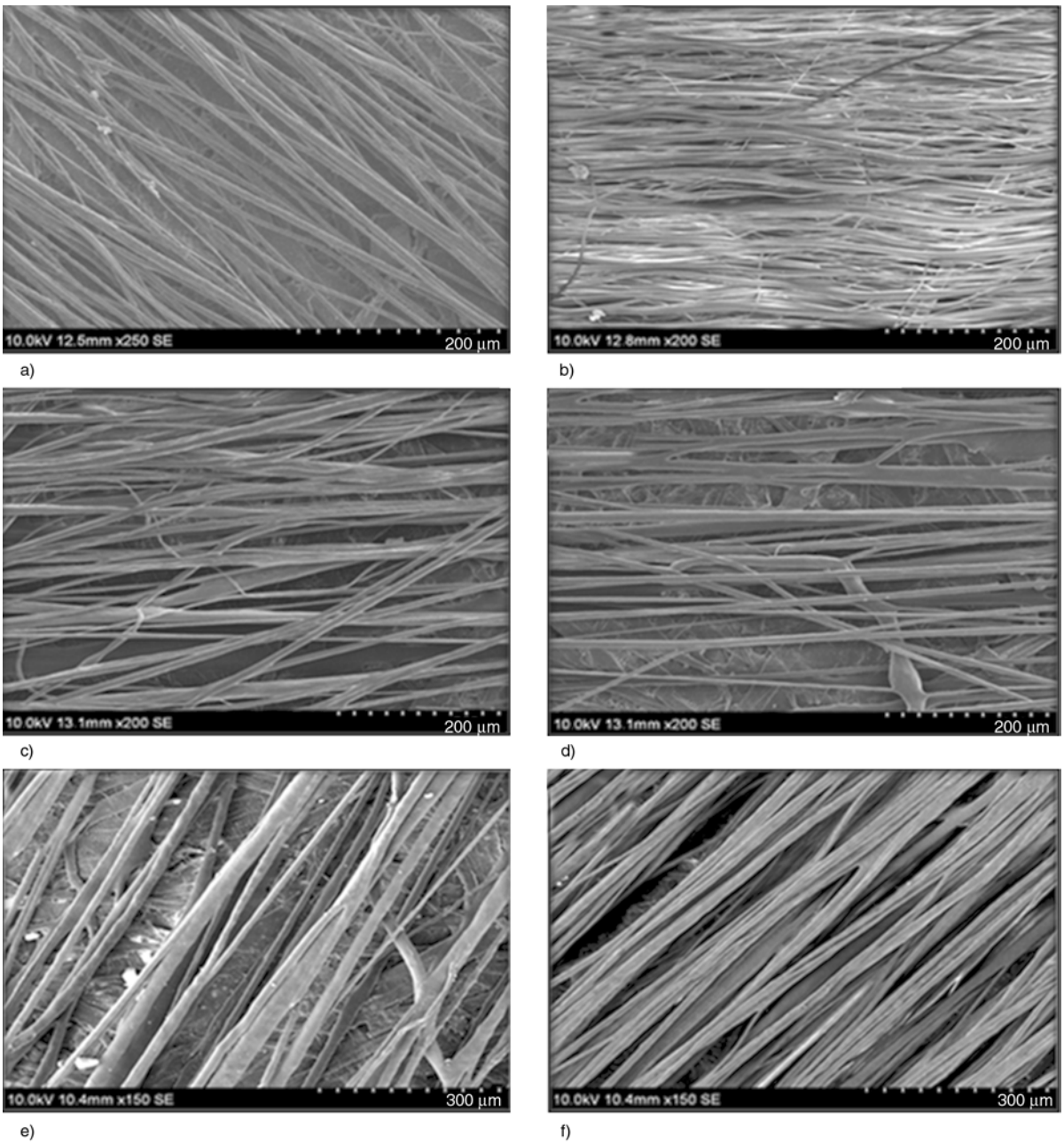

Figure 2. SEM micrographs of (a) 100% PCL (b) 100% PVP (c) 70:30 PCL/PVP (d) 30:70 PCL/PVP (e) 50:50 PCL/PVP (f) Drug loaded PCL/PVP

of C=O stretching vibrations at 1731 cm^{-1}, CH_2 bending modes at 1471, 1397 and 1365 cm^{-1} and –COO– vibrations at 1739 cm^{-1}. The C–O–C stretching vibrations yield peaks at 1169, 1108 and 1049 cm^{-1}. The spectrum of PVP is given in Figure 4b. The intense sharp peak at 1654cm^{-1} appeared due to C=O stretching vibrations of PVP. The CH_2 bending modes were observed at 1376, 1424, 1441 and 1463 cm^{-1} and that of the C–N vibrations occurred at 1291 cm^{-1}. The spectrum of PCL/PVP (50/50) shown in Figure 4c.The spectrum showed characteristics of both PCL (C=O stretch at 1734 cm^{-1}) and PVP (C=O stretch at 1654 cm^{-1}). In addition to the above peaks, the –COO stretch of PCL occurred at 1239 cm^{-1} and C–N stretch of PVP at 1293 cm^{-1}. The spectrum of drug loaded PCL/PVP (50/50) is given in Figure 4d. The spectrum showed the characteristics peaks of PCL and PVP. But the C=O stretching vibrations of PCL and PVP showed splits due to interactions of polymer with the drug. Further, the NH_2 symmetric and asymmetric stretching vibrations at 3300 and 3415 cm^{-1} was partly resolved and it confirms the presence of drug.

Figure 3. Photograph of (a) 100% PCL (b) 100% PVP (c) 50:50 PCL/PVP (d) drug loaded 50:50 PCL/PVP. The surface of C-spun fibers are rough and lack luster where as with corporation of PVP, the samples look lustrous due to the presence of homogeneity in diameter of the fibers.

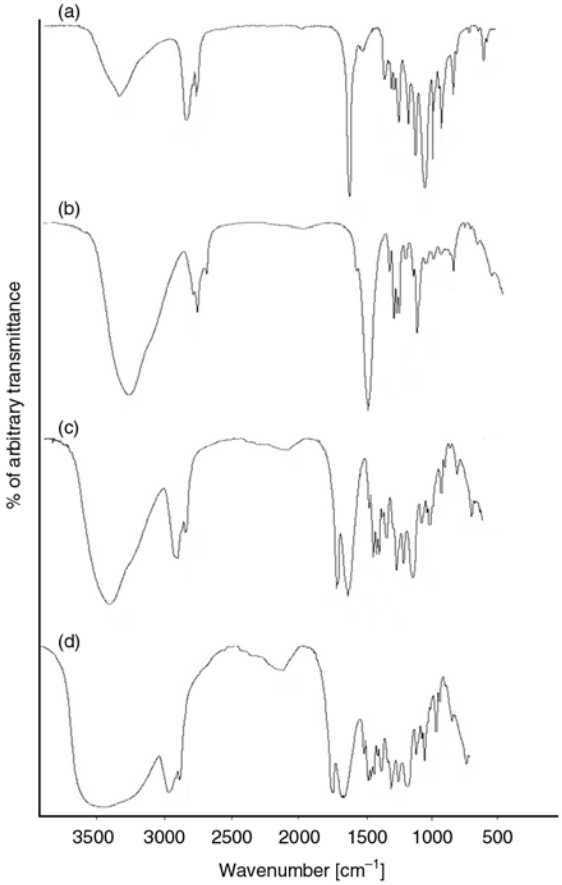

Figure 4. FTIR spectrum of (a) 100% PCL (b) 100% PVP (c) 50:50 PCL/PVP (d) drug loaded 50:50 PCL/PVP)

3.3. Thermo gravimetric analysis

Thermal stability of polymers and their blends are evaluated by TGA. Various blend characteristics such as interaction and miscibility of the blends are evaluated by thermogram. The samples weighed (~10 mg) were heated from 0 to 700°C at 20°C/min and held at an isotherm for 3 min. The TGA data's were plotted as temperature verses weight %, from which onset, peak and final decomposition temperature were obtained. Blending of Polymers results in negative (destabilizing) or positive (stabilizing) effect on thermal stability [26]. In Figure 5, neat PCL sample showed one step degradation profile as its degradation begins at 345°C and completely degraded around 490°C. The similar results have been observed by Abdellatif Mohamed *et al.* [27] and proved that PCL showed much higher degradation temperature than vital gluten. In neat PVP samples initial weight loss nearly around 19% below 100°C revealed the hydrophilic nature of PVP. PVP also shows one step degradation process and the degradation begins at 302°C and ends at 485°C as suggested in the literature [28]. Thermal behavior of PCL blended PVP obeys the single step degradation like PCL and PVP. The addition of tetracycline slightly improves the thermal stability of PCL

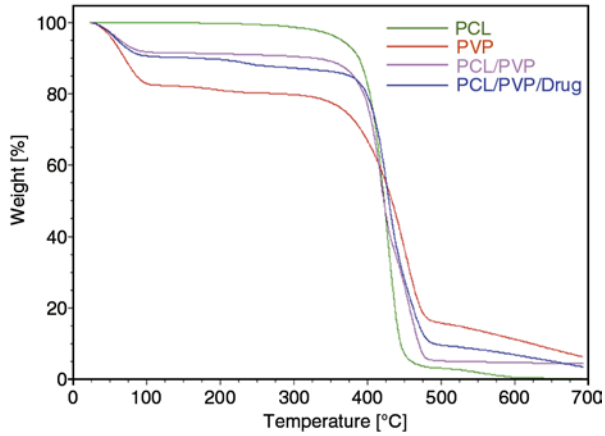

Figure 5. Thermogram of C-spun ultrafine fibrous web

blended PVP fibrous web and is evident from less residual weight obtained at elevated temperature. It also confirms that addition of drug has not significantly altered the crystallinity of the fibrous mat.

3.4. Degree of swelling and weight loss [%]

Figures 6 and 7 shows the degree of swelling and weight loss [%] of PCL, PVL/PVP, PVP ultrafine fibrous web kept in acetate buffer of pH 7.4 at the intervals of 2, 4, 12 and 24 hours. Degree of swelling and weight loss [%] are the two important parameters for designing drug delivery vehicle for particular biomedical application. From the Figure 6 it can be seen that PVP swells 583% in first 2 hours and after two hours the entire fiber network collapses and starts slowly dissolving in the medium. It substantiates that a hydrophobic biocompatible polymer such as PCL along with the PVP will aid in stability of matrices so that the loaded drug release

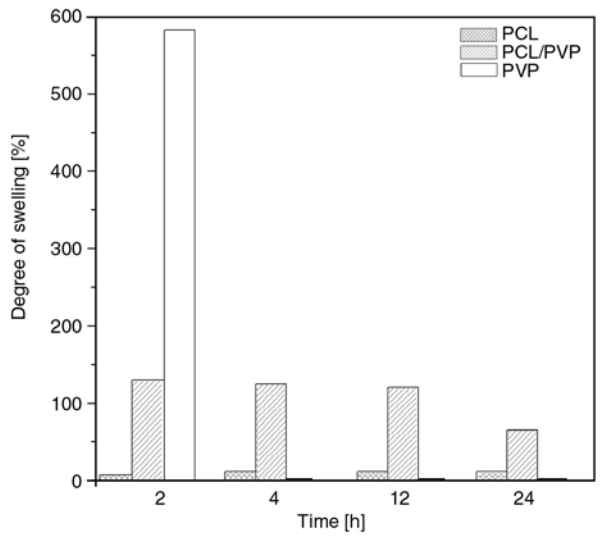

Figure 6. Degree of swelling for PCL, PCL/PVP, PVP ultrafine fibrous web

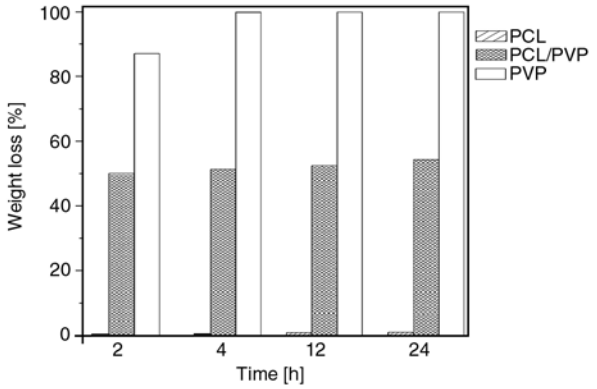

Figure 7. Weight loss [%] for PCL, PCL/PVP, PVP ultrafine fibrous web

from the matrices can be maintained for longer duration. The degree of swelling of PCL/PVP blends was around 60–130% for time interval taken for the study whereas the hydrophobic PCL mat showed negligible swelling compared to the blends. The weight loss [%] was found to be in the following order *PVP > PCL/PVP > PCL* and PCL and PCL/PVP blends were found to be more stable compared to the PVP matrices.

3.5. Antibacterial activity

The antibacterial efficiency of C-spun web was tested against two gram positive (*S.epidermidis*, *B.megaterium*) and gram negative bacteria (*E.coli*, *P.aeruginosa*) respectively. The microbes selected were skin pathogens and the developed C-spun fibrous web has a potential to be used as skin pathogens. The efficiency of the drug loaded C-spun fibres against skin pathogens is given in Table 2 and Figure 8. It can be seen that the drug taken for the study namely tetracycline has a classic broad spectrum activity against both gram positive and gram negative bacterial infections. Tetracycline works by binding specifically to 30 s ribosomes of the bacteria, preventing attachment of aminoacyl tRNA to the tRNA – ribosome complex and simultaneously inhibits other steps of protein biosynthesis. Tetracycline released from the C-spun fibrous web effectively inhibits the growth of gram positive bacteria such as *S.epidermidis* and *B.megaterium* which gives the zone of inhibition 42 mm 46 mm and moderately inhibits the growth of gram negative bacterium such as *E.coli* and *P.aeruginosa* which gives the zone of inhibition around 33 mm, 31 mm. The antimicrobial activity of tetracycline is more efficient to gram positive bacteria than gram nega-

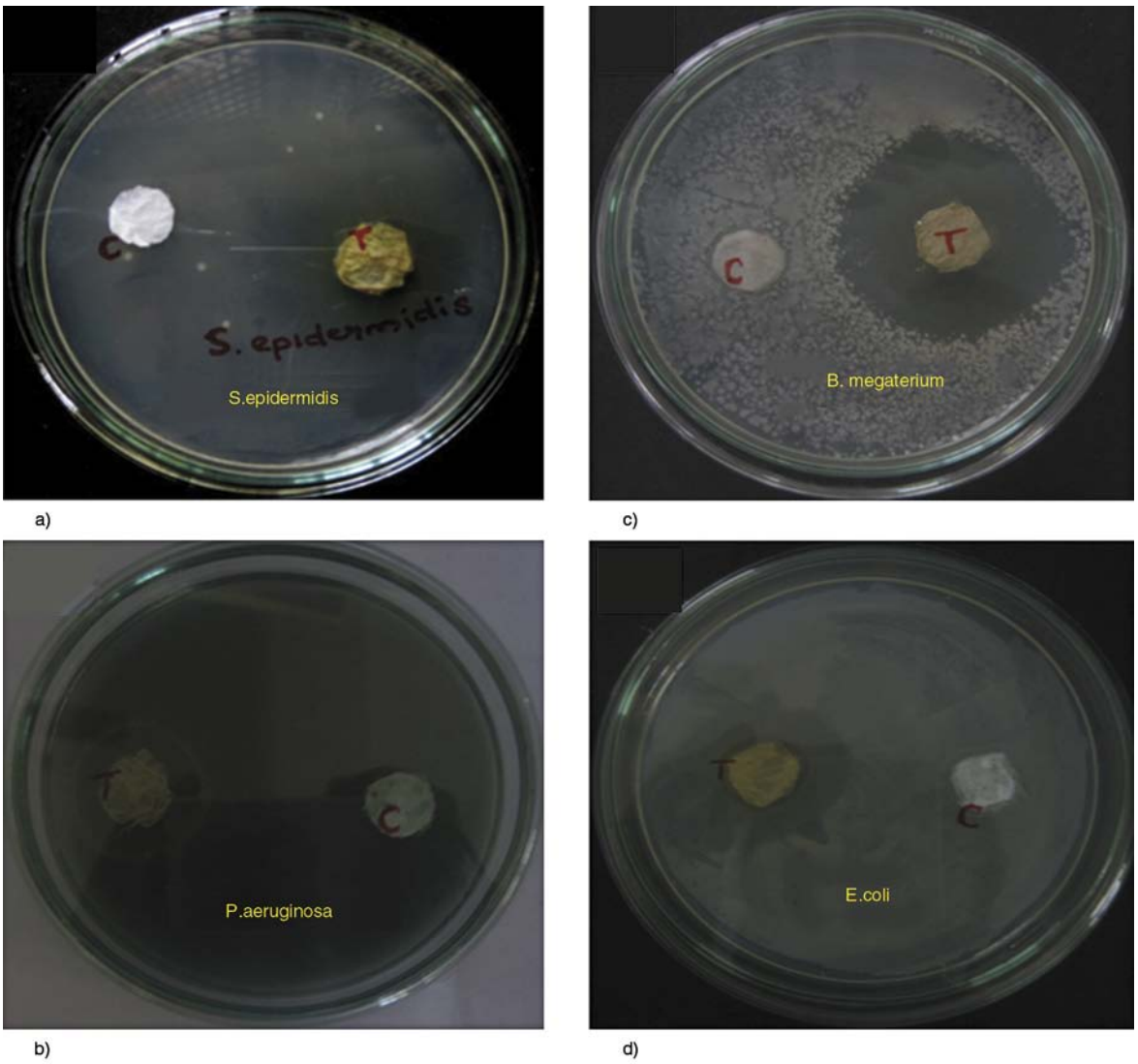

Figure 8. Antibacterial activity of the C-spun fibrous web, (a) *S.epidermidis*, (b) *P.aeruginosa*, (c) *B.megaterium*, (d) *E.coli*

Table 2. Measurements of average zone of inhibition of C-spun ultrafine fibres

Bacteria	Zone of inhibition in mm
S.epidermidis (Gram +ve)	42
P.aeruginosa (Gram –ve)	31
B.megaterium (Gram +ve)	46
E.coli (Gram –ve)	33

tive and it can be attribute the cell wall differentiations as reported in the literature [29].

3.6. Drug release

Figure 9 shows the release profile of tetracycline loaded C-spun fibers for both PCL, PCL/PVP blends. In the case of PCL polymer, the drug release is slow and only 12.5% of the drug is released within 24 hours even though PCL C-spun fibers provides better structural integrity. The slow release of the drug is attributed to the hydrophobic nature of PCL.

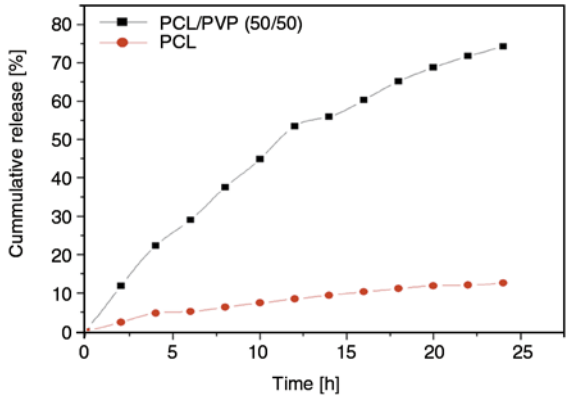

Figure 9. Drug releasing profiles of PCL/PVP C-spun ultrafine fibrous web

Blends of hydrophobic polymer along with hydrophilic polymer aids better drug release and it is evident from the drug release studies. It can be seen that around 74% of the drug is released within 24 hour in the case of PCL/PVP blends but still

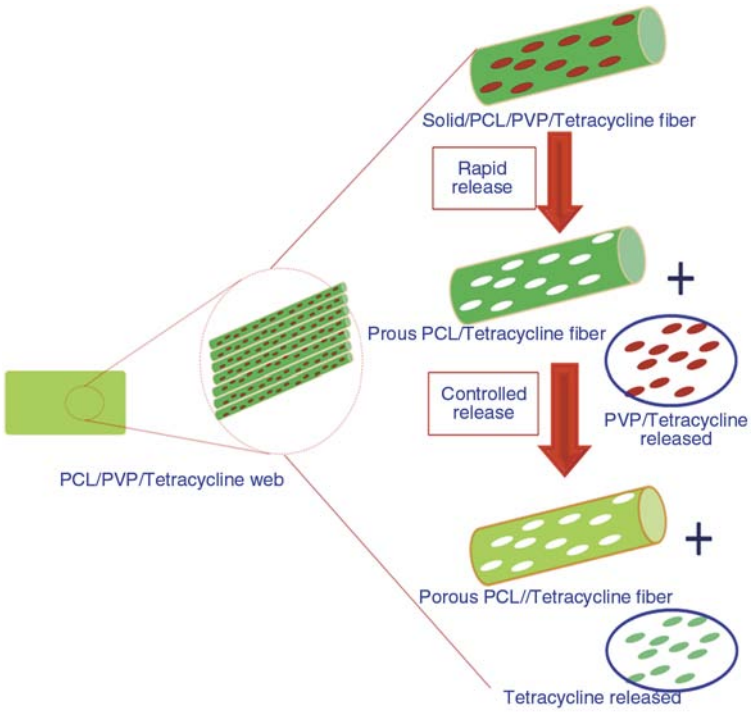

Figure 10. Schematic diagram of drug release from C-spun ultrafine fibrous web

drug is entrapped and released slowly. The conceptual diagram explaining the drug releasing mechanism is given in the Figure 10. From the figure it can be seen that drug loaded PCL/PVP fibers on contact with the releasing medium dissolves PVP readily and the drug which is intercalating with PVP is rapidly released leading to the formation of pores. The formed pores on C-spun matrices were confirmed by the SEM studies as shown in the Figure 11. Pores are uniformly distributed over the surface and the average pore size is found to be 375 nm. The developed drug loaded ultrafine fibrous web can act as a perfect drug releasing vehicle where the rapid release of the drug needed to inhibit the bacteria causing dermal infections followed by sustained release to prevent secondary infections. The addition of hydrophilic polymer has a unique advantage of the fibrous web as it aids cell adhesion and proliferation thereby acting as good wound dressing material to inhibit the microorganism [30]. Moreover the release profiles were analyzed by various models Zero order, First order, Higuchi, Hixson-crowell and Peppas model. The results of the peppas model and others are tabulated in Table 3 and Table 4. The co-efficient of determination values provide an indicator of how well the model can explain the variations is given in both the tables. From the tables it can be seen that the co-efficient of determination value of 0.99 is obtained for the

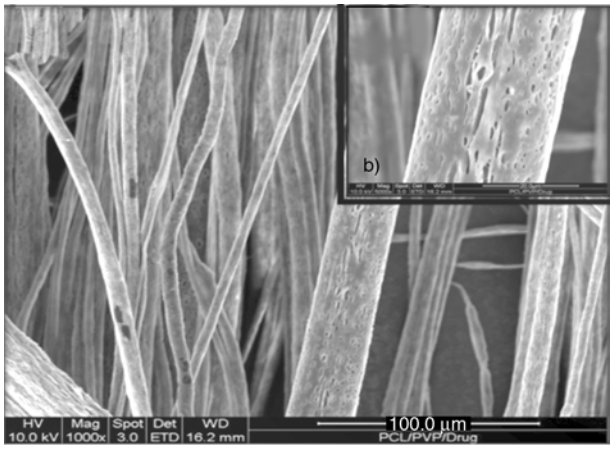

a)

Figure 11. SEM images after drug release, (a) fibrous web, (b) single fibre. Drug loaded PCL/PVP fibres on contact with the releasing medium dissolves PVP readily and the drug which is intercalating with PVP is rapidly released leading to the formation of pores.

Table 3. Diffusion constant (*n*) and regression coefficient of Tetracycline release from PCL, PCL/PVP blend ultrafine fibre mats calculated by Peppas equation

Ultra fine fiber type	r^2	n
PCL	0.99	0.628
PCL/PVP	0.98	0.631

Peppas model for both PVP and PCL/PVP indicating that the model best suits the release profile of the mat taken for the study. The *n* values in the

Table 4. Regression coefficients of different mathematical models fitted to the release of Tetracycline from PCL/PVP blend ultrafine fiber mats

Ultra fine fiber type	Zero order (r^2)	First order (r^2)	Higuchi model (r^2)	Hixon- crowell Model (r^2)
PCL	0.82	0.86	0.96	0.84
PCL/PVP	0.81	0.98	0.94	0.958

range of 0.628 suggest that the release behavior is both diffusion and swelling controlled drug release. The Higchui model also closely fits to the experimental data with r^2 of 0.96 and 0.94 for the PCL and PCL/PVP matrices respectively, suggesting the predominance of diffusion controlled release in the mat as suggested in literature.

4. Conclusions

Tetracycline incorporated PCL/PVP blended ultrafine fibrous web has been successively developed by our in-house built centrifugal spinning system. The developed fibrous web proved rapid drug release followed by sustained release and good antimicrobial activity against the tested pathogenic bacteria which is commonly found in dermal infections. The observed results concluded that it is possible to develop PCL/PVP blended ultrafine fibrous web by centrifugal spinning system and the developed web can be effectively used a wound dressing applications.

Acknowledgements

The Authors L. Amalorpava Mary & V. R. Giridev would like to acknowledge Indian Council of Medical Research (ICMR) for funding (Proceeding No: 5/20-6(Bio)/11-NCD-I).One of the authors wish to thank L. Sathish Kumar for helping to assemble the centrifugal spinning system.

References

[1] Zahedi P., Rezaeian I., Siadat S. O., Jafari S. H., Supaphol P.: A review on wound dressings with an emphasis on electrospun nanofibrous polymeric bandages. Polymers for Advanced Technologies, **21**, 21–77 (2010). DOI: 10.1002/pat.1625

[2] Hong K. H., Park J. L., Sul I. H., Youk J. H., Kang T. J.: Preparation of antimicrobial poly(vinyl alcohol) nanofibers containing silver nanoparticles. Journal of Polymer Science Part B: Polymer Physics, **44**, 2468–2474 (2006). DOI: 10.1002/polb.20913

[3] Puppi D., Piras A. M., Detta N., Dinucci D., Chiellini F.: Poly(lactic-*co*-glycolic acid) electrospun fibrous meshes for the controlled release of retinoic acid. Acta Biomaterialia, **6**, 1258–1268 (2010). DOI: 10.1016/j.actbio.2009.08.015

[4] Ma P. X., Zhang R.: Synthetic nano-scale fibrous extracellular matrix. Journal of Biomedical Materials Research, **46**, 60–72 (1999). DOI: 10.1002/(SICI)1097-4636(199907)46:1<60::AID-JBM7>3.0.CO;2-H

[5] Yang F., Murugan R., Ramakrishna S., Wang X., Ma Y-X., Wang S.: Fabrication of nano-structured porous PLLA scaffold intended for nerve tissue engineering. Biomaterials, **25**, 1891–1900 (2004). DOI: 10.1016/j.biomaterials.2003.08.062

[6] Senthilram T., Mary L. A., Venugopal J. R., Nagarajan L., Ramakrishna S., Dev V. R. G.: Self crimped and aligned fibers. Materials Today, **14**, 226–229 (2011). DOI: 10.1016/S1369-7021(11)70118-3

[7] Lin S-Y., Chen K-S., Run-Chu L.: Design and evaluation of drug-loaded wound dressing having thermoresponsive, adhesive, absorptive and easy peeling properties. Biomaterials, **22**, 2999–3004 (2001). DOI: 10.1016/S0142-9612(01)00046-1

[8] Purna S. K., Babu M.: Collagen based dressings – A review. Burns, **26**, 54–62 (2000).

[9] William H., Eaglstein M. D.: Moist wound healing with occlusive dressings: A clinical focus. Dermatologic Surgery, **27**, 175–182 (2001). DOI: 10.1046/j.1524-4725.2001.00299.x

[10] Pitt C. G.: Poly (ε-caprolactone) and its co-polymers. in 'Biodegradable polymers as drug delivery systems' (eds.: Chasin M., Langer R.) Marcel Decker, New York, 71–120 (1990).

[11] Luong-Van E., Grøndahl L., Chua K. N., Leong K. W., Nurcombe V., Cool S. M.: Controlled release of heparin from poly(ε-caprolactone) electrospun fibers. Biomaterials, **27**, 2042–2050 (2006). DOI: 10.1016/j.biomaterials.2005.10.028

[12] Heunis T. D. J., Dicks L. M. T.: Nanofibers offer alternativeways to the treatment of skin infections. Journal of Biomedicine and Biotechnology, 2010, 510682/1–510682/10 (2010). DOI: 10.1155/2010/510682

[13] Yang Q., Li Z., Hong Y., Zhao Y., Qiu S., Wang C., Wei Y.: Influence of solvents on the formation of ultrathin uniform poly(vinyl pyrrolidone) nanofibers with electrospinning. Journal of Polymer Science Part B: Polymer Physics, **42**, 3721–3726 (2004), DOI: 10.1002/polb.20222

[14] Zamani M., Morshed M., Varshosaz J., Jannesari M.: Controlled release of metronidazole benzoate from poly ε-caprolactone electrospun nanofibers for periodontal diseases. European Journal of Pharmaceutics and Biopharmaceutics, **75**, 179–185 (2010). DOI: 10.1016/j.ejpb.2010.02.002

[15] Kanawung K., Panitchanapan K., Puangmalee S-O., Utok W., Kreua-ongarjnukool N., Rangkupan R., Meechaisue C., Supaphol P.: Preparation and characterization of polycaprolactone/diclofenac sodium and poly(vinyl alcohol)/tetracycline hydrochloride fiber mats and their release of the model drugs. Polymer Journal, **39**, 369–378 (2007). DOI: 10.1295/polymj.PJ2006011

[16] Kenawy E-R., Bowlin G. L., Mansfield K., Layman J., Simpson D. G., Sanders E. H., Wnek G. E.: Release of tetracycline hydrochloride from electrospun poly(ethylene-*co*-vinylacetate), poly(lactic acid), and a blend. Journal of Controlled Release, **81**, 57–64 (2002). DOI: 10.1016/S0168-3659(02)00041-X

[17] Taepaiboon P., Rungsardthong U., Supaphol P.: Drug-loaded electrospun mats of poly(vinyl alcohol) fibres and their release characteristics of four model drugs. Nanotechnology, **17**, 2317–2329 (2006). DOI: 10.1088/0957-4484/17/9/041

[18] Jannesari M., Varshosaz J., Morshed M., Zamani M.: Composite poly(vinyl alcohol)/poly(vinyl acetate) electrospun nanofibrous mats as a novel wound dressing matrix for controlled release of drugs. International Journal of Nanomedicine, **6**, 993–1003 (2011). DOI: 10.2147/IJN.S17595

[19] Varelas C. G., Dixon D. G., Steiner C. A.: Zero-order release from biphasic polymer hydrogels. Journal of Controlled Release, **34**, 185–192 (1995). DOI: 10.1016/0168-3659(94)00085-9

[20] Mulye N. V., Turco S. J.: A simple model based on first order kinetics to explain release of highly water soluble drugs from porous dicalcium phosphate dihydrate matrices. Drug Development and Industrial Pharmacy, **21**, 943–953 (1995). DOI: 10.3109/03639049509026658

[21] Higuchi T.: Rate of release of medicaments from ointment bases containing drugs in suspension. Journal of Pharmaceutical Sciences, **50**, 874–875 (1961). DOI: 10.1002/jps.2600501018

[22] Niebergall P. J., Milosovich G., Goyan J. E.: Dissolution rate studies II. Dissolution of particles under conditions of rapid agitation. Journal of Pharmaceutical Sciences, **52**, 236–241 (1963). DOI: 10.1002/jps.2600520310

[23] Peppas N. A.: Analysis of Fickian and non-Fickian drug release from polymers. Pharmaceutica Acta Helvitiae, **60**, 110–111 (1985).

[24] Meng Z. X., Zheng W., Li L., Zheng Y. F.: Fabrication, characterization and in vitro drug release behavior of electrospun PLGA/chitosan nanofibrous scaffold. Materials Chemistry and Physics, **125**, 606–611 (2011). DOI: 10.1016/j.matchemphys.2010.10.010

[25] Zhong S., Teo W. E., Zhu X., Beuerman R. W., Ramakrishna S., Yung L. Y. L.: An aligned nanofibrous collagen scaffold by electrospinning and its effects on *in vitro* fibroblast culture. Journal of Biomedical Materials Research Part A, **79**, 456–463 (2006). DOI: 10.1002/jbm.a.30870

[26] Biresaw G., Mohamed A., Gordon S. H., Harry-O'kuru R. E., Carriere C. C.: Compatibility study in poly (tetramethyleneadipate-*co*-terephthalate)/polystyrene bioblends. Journal of Applied Polymer Science, **110**, 2932–2941 (2008). DOI: 10.1002/app.28893

[27] Mohamed A., Finkenstadt V. L., Gordon S. H., Biresaw G., Palmquist D. E., Rayas-Duarte P.: Thermal properties of PCL/gluten bioblends characterized by TGA, DSC, SEM, and infrared-PAS. Journal of Applied Polymer Science, **110**, 3256–3266 (2008). DOI: 10.1002/app.28914

[28] Moharram M. A., Khafagi M. G.: Thermal behavior of poly(acrylic acid)–poly(vinyl pyrrolidone) and poly (acrylic acid)–metal–poly(vinyl pyrrolidone) complexes. Journal of Applied Polymer Science, **102**, 4049–4057 (2006). DOI: 10.1002/app.24367

[29] Zahedi P., Karami Z., Rezaeian I., Jafari S-H., Mahdaviani P., Abdolghaffari A. H., Abdollahi M.: Preparation and performance evaluation of tetracycline hydrochloride loaded wound dressing mats based on electrospun nanofibrous poly(lactic acid)/poly(ε-caprolactone) blends. Journal of Applied Polymer Science, **124**, 4174–4183 (2012). DOI: 10.1002/app.35372

[30] Wan Y., Chen W., Yang J., Bei J., Wang S.: Biodegradable poly(L-lactide)-poly(ethylene glycol) multiblock copolymer: Synthesis and evaluation of cell affinity. Biomaterials, **24**, 2195–2203 (2003). DOI: 10.1016/S0142-9612(03)00107-8

eXPRESS Polymer Letters Vol.7, No.3 (2013) 249–260
Available online at www.expresspolymlett.com
DOI: 10.3144/expresspolymlett.2013.23

Synthesis of PMMA-*b*-PU-*b*-PMMA tri-block copolymers through ARGET ATRP in the presence of air

P. Król[*], *P. Chmielarz*

Department of Polymer Science, Faculty of Chemistry, Rzeszów University of Technology, Al. Powstańców Warszawy 6, 35-959 Rzeszów, Poland

Received 11 September 2012; accepted in revised form 10 November 2012

Abstract. ARGET (activators regenerated by electron transfer) ATRP (atom transfer radical polymerization) has been successfully performed (in flasks fitted with rubber septa without the need for use of Schlenk line) in the presence of limited amount of air and with a very small (370 ppm) amount of copper catalyst together with an appropriate reducing agent Cu(0). Novelty of this work is that the poly(methyl methacrylate)-block-polyurethane-block-poly(methyl methacrylate) tri-block copolymers were synthesized for the first time through ARGET ATRP, by using tertiary bromine-terminated polyurethane as a macroinitiator (MBP-PU-MBP), $CuBr_2$ or $CuCl_2$ as a catalyst and *N*,*N*,*N*′,*N*″,*N*″-pentamethyldiethylenetriamine (PMDETA) or 2,2′-bipyridine (Bpy) as a complexing agent. As the polymerization time increases, both the monomer conversion and $\ln([M]_0/[M])$ increased and the molecular weight of copolymer increases linearly with increasing conversion. Theoretical number-average molecular weight ($M_{n,th}$) of the tri-block copolymers was found to be comparable with number-average molecular weight determined by GPC analyses ($M_{n,GPC}$). These results indicate that the formation of the tri-block copolymers was through atom transfer radical polymerization mechanism. ^{1}H and ^{13}C NMR spectral methods were employed to confirm chemical structures of synthesized macroinitiator and tri-block copolymers. Mole percentage of PMMA in the tri-block copolymers was calculated using ^{1}H NMR spectroscopy and was found to be comparable with the GPC results. Additionally, the studies of surface properties (confocal microscopy and SFE) of tri-block copolymer coatings confirmed the presence of MMA segments.

Keywords: *polymer synthesis, molecular engineering, ATRP, ARGET ATRP, brominated polyurethanes*

1. Introduction

Atom transfer radical polymerization (ATRP) is one of the most rapidly developing areas of polymer science, allowing to obtain effective control over molecular weights, narrow molecular weight distributions, architectures, and well-defined compositions. However, normal ATRP has one notable limitation that is the catalyst used is sensitive to air and other oxidants. In order to overcome this drawback, Matyjaszewski's group has developed ATRP technique, namely activator regenerated by electron transfer atom transfer radical polymerization (ARGET ATRP) [1]. This method provides a continuous controlled polymerization with a significant reduction of the amount of copper-based catalyst complex (< 50 ppm) due to a constant regeneration of the Cu(I) activator species by reducing agents, which compensate for any loss of Cu(I) by termination [2]. ARGET ATRP was successfully applied to relatively nonpolar monomers (e.g., styrene, butyl acrylate, and methyl methacrylate) [3], for the preparation of polymeric materials with different structures and architectures including homopolymers, block copolymers, and development of a scalable process for preparation of molecular brushes on a flat surface [1]. However, tri-block copolymers have sparked

[*]Corresponding author, e-mail: pkrol@prz.edu.pl

much interest and their potential has been realized in many areas (membranes, biodegradable polymers). Block copolymers are an interesting class of materials that possess different properties compared to those of each individual homopolymer segments they are composed of. As block length is playing a major role on the properties of the block copolymers, effective control of the block lengths is important and this can easily be achieved using different controlled radical polymerization (CRP) methods [4].

Polyurethanes (PUs) are of commercial interest due to their excellent properties such as high chemical resistance and high strength. The physical and chemical properties of polyurethane (PU) depend on the type and composition of polyol, diisocyanate, the chain extender, and other additives. Conventional PU is hydrophobic in nature, but when ionic groups are incorporated, PU with both hydrophobic and hydrophilic segments is obtained, which, in turn, forms dispersion when water is added [5]. Meanwhile, in the present investigation, we focused on the synthesis of moderately hydrophobic PU macroinitiator modified by incorporating methyl methacrylate (MMA) as hydrophobic monomer in order to obtain copolymers with increased hydrophobicity.

Tri-block copolymers with using different polyurethane based macroinitiators were already obtained through ATRP classical mechanism [6, 7]. However, this method was arduous because of the degassing of the reaction mixture, therefore in the current study we used ARGET ATRP, with the aim of omitting the deoxygenation process. Although the chemical basis of polymerization ATRP has been known for about 5 years, this technique has not yet been used for the synthesis of tri-block copolymers using PU as a macroinitiator. In the present investigation, we focused on ARGET ATRP of MMA in the presence of tertiary bromine-terminated ($-C(CH_3)_2Br$) polyurethane (MBP-PU-MBP) as a macroinitiator, $CuBr_2$ and $CuCl_2$ as a catalyst, *N*,*N*,*N*′,*N*″,*N*″-pentamethyldiethylenetriamine (PMDETA) and 2,2′-bipyridine (Bpy) as a complexing agent. In this article, we report that ARGET ATRP can be successfully carried out in the presence of limited amounts of air and control is essentially unaffected by excess reducing agent. Reactions can be carried out without any deoxygenation, in flasks fitted with rubber septa. It is important here to mention that the resulting poly(methyl methacrylate)-block-polyurethane-block-poly(methyl methacrylate) (PMMA-*b*-PU-*b*-PMMA) tri-block copolymers obtained through ARGET ATRP is reported now for the first time.

2. Experimental section

2.1. Materials

4,4′-Methylene diphenyl diisocyanate (MDI), dibutyltin dilaurate (DBTDL), α-bromoisobutyryl bromide (BB; 98%), ethylene glycol (99.9%) and copper(0) metal turnings (≥99%) were used as received from Sigma-Aldrich Inc., St. Louis, USA. Polyoxytetramethylene glycol of molecular weight 1000 (PTMG; Merck, Darmstadt, Germany) was purified by heating at 105°C under vacuum for 3 h before use. Methyl methacrylate (MMA; 99%; Sigma-Aldrich, USA), $CuBr_2$ (99%; Sigma-Aldrich, USA), $CuCl_2$ (97%; Sigma-Aldrich, USA), Bpy (≥99%; Sigma-Aldrich, USA) and PMDETA (≥98%; Merck, Germany) were used without further purification. Sodium carbonate (99.5%), magnesium sulfate (98.5%), dichloromethane (99.5%), acetonitrile (99.5%), methanol (99.9%) and acetone (99.5%) were obtained from Chempur, Piekary Śląskie, Poland. Analytical grade *N*,*N*-dimethylformamide (DMF; Chempur, Poland) and methyl ethyl ketone (MEK; Chempur, Poland), were distilled and the middle portions were used after storing over type 4 Å molecular sieves.

2.2. Synthesis of 2-hydroxyethyl-2′-methyl-2′-bromopropionate (HMB)

HMB (ATRP initiator) was synthesized according to Figure 1.

Bromoisobutyryl bromide was reacted with cold anhydrous ethylene glycol (excess) under stirring for 4 h. The molar ratio of ethylene glycol and *a*-bromoisobutyryl bromide was 25 in order to avoid coupling reaction. The reaction mixture was added to deionized water, and the reaction product was extracted by dichloromethane. The organic solution

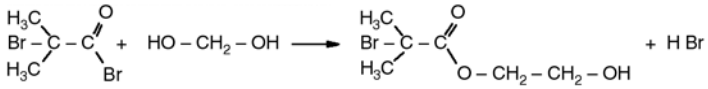

Figure 1. Synthesis of HMB initiator

was washed with water and sodium carbonate and dried over anhydrous magnesium sulfate. The final product was isolated as a liquid upon removal of the solvent (yield 88%) and stored at 0–4°C until use [8].

2.3. Synthesis of tertiary bromine-terminated polyurethane (MBP-PU-MBP)

2-methyl-2-bromopropionate terminated polyurethane macroinitiator was synthesized from one mole of PTMG, two moles of MDI, and two moles of HMB (Figure 2).

First stage includes synthesis of prepolymer from MDI (7.5 g, 0.03 mol) and PTMG (15 g, 0.015 mol) in 40 mL MEK at 40°C in a atmosphere of nitrogen for 1 h. The temperature was then raised to 65°C for 2 h and the reaction was allowed to proceed till the isocyanate content reached half the initial value (2,31% content of –NCO groups in the prepolymer about M_n = 6960 g/mol, as determined by dibutyl amine titration).

In the second stage, prepolymer was end-capped by addition of HMB (6.33 g, 0.03 mol) in the presence of MEK (20 mL). Then 0.03 g of DBTDL catalyst was added, the temperature was raised to 70°C and the reaction was allowed to go to completion as confirmed 0% content of –NCO groups and the disappearance of isocyanate peak by FT-IR (Figure 4). The resulting macroinitiator solution was dried at 70°C in vacuum and stored at 0–4°C until use. Recently, similar method was also used to synthesize polyurethane macroinitiator from PTMG, toluene diisocyanate (TDI) and HMB [6].

2.4. ARGET ATRP of MMA using MBP-PU-MBP/CuX_2/Ligand initiating system

Synthesis of the tri-block copolymers were conducted in 100°C for 30 h. PMMA-*b*-PU-*b*-PMMA were synthesized using polyurethane macroinitiator, reducing agent Cu(0), copper catalyst CuX_2 ($CuBr_2$, $CuCl_2$) and PMDETA or Bpy as a ligand (Figure 3). A typical example of the general procedure in the presence of air was as follows.

A solution of catalyst was made by dissolving copper catalyst $CuBr_2$ (3.57 mg, 0.016 mmol) or $CuCl_2$ (2.15 mg, 0.016 mmol) and ligand PMDETA (11.09 mg, 0.064 mmol) or Bpy (9.99 mg, 0.064 mmol) in DMF (1.4 mL). Then 13 mL glass vial containing a solution of catalyst was charged with MBP-PU-MBP (0.97 g, 0.16 mmol) dissolved in DMF (2 mL) and MMA (3.204 g, 32 mmol), after which metallic copper was added (81.3 mg, 1.28 mmol) to initiate polymerization. Next the system was partially deoxygenated by bubbling N_2 for two minutes, after which the initial sample was taken. The sealed vial with a plastic screw cap was placed in an oil bath thermostated at 100°C. For all 4 synthesis catalyst concentration was 370 ppm with respect to final polymer. Samples were taken at timed intervals and analyzed by GPC and NMR to

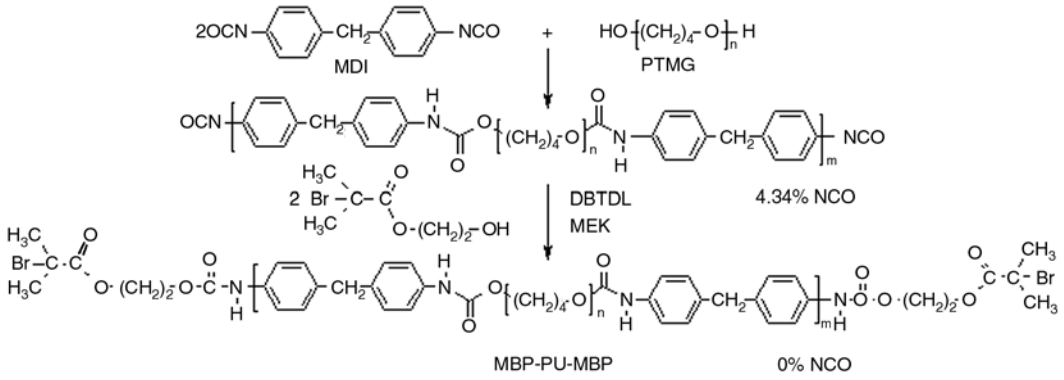

Figure 2. Synthesis of MBP-PU-MBP

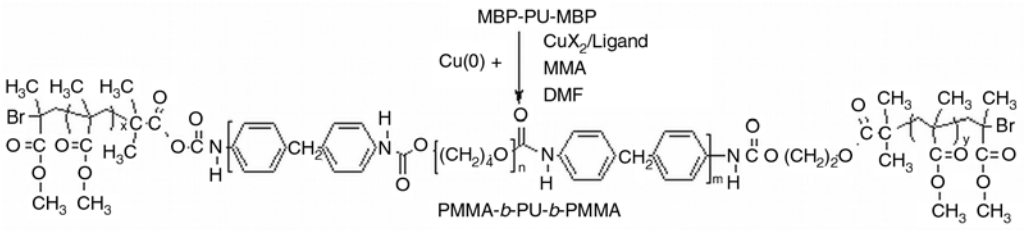

Figure 3. Synthesis of PMMA-*b*-PU-*b*-PMMA tri-block copolymers through ARGET ATRP

follow the progress of the reaction. The polymerization was stopped after 30 h by opening the vial and exposing the catalyst to air. The resulting solution was poured with methanol and acetonitrile. Resulting pure copolymers were dried at 70°C under vacuum.

2.5. Characterization techniques

FT-IR spectra were taken with the spectrophotometer Nicolet 6700 FT-IR (Thermo Scientific, Madison, USA), within 4000–500 cm^{-1}, with the use of attenuated total reflectance (ATR) technique (the polymer film was placed between prism walls).

Number-average (M_n) and weight-average (M_w) molecular weights and molecular weight distribution (MWD) were determined by GPC using a Viscotek T60A system (Viscotek, Houston, USA) equipped with a triple detector: refractometric (RI), light scattering (LS) and viscosity detector (DV). Separations were made at 25±0.1°C on a GMHHRL column packed with TSK-gel of pore diameter 5 μm Thoso-Haas, and Styragel 1 and 2 Waters. The THF flow rate was 1 mL/min. Operation of the chromatograph was controlled by original computer software TRISEC Data Acquisition System by Viscotec Corporation.

^1H and ^{13}C NMR spectra were taken with the use of the spectrometer FT-NMR Bruker Avance 500^{II} (Bruker, Karlsruhe, Germany). The sample of HMB was dissolved in $CDCl_3$, while samples of macroinitiator and copolymers were dissolved in DMSO-d_6/*h*-DMSO and the solutions with the concentration of about 0.2 g/dm^3 were prepared. TMS was used as a standard.

Monomer conversion (α) was calculated from the ^1H NMR spectra of the copolymer samples Equation (1) by comparison of the integration for methine proton of the MMA (δ = 5.68–6.03 ppm) [9], with the signals from aromatic protons of the macroinitiator (δ = 7.08–7.39 ppm):

$$\alpha = 100\% - \left[\frac{\dfrac{I_{q,n} + I_{q',n}}{I_{l,n} + I_{k,n}}}{\dfrac{I_{q,0} + I_{q',0}}{I_{l,0} + I_{k,0}}} \cdot 100\% \right] \quad (1)$$

where $I_{q,0}$ and $I_{q',0}$ denotes the initial integration of the methine proton of the MMA, $I_{q,n}$ and $I_{q',n}$ – integration of the methine proton of the MMA after time t =3, 6, 12, 18, 24, 30 h, $I_{l,0}$ and $I_{k,0}$ – initial integration of the aromatic protons of the MBP-PU-MBP, $I_{l,n}$ and $I_{k,n}$ – initial integration of the aromatic protons of the MBP-PU-MBP after time t =3, 6, 12, 18, 24, 30 h.

Based on the previous research [5], the theoretical molecular weight, $M_{n,th}$ of the synthesized copolymer could be calculated by Equation (2):

$$M_{n,th} = \left[\left(\frac{[M]_0}{[I]_0} \right) \cdot \alpha \cdot M_M \right] + M_I \quad (2)$$

where $[M]_0$ denotes the initial concentration of the MMA, $[I]_0$ – initial concentration of the MBP-PU-MBP, M_M – molecular weight of the MMA, M_I – molecular weight of the MBP-PU-MBP (determined by GPC analyses) and α – monomer conversion (1).

Molar content of PMMA (β_{NMR}) [6, 7] was calculated from the ^1H NMR spectra of the copolymer samples using Eqution (3), by comparing $M_{n,th}$ values of MBP-PU-MBP and PMMA-*b*-PU-*b*-PMMA:

$$\beta_{NMR} = \left(\frac{M_{n,th,n} - M_I}{M_I} \right) \cdot 100 \quad (3)$$

where $M_{n,th,n}$ denotes the $M_{n,th}$ of the PMMA-*b*-PU-*b*-PMMA after time t =3, 6, 12, 18, 24, 30 h, calculated by Equation (2), $M_I - M_{n,th}$ of the MBP-PU-MBP (determined by ^1H NMR analyses).

Also it can easily be found out by comparing $M_{n,GPC}$ of MBP-PU-MBP and PMMA-*b*-PU-*b*-PMMA copolymers (β_{GPC}) [6, 7], by Equation (4):

$$\beta_{GPC} = \left(\frac{M_{n,GPC,n} - M_I}{M_I} \right) \cdot 100 \quad (4)$$

where $M_{n,GPC,n}$ denotes the $M_{n,GPC}$ of the PMMA-*b*-PU-*b*-PMMA after time t =3, 6, 12, 18, 24, 30 h, M_I – M_n of the MBP-PU-MBP (determined by GPC analyses).

Thermal gravimetric analysis of the obtained MBP-PU-MBP and PMMA-*b*-PU-*b*-PMMA copolymers involved the use of a TGA/DSC1 thermobalance from Mettler Toledo (Warsaw, Poland). TG; $\Delta m/m = f(T)$ and DTG; $dm/dT = f(T)$ were derived. The measurements were taken within the temperature range of 25–600°C, at a constant heating rate of 10°/min, in nitrogen.

The tri-block copolymers coating for studies of surface properties were formed by applying the PMMA-*b*-PU-*b*-PMMA dissolved in acetone to a surface of silicon base and evaporation of water by air-drying at 25°C. The coatings were then subjected to seasoning under such conditions over 10 days.

Confocal microscopy analyses were taken with the optical 3D NanoFocus system (Oberhausen, Germany) using objectives 320×320μm and magnification 50×. Values of the coefficients of roughness R_a (arithmetic mean deviation of the assessed profile) and R_z (maximum height of the profile within a sampling length) were obtained from the *μsurf Premium* software.

As in our previous work [10] also here, the physical parameters of surface energy of a solid γ_S were found on the basis of the van-Oss-Good model. The contact angles Θ were measured with the use of Cobrabid Optica goniometer (Warsaw, Poland). Values of Θ obtained from the software *Kropla* were used to calculate by software *Energia* values of γ_S copolymer coatings.

3. Results and discussion

HMB was widely used to synthesize ATRP initiators, which were used to synthesize homopolymers (e.g. poly(methyl acrylate) [11]) and block copolymers (e.g. polystyrene-g-poly(methyl methacrylate) copolymer [12]) with desired functionality and composition.

As block copolymers with narrow MWD could not be achieved using our previously reported $–CH_2Br$ terminated PU macroinitiator (and $M_{n,th}$ values of the tri-block copolymers were not matching with $M_{n,GPC}$ values) [13], we decided to prepare $–C(CH_3)_2Br$ terminated PU macroinitiator and used as an ATRP initiator to synthesize hydrophobic poly(methyl methacrylate)-*b*-polyurethane-*b*-poly (methyl methacrylate) block copolymers with narrow MWD. It is expect, that the tertiary radical $\dot{C}(CH_3)_2$, can be generated from $–C(CH_3)_2Br$ terminated PU which is more stable than the $\dot{C}H_2$ radical from $–CH_2Br$ terminated PU [7].

3.1. Chemical structure of ATRP initiator, MBP-PU-MBP and copolymers

Figure 4 shows the FT-IR spectra of polyurethane-based macroinitiator MBP-PU-MBP.

In the FT-IR spectrum of MBP-PU-MBP (Figure 4) there is no presence the band at 2272 cm^{-1} which represent asymmetrical stretching vibrations of –NCO groups (specific for isocyanates). The lack of this band is confirming that the macroinitiator was end-capped by bromine.

The chemical structures of the synthesized HMB, MBP-PU-MBP and PMMA-*b*-PU-*b*-PMMA tri-block copolymer (CM4BrP6 sample) shown in Figure 5 were confirmed by ^1H NMR and ^{13}C NMR spectroscopy (Table 1 and 2). Moreover, in the ^1H NMR spectrum of MBP-PU-MBP the characteristic signal of the NH proton derived from allophanates is not observed at 10.65 ppm, as well as in the ^{13}C NMR spectrum of MBP-PU-MBP the characteristic signal of the C=O group from allophanates is not observed at about 151 and 155 ppm [14].

These results of ^1H NMR and ^{13}C NMR spectroscopy show that HMB, MBP-PU-MBP and CM4BrP6 copolymer were successfully synthesized.

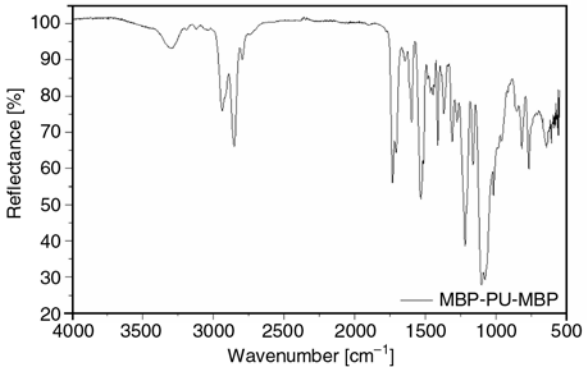

Figure 4. FT-IR spectra of MBP-PU-MBP

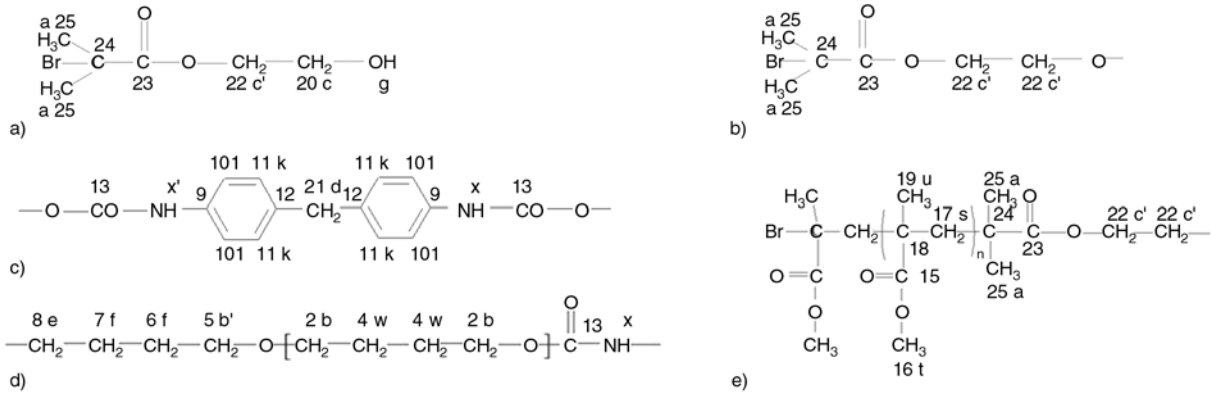

Figure 5. Chemical structure of (a) HMB, (b-d) MBP-PU-MBP and (c-e) PMMA-*b*-PU-*b*-PMMA tri-block copolymer, (CM4BrP6 sample)

Table 1. ^{1}H NMR data of HMB, MBP-PU-MBP and PMMA-*b*-PU-*b*-PMMA copolymer, (CM4BrP6 sample)

Type of nucleus ^{1}H	HMB	MBP-PU-MBP	PMMA-*b*-PU-*b*-PMMA, CM4BrP6
	Chemical shift [ppm]		
g	2.35	–	–
c	3.82–3.85	–	–
a	1.94–1.95	1.88–1.92	1.88–1.90
c′	4.28–4.30	4.32–4.46	4.32–4.37
x	–	9.50	9.50
l	–	7.32–7.35	7.34
k	–	6.98–7.01	7.07
d	–	3.78–3.82	3.78
b′	–	3.60–3.62	3,68
b	–	3.24–3.32	3.31
x′	–	8.50	8.00–8.50
e	–	4.04–4.06	4.04
f	–	1.56–1.68	1.56–1.64
w	–	1.44–1.49	1.49
t	–	–	3.56
s	–	–	2.07
u			0.74–1.28
			–CH_3 of PMMA (*rr*) 0.74
			–CH_3 of PMMA (*mr*) 0.91
			–CH_3 of PMMA (*mm*) 1.07–1.28

Table 2. ^{13}C NMR data of HMB, MBP-PU-MBP and PMMA-*b*-PU-*b*-PMMA copolymer, (CM4BrP6 sample)

Type of nucleus ^{13}C	HMB	MBP-PU-MBP	PMMA-*b*-PU-*b*-PMMA, CM4BrP6
	Chemical shift [ppm]		
25	30.67–30.69	30.10–30.22	30.67
24	55.36–55.85	56.82–57.26	48.50
23	171.47–171.94	170.65–170.84	176.07–177.27
22	60.57–60.75	61.65	63.81
20	67.24–67.41	67.28	–
21		40.00	38.93–39.93
13		153.17–153.47	162.20
9		135.22	135.66
10		118.17–121.08	118.16
11		126.55–128.71	125.65–128.73
12		136.78–137.04	137.06
2		69.61–69.66	69.62
4		26.00	25.99
5		69.35	69.36
6		25.47	25.48
7		25.64	25.65
8		63.79–64.06	63.81
15			177.27
16			51.62
17			53.58
18			43.81–44.18
19			17.95–18.51
			–CH_3 of PMMA (*rr*) 15.89
			–CH_3 of PMMA (*mr*) 17.95
			–CH_3 of PMMA (*mm*) 18.51

The tacticity of PMMA can be identified using the integration values of peaks at 0.75, 0.91, and 1.07–1.28 ppm which correspond to syndiotactic (*rr*), atactic (*mr*), and isotactic (*mm*) PMMA, respectively [4]. The ratio among rr, mr, and mm in our study for CM4BrP6 is 53:34:13 which is similar to the reported tacticity ratio of PMMA prepared by ATRP [15].

The molar content of PMMA in the tri-block copolymers (4) can easily be found out by comparing molecular weights (obtained by GPC) of MBP-PU-MBP and copolymers which are given in Table 3–6. It can also be found out using ^{1}H NMR technique (3) and the results are included in Table 3–6. The molar content of PMMA from GPC and ^{1}H NMR technique are comparatively similar.

3.2. Kinetics and mechanism of the polymerization

Reactions were carried out under homogeneous conditions. In this case we applied large excess of reducing agent in relation to the macroinitiator MBP-PU-MBP (8-fold; [Cu(0)]/[MBP-PU-MBP] = 8). An excess of reducing agent consumes the oxygen present in the system and, therefore, provides a deoxygenated environment for ATRP. The appropriate amount of reducing agent is crucial to achieve a controlled polymerization. The required amount of reducing agent is determined not only by the amount of Cu(II) complexes in the reaction system, but also by the amount of oxygen present in the vial. The volume of free space in a small glass vial was ~4 mL, which corresponds to 0.0375 mmol of O_2. Assuming that one O_2 molecule oxidizes two Cu(0) molecules, this would correspond to the molar ratio of [Cu(0)]air/[MBP-PU-MBP] = 2·0.0375/0.32 = 0.23, what is the amount of reducing agent needed to consume the oxygen present in the free space in a glass vial. Therefore, in this case amount of effective reducing agent is about 7.77 ([Cu(0)] – $[Cu(0)]_{air}$/[MBP-PU-MBP]) [3].

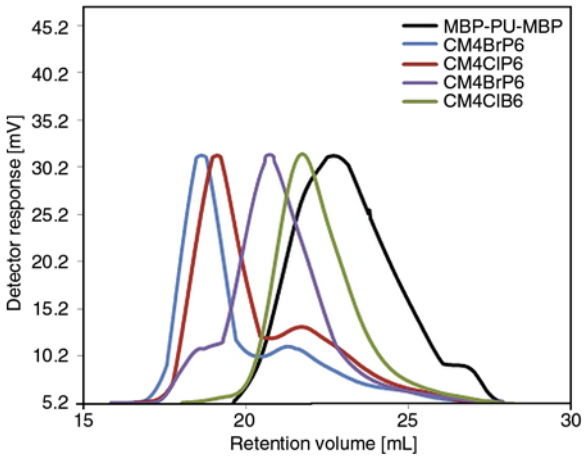

Figure 6. GPC eluograms of MBP-PU-MBP and copolymers CM4BrP6, CM4ClP6, CM4BrB6, CM4BrB6

PMMA-*b*-PU-*b*-PMMA tri-block copolymers with narrow MWD were obtained, as confirmed by the GPC eluograms (Figure 6). The MWDs of the resulting copolymers are quite low in most cases.

To understand the mechanism of polymerization, effect of time on the polymerization of MMA was carried out and the results are presented in Table 3–6.

Table 3. Effect of time on ARGET ATRP of MMA using $CuBr_2$/PMDETA. Polymerization conditions: $[MMA]_0/[MBP\text{-}PU\text{-}MBP]_0/[CuBr_2]_0/[PMDETA]_0/[Cu(0)]$ = 200/1/0.1/0.4/8 in DMF

Sample No.	Time [h]	α [%]	β_{NMR} [%]	β_{GPC} [%]	$M_{n,th}\cdot10^{-3}$ [g/mol]	$M_{n,GPC}\cdot10^{-3}$ [g/mol]	$M_{w,GPC}\cdot10^{-3}$ [g/mol]	M_w/M_n
MBP-PU-MBP	0	0.0	0.0	0.0	7.4	7.4	11.8	1.60
CM4BrP1	3	3.8	10.4	15.3	8.2	8.5	13.6	1.59
CM4BrP2	6	9.3	25.1	32.5	9.2	9.8	14.8	1.51
CM4BrP3	12	20.3	54.9	62.0	11.4	12.0	16.1	1.35
CM4BrP4	18	30.6	83.0	90.6	13.5	14.1	18.2	1.29
CM4BrP5	24	43.0	116.5	119.8	16.0	16.2	26.1	1.61
CM4BrP6	30	52.1	141.3	150.1	17.8	18.5	42.2	2.34

Table 4. Effect of time on ARGET ATRP of MMA using $CuCl_2$/PMDETA. Polymerization conditions: $[MMA]_0/[MBP\text{-}PU\text{-}MBP]_0/[CuCl_2]_0/[PMDETA]_0/[Cu(0)]$ = 200/1/0.1/0.4/8 in DMF

Sample No.	Time [h]	α [%]	β_{NMR} [%]	β_{GPC} [%]	$M_{n,th}\cdot10^{-3}$ [g/mol]	$M_{n,GPC}\cdot10^{-3}$ [g/mol]	$M_{w,GPC}\cdot10^{-3}$ [g/mol]	M_w/M_n
MBP-PU-MBP	0	0.0	0.0	0.0	7.4	7.4	11.8	1.60
CM4ClP1	3	3.8	10.4	16.2	8.2	8.6	13.6	1.58
CM4ClP2	6	9.3	25.1	29.9	9.2	9.6	15.4	1.60
CM4ClP3	12	16.3	44.2	53.7	10.6	11.4	16.6	1.47
CM4ClP4	18	27.5	74.7	79.6	12.9	13.3	28.5	2.15
CM4ClP5	24	35.4	96.0	106.1	14.5	15.2	26.6	1.75
CM4ClP6	30	46.4	125.8	135.6	16.7	17.4	38.8	2.23

Table 5. Effect of time on ARGET ATRP of MMA using $CuBr_2$/Bpy. Polymerization conditions: $[MMA]_0/[MBP\text{-}PU\text{-}MBP]_0/[CuBr_2]_0/[Bpy]_0/[Cu(0)] = 200/1/0.1/0.4/8$ in DMF

Sample No.	Time [h]	α [%]	β_{NMR} [%]	β_{GPC} [%]	$M_{n,th}\cdot10^{-3}$ [g/mol]	$M_{n,GPC}\cdot10^{-3}$ [g/mol]	$M_{w,GPC}\cdot10^{-3}$ [g/mol]	M_w/M_n
MBP-PU-MBP	0	0.0	0.0	0.0	7.4	7.4	11.8	1.60
CM4BrB1	3	2.1	5.6	12.6	7.8	8.3	13.5	1.62
CM4BrB2	6	6.4	17.4	23.5	8.7	9.1	14.7	1.61
CM4BrB3	12	13.3	36.0	47.3	10.0	10.9	15.4	1.41
CM4BrB4	18	18.5	50.2	66.2	11.1	12.3	16.8	1.37
CM4BrB5	24	27.5	74.7	85.1	12.9	13.7	25.6	1.87
CM4BrB6	30	35.9	97.3	106.0	14.6	15.2	29.0	1.91

Table 6. Effect of time on ARGET ATRP of MMA using $CuCl_2$/Bpy. Polymerization conditions: $[MMA]_0/[MBP\text{-}PU\text{-}MBP]_0/[CuCl_2]_0/[Bpy]_0/[Cu(0)] = 200/1/0.1/0.4/8$ in DMF

Sample No.	Time [h]	α [%]	β_{NMR} [%]	β_{GPC} [%]	$M_{n,th}\cdot10^{-3}$ [g/mol]	$M_{n,GPC}\cdot10^{-3}$ [g/mol]	$M_{w,GPC}\cdot10^{-3}$ [g/mol]	M_w/M_n
MBP-PU-MBP	0	0.0	0.0	0.0	7.4	7.4	11.8	1.60
CM4ClB1	3	2.1	5.7	10.2	7.8	8.1	12.5	1.54
CM4ClB2	6	3.3	9.0	16.7	8.0	8.6	13.6	1.58
CM4ClB3	12	9.7	26.2	37.4	9.3	10.2	15.1	1.49
CM4ClB4	18	17.6	47.7	53.7	10.9	11.4	15.5	1.37
CM4ClB5	24	21.5	58.3	66.8	11.7	12.3	16.5	1.37
CM4ClB6	30	27.1	73.6	82.3	12.8	13.5	17.7	1.32

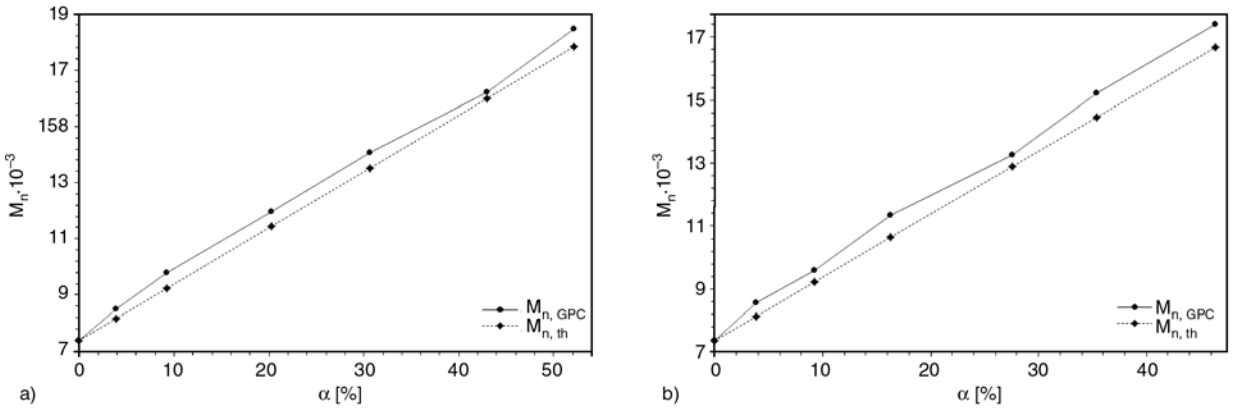

Figure 7. Comparison of $M_{n,th}$ and $M_{n,GPC}$ as a function of monomer conversion plots for the polymerization of MMA at using MBP-PU-MBP/$CuBr_2$/PMDETA (a) and MBP-PU-MBP/$CuCl_2$/PMDETA (b) initiating system

As the polymerization time increases, there is an increase in conversion and $M_{n,th}$. Here the concentration of Br in MBP-PU-MBP was calculated using molecular weight of MBP-PU-MBP obtained through GPC ($2\cdot1.18/7400 = 3.2\cdot10^{-4}$ mol Br).

Figures 7a and 7b shows M_n versus monomer conversion plots for the polymerization of MMA, whereas Figure 8 present $\ln([M]_0/[M])$-vs-time plots for the polymerization of MMA, where $[M]_0$ and [M] represent the initial monomer concentration and the monomer concentration at time *t*, respectively. The straight line obtained in semi-logarithmic plots of $\ln([M]_0/[M])$ versus time shows that the concentration of propagating radical is constant dur-

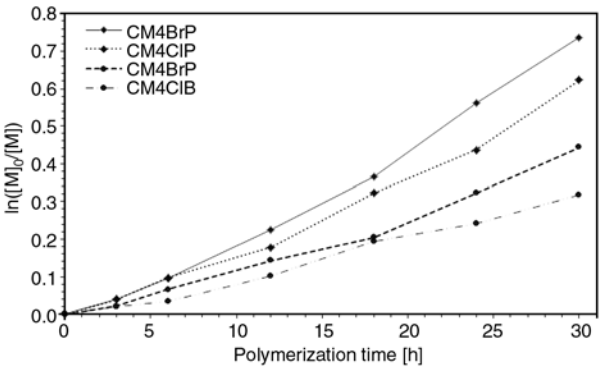

Figure 8. Comparison of $\ln([M]_0/[M])$–polymerization time plots for the polymerization of MMA at using $CuBr_2$/PMDETA (CM4BrP), $CuCl_2$/PMDETA (CM4ClP), $CuBr_2$/Bpy (CM4BrB) and $CuCl_2$/Bpy (CM4ClB) catalyst complex

ing the studied period of time. In all cases (Table 3–6) $M_{n,GPC}$, increases with increasing monomer conversion which is a clear evidence for the 'living' nature of the initiating systems (and its values found to be comparable). Moreover MWD of the tri-block copolymers remains narrow in the polymers from higher polymerization time (Table 3–6).

After 30 h, maximum conversion obtained for the MBP-PU-MBP/$CuBr_2$/PMDETA initiating system was 52.1% (M_n = 18500 g/mol, Table 3, CM4BrP sample). However copolymer with MWD amount 2.34 was received. Therefore, to study the effect of nature of the catalyst, $CuCl_2$ was used instead of $CuBr_2$ for the polymerization of MMA (Table 4). Similarly to the previous system, MBP-PU-MBP/$CuCl_2$/PMDETA initiating system also shows 'livingness' during the formation of the tri-block copolymers. After 30 h, the reaction reached 46.4% conversion and M_n was 17 400 g/mol (Table 4, CM4ClP sample). The conversion in $CuCl_2$ system is lower than the $CuBr_2$ system, but based on the MWD values former system is more controlled than the latter system.

As R–Cl bond is stronger than R–Br bond, $CuCl_2$ acts as a good deactivator of the radical generated from MBP-PU-MBP than $CuBr_2$ and as a result conversion in $CuCl_2$ system was lower than the $CuBr_2$ system. However 'living' nature of both the initiating systems was confirmed by linear increase of M_n with conversion plots. Moreover 'living' nature was further supported by the good agreement between $M_{n,th}$ and $M_{n,GPC}$ values [16].

To study the effect of nature of the complexing agent, Bpy was used instead of PMDETA for the ARGET ATRP of MMA and the results are presented in Table 5 and 6. The monomer conversion in Bpy systems is lower than the PMDETA systems but based on the MWD values former system is more controlled than the latter system. The higher monomer conversion in PMDETA systems follows directly from the fact that catalyst activity depends on type of ligand [17] and their activation rate constants – PMDETA has activation rate constant higher by an order of magnitude in relation to bpy [18]. There is a little lack of linearity especially in the $\ln([M]_0/[M])$-vs-time plot (Figure 8), this might be due to the lack of inefficient deactivation by $CuBr_2$/Bpy and $CuCl_2$/Bpy initiating system complex, which leads to the irreversible radical-radical termination as side reactions.

One of the drawbacks of ARGET is that ligand must be added to metal at 3 to 10 times molar excess in order to achieve a controlled polymerization. The excess ligand helps to maintain the catalyst complex and protect it from destabilizing side reactions. These side reactions vary depending on reaction conditions, but generally include monomer complexation to catalyst, and destabilization or complexation of catalyst to Lewis acids formed from the reduction mechanism [5].

It is interesting to note that when $–CH_2Br$ terminated polyurethane was used in our earlier investigation [13], $M_{n,GPC}$ and $M_{n,th}$ values were nowhere near, but in the present case it is comparable. Dibromo PU macroinitiator contains primary alkyl halide groups, show slow activation rate (and fast deactivation rate) are compared it the high activation (and slow deactivation) of the propagating PMMA chain end [4]. This result shows that 2-methyl-2-bromopropionate terminated PU is better macroinitiator than $–CH_2Br$ terminated PU, because it can generated the tertiary radical, which is more stable than the previously reported primary radical [7]. Another important fact is that the ATRP of MMA is itself difficult to control. Though the initiation is slow, the controlled polymerization of the present initiating system and the formation block copolymers can be confirmed by $\ln([M]_0/[M])$-polymerization time, M_n-monomer conversion and spectral results.

3.3. Thermal studies

Thermal stability of MBP-PU-MBP and copolymers (CM4BrP6, CM4ClP6, CM4BrB6, CM4BrB6) was also studied using TGA and the results are presented in Figure 9 and Table 7.

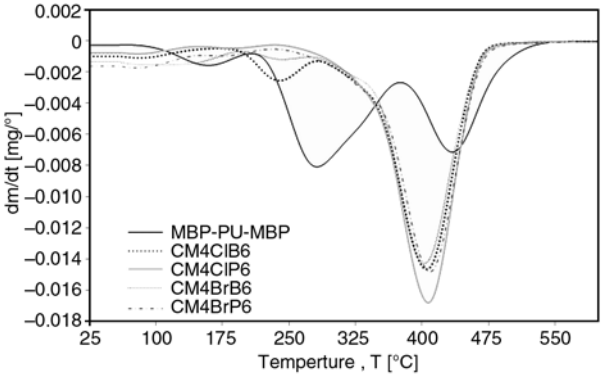

Figure 9. DTG thermograms for MBP-PU-MBP and copolymers CM4BrP6, CM4ClP6, CM4BrB6, CM4BrB6

Table 7. Thermal stability of MBP-PU-MBP and copolymers CM4BrP6, CM4ClP6, CM4BrB6, CM4BrB6

Sample No.	I stage degradation		II stage degradation		III stage degradation		Sumary mass loss [%]
	Mass loss [%]	T [ºC]	Mass loss [%]	T [ºC]	Mass los [%]	T [ºC]	
MBP-PU-MBP	8.16	162	48.54	282	39.21	438	95.91
CM4BrP6	–	–	–	–	95.02	413	95.02
CM4ClP6	–	–	–	–	95.29	409	95.29
CM4BrB	–	–	–	–	93.55	404	93.55
CM4ClB	–	–	16.15	240	78.12	408	94.27

MBP-PU-MBP undergoes three-stage decomposition, while the overall thermal stability of tri-block copolymers is higher than the MBP-PU-MBP. Thermal degradation of the polymers CM4BrP6, CM4ClP6 and CM4BrB6 occurred around 413, 409 and 404°C respectively which shows the presence random scission only. Whereas, CM4ClB6 copolymer undergoes two-stage decomposition, first is due to the decomposition of the NHCOO groups (240°C) and another is due to the decomposition of PTMG blocks (408°C), it is probably due to the low content of PMMA segments (molar content of PMMA at about 74–82%). This result is a further indication of the absence of abnormal linkages therefore confirming the high regioselectivity and absence of unwanted irreversible termination or transfer reactions.

3.4. Studies of surface properties of the tri-block copolymer coatings

Images of tri-block copolymer coatings and the level of them roughness parameters vary from contains of hard phase, which comes from MMA segments (Figure 10).

Surface images of CM4BrP6 (Figure 10a), CM4ClP6 (Figure 10b) and CM4BrB6 (Figure 10c) copolymer samples with molar content of PMMA at about 141–150, 126–137 and 97–106% exhibit higher values of the roughness parameters (R_a = 0.30–0.45 μm, R_z = 1.55–2.39 μm) in relation to CM4ClB6 (Figure 10d) sample obtained at the lowest molar content of PMMA 74–82% (R_a = 0.20 μm, R_z = 1.14 μm).

The shape of the surface (roughness and physical form) copolymer coatings justifies the designation of Θ and SFE.

Table 8 provides the values of Θ as found and also components of SFE calculated on the basis of those angles in accordance with the van Oss–Good method, for coatings obtained from the studied tri-block copolymers. One can see a decrease in Θ values for both polar liquids (water and formamide) and non-polar liquid (diiodomethan), together with lower content MMA segments. The presented data show that MMA segments, when incorporated into hard segments of copolymers, are responsible for considerable reduction in SFE of the coatings obtained from those copolymers. The findings from the van Oss–Good method bring us to the conclusion that the basic impact on the value of γ_S comes from the γ_S^{LW} component of long-range interactions. However, the values of acid–base interactions γ_S^{AB} cannot be evaluated precisely and these should be estimated as 0.30–0.56 mJ/m^2.

4. Conclusions

Polyurethane-based macroinitiator, MBP-PU-MBP has been used to synthesize PMMA-*b*-PU-*b*-PMMA tri-block copolymers through ARGET ATRP in the presence of limited amounts of air. Excess reducing

Table 8. Experimental values of contact angles, parameters of FSE as calculated by van Oss-Good method and roughness parameters for tri-block copolymer coatings

Sample No.	Experimental values of contact angles Θ [°]						Parameters of FSE [mJ/m^2]					Roughness parameters [μm]	
	Model measuring fluids												
	CH_2I_2	Standard deviation	Formamide	Standard deviation	Water	Standard deviation	γ_S^{LW}	γ_S^-	γ_S^+	γ_S^{AB}	γ_S	R_a	R_z
CM4BrP6	36.10	1.29	63.56	1.96	86.28	1.53	40.90	2.16	0.01	0.30	41.2	0.45	2.39
CM4ClP6	35.35	1.03	61.78	1.61	84.20	1.70	41.68	2.75	0.01	0.32	42.0	0.40	1.94
CM4BrB6	34.10	1.21	59.62	1.20	81.68	1.73	42.61	3.67	0.01	0.32	42.9	0.30	1.55
CM4ClB6	33.18	0.58	56.93	1.52	80.65	1.36	42.94	4.05	0.02	0.56	43.5	0.20	1.14

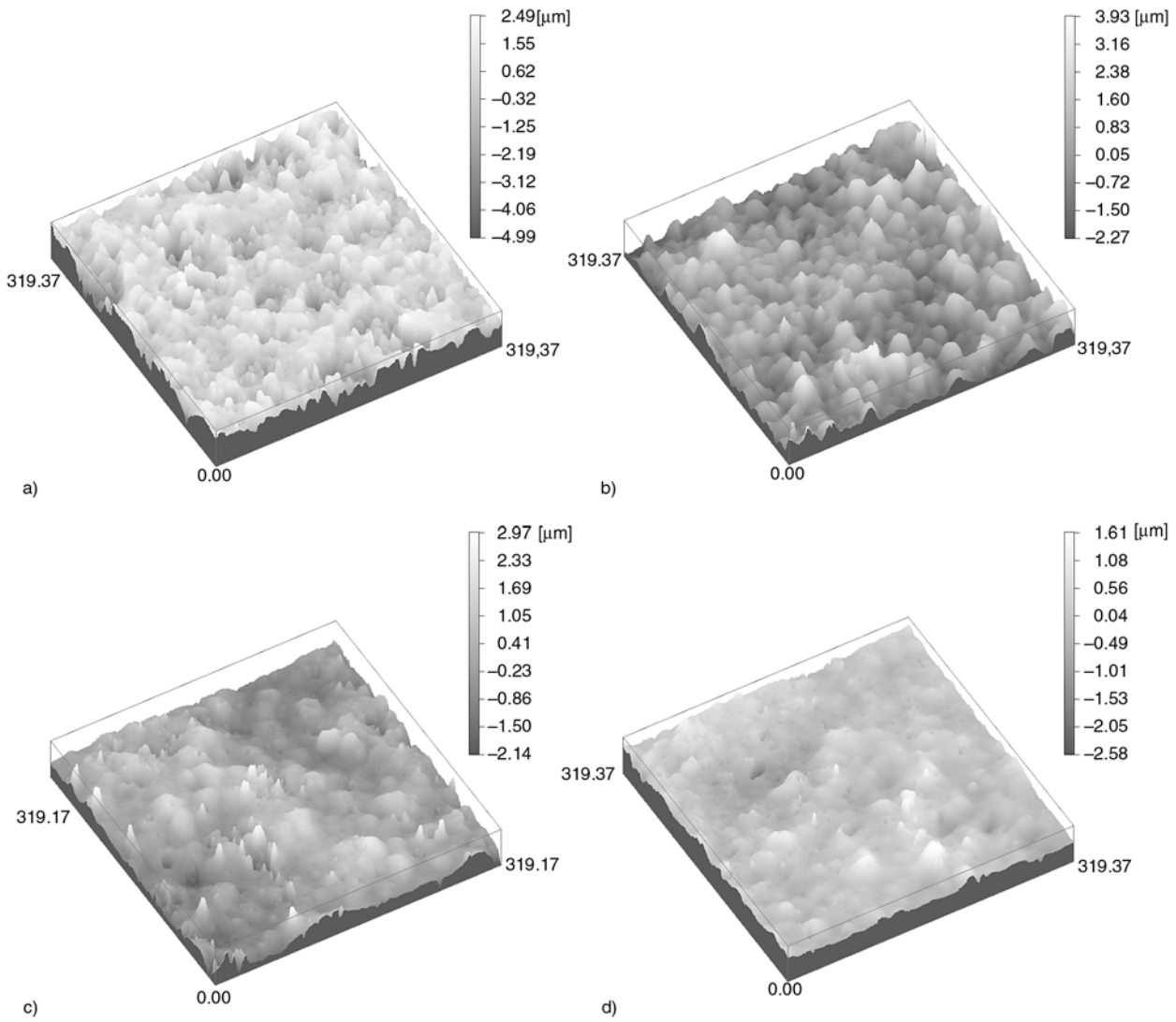

Figure 10. Pictures of the surface of CM4BrP6 (a), CM4ClP6 (b), CM4BrB6 (c) and CM4ClB6 (d) tri-block copolymers, taken for the objects 320×320 µm with magnification 50×

agent slightly accelerates ATRP but does not interfere with the controlled growth. This approach virtually eliminates any requirement for the deoxygenation of reaction mixtures or the use of a vacuum line or Schlenk line. The linear increase of monomer conversion and $\ln([M]_0/[M])$ during the increase of polymerization time confirms that the formation of tri-block copolymers was through controlled radical polymerization. Moreover, the linear increase of number average molecular weight with increase of monomer conversion is also the clear evidence to prove the controlled radical polymerization mechanism. $M_{n,th}$ of the tri-block copolymers was found to be more or less similar to $M_{n,GPC}$. In contrast to $–CH_2Br$ terminated PU, tertiary bromine-terminated PU produced PMMA-*b*-PU-*b*-PMMA tri-block copolymers with narrow MWD values. The molar percentage of PMMA calculated through ^1H NMR is matching with GPC results. The results from ^1H and ^{13}C NMR spectral and thermal studies support the formation of HMB, MBP-PU-MBP and PMMA-b-PU-b-PMMA tri-block copolymers. The studies of surface properties of tri-block copolymer coatings confirmed the presence of MMA segments.

Structures of PMMA-*b*-PU-*b*-PMMA tri-block copolymers are already common used as biomedical materials [19] as well as biodegradable scaffolds in the tissue engineering of skeletal muscles [20]. Moreover they are finding application as adhesives, emulsifiers, modifiers of surface properties and polymer blend compatibilizers [19].

Acknowledgements

The scientific work is co-financed by resources of European Union, in frames of European Social Fund, and project Podkarpacki scholarship fund for doctoral students realized by Podkarpackie Province – Marshall office of the Podkarpacki Province in Rzeszów in frames of Operating Programme the Human Capital in years 2007-2013.

References

[1] Matyjaszewski K., Dong H., Jakubowski W., Pietrasik J., Kusumo A.: Grafting from surfaces for 'Everyone': ARGET ATRP in the presence of air. Langmuir, **23**, 4528–4531 (2007).
DOI: 10.1021/la063402e

[2] Jakubowski W., Min K., Matyjaszewski K.: Activators regenerated by electron transfer for atom transfer radical polymerization of styrene. Macromolecules, **39**, 39–45 (2006).
DOI: 10.1021/ma0522716

[3] Dong H., Matyjaszewski K.: ARGET ATRP of 2-(dimethylamino)ethyl methacrylate as an intrinsic reducing agent. Macromolecules, **41**, 6868–6870 (2008).
DOI: 10.1021/ma8017553

[4] Tharanikkarasu K., Verma H., Jang W., Lee S. K., Seo J., Baek S., Han H.: Novel poly(methyl methacrylate)-*block*-polyurethane-*block*-poly(methyl methacrylate) tri-block copolymers through atom transfer radical polymerization. Journal of Applied Polymer Science, **108**, 1538–1544 (2008).
DOI: 10.1002/app.27642

[5] Tharanikkarasu K., Kim B. K.: Modification of aqueous polyurethane dispersions via tetraphenylethane iniferters. Journal of Applied Polymer Science, **73**, 2993–3000 (1999).
DOI: 10.1002/(SICI)1097-4628(19990929)73:14<2993::AID-APP24>3.0.CO;2-B

[6] Verma H., Kannan T.: Novel telechelic 2-methyl-2-bromopropionate terminated polyurethane macroinitiator for the synthesis of ABA type tri-block copolymers through atom transfer radical polymerization of methyl methacrylate. Polymer Journal, **40**, 867–874 (2008).
DOI: 10.1295/polymj.PJ2007236

[7] Nayak S., Verma H., Kannan T.: Synthesis and characterization of amphiphilic and hydrophobic ABA-type tri-block copolymers using telechelic polyurethane as atom transfer radical polymerization macroinitiator. Colloid and Polymer Science, **288**, 181–188 (2010).
DOI: 10.1007/s00396-009-2149-2

[8] Yin Z., Koulic C., Pagnoulle C., Jérôme R.: Reactive blending of functional PS and PMMA: Interfacial behavior of in situ formed graft copolymers. Macromolecules, **34**, 5132–5139 (2001).
DOI: 10.1021/ma001798+

[9] Viala S., Antonietti M., Tauer K., Bremser W.: Structural control in radical polymerization with 1,1 diphenylethylene: 2. Behavior of MMA–DPE copolymer in radical polymerization. Polymer, **44**, 1339–1351 (2003).
DOI: 10.1016/S0032-3861(03)00004-1

[10] Król B., Król P., Pikus S., Chmielarz P., Skrzypiec K.: Synthesis and characterisation of coating polyurethane cationomers containing fluorine built-in hard urethane segments. Colloid and Polymer Science, **288**, 1255–1269 (2010).
DOI: 10.1007/s00396-010-2244-4

[11] Sarbu T., Lin K-Y., Spanswick J., Gil R. R., Siegwart D. J., Matyjaszewski K.: Synthesis of hydroxy-telechelic poly(methyl acrylate) and polystyrene by atom transfer radical coupling. Macromolecules, **34**, 9694–9700 (2004).
DOI: 10.1021/ma0484375

[12] Koulic C., Yin Z., Pagnoulle C., Gilbert B., Jérôme R.: Premade versus in situ formed compatibilizer at the PS/PMMA interface: Contribution of the Raman confocal microscopy to the fracture analysis. Polymer, **42**, 2947–2957 (2001).
DOI: 10.1016/S0032-3861(00)00553-X

[13] Król P., Chmielarz P.: Controlled radical polymerization as the method for modification of polyurethanes by vinyl polymers. in 'Modern Polymeric Materials for Environmental Applications 4th International Seminar, Kraków, Poland' 169–174 (2010).

[14] Lapprand A., Boisson F., Delolme F., Méchin F., Pascault J-P.: Reactivity of isocyanates with urethanes: Conditions for allophanate formation. Polymer Degradation and Stability, **90**, 363–373 (2005).
DOI: 10.1016/j.polymdegradstab.2005.01.045

[15] de la Fuente J. L., Fernández-Garcia M., Fernández-Sanz M., Madruga E. L.: Sequence distribution and stereoregularity of methyl methacrylate and butyl acrylate statistical copolymers synthesized by atom transfer radical polymerization. Macromolecules, **34**, 5833–5837 (2001).
DOI: 10.1021/ma010428y

[16] Verma H., Kannan T.: Synthesis of tri-block copolymers through reverse atom transfer radical polymerization of methyl methacrylate using polyurethane macroiniferter. Express Polymer Letters, **2**, 579–588 (2008).
DOI: 10.3144/expresspolymlett.2008.70

[17] di Lena F., Matyjaszewski K.: Transition metal catalysts for controlled radical polymerization. Progress in Polymer Science, **35**, 959–1021 (2010).
DOI: 10.1016/j.progpolymsci.2010.05.001

[18] Tsarevsky N. V., Matyjaszewski K.: 'Green' atom transfer radical polymerization: From process design to preparation of well-defined environmentally friendly polymeric materials. Chemical Reviews, **107**, 2270–2299 (2007).
DOI: 10.1021/cr050947p

[19] Król P., Chmielarz P.: Controlled radical polymerization (CRP) methods in the synthesis of polyurethane copolymers (in Polish). Polimery, **56**, 530–540 (2011).

[20] Sharifpoor S., Labow R. S., Santerre J. P.: Synthesis and characterization of degradable polar hydrophobic ionic polyurethane scaffolds for vascular tissue engineering applications. Biomacromolecules, **10**, 2729–2739 (2009).
DOI: 10.1021/bm9004194

eXPRESS Polymer Letters Vol.7, No.3 (2013) 261–271
Available online at www.expresspolymlett.com
DOI: 10.3144/expresspolymlett.2013.24

Selective localization of titanium dioxide nanoparticles at the interface and its effect on the impact toughness of poly(L-lactide)/poly(ether)urethane blends

*H. Xiu, H. W. Bai, C. M. Huang, C. L. Xu, X. Y. Li, Q. Fu**

College of Polymer Science and Engineering, State Key Laboratory of Polymer Materials Engineering, Sichuan University, 610065 Chengdu, P. R. China

Received 12 September 2012; accepted in revised form 10 November 2012

Abstract. Inorganic nanofillers are often added into polymer/elastomer blends as a third component to modify their performance. This work aims to clarify the role of interface-localized spherical nanoparticles in determining the impact toughness of polymer blends. The selective distribution of titanium dioxide (TiO_2) nanoparticles in poly(L-lactide)/poly(ether) urethane (PLLA/PU) blends was investigated by using scanning electron microscope. It is interesting to find that, regardless of the method of TiO_2 introduction, nano-TiO_2 particles are always selectively localized at the phase interface between PLLA and PU, leading to a significant improvement in notched Izod impact toughness. The moderately weakened interfacial adhesion induced by the interfacially-localized nano-TiO_2 particles is believed to be the main reason for the largely enhanced impact toughness.

Keywords: *biodegradable polymers, poly(L-lactide), mechanical properties, toughness, microstructure*

1. Introduction

With increasing environmental concerns and decreasing petroleum resources, bio-based and biodegradable polymers have gained growing interest during recent years. As one of the most promising biodegradable polymers derived from renewable sources (e.g. corn and sugar beets), poly(L-lactide) (PLLA) exhibits great potential to replace traditional petroleum-based plastics (e.g. polypropylene (PP) and polystyrene (PS)) in a wide variety of applications due to its excellent transparency, good mechanical strength and easy processability [1–7]. Furthermore, similar to poly(ε-caprolactone) (PCL) [8, 9], PLLA has been already used in biomedical fields owing to its good biocompatibility [2, 5]. However, the practical applications of PLLA are far from as widespread as expected because there are some drawbacks such as its inherent brittleness. Therefore, considerable efforts have been devoted to toughen PLLA [10–22]. Blending PLLA with other rubbery polymers, such as poly(ether)urethane (PU) elastomer [15], polyamide elastomer (PAE) [16], PCL [17, 18], poly(butylene succinate) (PBS) [18, 19], and ethylene-co-vinyl acetate (EVA) [20], provides a practical and economical way to improve the toughness of PLLA. Unfortunately, a substantial elastomer concentration of about 15–20 wt% is required to achieve effective toughening, which, in turn, leads to a significant deterioration in strength and stiffness [15, 17, 20]. To overcome this problem, inorganic nanofillers are often added into these blends as a third component to enhance the strength and stiffness, while maintaining or even further improving the obtained toughness [23–35].

Hitherto numerous studies have demonstrated that the key issue in achieving the optimal combination

*Corresponding author, e-mail: qiangfu@scu.edu.cn

of mechanical properties of polymer/elastomer/filler ternary nanocomposites is to tailor the phase morphology, especially the distribution of nanofillers in the matrix blends [28, 29]. Generally, when nanofillers are introduced into an immiscible or partially miscible polymer blend, they often distribute heterogeneously, i.e. selectively dispersed in polymer matrix, in elastomer phase or at the interface between the two polymer phases, thus forming separated dispersion, rigid core-soft shell and soft core-rigid shell structures, respectively. In most cases, the formation of the rigid core-soft shell structure is found to be more favorable to achieve satisfactory toughness at lower elastomer concentration and, consequently, a good balance between toughness and stiffness as compared to the separated dispersion structure [23–25]. However, much less attention has been paid to the soft core-rigid shell structure possibly because it is difficult to realize the exclusive localization of nanofillers at the phase interface [33–37]. More importantly, to the best of our knowledge, so far very little information has been obtained about its effect on the mechanical properties of such nanocomposites. Excitedly, in the present work, we find that isotropic titanium dioxide (TiO_2) nanoparticles have a strong tendency to preferentially distribute at the interface of PLLA/PU blends with 'sea-island' morphology, forming a unique soft core-rigid shell structure, i.e. PU particles are closely surrounded by a large amount of nano-TiO_2 particles, which gives us a good chance to gain full insight into the role of the interface-localized nanoparticles in determining the performance of polymer blends, especially the impact toughness. To this aim, the relationship between microstructure and impact toughness of PLLA/PU/TiO_2 nanocomposites is analyzed carefully and then several possible toughening mechanisms are discussed.

2. Experimental

2.1. Materials

PLLA (4032D, D-isomer content = 1.2–1.6%) used as the matrix polymer was purchased from NatureWorks Co. Ltd, USA. It has a density of 1.25 g/cm^3, weight-averaged molecular weight (M_w) of 207 kDa, and polydispersity of 1.74, respectively. PU (WHT-1570, Yantai Wanhua Polyurethanes Co., Ltd, China) with a density of 1.21 g/cm^3 was selected as the impact modifier in this work. Nano-sized titanium dioxide (TiO_2, purity >98%, density = 4.25 g/cm^3, average particle size = 200 nm) without any surface modification was produced by Chengdu Kelong Chemical Reagent Factory, China.

2.2. Sample preparation

PLLA/PU/TiO_2 ternary nanocomposites were prepared by melt blending various amounts of TiO_2 (0~25 wt%) with PLLA/PU blend matrix (90:10 or 75:25 w/w) in a Haake mixer (XSS-300, USA) at a temperature of 190°C and rotor speed of 50 rpm for 5 min. In this case, TiO_2, PLLA, and PU were loaded to the mixing chamber simultaneously. For comparison, PLLA/PU binary blends were blended under the same conditions. Specially, in order to investigate the effect of mixing procedure on the distribution of TiO_2 in the nanocomposites, the other two blending procedures were also employed: blending of precompounded PU/TiO_2 or PLLA/TiO_2 with the second polymer (PLLA or PU) during a second blending step. All raw materials including PLLA, PU and TiO_2 were dried under vacuum before using. To obtain standard specimens for mechanical testing, the obtained materials were then compression molded at 190°C for 5 min and then quenched to room temperature.

2.3. Scanning electron microscopy (SEM)

The phase morphologies of PLLA/PU blends with and without TiO_2 were observed using an FEI Inspect F scanning electron microscope (SEM, USA) with an accelerating voltage of 5.0 kV. The specimens for the SEM observation were prepared by cryogenic fracture in liquid nitrogen. The impact fractured surfaces of the specimens after the impact testing were also observed by SEM.

2.4. Surface energy measurement

Contact angles measurement is a traditional and valid method to evaluate the surface energy of solids [38].The surface energy of a solid or a liquid and its dispersive and polar components can be calculated from the contact angle data by using Owens-Wendt method [39] (Equation (1) and (2)):

$$\gamma_s = \gamma_s^d + \gamma_s^p \quad (1)$$

$$\gamma_l(1 + \cos\theta) = 2\sqrt{\gamma_s^d\gamma_l^d} + 2\sqrt{\gamma_s^p\gamma_l^p} \quad (2)$$

where θ is the contact angle, γ is the surface energy, subscripts '*s*' and '*l*' indicate solid and liquid, respec-

tively, while superscripts '*d*' and '*p*' indicate the dispersive and polar components, respectively. Generally, in order to obtain the surface energy γ_s of the measured solid from Equations (1) and (2), at least two liquids, usually a polar and a nonpolar liquid, should be used. Here, two test liquids (i.e. distilled water (H_2O) and diiodomethane (CH_2I_2)) were selected as widely reported in the literature [28, 40]. The values of surface energy of the two test liquids are γ^p = 50.7 mN/m and γ^d = 22.1 mN/m for H_2O, and γ^p = 6.7 mN/m and γ^d = 44.1 mN/m for CH_2I_2 [28].

The contact angle tests were conducted on a DSA100 apparatus (Krüss GmbH, Germany) based on the sessile drop method, i.e. depositing a drop of test liquid onto the sample surface. At least six replicates were performed for each sample to ensure the reproducibility of the measured data. Prior to the measurements, TiO_2 powders were compression molded by using a home-made metal mold at room temperature under a pressure of 15 MPa, while PLLA and PU specimens were compression molded at 190°C for 5 min and then quenched to 25°C.

2.5. Mechanical testing

The notched Izod impact strength was measured using an impact tester (XJU-5.5, China), according to ISO180/179 standard. Pendulum impact velocity is 3.5 m/s. Tensile testing was performed with a SANS universal tensile testing machine (China) at a cross-head speed of 5 mm/min, according to ISO 527-3 standard. For each sample, the measurements were carried out at room temperature (23°C) and the results obtained were averaged at least five specimens.

2.6. Differential scanning calorimetry (DSC)

The degree of crystallinity (X_c) of the PLLA matrix in the compression molded samples was evaluated using differential scanning calorimetry (DSC, Perkin-Elmer pyris-1, USA) in a dry nitrogen atmosphere. For each measurement, about 5 mg of the sample was directly heated from 0 to 200°C at a heating rate of 10°C/min. The value of were determined using the most commonly used Equation (3) [21, 22, 41]:

$$X_c = \frac{\Delta H_m - \Delta H_c}{w_f \Delta H_m^0} \cdot 100\% \quad (3)$$

where ΔH_m and ΔH_c are the enthalpies of melting and cold crystallization, respectively; w_f is the weight percent of the PLLA matrix, and ΔH_m^0 is the melting enthalpy of completely crystalline PLLA (93.7 J/g [42]).

3. Results and discussion

3.1. Phase morphology and selective localization of nano-TiO_2 particles

In order to elucidate the microstructure and morphology of PLLA/PU blends with and without TiO_2, SEM experiment was carried out and the results are shown in Figure 1. Obviously, all samples exhibit typical 'sea-island' morphologies, where discrete PU spherical domains are uniformly dispersed in the PLLA matrix. Unexpectedly, with the introduction of 15 phr nano-TiO_2 particles into the blend of PLLA/10PU, the size of the PU domains increases slightly (Figure 1b). This result is opposite to that usually seen in polymer blends filled with other nanofillers, such as silicon dioxide (SiO_2), clay and multi-walled carbon nanotubes (MWCNTs), where the size of dispersed-phase domains decreases significantly with adding small amounts of nanofillers [43–45]. Recently, Cai *et al*. [46] confirmed that morphology evolution of immiscible polymer blends is strongly dominated by the self-agglomerating pattern of nanoparticles in polymer melts. An increase in the size of PA6 domains is observed as high loading of nano-TiO_2 (e.g. 25 phr) is added into PS/30PA6 blend due to its unique self-agglomerating pattern completely different from other nanofillers. Similarly, the increased size of the PU domains may be associated with the unique self-agglomerating pattern of the TiO_2, which needs further investigation in our future work. Very interestingly, almost all nano-TiO_2 particles are selectively located at the phase interface between PLLA and PU in PLLA/10PU/15TiO_2 ternary nanocomposite, which can be observed more clearly in the ternary samples containing relatively high content of PU, such as PLLA/25PU/15TiO_2 nanocomposite (Figure 1c). In this case, spherical PU domains are surrounded by a large number of nano-TiO_2 particles, forming a special soft core-rigid shell structure in the PLLA matrix. More interestingly, the distribution of nano-TiO_2 particles in the obtained PLLA/PU/TiO_2 nanocomposites is independent on the method of TiO_2 introduction, as shown in Figure 2. In all cases, nano-TiO_2 particles are mainly located at the interface

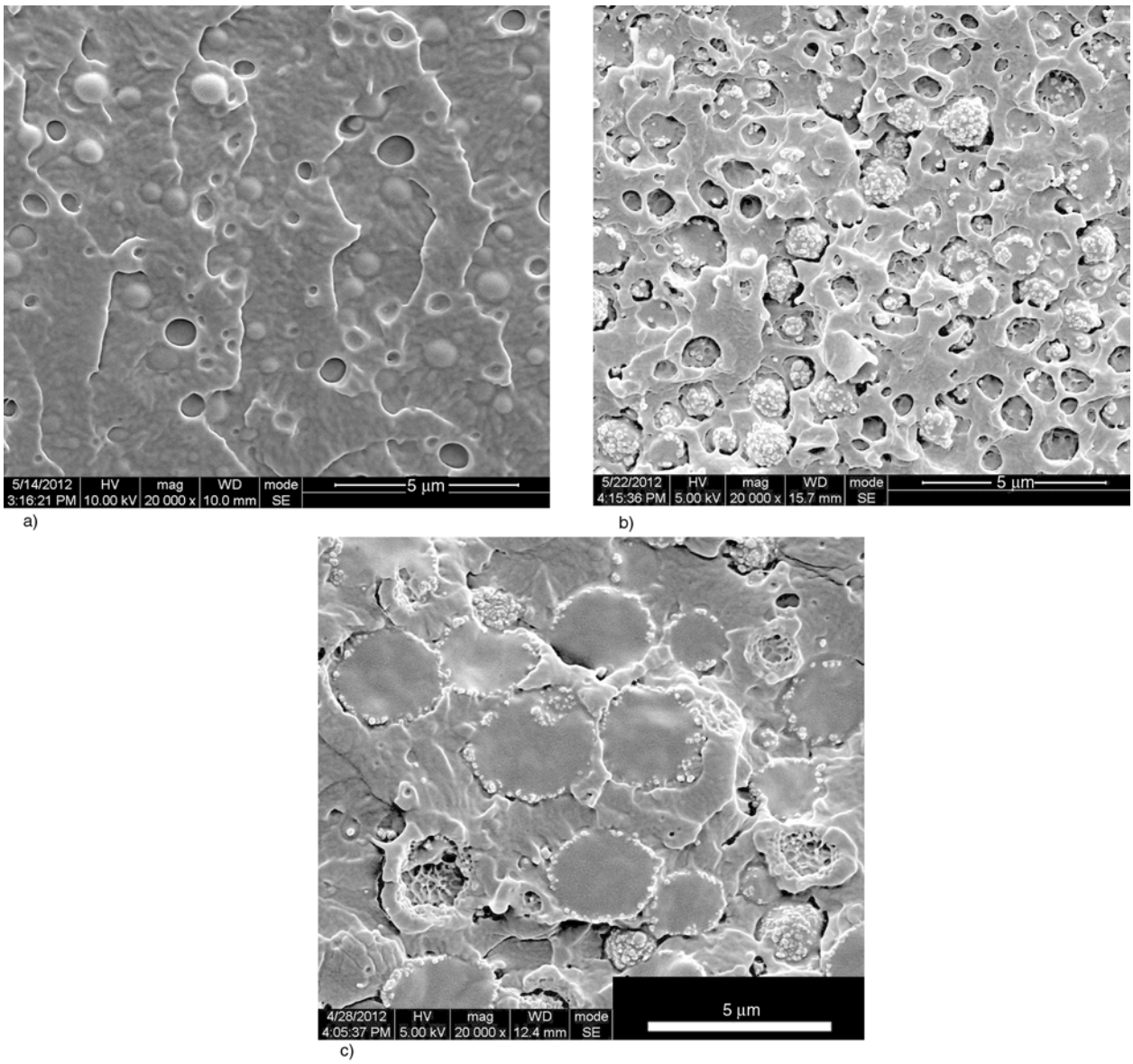

Figure 1. SEM micrographs of the cryofractured surfaces of PLLA/PU blends with and without TiO_2: (a) PLLA/10PU, (b) PLLA/10PU/15TiO_2, and (c) PLLA/25PU/15TiO_2

and almost no nano-TiO_2 particles can be found in the two blend components (PLLA and PU), suggesting that the nano-TiO_2 particles should be thermodynamically driven into the phase interface during mixing process. This conclusion can be further confirmed by theoretical calculation using the wetting coefficient ω_a defined by Equation (4) [47]:

$$\omega_a = \frac{\gamma_{PLLA-TiO_2} - \gamma_{PU-TiO_2}}{\gamma_{PLLA-PU}} \quad (4)$$

where $\gamma_{PLLA\text{-}TiO_2}$, $\gamma_{PU\text{-}TiO_2}$, and $\gamma_{PLLA\text{-}PU}$ are the interfacial energies between PLLA and TiO_2, between PU and TiO_2, between PLLA and PU, respectively. ω_a has been widely used to predict the thermodynamic equilibrium distribution of nanofillers in polymer blends [25, 40]. Generally, for $\omega_a > 1$, TiO_2 particles are only found in PU; for $\omega_a < -1$, TiO_2 particles are present only in PLLA and for $-1 < \omega_a < 1$, TiO_2 particles are selectively located at the interface between PLLA and PU.

The interfacial energy can be obtained from surface energies of the corresponding components and their dispersive and polar parts, based on the two most commonly used methods, i.e. harmonic-mean Equation (5) and geometric-mean Equation (6) [38]:

Harmonic-mean equation:

$$\gamma_{12} = \gamma_1 + \gamma_2 - 4\left(\frac{\gamma_1^d\gamma_2^d}{\gamma_1^d + \gamma_2^d} + \frac{\gamma_1^p\gamma_2^p}{\gamma_1^p + \gamma_2^p}\right) \quad (5)$$

Geometric-mean equation:

$$\gamma_{12} = \gamma_1 + \gamma_2 - 2(\sqrt{\gamma_1^d\gamma_2^d} + \sqrt{\gamma_1^p\gamma_2^p}) \quad (6)$$

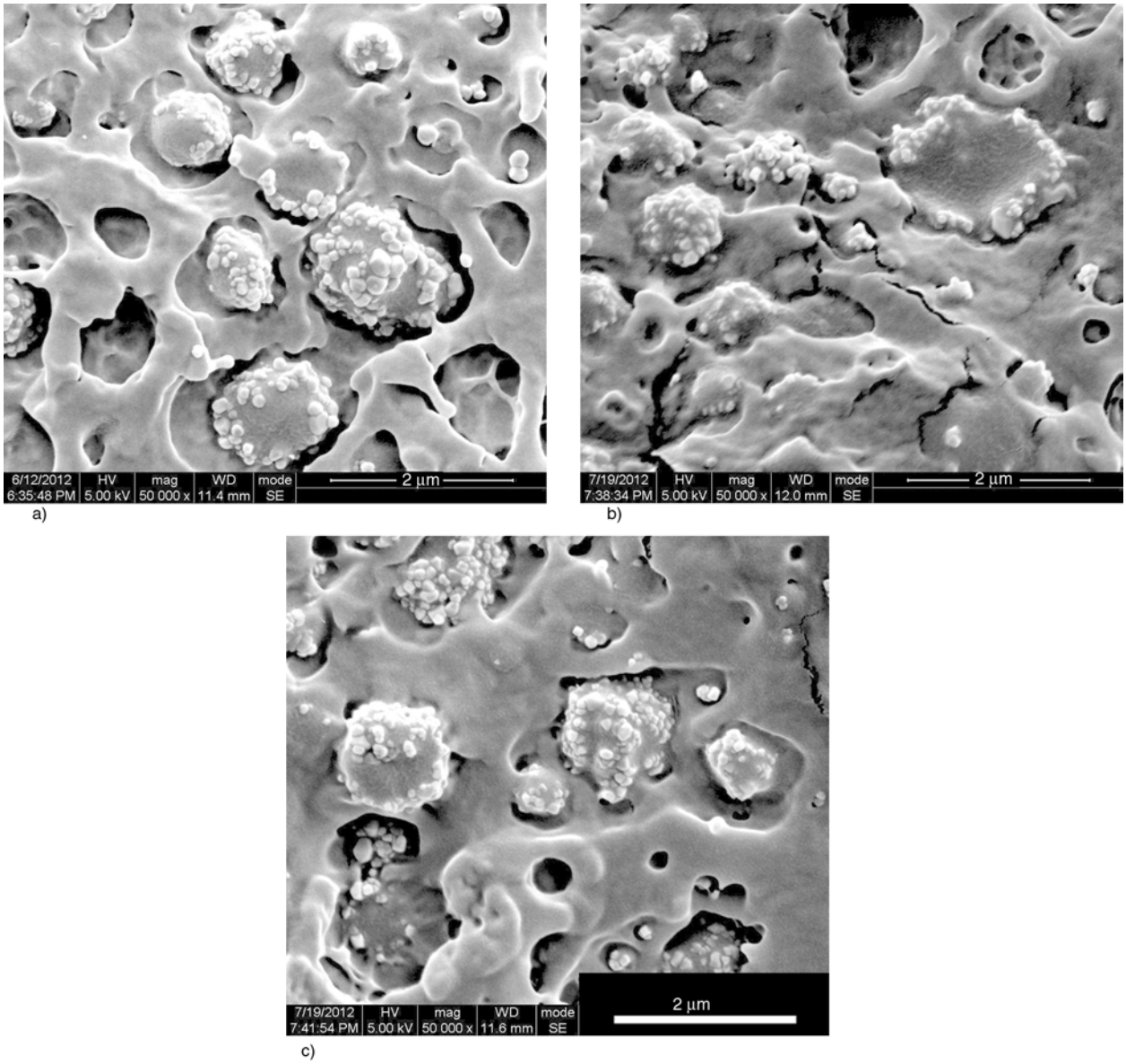

Figure 2. SEM micrographs of the cryofractured surfaces of PLLA/10PU/15TiO_2 composites prepared by different blending procedures: (a) direct blending of all three components, (b) blending of premixed PU/TiO_2 with PLLA, and (c) blending of premixed PLLA/TiO_2 with PU

Table 1. The measured contact angles and calculated surface energy data of PLLA, PU and TiO_2

Sample	Contact angles[°]		Surface energy [mN/m]		
	H_2O	CH_2I_2	γ	γ^d	γ^p
PLLA	78.5	37.7	47.74	38.37	9.37
PU	78.1	55.2	41.69	30.36	11.33
TiO_2	19.7	10.1	80.70	46.40	34.30

Table 2. Interfacial tensions and wetting coefficient as calculated using harmonic-mean and geometric-mean equations

Component couple	Based on harmonic-mean equation [mN/m]	Based on geometric-mean equation [mN/m]
PLLA/PU	1.06	0.56
PLLA/TiO_2	15.00	8.20
PU/TiO_2	14.91	7.89
ω_a	0.08	0.55

where γ_i is the surface energy of component *i*, γ_i^d and γ_i^p are the dispersive and polar contributions to the surface energy of component *i*, respectively.

In this work, the values of surface energies were calculated from the contact angle data by using Equation (1) and Equation (2) and the results are summarized in Table 1. The values of interfacial energies and are listed in Table 2. As expected, the value of is 0.08 based on Harmonic-mean equation, and 0.55 based on Geometric-mean equation, indicating that the state of thermodynamic equilibrium distribution of nano-TiO_2 particles should be selec-

tively concentrated at the interface between PLLA and PU.

3.2. Mechanical properties

As discussed in the introduction, the distribution of nanofillers plays a decisive role in controlling the performance of polymer/elastomer/filler nanocomposites. In order to know the effect of such interfacially-localized nano-TiO_2 particles on the mechanical properties of PLLA/PU blends, notched Izod impact toughness and tensile properties were evaluated. Figure 3 shows the impact strength of PLLA and PLLA/10PU blends as a function of nano-TiO_2 content. It is very interesting to observe that, although no obvious toughening effect on PLLA matrix can be obtained by only adding low content (e.g. 10 wt%) of nano-TiO_2 or PU, the presence of nano-TiO_2 particles at the interface gives rise to a largely improved impact toughness of PLLA/10PU blend. For example, the impact strength of PLLA/10PU blend increases remarkably from 5.61 to 30.41 kJ/m^2 with increasing nano-TiO_2 content up to 15 phr. This indicates that realizing selective distribution of nano-TiO_2 particles at the interface is an effective method to toughen PLLA/PU blends. Meanwhile, it should be noted that there is a saturation of the toughening effect. With further increasing nano-TiO_2 content, the high-concentration (e.g. 25 phr) nano-TiO_2 induces a slight decrease of impact toughness due to the serious aggregation of nano-TiO_2 particles in this condition (as discussed below). Unfortunately, the nano-TiO_2 induces dramatic improvement in the impact toughness, but evident deterioration in tensile strength and elongation at break, as can be observed in Figure 4 and Table 3. This can be explained as follows. On one hand, the existence of large amounts of nano-TiO_2 around PU domains can lead to a moderate increase in the effective vol-

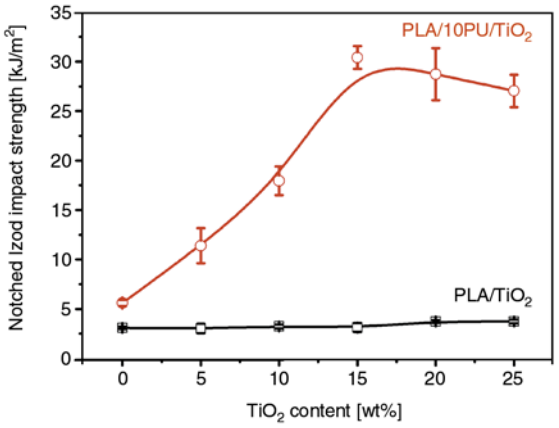

Figure 3. Notched Izod impact strength of PLLA and PLLA/10PU blends with various amounts of TiO_2

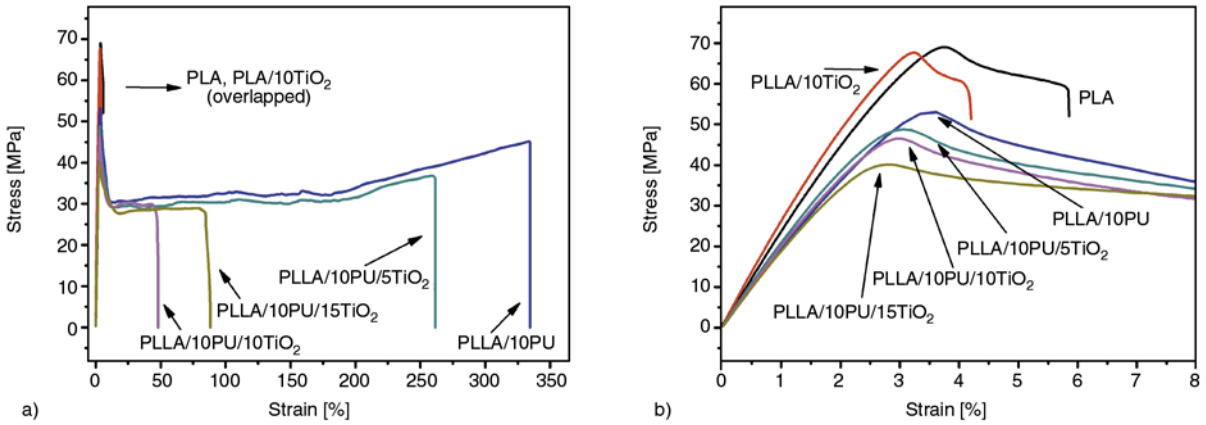

Figure 4. (a) Stress-strain curves of PLLA and PLLA/10PU blends with various amounts of TiO_2, and (b) enlarged part of the curves

Table 3. Mechanical properties of PLLA and PLLA/10PU blends with various amounts of TiO_2

Sample	Yield stress [MPa]	Modulus MPa[	Elongation at break [%]	Notched impact strength [kJ/m^2]
PLLA	68.36±0.67	2452.80±29.69	5.67±0.18	3.10±0.12
PLLA/10TiO_2	67.21±0.98	2730.10±22.65	4.17±0.07	3.23±0.23
PLLA/10PU	53.35±0.63	1946.75±59.75	313.42±32.81	5.61±0.32
PLLA/10PU/5TiO_2	49.02±0.36	2143.17±62.43	235.37±59.77	11.39±1.78
PLLA/10PU/10TiO_2	47.04±0.58	2099.11±23.87	41.24±20.00	17.95±1.44
PLLA/10PU/15TiO_2	41.21±0.68	1969.38±20.90	69.04±37.04	30.41±0.16
PLLA/15PU	46.87±0.10	1939.78±27.39	294.09±29.11	23.19±2.93

ume of PU dispersed phase. One the other hand, unlike bridge effect of MWCNTs with high aspect ratio, the interfacially-localized nano-TiO_2 particles are most likely to weaken the interfacial bonding strength between PLLA and PU because of the shielding effect, thus promoting debonding of PU domains from PLLA matrix during deformation. Both factors are believed to contribute to the substantially reduced tensile strength, based on the fact that, although the true volume fraction of PU phase (18.4%) in PLLA/15PU blend is higher than the effective volume fraction of PU phase (14.9%) in PLLA/10PU/15TiO_2 nanocomposite, the former sample exhibits a much higher tensile strength as compared with the latter one (Table 3). With regard to the remarkably decreased extensibility, undoubtedly, the latter factor is the main reason. Furthermore, one thing should be stressed that tensile testing and notched Izod impact testing were carried out at remarkably different test speeds. Thus, the materials are most likely to exhibit different mechanical responses when they are subjected to different loading conditions. For the tensile testing, the tensile speed is only 5 mm/min, indicating a quasi-static loading condition. In this case, the presence of nano-TiO_2 particles at the interface is unfavorable to the stress transferring between PLLA and PCL because of the reduced interfacial adhesion, thus giving rise to the notably reduced extensibility. However, for the notched Izod impact testing, the impact speed is as high as 3.5 m/s, indicating a dynamic loading condition. In this case, the interfacial-localized nano-TiO_2 particles seem to be favorable to the toughening.

3.3. Toughening mechanism

To make clear the role of the interfacial-localized nano-TiO_2 particles in the toughening of PLLA/PU blends, the impact fractured surfaces of PLLA/10PU blends with and without TiO_2 particles were characterized by SEM, and the results are given in Figure 5. Clearly, the blank PLLA/10PU blend exhibits a typical brittle failure. The fractured surface is very smooth and no evident deformation of PLLA matrix appears (Figure 5a). This suggests that fast crack propagation occurs during impact fracture process. In contrast, after adding 10–15 phr TiO_2, many fibrils as a result of crazing of PLLA matrix can be clearly observed on the whole surface (Figure 5b and 5c), indicating that the interfacial-localized nano-TiO_2 particles effectively facilitate the deformation of PLLA matrix through crazing mechanism. Moreover, these highly stretched fibrils can prevent the crack initiation and propagation, allowing for a considerable plastic deformation to develop [48]. As a result, substantial energy is consumed, leading to the high impact toughness. Now it is logical to ask how the nano-TiO_2 particles induce the stable crazes in PLLA matrix. In fact, it has been widely accepted that the role of elastomer in toughening polymers is mainly associated with the cavitation of elastomer particles and the cavitation caused by interfacial debonding can promote energy dissipation through relaxing the locally triaxial stress that favors brittle failure [49–51]. Here, since spherical nano-TiO_2 particles located at the interface can weaken the interfacial adhesion between PLLA matrix and PU dispersed phase to a certain extent (evidenced by the decreased tensile strength as discussed above), the interfacial debonding and, consequently, the plastic deformation of PLLA matrix become easier to be triggered as compared to the blank PLLA/PU blends. This mechanism has been successfully used to explain the reason for the enhanced toughness of epoxy/acrylic rubber blends induced by the interfacial-localized clay [52]. On the other hand, Shi *et al*. [35] have demonstrated that the introduction of interface-localized MWCNTs causes a decrease in the impact strength of PLLA/EVA blends, suggesting that the enhanced interfacial adhesion seems to be unfavorable to the toughening of PLLA/elastomer blends. Furthermore, by considering that the impact strength of PLLA/10PU/15TiO_2 nanocomposite with a lower effective volume fraction of PU phase (14.9%) is much higher than PLLA/15PU blend with a higher true volume fraction of PU phase (18.4%) (Table 3), we believe that the increase in the effective volume fraction of PU phase has little influence on the improvement in the impact toughness. Therefore, the largely enhanced impact toughness of PLLA/PU blends induced by the interfacial-localized nano-TiO_2 is mainly attributed to the moderately reduced interfacial debonding. Most importantly, it should be noted that appropriate concentration of TiO_2 is the prerequisite to obtain the blends with good impact toughness. At high concentrations (e.g. 25 phr), some of nano-TiO_2 particles aggregate together and form large aggregates at the phase interface and, subsequent, only small amounts of

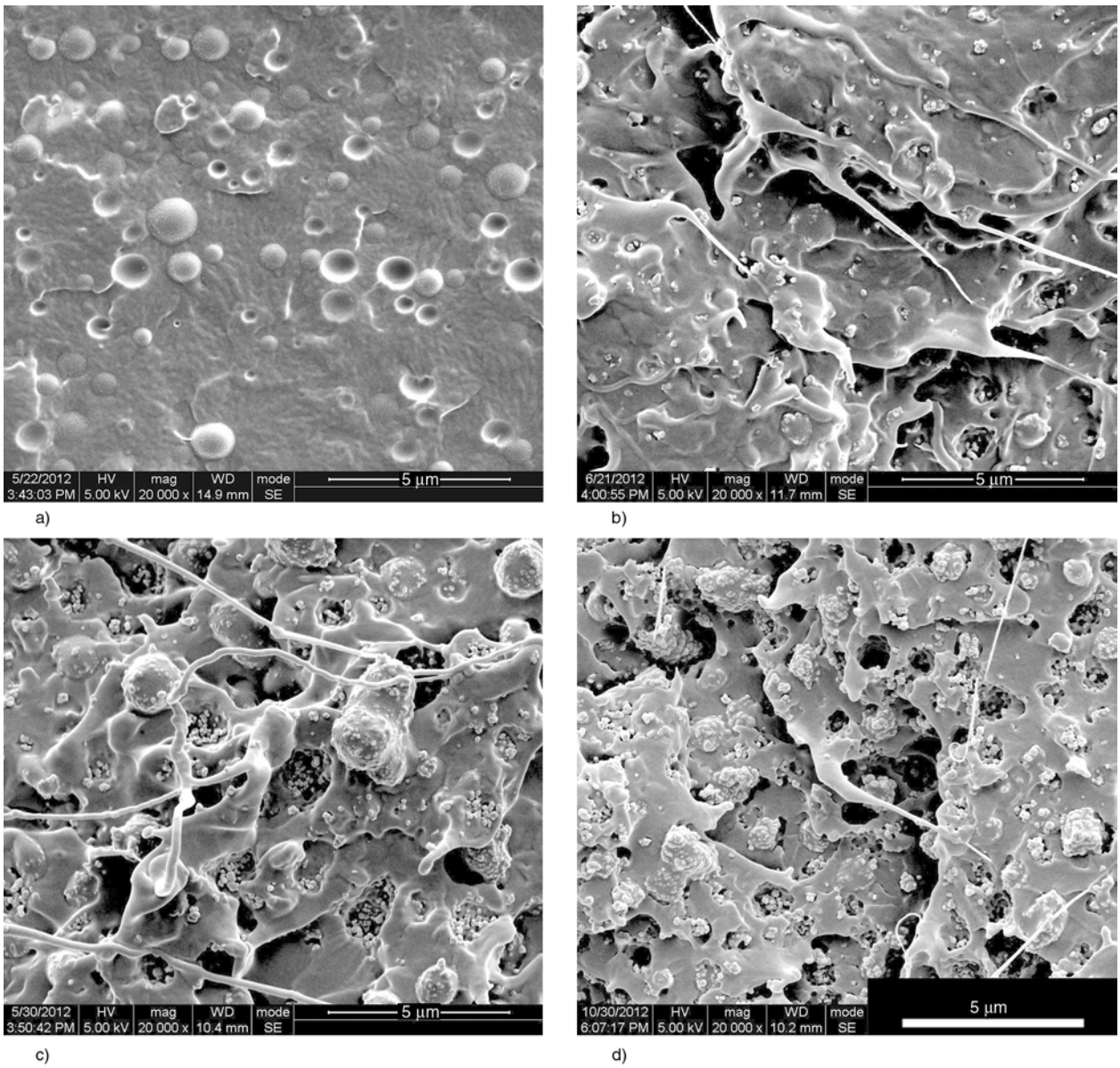

Figure 5. SEM micrographs of impact fractured surfaces of PLLA/10PU blends with and without TiO_2: (a) PLLA/10PU, (b) PLLA/10PU/10TiO_2, (c) PLLA/10PU/15TiO_2, and (d) PLLA/10PU/25TiO_2

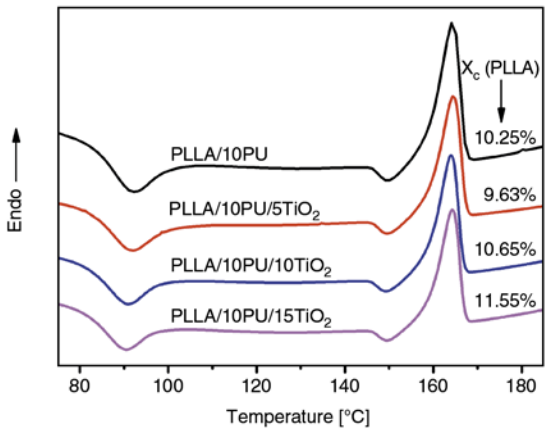

Figure 6. DSC heating curves of PLLA/10PU blends with various amounts of TiO_2

highly stretched fibrils and less evident matrix deformation can be observed on the impact fractured surface (Figure 5d). This observation is well consistent with the deteriorated impact toughness of the blends with high-concentration TiO_2 as mentioned above.

In addition, our previous work has shown that the crystallinity of PLLA matrix may influence the impact toughness of PLLA/elastomer blend [53]. However, it can be disregarded completely in this work. All the samples present the same low level of the PLLA matrix crystallinity (~10%), as displayed in Figure 6.

4. Conclusions

In this work, PLLA/PU/TiO_2 ternary nanocomposites were prepared by three different mixing procedures. Regardless of the method of TiO_2 introduction, almost all nano-TiO_2 particles are located around spherical PU domains, forming a unique soft core-rigid shell structure in the PLLA matrix. The results show that the addition of nano-TiO_2 leads to a largely enhanced impact toughness of PLLA/PU blend mainly due to the weakened interfacial debonding in the presence of the interfacial-localized nano-TiO_2 particles. During the impact process, nano-TiO_2 particles induce interfacial debonding, promoting the plastic deformation of PLLA matrix through crazing rather than crack, thus dissipating large amounts of energy. This work not only provides a simple and effective method to largely improve the impact toughness of polymer blends, but also gives a comprehensive understanding of the role of interfacial-localized spherical

Acknowledgements

We would like to express our great thanks to the National Natural Science Foundation of China (50903048 and 51121001) for Financial Support.

References

[1] Auras R., Harte B., Selke S.: An overview of polylactides as packaging materials. Macromolecular Bioscience, **4**, 835–864 (2004).
DOI: 10.1002/mabi.200400043

[2] Nampoothiri K. M., Nair N., R., John R. P.: An overview of the recent developments in polylactide (PLA) research. Bioresource Technology, **101**, 8493–8501 (2010).
DOI: 10.1016/j.biortech.2010.05.092

[3] Gross R. A., Kalra B.: Biodegradable polymers for the environment. Science, **297**, 803–807 (2002).
DOI: 10.1126/science.297.5582.803

[4] del Valle L. J., Díaz A., Royo M., Rodríguez-Galán A., Puiggalí J.: Biodegradable polyesters reinforced with triclosan loaded polylactide micro/nanofibers: Properties, release and biocompatibility. Express Polymer Letters, **6**, 266–282 (2012).
DOI: 10.3144/expresspolymlett.2012.30

[5] Rasal R. M., Janorkar A. V., Hirt D. E.: Poly(lactic acid) modifications. Progress in Polymer Science, **35**, 338–356 (2010).
DOI: 10.1016/j.progpolymsci.2009.12.003

[6] Drumright R. E., Gruber P. R., Henton D. E.: Polylactic acid technology. Advanced Materials, **12**, 1841–1846 (2000).
DOI: 10.1002/1521-4095(200012)12:23<1841::AID-ADMA1841>3.0.CO;2-E

[7] Lim L-T., Auras R., Rubino M.: Processing technologies for poly(lactic acid). Progress in Polymer Science, **33**, 820–852 (2008).
DOI: 10.1016/j.progpolymsci.2008.05.004

[8] De Santis R., Catauro M., Di Silvio L., Manto L., Raucci M., Ambrosio L., Nicolais L.: Effects of polymer amount and processing conditions on the in vitro behaviour of hybrid titanium dioxide/polycaprolactone composites. Biomaterials, **28**, 2801–2809 (2007).
DOI: 10.1016/j.biomaterials.2007.02.014

[9] Russo T., Gloria A., D-Antò V., D'Amora U., Ametrano G., Bollino F., De Santis R., Ausanio G., Catauro M., Rengo S., Ambrosio L.: Poly(ε-caprolactone) reinforced with sol-gel synthesized organic-inorganic hybrid fillers as composite substrates for tissue engineering. Journal of Applied Biomaterials and Biomechanics, **8**, 146–152 (2010).
DOI: 10.5301/jabb.2010.6094

[10] Liu H., Zhang J.: Research progress in toughening modification of poly(lactic acid). Journal of Polymer Science Part B: Polymer Physics, **49**, 1051–1083 (2011).
DOI: 10.1002/polb.22283

[11] Martin O., Avérous L.: Poly(lactic acid): Plasticization and properties of biodegradable multiphase systems. Polymer, **42**, 6209–6219 (2001).
DOI: 10.1016/S0032-3861(01)00086-6

[12] Kulinski Z., Piorkowska E., Gadzinowska K., Stasiak M.: Plasticization of poly(L-lactide) with poly(propylene glycol). Biomacromolecules, **7**, 2128–2135 (2006).
DOI: 10.1021/bm060089m

[13] Ljungberg N., Wesslén B.: Preparation and properties of plasticized poly(lactic acid) films. Biomacromolecules, **6**, 1789–1796 (2005).
DOI: 10.1021/bm050098f

[14] Ljungberg N., Wesslén B.: Tributyl citrate oligomers as plasticizers for poly(lactic acid): Thermo-mechanical film properties and aging. Polymer, **44**, 7679–7688 (2003).
DOI: 10.1016/j.polymer.2003.09.055

[15] Li Y., Shimizu H.: Toughening of polylactide by melt blending with a biodegradable poly(ether)urethane elastomer. Macromolecular Bioscience, **7**, 921–928 (2007).
DOI: 10.1002/mabi.200700027

[16] Zhang W., Chen L., Zhang Y.: Surprising shape-memory effect of polylactide resulted from toughening by polyamide elastomer. Polymer, **50**, 1311–1315 (2009).
DOI: 10.1016/j.polymer.2009.01.032

[17] López-Rodríguez M., López-Arraiza A., Meaurio E., Sarasua J. R.: Crystallization, morphology, and mechanical behavior of polylactide/poly(ε-caprolactone) blends. Polymer Engineering and Science, **46**, 1299–1308 (2006).
DOI: 10.1002/pen.20609

[18] Vilay V., Mariatti M., Ahmad Z., Pasomsouk K., Todo M.: Characterization of the mechanical and thermal properties and morphological behavior of biodegradable poly(L-lactide)/poly(ε-caprolactone) and poly(L-lactide)/poly(butylene succinate-*co*-L-lactate) polymeric blends. Journal of Applied Polymer Science, **114**, 1784–1792 (2009).
DOI: 10.1002/app.30683

[19] Shibata M., Inoue Y., Miyoshi M.: Mechanical properties, morphology, and crystallization behavior of blends of poly(L-lactide) with poly(butylene succinate-*co*-L-lactate) and poly(butylene succinate). Polymer, **47**, 3557–3564 (2006).
DOI: 10.1016/j.polymer.2006.03.065

[20] Yoon J-S., Oh S-H., Kim M-N., Chin I-J., Kim Y-H.: Thermal and mechanical properties of poly(L-lactic acid)–poly (ethylene-*co*-vinyl acetate) blends. Polymer, **40**, 2303–2312 (1999).
DOI: 10.1016/S0032-3861(98)00463-7

[21] Liu H., Chen F., Liu B., Estep G., Zhang J.: Super toughened poly(lactic acid) ternary blends by simultaneous dynamic vulcanization and interfacial compatibilization. Macromolecules, **43**, 6058–6066 (2010).
DOI: 10.1021/ma101108g

[22] Liu H., Song W., Chen F., Guo L., Zhang J.: Interaction of microstructure and interfacial adhesion on impact performance of polylactide (PLA) ternary blends. Macromolecules, **44**, 1513–1522 (2011).
DOI: 10.1021/ma1026934

[23] Matonis V. A., Small N. C.: A macroscopic analysis of composites containing layered spherical inclusions. Polymer Engineering and Science, **9**, 90–99 (1969).
DOI: 10.1002/pen.760090204

[24] Matonis V. A.: The interfacial stresses in particulate composite systems. Polymer Engineering and Science, **9**, 100–104 (1969).
DOI: 10.1002/pen.760090205

[25] Jancar J., Dibenedetto A. T.: The mechanical properties of ternary composites of polypropylene with inorganic fillers and elastomer inclusions. Journal of Materials Science, **29**, 4651–4658 (1994).
DOI: 10.1007/BF00376292

[26] Jancar J., Dibenedetto A. T.: Effect of morphology on the behaviour of ternary composites of polypropylene with inorganic fillers and elastomer inclusions. Journal of Materials Science, **30**, 1601–1608 (1995).
DOI: 10.1007/BF00375271

[27] Jancar J., Dibenedetto A. T.: Failure mechanics in ternary composites of polypropylene with inorganic fillers and elastomer inclusions. Journal of Materials Science, **30**, 2438–2445 (1995).
DOI: 10.1007/BF01184598

[28] Yang H., Zhang X., Qu C., Li B., Zhang L., Zhang Q., Fu Q.: Largely improved toughness of PP/EPDM blends by adding nano-SiO_2 particles. Polymer, **48**, 860–869 (2007).
DOI: 10.1016/j.polymer.2006.12.022

[29] Yang H., Zhang Q., Guo M., Wang C., Du R., Fu Q.: Study on the phase structures and toughening mechanism in PP/EPDM/SiO_2 ternary composites. Polymer, **47**, 2106–2115 (2006).
DOI: 10.1016/j.polymer.2006.01.076

[30] Chow W. S., Leu Y. Y., Mohd Ishak Z. A.: Effects of SEBS-g-MAH on the properties of injection moulded poly(lactic acid)/nano-calcium carbonate composites. Express Polymer Letters, **6**, 503–510 (2012).
DOI: 10.3144/expresspolymlett.2012.53

[31] Gao X., Qu C., Zhang Q., Peng Y., Fu Q.: Brittle-ductile transition and toughening mechanism in POM/TPU/$CaCO_3$ ternary composites. Macromolecular Materials and Engineering, **289**, 41–48 (2004).
DOI: 10.1002/mame.200300222

[32] Premphet K., Horanont P.: Phase structure of ternary polypropylene/elastomer/filler composites: Effect of elastomer polarity. Polymer, **41**, 9283–9290 (2000).
DOI: 10.1016/S0032-3861(00)00303-7

[33] Wu D., Zhang Y., Zhang M., Yu W.: Selective localization of multiwalled carbon nanotubes in poly(ε-caprolactone)/polylactide blend. Biomacromolecules, **10**, 417–424 (2009).
DOI: 10.1021/bm801183f

[34] Shi Y. Y., Li Y. L., Wu J., Huang T., Chen C., Peng Y., Wang Y.: Toughening of poly(L-lactide)/multiwalled carbon nanotubes nanocomposite with ethylene-*co*-vinyl acetate. Journal of Polymer Science Part B: Polymer Physics, **49**, 267–276 (2011).
DOI: 10.1002/polb.22177

[35] Shi Y. Y., Li Y. L., Xiang F. M., Huang T., Chen C., Peng Y., Wang Y.: Carbon nanotubes induced microstructure and mechanical properties changes in cocontinuous poly(L-lactide)/ethylene-*co*-vinyl acetate blends. Polymers for Advanced Technologies, **23**, 783–790 (2011).
DOI: 10.1002/pat.1959

[36] Li W., Karger-Kocsis J., Schlarb A. K.: Dispersion of TiO_2 particles in PET/PP/TiO_2 and PET/PP/PP-*g*-MA/TiO_2 composites prepared with different blending procedures. Macromolecular Materials and Engineering, **294**, 582–589 (2009).
DOI: 10.1002/mame.200900123

[37] Li W., Karger-Kocsis J., Thomann R.: Compatibilization effect of TiO_2 nanoparticles on the phase structure of PET/PP/TiO_2 nanocomposites. Journal of Polymer Science Part B: Polymer Physics, **47**, 1616–1624 (2009).
DOI: 10.1002/polb.21752

[38] Wu S.: Polymer interface and adhesion. Marcel Dekker, New York (1982).

[39] Owens D. K., Wendt R. C.: Estimation of the surface free energy of polymers. Journal of Applied Polymer Science, **13**, 1741–1747 (1969).
DOI: 10.1002/app.1969.070130815

[40] Wu D., Sun Y., Lin D., Zhou W., Zhang M., Yuan L.: Selective localization behavior of carbon nanotubes: Effect on transesterification of immiscible polyester blends. Macromolecular Chemistry and Physics, **212**, 1700–1709 (2011).
DOI: 10.1002/macp.201100095

[41] Wei J-C., Sun J-R., Wang H-J., Chen X-S., Jing X-B.: Isothermal crystallization behavior and unique banded spherulites of hydroxyapatite/poly(L-lactide) nanocomposites. Chinese Journal of Polymer Science, **28**, 499–507 (2010).
DOI: 10.1007/s10118-010-9060-7

[42] Garlotta D.: A literature review of poly(lactic acid). Journal of Polymers and the Environment, **9**, 63–84 (2002).
DOI: 10.1023/A:1020200822435

[43] Hong J. S., Namkung H., Ahn K. H., Lee S. J., Kim C. Y.: The role of organically modified layered silicate in the breakup and coalescence of droplets in PBT/PE blends. Polymer, **47**, 3967–3975 (2006).
DOI: 10.1016/j.polymer.2006.03.077

[44] Si M., Araki T., Ade H., Kilcoyne A. L. D., Fisher R., Sokolov J. C., Rafailovich M. H.: Compatibilizing bulk polymer blends by using organoclays. Macromolecules, **39**, 4793–4801 (2006).
DOI: 10.1021/ma060125+

[45] Gubbels F., Jerome R., Teyssie Ph., Vanlathem E., Deltour R., Calderone A., Parente V., Bredas J. L.: Selective localization of carbon black in immiscible polymer blends: A useful tool to design electrical conductive composites. Macromolecules, **27**, 1972–1974 (1994).
DOI: 10.1021/ma00085a049

[46] Cai X., Li B., Pan Y., Wu G.: Morphology evolution of immiscible polymer blends as directed by nanoparticle self-agglomeration. Polymer, **53**, 259–266 (2012).
DOI: 10.1016/j.polymer.2011.11.032

[47] Bose S., Bhattacharyya A. R., Kodgire P. V., Misra A.: Fractionated crystallization in PA6/ABS blends: Influence of a reactive compatibilizer and multiwall carbon nanotubes. Polymer, **48**, 356–362 (2007).
DOI: 10.1016/j.polymer.2006.11.019

[48] Jiang L., Zhang J., Wolcott M. P.: Comparison of polylactide/nano-sized calcium carbonate and polylactide/montmorillonite composites: Reinforcing effects and toughening mechanisms. Polymer, **48**, 7632–7644 (2007).
DOI: 10.1016/j.polymer.2007.11.001

[49] Kayano Y., Keskkula H., Paul D. R.: Fracture behaviour of some rubber-toughened nylon 6 blends. Polymer, **39**, 2835–2845 (1998).
DOI: 10.1016/S0032-3861(97)00600-9

[50] Kim G-M., Michler G. H., Gahleitner M., Fiebig J.: Relationship between morphology and micromechanical toughening mechanisms in modified polypropylenes. Journal of Applied Polymer Science, **60**, 1391–1403 (1996).
DOI: 10.1002/(SICI)1097-4628(19960531)60:9<1391::AID-APP15>3.0.CO;2-5

[51] Galeski A., Bartczak Z.: Cavitation and cavity-free deformation of filled crystalline polymer systems. Macromolecular Symposia, **194**, 47–62 (2003).
DOI: 10.1002/masy.200390105

[52] Balakrishnan S., Start P. R., Raghavan D., Hudson S. D.: The influence of clay and elastomer concentration on the morphology and fracture energy of preformed acrylic rubber dispersed clay filled epoxy nanocomposites. Polymer, **46**, 11255–11262 (2005).
DOI: 10.1016/j.polymer.2005.10.053

[53] Bai H., Xiu H., Gao J., Deng H., Zhang Q., Yang M., Fu Q.: Tailoring impact toughness of poly(L-lactide)/poly(ε-caprolactone) (PLLA/PCL) blends by controlling crystallization of PLLA matrix. ACS Applied Materials and Interfaces, **4**, 897–905 (2012).
DOI: 10.1021/am201564f

eXPRESS Polymer Letters Vol.7, No.3 (2013) 272–292
Available online at www.expresspolymlett.com
DOI: 10.3144/expresspolymlett.2013.25

Vegetable oil-derived epoxy monomers and polymer blends: A comparative study with review

*R. Wang, T. P. Schuman**

Department of Chemistry, Missouri University of Science and Technology, MO 65409 Rolla, USA

Received 13 September 2012; accepted in revised form 18 November 2012

Abstract. Glycidyl esters of epoxidized fatty acids derived from soybean oil (EGS) and linseed oil (EGL) have been synthesized to have higher oxirane content, more reactivity and lower viscosity than epoxidized soybean oil (ESO) or epoxidized linseed oil (ELO). The EGS and ESO, for comparison, were used neat and in blends with diglycidyl ether of bisphenol A (DGEBA). Thermosetting resins were fabricated with the epoxy monomers and either BF_3 catalyst or anhydride. The curing behaviors, glass transition temperatures, crosslink densities and mechanical properties were tested. The results indicated that polymer glass transition temperatures were mostly a function of oxirane content with additional influence of glycidyl versus internal oxirane reactivity, pendant chain content, and chemical structure and presence of saturated components. EGS provided better compatibility with DGEBA, improved intermolecular crosslinking and glass transition temperature, and yielded mechanically stronger polymerized materials than materials obtained using ESO. Other benefits of the EGS resin blend systems were significantly reduced viscosities compared to either DGEBA or ESO-blended DGEBA counterparts. Therefore, EGS that is derived from renewable sources has improved potential for fabrication of structural and structurally complex epoxy composites, *e.g.*, by vacuum-assisted resin transfer molding.

Keywords: *thermosetting resins, mechanical properties, thermal properties, biopolymers, epoxy*

1. Introduction

Since petroleum resources are ultimately limited, polymers based on vegetable oils are of great interest because they are renewable and could significantly contribute to a more sustainable development [1, 2]. Vegetable oils such as linseed and tung oil are drying oils, which can self-crosslink under atmospheric oxygen, have long been used in the coating industry [3]. Semi-drying oils like soybean oil are of plentiful supply and therefore of relatively low cost, have also attracted great interest for the preparation of polymers or resins [4]. In recent years, with the rising cost of fossil raw materials and environmental issues, polymers derived from soybean oil have demonstrated strong cost/performance competitiveness in many market applications [5]. However, the ability to obtain structures of sufficient mechanical or thermal properties has remained a challenge.

For instance, direct radical or cationic polymerization of vegetable oils is structurally difficult due to the non-conjugated, internal double bonds and only viscous liquid polymers with low molecular weight are formed [6]. On the other hand, polymers ranging from soft rubbers to hard plastics have been prepared by the cationic copolymerization of soybean oil blended with divinylbenzene (DVB). Styrene was added to reduce the heterogeneity of the crosslinked structures caused by incompatibility between monomers and the modulus of polymer was dependent on the styrene and, particularly, the DVB content [7].

Epoxidation of vegetable oils using peracids, such as Epoxidized soybean oil (ESO) and epoxidized

*Corresponding author, e-mail: tschuman@mst.edu

linseed oil (ELO), is one of the most important and useful exploitations of double bonds since epoxides are reactive intermediates that are also readily converted to other functional groups through ring-opening reactions. Sheet molding compound (SMC) resins have been made from epoxidized soybean oil modified with unsaturated functional groups like acrylic acid or maleic anhydride where styrene was employed as a comonomer to reduce the viscosity of the resin [8, 9]. The SMC was obtained via common radical polymerization fashion. Allyl alcohol ring-opened ESO has been copolymerized with maleic anhydride (MA) to prepare thermosets by esterification and free radical polymerization. The resulting glass transition temperatures (T_g) and mechanical strengths were dependent on the loading of MA [10]. Soy based polyols derived from ESO have also been widely used to produce polyurethanes that are comparable in many aspects with polyurethanes obtained from petrochemical polyols [11].

ESO can be crosslinked into thermosetting polymers by various curing agents [12]. However, due to lower oxirane content and sluggish reactivity of the internal oxirane, the cured ESO polymers normally have low crosslinking density. Poorer thermal and mechanical properties result from both partially unreacted ESO and saturated fatty acid (FA) chains that reduce reactivity and self-plasticize. Most ESO industrial uses are thus limited to nonstructural, additive applications such as plasticizers or stabilizers for poly (vinyl chloride) [13], oil-base coatings [14] with low strength requirements [15]. Though the mechanical strength of cured ESO can be improved with the addition of nano-reinforcements [16], or fiber reinforcement [17], an inherently low T_g inevitably limits practical applications because T_g for a polymer must be appropriately higher than the temperature of its intended work environment to serve as a useful plastic [18]. When used as a matrix material in composites, the resin state is desired to be rigid/glassy, *i.e.*, below its T_g, to effectively transfer energy to fibers [19].

ESO has a moderate viscosity so ESO or their derivatives can be used as reactive diluents for the partial replacement of diglycidyl ether of bisphenol A (DGEBA) resins, which are relatively high viscosity liquids or solids, to decrease the overall cost and improve the processability [20–22]. Generally, the mechanical strengths and thermal properties of ESO blended resins are not comparable to those of pure DGEBA epoxy resins, while their toughness can be better due to the introduction of a two phase structure [23–26]. However, due to the inhomogeneous structure, ESO is not as efficient in reducing the viscosity of epoxy resin compared to most petroleum based reactive diluents. A further increase in the ESO concentration inevitably leads to a significant decrease in performance of cured resin. There are few reports of high ESO replacement [20] because low oxirane content and the unreactive saturated component of ESO both lead to a low crosslink density upon cure and a poor miscibility exists between ESO and the DGEBA. There is an especially large difference in the reactivity of the internal oxirane in ESO and terminal oxirane in DGEBA and, as we will show, heterogeneous structures form during the curing reaction that leads to a phase separated materials of poorer mechanical /thermal performance.

More reactive terminal epoxy derived from chlorinated ESO has been reported and used as a matrix with DGEBA for glass fiber composites [27]. The dehydrochlorination under alkaline conditions will hydrolyze ester groups of triglycerides, even at room temperature. A triglyceride with terminal epoxy has been synthesized from 10-undecenoic acid and successfully used in epoxy-amine curing [28, 29], whereas 10-undecylenic acid, a derivative of castor oil, has only one terminal double bond so the epoxidized triglyceride ester of 10-undecylenic acid has a lower oxirane content compared to ESO. Large-scale production also seems impractical [30]. Only those oils of poly-unsaturated FA content, especially soybean or linseed oils, that can produce dense oxirane functional resins are capable to produce satisfactory properties [12, 31–33]. Epoxidized vegetable oils (EVO) of low oxirane values either are not reactive or impart waxy, non-curing properties to the resin system.

Vegetable oils contain several actives sites amenable to chemical modification. The double bonds in FA chains and the ester groups in the glyceryl part are the most important. These active sites can be used to introduce reactive groups. ESO and aforementioned derivatives are most focused on the modification of FA chain. On the ester side, epoxidized methyl oleate [34], epoxidized methyl soyate, epoxidized allyl soyate [35], epoxidized sunflower oil biodiesel [36] and linseed oil epoxidized methyl

esters [37] have been shown to have lower viscosity and more reactive compared to their ESO or ELO counterparts.

A caveat in the addition of functional groups, such as unreactive methyl or reactive allyl through transesterification, is a potential decrease of crosslinking density and final properties of cured resins upon breaking the oligomeric triglyceride structure. FA chain ends at the ester become pendant after transesterification and are dependent on crosslinking to build molecular weight. Esters of saturated FAs may only behave as plasticizers [38]. Novel epoxy compounds such as epoxidized sucrose esters of fatty acids have been synthesized and crosslinked to prepare polyester thermosets [30, 39]. High modulus polymer was achieved due to the well-defined compact macromolecular structures and high oxirane functionality. Some applications may be hampered by their high viscosities.

Modified ELO synthesized through Diels–Alder reaction of dicyclopentadiene [40] or 1,3-butadiene [41] with linseed oil have been reported. The modified ELO resins still possessed internal oxirane and thus are more suitable for cationic cure. End users still seek economical bio-based epoxies that are competitive with petroleum-based epoxies [30].

Vegetable oils generally have variable levels of saturated FA content, for example, soybean oil normally has about 15% saturated FAs (~4.0 % stearic and ~11% palmitic) that varies with plant variety, growing regions, and weather. Saturated FAs have no functional groups within the FA chain that then act as dangling chains, low in reactivity, to plasticize the final polymer. The saturated chains are detrimental to the final properties of polymers [42, 43].

To improve reactivity and to increase hydroxyl number of soy based polyols, regionally selective enzymatic hydrolysis has been attempted to liberate saturated FAs, which were then removed by alkaline washing [44]. Total removal of saturated components is difficult and is also accompanied by partial hydrolysis of unsaturated FA esters. Conversion of oil triglyceride into free fatty acid (FFA) or FA derivatives allows separation of unsaturated and saturated components on the basis of solubility through crystallization. The degree of unsaturation of FFA considerably changes the melting point and thus separation of mixtures of saturated and unsaturated FFAs can be readily achieved by proper choice of organic solvents and temperatures [45].

In this research, EGS were synthesized and examined. The goals were to remove and assess the role of the plasticizing effect of saturated components, to increase and assess the role of the oxirane content, and to minimize viscosity toward developing either a capable reactive diluent for commercial epoxy or a new commercial epoxy resin of its own right. The study gave us the opportunity to study how saturated component, oxirane type and oxirane content translate into curing, thermal and mechanical properties. We hypothesized that EGS as the ester of a terminal oxirane group (glycidyl), which is then readily accessible to nucleophilic attack, should further enable reactivity compared with the currently standard, commercial ESO and consequently reduce the molecular size and facilitate removal of the saturated FA components. We thus proposed to increase oxirane content. The goals and resin design were intended to provide a dense, intermolecular crosslinking structure and yield a more consistent thermosetting resin material with improved properties.

2. Experimental

2.1. Materials

Refined, food grade soybean oil (Great Value™, Wal-Mart, Bentonville, AR, USA) was purchased. Linseed oil was purchased from Archer Daniels Midland Company (Red Wing, MN, USA). The major FA distributions [46] reported for soybean oil and linseed oil are listed in Table 1. ESO was obtained from Union Carbide Corporation (Danbury, CT, USA). ELO was obtained from Arkema, Inc. (Philadelphia, PA, USA). Acetone, allyl alcohol, epichlorohydrin (EPCH), methylene chloride, methanol, meta-chloroperoxybenzoic acid (MCPBA), potassium hydroxide, sodium carbonate, sodium bicarbonate, sodium hydroxide, sodium sulfite, and anhy-

Table 1. Fatty acids profile in vegetable oils

Fatty Acid (x:y)	Palmitic (14:0)	Stearic (18:0)	Oleic (18:1)	Linoleic (18:2)	Linolenic (18:3)
Soybean oil [%]	11	4	23	53	8
Linseed oil [%]	5	4	19	15	57

Legend (*x*:*y*): *x*, number of carbon atoms; *y*, number of double bonds. Fatty acid contents do not add to 100% due to presence of minor fatty acid content.

drous sodium sulfate were purchased from Fisher Scientific (St. Louis, MO, USA). Cetyltrimethylammonium bromide (CTAB), boron trifluoride monoethyl amine complex (BF_3-MEA), 2-ethyl-4-methylimidazole (EMI), hydrochloric acid and 4-methyl-1,2-cyclohexanedicarboxylic anhydride (MHHPA) were purchased from Aldrich (St. Louis, MO, USA). Commercial DGEBA was supplied by Momentive (Deer Park, TX, USA) with trade name EPON™ Resin 828. Mold release agent Chemlease® 41-90 EZ was purchased from Chem-Trend, Inc. (Howell, MI, USA)

2.2. Chemical characterization

Infrared spectra (IR) were measured with a Nicolet Nexus 470 E.S.P. spectrophotometer (Waltham, MA, USA). ^{1}H NMR spectra were obtained on a Varian INOVA 400 MHz spectrometer (Palo Alto, CA, USA) using d_6-DMSO as solvent. Iodine value was assessed using ASTM Method D5554-95. Oxirane oxygen value was measured using AOCS Method Cd 9-57.

2.3. Soap and free fatty acid preparation

Free fatty acids were made via acid neutralization of soap. Vegetable oil and water mixture (800 g, 50:50) was reacted with sodium hydroxide solution (200 g, 30 wt%) at 60°C for 4 hr to generate soap and then acidified with sulfuric acid (270 g, 30 wt%) to pH < 2. The lower aqueous layer including sodium sulfate and glycerin was separated, washing the top FFA layer using 60°C water. Finally the liquid organic FFA layer (339 g) was dried using anhydrous sodium sulfate. The iodine value of the soybean FFA was 133.

Freshly prepared FFA was dissolved in acetone based on the weight ratio of 1:6 and then purged with nitrogen gas, cooled to –20°C for overnight. The formed crystals were removed by vacuum filtration. The procedure could be repeated several times until no further crystals were generated. For these studies, four times filtration were performed resulting in an iodine value for refined unsaturated soybean FFA of 150.

To a FFA/acetone solution (500 g) of weight ratio of 1:10, 110% of stoichiometric sodium hydroxide solution (18 mL, 10 M) based on amount of FFA (average molecular weight treated as 278 g/mol) was added dropwise. The neutralization reaction was continued for 4 hr under nitrogen gas to prevent air oxidation of the soap. The soap powder was readily filtered by vacuum filtration and then dried at 110°C for 1.5 hr.

2.4. Glycidyl esters of epoxidized fatty acids preparation

Dry soap (302 g) and EPCH (925 g) were heated to reflux. Phase transfer catalyst CTAB (7.3 g) at 2 equivalent-% per equivalent soap was then added. Reflux was continued for 30 min, cooled and centrifuged, the clear solution was decanted to a flask. Excess EPCH was removed using *in vacuo* rotary evaporation. Oxirane oxygen value of prepared glycidyl ester was 4.4% (theoretical value of 4.7% for glycidyl oleate).

Glycidyl ester (341 g) and sodium carbonate (64 g) were mixed with methylene chloride (200 ml). MCPBA (367 g, 75 wt%) dissolved in methylene chloride at 0.1 g/ml concentration was added dropwise at a reaction temperature below 15°C and then reacted for 4 hr to complete epoxidation. The reaction mixture was washed with 10 wt% sodium sulfite (200 g) and then by 10 wt% aqueous sodium bicarbonate (150 g). Methylene chloride was removed by *in vacuo* rotary evaporation and the product EGS (345 g) was dried over anhydrous sodium sulfate. Linseed oil based glycidyl esters of epoxidized fatty acids (EGL) were also prepared based on the above mentioned procedure. For EGS-S/EGL-S, saturated FFAs were not removed and remain in EGS/EGL. For EGS-P/EGL-P, FAs were partially epoxidized. Soybean oil based epoxidized methyl ester (EMS) and epoxidized allyl ester (EAS) were formed by standard alkaline transesterification with the corresponding alcohols and then epoxidized by MCPBA, *e.g.*, potassium hydroxide (2.2 g) was first crushed and dissolved in allyl alcohol (260 g), then poured into soybean oil (220 g). Mixtures were heated under reflux condition for 4 hrs. Workup included potassium hydroxide discharged by the addition of concentrated hydrochloric acid (3.9 g, 37 wt%), removal of the excess allyl alcohol using *in vacuo* rotary evaporation, washing of the allyl esters of soybean oil four times with distilled water to remove glycerin, salt, and any residual allyl alcohol, and then drying with anhydrous sodium sulfate and filtration to remove the sodium sulfate. The method for epoxidation of allyl esters of soybean oil by MCPBA is the above-mentioned method for epoxidation of glycidyl esters.

2.5. Thermal characterization

2.5.1. Curing reactions

The weight ratios of EGS/ESO to DGEBA resin blend chosen for the present work were 0:100 (pure DGEBA), 10:90, 30:70, 50:50, 70:30; 90:10 and 100:0 (pure EGS/ESO). A stoichiometric ratio r = 1.0 of epoxy/anhydride was used for all samples and 1 wt% (based on epoxy part) of EMI were added to the blend. After mixing by a PowerGen 1000 homogenizer (Fisher Scientific, St. Louis, MO, USA) for 10 min, the mixture was degassed under vacuum for 30 min, then poured into a mold treated with mold release agent. Curing was performed at 145°C for 15 hr for all blends except ESO-DGEBA (90:10) and pure ESO blend, which were inducted for 12 hr at room temperature, remixed, poured into the mold and cured at 125°C for 15 hr. ESO required more stringent curing conditions due to the low reactivity and phase separation exhibited by ESO. Postcure for all samples was performed at 175°C for 1 hr.

Two to three milligrams of mixture was hermetically sealed in an aluminum pan and cured on a model Q2000 differential scanning calorimetry (DSC) machine (TA Instruments, New Castle, DE, USA) by scanning temperature at a heating rate of 10°C/min from 40–250°C to study the cure behavior of each formulation.

Neat epoxy monomers were also cationically cured. A 3 wt% (based on epoxy) of BF_3-MEA was mixed with monomer and cured at 150°C for 3 hr followed by 185°C for 1 hr.

2.5.2. Glass transition and degradation temperatures

DSC was used to determine the glass transition of cured resin. Samples were first preheated at 20°C/min to 180°C to remove any previous thermal history, and then quenched to –40°C. Heat flow was measured over a temperature range scanned from –40 to 180°C at a heating rate of 20°C/min. Universal Analysis 2000 software (TA Instruments, New Castle, DE, USA) was used to analyze the curve, inflection temperature (T_i) was reported as the glass transition temperature.

A model Q50 thermogravimetric analysis instrument (TGA, TA Instruments, New Castle, DE, USA) was used to determine the thermal degradation onset temperature of cured resin. Measurement was performed while scanning temperature from 30 to 750°C at a heating rate of 10°C/min under an ambient air flow environment.

2.6. Swelling test

Approximately 0.2 g of the cured resins with a cubic shape (8 mm × 8 mm × 3 mm) were placed in toluene solvent until equilibrium was attained. To accelerate the swelling, samples were placed into a 45°C oven to attain a constant weight, then equilibrated at room temperature for one week. The swollen samples were removed from the solvents, quickly blotted dry with paper towel, and weighed. The equilibrium swelling ratio [47] of the cured resin was calculated based on Equation (1):

$$Q = \frac{1}{\nu_2} = 1 + \frac{\left(\frac{m_s}{m_0} - 1\right)\cdot\rho_{poly}}{\rho_{sol}} \quad (1)$$

where Q is the equilibrium swelling ratio of the polymeric network, υ_2 is the volume fraction of polymer at equilibrium swelling, m_0 is the mass of the polymeric network before swelling, m_s is the mass of the polymeric network at equilibrium swelling, and ρ_{sol} and ρ_{poly} are the densities of the solvent and polymeric network, respectively.

2.7. Mechanical tests

Tensile strengths and moduli were measured on a model 4469 Universal testing machine (Instron, Norwood, MA, USA) according to ASTM D638. All the tensile tests were performed at a crosshead speed of 10 mm/min. At least five specimens were tested for each different resin system. The flexural strengths and moduli were determined according to the ASTM method D790. The span was 50.8 mm, the crosshead speed was set at 12.7 mm/min.

2.8. Physical properties

Viscosity was tested on a model LVDV-III+ Ultra Rheometer (Brookfield, Middleboro, MA, USA) at 25°C. Liquid density was determined using the pycnometer method. Specific gravity of solid samples was measured by immersion in water using a model XP 204S balance (Mettler-Toledo, Columbus, OH, USA) with density measurement kits.

3. Results and discussion

3.1. Preparation of glycidyl esters of epoxidized fatty acids

Figure 1 shows the synthetic route to EGS, generalized for oleic acid showing the process for a soybean triglyceride. Preparation of mixed FFAs from triglyceride is straightforward and well-developed. Methods of low temperature crystallization to remove the unsaturated FFAs are also well documented [48]. Most unsaturated FFAs are soluble in most organic solvents at temperature above 0°C while the saturated FFAs, which have higher melting points than unsaturated FFAs, are prone to form crystals/precipitates at low temperature in solvents like acetone or methanol. Although trace amounts of saturated FFAs remain unavoidably in the unsaturated FFAs after low temperature crystallization [49], further removal of saturated FA components was achieved after synthesis of glycidyl ester or EGS because glycidyl esters, or the epoxidized glycidyl esters, of unsaturated FAs are each liquid at room temperature and much lower in melting point than glycidyl esters of saturated FAs. The unsaturated esters are poorer solvents for saturated carbon chains, which are then more easily precipitated at room temperature. Although no FFA component analyses, like chromatography, were performed in this research, we believe the saturated components were minimized after three precipitations.

Acetone was used as a low boiling, recoverable solvent to prepare soap. A slight excess of NaOH and higher concentration was preferable when preparing soap from FFA because unsaturated FFAs were prone to dissolve in acetone rather than react with base. Unsaturated FFA soaps are more soluble in water [50]. Carefully dried and finely powdered soaps resulted in greater yields of glycidyl esters of FAs. [51]

A low solubility of soap in EPCH suggested that a phase transfer catalyst would be useful to accelerate the reaction. With CTAB catalyst, the consumption of soap was completed within half an hour under reflux condition. Glycidyl esters can also be prepared directly from FFA in EPCH medium but the yield and purity were lower than obtained by the soap process [50]. The epoxidation of glycidyl ester was carried out using MCPBA or in situ generated performic acid. The former was more efficient. Due to the low solubility of MCPBA in methylene chlo-

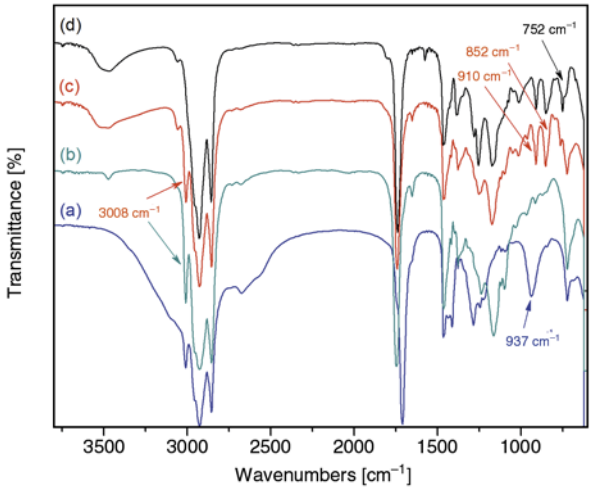

Figure 2. IR spectra of (a): mixed-FFA (b): soybean oil (c): glycidyl esters (d): EGS

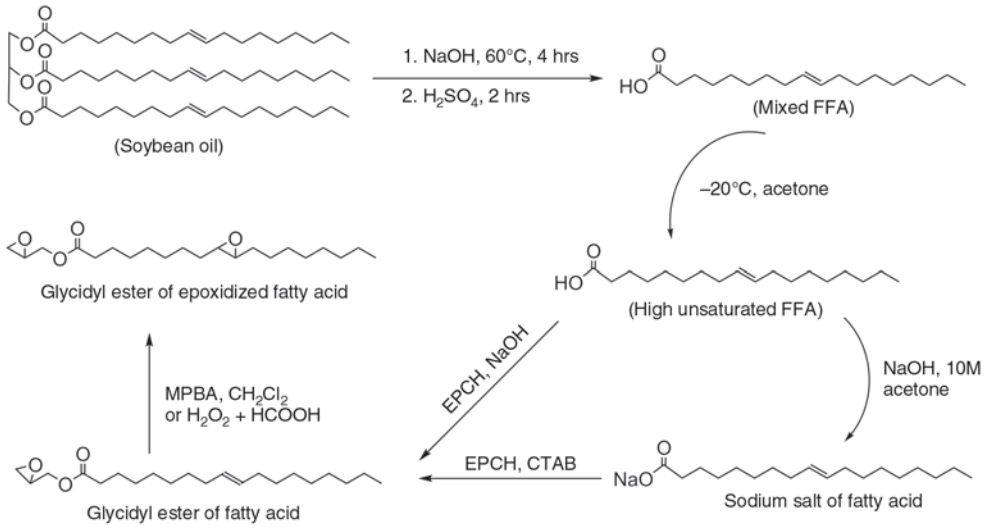

Figure 1. Synthetic route to EGS. (Vegetable oil and FAs are shown as simplified structures containing only oleic acid though they also contain other FAs. See Table 1)

ride, large amounts of recoverable solvent was required for the epoxidation.

Figure 2 shows the FT-IR spectra of mixed FFA, soybean oil, glycidyl esters and EGS. The band at 3008 cm^{-1} was attributed to the C–H stretching of =CH in unsaturated FAs, such as oleic acid, linoleic acid or linolenic acid. New bands at 910 and 852 cm^{-1} were observed in the spectrum of glycidyl esters with the disappearance of the absorption at 937 cm^{-1} in the mixed-FFA spectrum that showed presence of glycidyl group. The conversion of double bonds to epoxy was confirmed by the disappear-

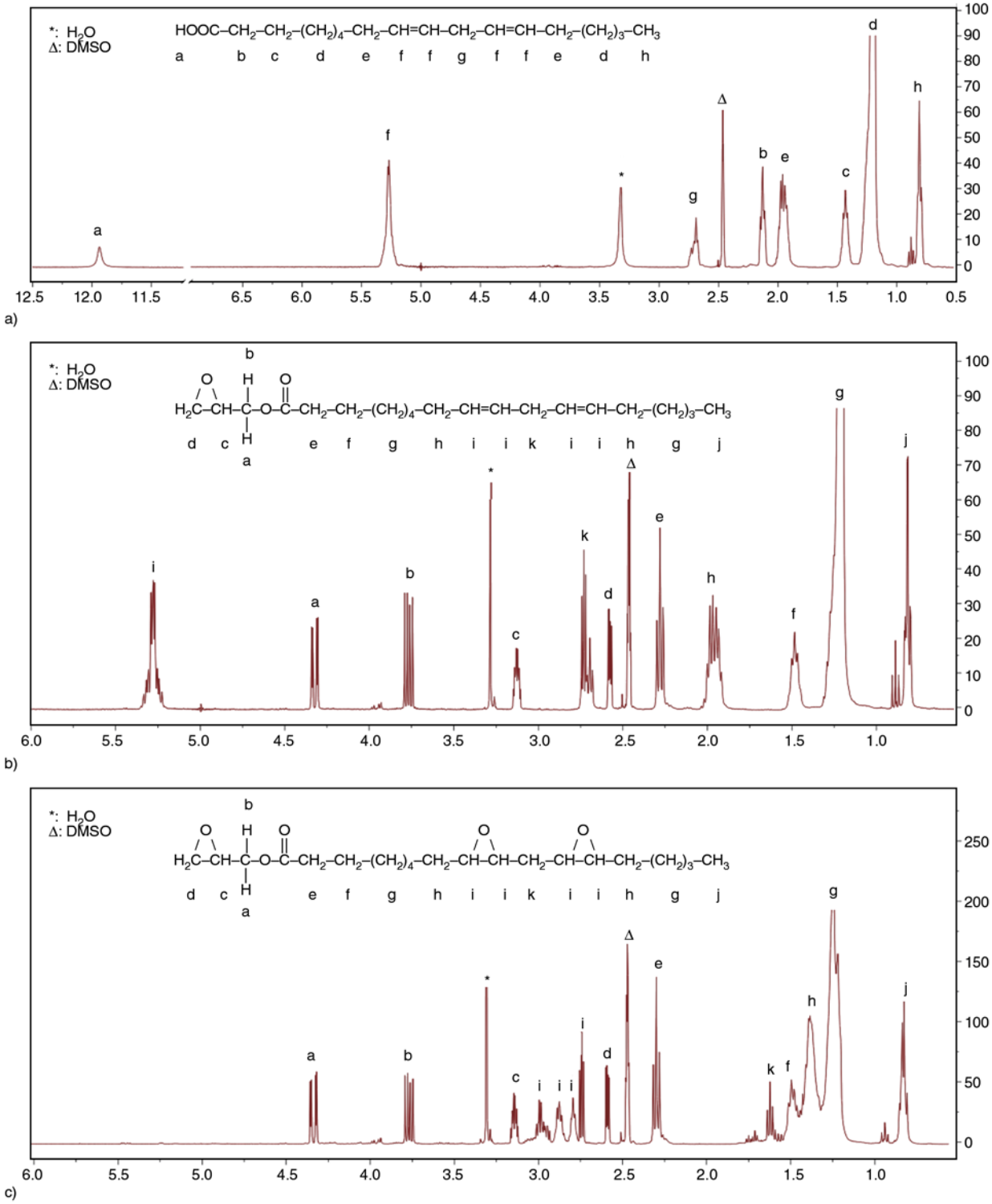

Figure 3. [1]H NMR spectrum and structural assignments of a) FFA mixture; b) glycidyl ester of FFA mixture; and c) EGS monomer (see text for structural assignment details)

Table 2. General physical properties of epoxy resins

Epoxy resin	Oxirane oxygen [g/100 g sample]	EEW [g/equivalent]	Viscosity at 25°C [mPa·s]	Density [g/mL]
EGS	10.1	158	70	1.03
ESO	6.9	232	430	0.98
EGL	12.0	134	85	1.04
ELO	9.3	171	800	1.03
DGEBA	8.6	186	13 000	1.16

ance of the 3008 cm^{-1} band observed in glycidyl esters and the concurrent appearance of absorption at 752 cm^{-1} in EGS.

Figure 3 shows the ^1H NMR spectra of mixed-FFA, glycidyl ester and EGS, where linoleic acid is shown as a generalized compound for structural assignments. The spectra showed no evidence of side reactions in preparing glycidyl esters using the soap process, nearly quantitative conversion of double bonds to epoxy groups, and no oxirane ring opening during the epoxidation of glycidyl esters to EGS using MCPBA, *i.e.*, showed complete conversion but a lack of side reactions.

General properties of EGS product compared to ESO and DGEBA is shown in Table 2.

3.2. Curing reaction

Differential scanning calorimetry was applied to study the curing behavior of the blended epoxy resins (Figure 4). The exothermic peaks were characteristic of the epoxy and anhydride curing reaction [52, 53]. Integration of the peaks allows the determination of the enthalpy of curing reaction (ΔH), cure onset temperature (T_o) and peak exothermic (T_p).

From Figure 4, the pure DGEBA and ESO reactions with MHHPA show single exothermic reaction peak at 152°C and 216°C, respectively. The higher predominance of the T_p value of ESO means a slower reaction rate, which was also confirmed by a lower ΔH value. A lower oxirane content of ESO and the internal oxiranes versus glycidyl functional groups react more sluggishly with MHHPA curing agent.

The addition of ESO to DGEBA leads to a shifting of T_p and T_o to higher values. With a decrease of ΔH value, two partially convoluted peaks were clearly observed that became pronounced for 50 wt% ESO or higher ESO concentrations, which suggested that there was decreasing ESO miscibility in the DGEBA. Immiscibility would lead to an inhomogeneous cure of the epoxy resin. Group reactivity also affects the polymerization reactions. ESO has internal, hindered oxiranes whereas DGEBA has glycidyl groups of less steric hindrance and greater reactivity than the internal oxirane.

The prepared EGS resin showed quite different and interesting curing behavior. The neat EGS showed two convoluted peaks, analogous to the blend of DGEBA and ESO, which is believed to be due to the inherently different reactivity of glycidyl and internal oxirane groups. The T_p and T_o values of EGS were more than 40°C lower than ESO, which indicated EGS was much more reactive than ESO. Increased addition of EGS to DGEBA also lead to shifting of T_p to higher values but the T_o remained nearly constant. Only a 16°C increase of T_p was observed for 90 wt% EGS concentration compared to pure DGEBA while it was 54°C for a 90 wt% ESO concentration.

The ΔH's [J/g] also followed a similar trend. The higher oxirane content of EGS and EGS blends, which bear glycidyl groups like pure DGEBA, would appear to facilitate a more homogenous three dimensional polymer structure upon curing compared to ESO blends. Also of interest, a lower concentration of EGS/ESO, *e.g.*, 30 wt% EGS or below, or 10 wt% ESO, had little effect on the ΔH or T_p values compared to pure DGEBA cure, which may then be related to homogeneity and compatibility with the DGEBA.

3.3. Compatibility

The DGEBA-ESO system generally has a heterogeneous structure [52] and, not surprisingly, a non-uniform crosslinked structure will lead to a poorer mechanical performance compared to a more homogeneous structure. Cured aromatic DGEBA polymers are much more rigid compared to cured aliphatic ESO, which behave as weak points or flaws when applying load. Fracture is initiated by the stress concentration at weak points. For instance, the mechanical properties of soybean oil/DVB plastics are significantly improved after increasing the

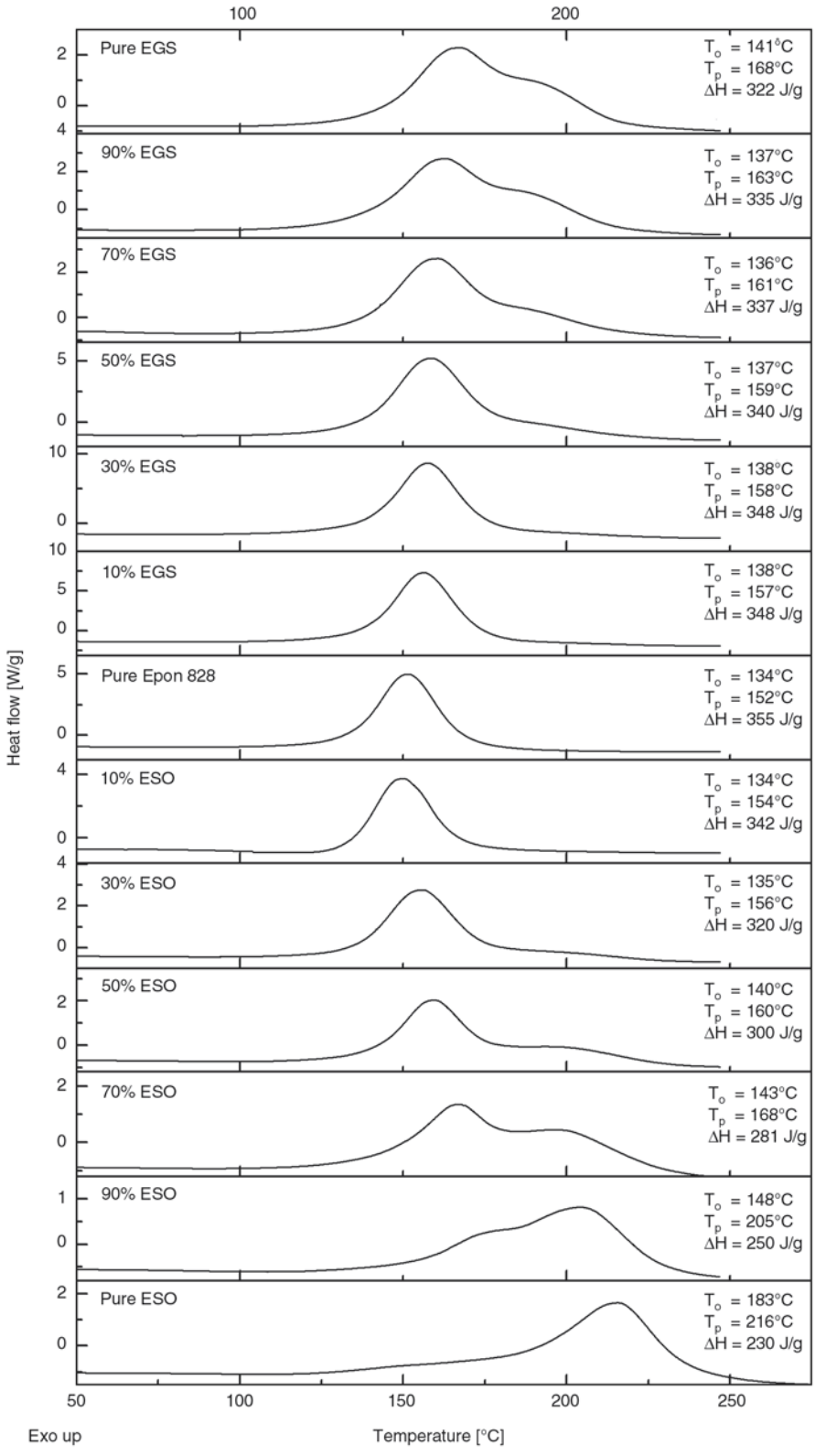

Figure 4. Dynamic thermograms of DGEBA-EGS/ESO-MHHPA systems

uniformity of the crosslinked structure [7]. A heterogeneous polymer structure is mainly due to the reactivity differences between internal and terminal oxirane. Moreover, the miscibility/compatibility between the monomer-monomer and monomer-polymer structures should also play an important role during the formation of crosslinked structure.

Solubility parameter is one method to assess the compatibility of epoxy resin with an additive or modifie [54]. To form a homogeneous structure, the

monomers and copolymers should have similar solubility parameters in accordance with the general rule that chemical and structural similarity favors solubility, *i.e.*, 'like dissolves like'. Direct determination of polymer solubility parameters from heat of vaporization data is not possible because of their non-volatility [55].

Thus, Hildebrand solubility parameters were calculated based on the group contribution method [56]. The group contribution equation is given by Equation (2):

$$\delta = \frac{\rho \sum_{i} F_i}{M} \tag{2}$$

where δ is the calculated solubility parameter, $\Sigma_i F_i$ is the molar attraction constant summation over discreet i structural group present in the compound and ρ and M are the density and molar mass of the compound, respectively. For polymers, $\Sigma_i F_i$ is the sum of all the molar attraction constants in the repeat unit, ρ is the density of the polymer, and M is the molar mass of the repeat unit. For copolymers or polymer blends, following Equation (3) was used:

$$\delta_{mix} = \frac{\sum_{i} x_i V_i \delta_i}{\sum_{i} x_i V_i} \tag{3}$$

where x_i is mole fraction of component i, V_i is component i molar volume, and δ_i is component i solubility parameter. In this study, the solubility parameter of each resin was calculated based on Hoy or van Krevelen model [56]. All compounds structures are listed in Figure 5. For EGS, a total 2.3 epoxy groups were used for the calculation, which was calculated from titrated oxirane content. Calculated δ values are listed in Table 3.

From Table 3, DGEBA, MHHPA and EGS have larger solubility parameters while ESO has the lowest solubility parameter in the blend system. Calculated values of DGEBA are close to the lower limits of the experimental values [13], which are often more reliable than upper-limit ones [57]. There are some differences in the calculated values using Hoy versus van Krevelen models because epoxy group and ether group have different values in Hoy's model. Epoxy groups should convert to ether/ester after

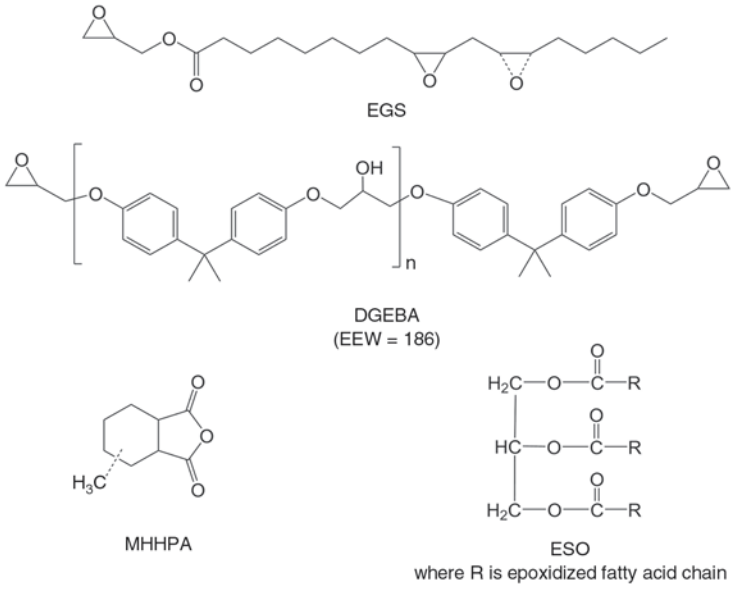

Figure 5. Compounds structure used for solubility parameters calculation

Table 3. Calculated solubility parameters of monomer and cured matrix

δ [MPa$^{1/2}$]	EGS	DGEBA	ESO	MHHPA	DGEBA-MHHPA	EGS-MHHPA	ESO-MHHPA
δ (van Krevelen)	17.8	20.5	17.5	18.2	19.4	18.0	17.8
δ (Hoy)*	19.5 (18.6)	21.9 (21.1)	19.0 (18.4)	20.9	21.0	19.4	19.7

*Values in brackets are calculated based on linear ether functional group instead of cyclic oxirane.

curing reaction, so values based only on ether groups instead of epoxy were also listed in Table 3. There is a considerable difference in the values of MHHPA due to the large difference between the group contributions of the anhydride group quoted by Hoy and by van Krevelen. Only van Krevelen values were used for the further calculation because there is evidence showing experimental values matched well with van Krevelen calculated values in the DGEBA-anhydride system [58].

It has been reported that ESO [59] or pre-polymerized ESO [60] is only partially miscible, *i.e.*, has phase separation, with the epoxy resins. The thermodynamic condition for polymer compatibility is that free energy change of mixing (ΔG_{mix}) should be small or negative, based on Flory-Huggins equation combined and Hildebrand solubility parameters [61]. ΔG_{mix} can be expressed by Equation (4):

$$\Delta G_{mix} = \phi_1\phi_2 V(\delta_1 - \delta_2)^2 + \\ + RTV\left(\frac{\phi_1\rho_1}{M_1}\ln\phi_1 + \frac{\phi_2\rho_2}{M_2}\ln\phi_2\right) \quad (4)$$

where ϕ_n is the phase volume fraction, V is volume of lattice, ρ_i is the density of component i, M_i is the molecular weight of component i, R is gas constant and T is absolute temperature. The first term of the right side in Equation (4) is related to the enthalpy of mixing (ΔH_{mix}) and the second term is assigned to the entropy of mixing ($-T\Delta S_{mix}$). Since ϕ_1 and ϕ_2 are fractions, for a fixed DGEBA-EGS/ESO composition, ΔG_{mix} at constant temperature depends only on $\Delta\delta_i$ and ρ_i/M_i, which are determined by the chemical nature and molecular weight of the EGS/ESO/DGEBA, respectively. Proximity of δ_i between DGEBA and EGS/ESO and a low molecular weight EGS/ESO favors the mixing process. It is not then surprising that EGS of higher solubility parameter and lower molecular weight favors better compatibility with DGEBA than ESO.

We have noticed turbid blends indicating phase separation were formed only for high contents of DGEBA replacement by ESO (90 and 100 wt%, Figure 6b, 6c and 6d), especially when using EMI as accelerator. While using tertiary amine a more transparent solution was formed but tertiary amine generally lead to lower T_g compared to using imidazole as accelerator [53]. These blends were prone to form cracked samples after curing and spots with dark brown or yellow colors were also observed

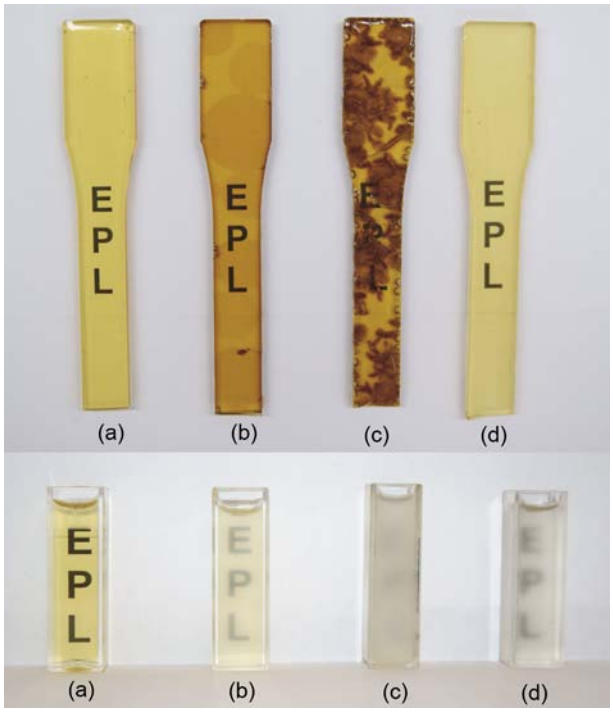

Figure 6. Physical appearances of MHHPA cured EGS/ESO-DGEBA polymers and uncured monomers blends (a): EGS-DGEBA (90:10); (b): ESO-DGEBA (90:10) precured at 145°C for 10 min; (c): ESO-DGEBA (90:10) without procuring; (d): Pure ESO inducted for 12 hrs

(Figure 6b and 6c). We ascribed these to phase separation and internal stress due to incompatibility and low reactivity of ESO in these curing systems. The terminal oxirane of DGEBA is more reactive than the internal oxirane of ESO so gelation always occurs first in the DGEBA phase. At low ESO concentration, ESO is firstly dissolved and plasticizes the rigid DGEBA matrix but is finally cured by anhydride and becomes part of the crosslinked structure as two phase thermoset polymer. At high curing temperatures, the ΔG_{mix} is marginally negative and ESO is better compatible with DGEBA but slower to react. With the advancement of curing reaction the molecular weight of crosslinked DGEBA and ESO will increase, which will result in a decrease of ΔS_{mix}. At a certain stage ΔG_{mix} becomes positive and crosslinked ESO phase separates, which should be analogous to a phase separation of rubber in epoxy resin [62].

At higher ESO concentrations, due to a faster gelation rate of the glycidyl-DGEBA network occurring at low degree of conversions of ESO, internal stress can result after vitrification but which can be avoided by proper cure temperature profile [63]. Such internal stress and incompatibility can easily

lead to crack initiation or defect structure as observed in Figure 6c. Prolonged induction via heated mixing of the ESO blend and carefully choosing the curing conditions led to more transparent polymers and uncracked samples that were used for further testing.

For EGS blends, due to the terminal oxirane as in DGEBA, EGS may remain part of the DGEBA matrix during curing where a more homogeneous crosslinked structure is formed. An increase in oxirane value in EGS also boosts compatibility with the DGEBA system and may yield cured products with improved properties.

3.4. Crosslink density

Crosslink density is one of the most important factors determining the properties of cured thermoset resins and is typically reported as an average molecular weight (M_c) between crosslinks. The crosslink density increases as M_c decreases. Several methods are available for measuring the crosslink density of a thermoset. A common method is to measure the elastic modulus of the thermoset in the rubbery plateau region using dynamic mechanical analysis (DMA). Solvent swelling measurements are also used to determine the crosslink density of epoxy resin [47, 64, 65]. Good agreement between M_c values from the swelling measurements based on the stoichiometry considerations has been reported [66].

A structure based on a stoichiometric curing condition was assumed because the dominant reaction in the present epoxy-anhydride-imidazole system is esterification while etherification of epoxy groups is much slower [67]. The M_c of the cured resin was calculated from equilibrium solvent swelling data based on the Flory–Rehner equation [47] (Equation (5)):

$$\nu = \frac{\rho_{poly}}{M_c} = \frac{\ln(1 - \nu_2) + \nu_2 + \chi\nu_2}{V_1\left(\frac{\nu_2}{2} - \nu_2^{\frac{1}{3}}\right)} \quad (5)$$

where υ is the strand density, υ_2 is the volume fraction of polymer at equilibrium swelling as measured by swelling test (Equation (1)), V_1 is the molar volume of the solvent, and χ is the polymer-solvent interaction parameter, which is related to the solubility parameters via Equation (6):

$$\chi = 0.34 + \frac{V_1}{RT}(\delta_1 - \delta_2)^2 \quad (6)$$

where R is the gas constant, T is the absolute temperature, V_1 is the molar volume of the solvent, and δ_1 and δ_2 are the solubility parameters of solvent and polymer, respectively. δ_2 was calculated by Equation (3), and where for toluene δ_1 =18.3 $MPa^{1/2}$. The calculated and experimental results are listed in Table 4.

In ESO or EGS, the epoxy crosslink sites in the FA chains are located at the 9th and 10th carbons in the oleic acid and could be also at the 12nd and 13th carbons in linoleic acid, which leave the rest of the chain up through 18th carbon as an ineffective chain end in the crosslinked polymer (Figure 7). Furthermore, the presence of saturated palmitic or stearic acids in ESO triglyceride structure also behave like pendant chain [42], so the inactive parts, *e.g.*, pendant chains and saturated FAs, in ESO and EGS constitute 34.8 and 18% of total mass, respectively. These maybe subtracted from the dry and swollen sample weights to obtain a corrected M_c^*, because

Table 4. Swelling properties of cured epoxy resins in toluene

MHHPA cured samples	δ [$MPa^{1/2}$]	ρ_{poly} [g/mL]	Q Swelling ratio	χ	M_c [g/mol]	M_c^* [g/mol]
Pure DGEBA	19.4	1.18	1.49	0.388	257	257
EGS-DGEBA (10:90)	19.2	1.17	1.50	0.375	253	256
EGS-DGEBA (30:70)	18.9	1.16	1.54	0.356	268	278
EGS-DGEBA (50:50)	18.6	1.16	1.57	0.345	281	299
EGS-DGEBA (70:30)	18.4	1.15	1.61	0.340	304	330
EGS-DGEBA (100:0)	18.0	1.12	1.66	0.344	332	376
ESO-DGEBA (10:90)	19.3	1.17	1.51	0.375	261	267
ESO-DGEBA (30:70)	19.0	1.15	1.55	0.355	273	293
ESO-DGEBA (50:50)	18.6	1.14	1.58	0.343	285	324
ESO-DGEBA (70:30)	18.3	1.12	1.64	0.340	314	382
ESO-DGEBA (100:0)	17.8	1.09	1.84	0.350	464	640

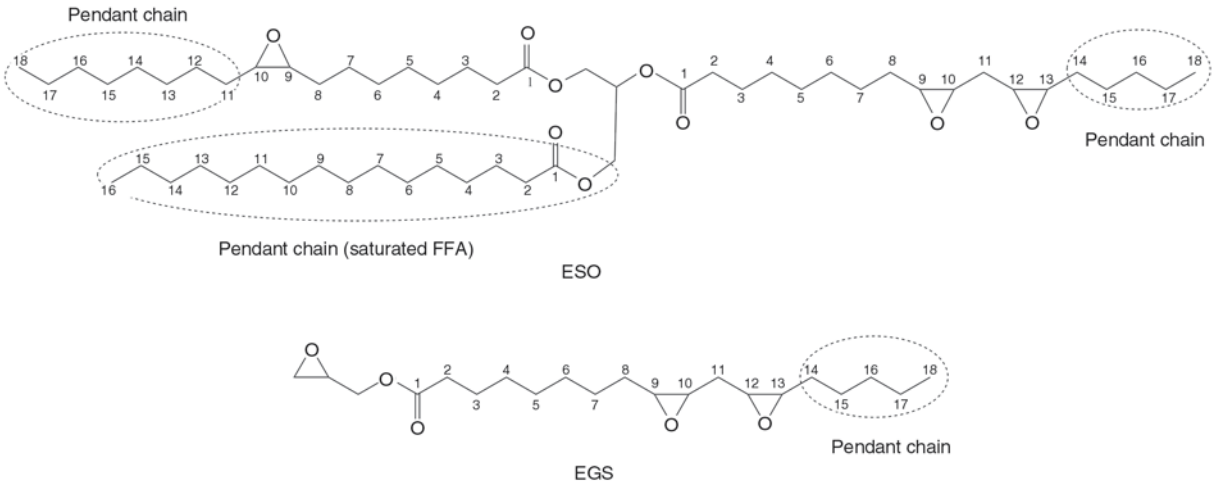

Figure 7. Schematic representation of pendant chain in ESO structure (epoxy moieties in ESO/EGS and methane moiety in glycerol part of ESO are the crosslink sites)

end-linked networks were assumed during swelling test, in fact pendant chains are not contributed to the total crosslink densities [38]. M_c and corrected M_c^* values are listed in Table 4.

From Table 4, the ρ values of both EGS and ESO systems decrease with the increase of EGS/ESO content that can be attributed to the addition of a large soft/flexible vegetable oil component to decrease the rigid, compact structure of DGEBA polymer. Increase in EGS/ESO content also leads to a higher swelling ratio Q, which could indicate not only lower crosslinking density but also a higher solubility of the network in the toluene solvent that is supported by a decreased χ value. M_c and M_c^* values of MHHPA cured neat DGEBA [68] and neat ESO [31] are similar to reported DMA test results. Pure EGS, which has similar oxirane content as ELO, also is close to a reported DMA test result for polymerized ELO [53]. Calculated values based on the van Krevelen model are also comparable to DMA tests.

In general, an increase in ESO or EGS content decreased crosslink density compared to a neat anhydride cured DGEBA. This result is due to the inherently flexible structure of fatty acid chain and thereby prone to form a less compact crosslinked structure compared to the stiffer aromatic repeat unit of DGEBA. A decrease in crosslink density was also reported by others [20].

Crosslink density is also related to the oxirane value. EGS has higher oxirane value than ESO so all EGS blends had higher crosslink densities compared to ESO blends at the same concentration level. Crosslinking density increasing with oxirane value has also been observed within various EVOs of different oxirane content [69] or for the same vegetable oil with different oxirane content [16]. Surprisingly, 10 wt% EGS concentration had a similar crosslink density as pure DGEBA, which is in part probably due to a higher functionality of EGS compared to pure DGEBA. More anhydride needed to cure the blend would lead to higher crosslink densities. With increases in the EGS content in blends, a lower crosslink density was observed though the crosslink density had minimal change even at 50 wt% concentration. ELO has similar epoxy content as EGS and has been reported to maintain nearly constant crosslink density of the anhydride-cured epoxy at up to 70 wt% concentration [70]. For ESO with much lower oxirane value compared to DGEBA or EGS, the crosslink density of ESO blends decreased with increased ESO concentration that is especially noticeable after M_c correction for pendant chains. The saturated component in ESO thus plays a significant role in reducing the crosslink density. Though crosslink density has been reported to not be changed by the replacement of DGEBA by ESO using mechanical analysis of the rubbery plateau [52], an artificially larger modulus can result for the inherently heterogeneous DGEBA–ESO–anhydride network due to a broadened glass transition temperature range. As heterogeneity will broaden the modulus signal in the rubbery region, a shear storage modulus value near the glass transition in the rubbery region can be artificially increased resulting in an inflated value for the calculated crosslink density.

3.5. Thermal properties

The glass transition temperature (T_g) is considered a fundamental polymer characteristic related to polymer properties and processing. In general, polymers with high crosslink density have higher T_g; however, the composition in the polymer within the crosslinked structure also plays an important role in the T_g behavior. DSC and DMA are widely used to characterize T_g. For most thermosetting plastics, the DMA measurement based on the tan δ peak at a frequency of 1 Hz generally occurs at a temperature as much as 15–20°C above T_g as measured by dilatometry or DSC [16, 26] but inflection temperature typically correlate better with DMA tan δ than a midpoint value.

The trend of cured epoxy resin blends (polymers) T_g as measured by DSC is shown in Figure 8. The MHHPA cured pure EGS had higher T_g (88°C) which was nearly 40°C higher than ESO-MHHPA. Pure DGEBA-MHHPA polymers which is aromatic and had the highest T_g measured (152°C). Aliphatic amine [12, 71], or boron trifluoride diethyl etherate [72, 73], cured ESO polymers had low T_g, usually less than 0°C. While aromatic amine [29], cycloaliphatic amine [74], thermally latent initiator [75], or anhydride [76] cured EVO polymers generally have higher T_g, it is still rare to observe cured ESO polymers [31, 77] with T_g above 60°C.

Addition of ESO or EGS led to a decrease of T_g. For small EGS/ESO concentration, *e.g.*, below 30 wt%, the T_g values of ESO-DGEBA or EGS-DGEBA systems were quite similar to each other and slightly decreased compared to pure DGEBA-MHHPA, which indicated the T_g behavior was mainly determined by the crosslink density as measured in the swelling test where only slight increases of M_c or M_c^* were observed. However, the aromatic DGEBA versus aliphatic EGS structure also plays a role because 10 wt% EGS concentration appears to have a slightly higher crosslink density but still a lower T_g. It has been reported that aromatic phthalic anhydride cured EVO had higher T_g but lower crosslink density [31, 53].

For further increases in the concentration of EGS/ESO, the T_g values decreased more rapidly, especially for the ESO system. The inherent, long aliphatic chain structure of ESO, sluggish reactivity of internal oxirane, and lower oxirane content preclude polymer as densely crosslinked as those of EGS or DGEBA. Unreactive saturated components like stearic acid and palmitic acid pendant chains enhance the flexibility and degree of freedom for movements of the molecular chains in the epoxy network. These factors decrease the polymer T_g. Further depressed T_g was also reported for an epoxidized palm oil system, which had lower oxirane content than ESO [26].

At low ESO concentrations ($\leq$50 wt%) a linear, decreasing T_g trend was observed, however, neat ESO or higher ESO concentrations ($\geq$50 wt%) thermosetting polymers showed broad transitions from the glassy to the rubbery state. The blends' T_g seems predominately controlled by the ESO part. Similar behavior was also found in ELO replacement of diglycidyl ether of bisphenol F resin [78]. The plasticizing effect of saturated FAs and/or the different reactivity of ESO and DGEBA leads to a broad distribution of chain segment mobilities [79] and indicate a heterogeneous polymer network [80]. Broad T_g range behavior was not found in the EGS-DGEBA systems. Also a nearly linear transition of T_g with increase of EGS was observed, which indi-

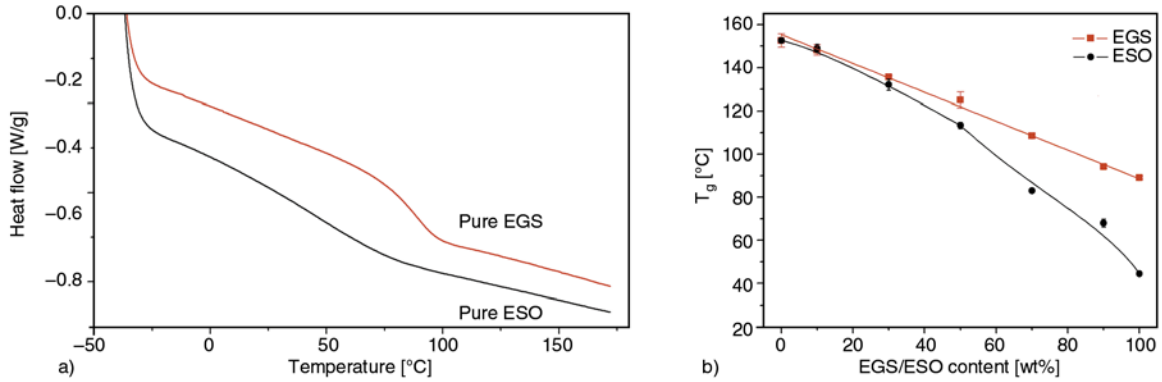

Figure 8. Plots of a) the glass transition region of ESO/EGS-MHHPA neat polymer showing the differences in breadth of the transition; b) the measured inflection point glass transition temperatures of cured epoxy monomer(s) as a function of ESO/EGS-DGEBA blend composition (Lines only to aid visualization of trend)

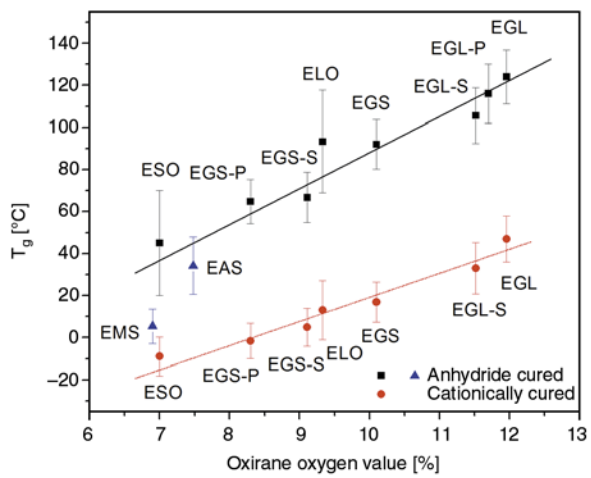

Figure 9. Polymer glass transition temperatures as a function of monomer oxirane contents through cationic homopolymerization and MHHPA copolymerization. [Note: straight lines are to indicate trend; vertical bars indicate the breadth of glass transition region equal to the difference between onset temperature and endset temperature as determined in DSC].

cated good synergy and homogeneity of the crosslink structure formation between EGS and DGEBA.

Researchers [16, 69] have noted the influence of EVO monomer oxirane value on polymer T_g. We present trends in relationship between T_g and EVO structure with and without saturated components. Several epoxy resins made from vegetable oils were synthesized and polymerized by MHHPA with EMI as catalyst and/or cationically polymerized with BF_3-MEA initiation. The obtained plot of polymer T_g as a function of oxirane oxygen value is presented in Figure 9.

The glass transition temperatures of anhydride cured copolymers are higher than those of the neat of cationically cured monomers due to the anhydride structural stiffness elevating the copolymer T_g. The T_g are observed to increase fairly linearly with oxirane value. Higher oxirane values are expected to lead to higher crosslink densities upon curing. A similar T_g for anhydride cured ELO and EGS was observed though ELO has a slightly lower oxirane value. The ELO structure is partially crosslinked, *i.e.*, glycerol crosslinks the three FFAs, and would have a slightly higher oxirane value if converted to the glycidyl structure like EGS. Linseed oil is also richer in linolenic acid content that may facilitate a dense crosslinked structure.

EGS and EGL have much higher T_g compared to their respectively ESO or ELO counterparts. A T_g value of 124°C was measured for EGL, which appears unprecedented for a vegetable oil based thermoset polymer. The T_g increases in EGS-S/EGS-P and EGL-S/EGL-P are mainly due to the addition of the reactive glycidyl group compared to ESO and ELO. Removal of the saturated components greatly increases the T_g. A 30 and 20°C increase in polymer T_g was observed for MHHPA cured EGS and EGL compared to EGS-S and EGL-S, respectively. Such trends are observed in the M_c calculations as a significant increase of crosslink density upon exclusion of the saturated components.

Adding an unreactive function group, *e.g.*, allyl (EAS) or methyl groups (EMS), generates a lower T_g though the oxirane values are similar to that of ESO. Since the allyl group in EAS is partially epoxidized, EAS has even slightly higher oxirane value than ESO. The T_g's are greatly decreased compared to ESO because, unlike ESO that is partially crosslinked through glycerol, transesterification engenders all the fatty acid carbons except carbons in the epoxy groups into pendant chains. In addition, the liberated saturated FFA esters behave as plasticizers in the matrix to increase the chain segment mobility and decrease crosslink density. Monofunctional epoxidized methyl oleate and epoxidized oleic acid have lower oxirane content compared to EMS and were difficult to polymerize by our current curing conditions though polymer T_g of –14 to –50°C have been reported [36, 81].

Broader T_g regions (onset-endset ranges are provided in Figure 9 using bars; NOTE: the vertical bars are not 'error' bars or deviations but indicate the measured temperature range breadth of the glass transition) indicate a broader distribution of chain environments and heterogeneous structures were observed in anhydride cured ELO and ESO. We ascribe the less homogenous polymer structures to a low reactivity of internal oxirane in ELO or ESO instead of saturated components because even EGS-S and EGL-S with saturated FFAs show relatively sharp glass transition ranges. Indeed, internal epoxy is more reactive in cationic polymerization where all epoxies show a similar transition breadth when initiated by BF_3-MEA. EMS of all internal oxirane structure and saturated FFA also show a narrow glass transition region, which could be due

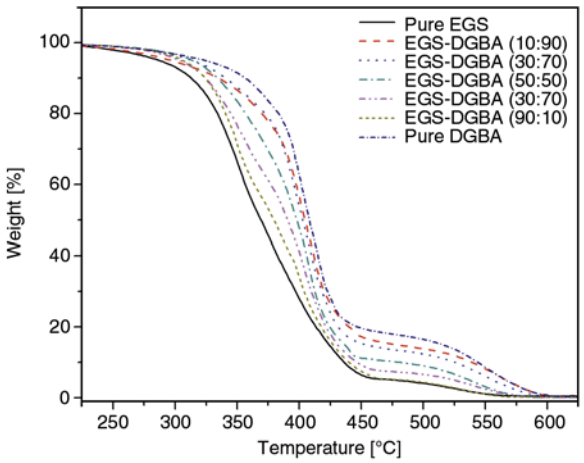

Figure 10. TGA of MHHPA cured EGS-DGEBA blends compared to pure EGS and pure DGEBA

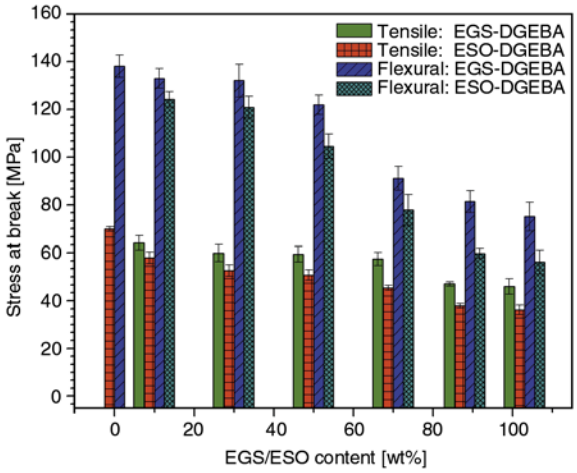

Figure 11. Tensile and flexural strengths of MHHPA and EGS/ESO-DGEBA blend copolymerization products

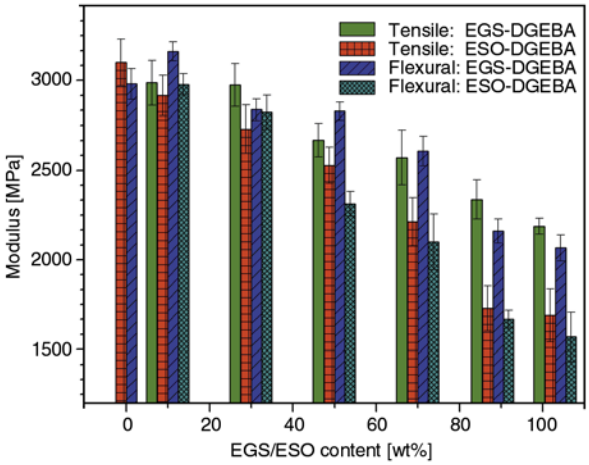

Figure 12. Tensile and flexural moduli of MHHPA and EGS/ESO-DGEBA blends copolymerization products

to greater reactivity of the small molecules during curing compared to large oligomers of ESO or ELO [37].

Figure 10 presents the TGA weigh loss as a function of temperature curves for the polymerized epoxy resin. Since the ESO-DGEBA blend had a similar thermal stability as the EGS-DGEBA blend, only the latter is shown here. TGA results indicated all cured EGS-DGEBA resins appear thermally stable to temperatures at least 300°C. Replacements of DGEBA by EGS led to an earlier onset of degradation. All epoxies presented two stage degradation behavior. The first stage of decomposition from 300 to 450°C is believed to be due to decomposition of unreacted MHHPA, dehydration of hydroxyl groups, and the pyrolysis of the crosslinked epoxy resin network. The second stage loss from ~450 to 600°C was considered to be the complete decomposition of the smaller fragments like cyclized or aromatic degradation byproducts as indicated by the decrease of char residue when EGS component was increased.

3.6. Mechanical performance

Flexural and tensile properties of the polymerized resin systems as a function of ESO/EGS content were determined. The results are shown in Figures 11 and 12. Smaller concentrations of EGS led to only minor changes in strength or modulus compared to neat DGEBA. An improvement in flexural modulus was observed for 10 wt% EGS. Similar results, showing improved modulus at low replacement concentrations, have also been reported for an amine cured, soy-based epoxy resin system [35]. These data correlate with minor changes of M_c calculated at low concentrations of EGS/ESO in DGEBA system blends.

However, the modulus and strength values of the blends systematically decreased with further increases in ESO/EGS concentration. These phenomena are readily explained by a decrease of stiffer, bulky aromatic group content and a decreased crosslinking density of the cured blends. All the EGS-DGEBA blends showed higher strength and modulus than the ESO-DGEBA blends of comparable concentration, which is supported by smaller M_c or M_c^* of EGS compared to ESO. The flexural stress and modulus of EGS-DGEBA exhibited a gradual decrease until 50 wt% followed by a more abrupt change. For ESO-DGEBA, large materials property losses occurred at ≥30 wt%. The study of ref [35] studied compositions only up to 30 wt% soy epoxy resin. Similarly, the tensile strength of EGS-DGEBA

had only minor changes up to 70 wt% concentration whereas a continuous decrease in strength was observed for ESO-DGEBA blends. As observed in Figures 4 and 6, EGS was observed to be more reactive and compatible with DGEBA and a higher content of EGS was achieved with greater homogeneity than comparable ESO blends and greater mechanical strengths.

3.7. Viscosity reducing ability

Reactive diluents are used for reducing and controlling the viscosity of epoxy resins to improve wetting and handling characteristics because in the liquid-molding technologies like resin transfer molding or pultrusion, the viscosity and resin flow are critical to achieving a quality laminate [82]. Recent trends toward lower volatile organic compounds (VOC), higher solids epoxy formulations have also resulted in increased utilization of reactive diluents [83]. It was found that EGS had inherently lower viscosity than ESO. EGS has an extra glycidyl group and lower molecular weight compared to ESO, which is a triglyceride and has oligomeric behavior. The viscosity reducing abilities of EGS and ESO were compared at different concentrations of replacement of the DGEBA resin, which had a relatively high viscosity of 13 000 mPa·s (see Figure 13). ESO and EGS have different miscibility with DGEBA resin; however, EGS exhibited a much better viscosity reducing efficiency than ESO. A 30 wt% concentration of EGS reduced the DGEBA resin viscosity to value below 1000 mPa·s, which is indispensable for many applications. At least 50 wt% of ESO was needed to reduce DGEBA resin to 1000 mPa·s viscosity.

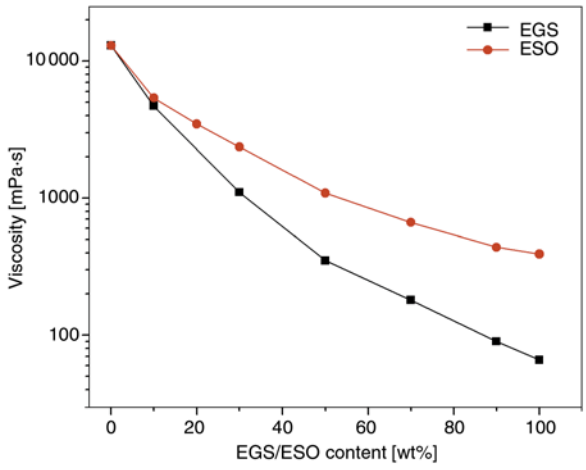

Figure 13. Viscosity of DGEBA blended with various EGS or ESO concentrations

4. Conclusions

Bio-based epoxy resins, glycidyl ester of epoxidized fatty acids, were produced from soybean or linseed oils with a reduced saturated FFA fraction content. The products were characterized and showed high oxirane contents that were more reactive than ESO or ELO, which was shown to directly impact polymer homogeneity and glass transition temperature. Epoxy monomers from other vegetable oil sources such as canola, palm, corn, *etc*., could be fabricated in similar fashion and have similar properties and curing behaviors providing that saturated fatty ester chains are similarly removed.

The vegetable oil based epoxy resins displayed glass transitions that appear to be mostly a function of oxirane content but with additional influences of glycidyl versus internal oxirane reactivity, pendant chain content, and chemical structure and presence of saturated components. Generally, higher oxirane contents (epoxy functionality) lead to higher glass transition temperatures whereas reduced epoxy functionality, non-glycidyl FFA esters, and greater pendant chain contents lead to lower glass transition temperatures. In blends with DGEBA, monomers with only less reactive internal epoxies led to a more heterogeneous polymer structure compared to monomers possessing the more reactive glycidyl group and improved polymer homogeneity, in cure and structure. The inherent, long chain aliphatic structure of these thermoset monomers limits polymer glass transition temperatures compared to commercial, aromatic based epoxy monomers (DGEBA) but our data provide a clear trend and role of oxirane content.

The EGS blends with DGEBA were cured by MHHPA and their thermosetting polymer T_g's measured in comparison to control ESO blends with DGEBA, which were polymerized in similar fashion. The EGS polymers displayed improved T_g's and mechanical properties compared to their ESO counterparts and, in addition to an inherently low viscosity and efficient viscosity reduction, should therefore be more attractive as a reactive diluent. For instance, EGS derived from renewable sources could further enable defect-free fabrication of complex, shaped epoxy composites for structural com-

posite applications. Our data show ESO produced less homogeneous polymers when blended with DGEBA epoxy that resulted in thermal cure, thermal property, and mechanically inferior materials compared to the more compatible EGS epoxy resin and blends. The compatibility and superior properties arise from the removal of saturated pendant chains, addition of the glycidyl structure, and larger internal oxirane content inherent of EGS.

Acknowledgements

Portions of this paper were presented at the 2011 Thermoset Resin Formulators Association annual meeting and at the 2012 American Oil Chemists' Society Annual Meeting & Expo. Authors would like to thank Pranita Nayak and Dr. Rama Vuppalapati for assistance in resin synthesis and mechanical testing and acknowledge facilities and equipment support provided through the Missouri S&T Materials Research Center.

Abbreviations

DGEBA	diglycidyl ether of bisphenol A
EAS	epoxidized allyl ester of soybean oil
EMI	2-ethyl-4-methylimidazole
EMS	epoxidized methyl ester of soybean oil
EPCH	epichlorohydrin
EGL	glycidyl esters of epoxidized fatty acids derived from linseed oil
EGL-P	EGL with partially epoxidized fatty acids
EGL-S	EGL included saturated fatty acids
EGS	glycidyl esters of epoxidized fatty acids derived from soybean oil
EGS-P	EGS with partially epoxidized fatty acids
EGS-S	EGS with saturated fatty acids
ELO	epoxidized linseed oil
ESO	epoxidized soybean oil
EVO	epoxidized vegetable oils
FA	fatty acid
FFA	free fatty acid
MCPBA	meta-chloroperoxybenzoic acid
MHHPA	4-methyl-1,2-cyclohexanedicarboxylic anhydride

References

[1] Raquez J-M., Deléglise M., Lacrampe M-F., Krawczak P.: Thermosetting (bio)materials derived from renewable resources: A critical review. Progress in Polymer Science, **35**, 487–509 (2010). DOI: 10.1016/j.progpolymsci.2010.01.001

[2] Gandini A.: Polymers from renewable resources: A challenge for the future of macromolecular materials. Macromolecules, **41**, 9491–9504 (2008). DOI: 10.1021/ma801735u

[3] Sharma V., Kundu P. P.: Addition polymers from natural oils – A review. Progress in Polymer Science, **31**, 983–1008 (2006). DOI: 10.1016/j.progpolymsci.2006.09.003

[4] Pfister D. P., Xia Y., Larock R. C.: Recent advances in vegetable oil-based polyurethanes. ChemSusChem, **4**, 703–717 (2011). DOI: 10.1002/cssc.201000378

[5] United Soybean Board: A survey of recent chemical price trends: The potential impact of rising petrochemical prices on soy use for industrial applications. Omni Tech International Ltd. (2010).

[6] Petrović Z. S.: Polyurethanes from vegetable oils. Polymer Reviews, **48**, 109–155 (2008). DOI: 10.1080/15583720701834224

[7] Xia Y., Larock R. C.: Vegetable oil-based polymeric materials: Synthesis, properties, and applications. Green Chemistry, **12**, 1893–1909 (2010). DOI: 10.1039/C0GC00264J

[8] Lu J., Khot S., Wool R. P.: New sheet molding compound resins from soybean oil. I. Synthesis and characterization. Polymer, **46**, 71–80 (2005). DOI: 10.1016/j.polymer.2004.10.060

[9] Campanella A., La Scala J. J., Wool R. P.: Fatty acid-based comonomers as styrene replacements in soybean and castor oil-based thermosetting polymers. Journal of Applied Polymer Science, **119**, 1000–1010 (2011). DOI: 10.1002/app.32810

[10] Luo Q., Liu M., Xu Y., Ionescu M., Petrović Z. S.: Thermosetting allyl resins derived from soybean oil. Macromolecules, **44**, 7149–7157 (2011). DOI: 10.1021/ma201366e

[11] Lligadas G., Ronda J. C., Galià M., Cádiz V.: Plant oils as platform chemicals for polyurethane synthesis: Current state-of-the-art. Biomacromolecules, **11**, 2825–2835 (2010). DOI: 10.1021/bm100839x

[12] Xu J., Liu Z., Erhan S., Carriere C. J.: Cross-linkers control the viscoelastic properties of soybean oil-based biomaterials. Journal of the American Oil Chemists' Society, **81**, 813–816 (2004). DOI: 10.1007/s11746-004-0984-6

[13] May C. A.: Epoxy resins chemistry and technology. Marcel Dekker, New York (1988).

[14] Raghavachar R., Sarnecki G., Baghdachi J., Massingill J.: Cationic, thermally cured coatings using epoxidized soybean oil. Journal of Coatings Technology, **72**, 125–133 (2000). DOI: 10.1007/bf02733784

[15] Chandrashekhara K., Sundararaman S., Flanigan V., Kapila S.: Affordable composites using renewable materials. Materials Science and Engineering: A, **412**, 2–6 (2005). DOI: 10.1016/j.msea.2005.08.066

[16] Tanrattanakul V., Saithai P.: Mechanical properties of bioplastics and bioplastic–organoclay nanocomposites prepared from epoxidized soybean oil with different epoxide contents. Journal of Applied Polymer Science, **114**, 3057–3067 (2009).
DOI: 10.1002/app.30842

[17] Liu Z., Erhan S. Z., Akin D. E., Barton F. E.: 'Green' composites from renewable resources: Preparation of epoxidized soybean oil and flax fiber composites. Journal of Agricultural and Food Chemistry, **54**, 2134–2137 (2006).
DOI: 10.1021/jf0526745

[18] Stevens M. P.: Polymer chemistry: An introduction. Oxford University Press, New York (1999).

[19] Adamson M. J.: Thermal expansion and swelling of cured epoxy resin used in graphite/epoxy composite materials. Journal of Materials Science, **15**, 1736–1745 (1980).
DOI: 10.1007/bf00550593

[20] Gupta A. P., Ahmad S., Dev A.: Modification of novel bio-based resin-epoxidized soybean oil by conventional epoxy resin. Polymer Engineering and Science, **51**, 1087–1091 (2011).
DOI: 10.1002/pen.21791

[21] Gelb L., Ault W., Palm W., Witnauer L., Port W.: Epoxy resins from fats. III. Preparation and properties of resins from blends of a commercial diglycidyl ether and epoxidized glycerides cured with phthalic anhydride. Journal of the American Oil Chemists' Society, **37**, 81–84 (1960).
DOI: 10.1007/bf02667729

[22] Czub P.: Characterization of an epoxy resin modified with natural oil-based reactive diluents. Macromolecular Symposia, **245–246**, 533–538 (2006).
DOI: 10.1002/masy.200651377

[23] Kar S., Banthia A. K.: Epoxy resin modified with epoxidized soybean rubber. Materials and Manufacturing Processes, **19**, 459–474 (2004).
DOI: 10.1081/AMP-120038655

[24] Miyagawa H., Misra M., Drzal L. T., Mohanty A. K.: Fracture toughness and impact strength of anhydride-cured biobased epoxy. Polymer Engineering and Science, **45**, 487–495 (2005).
DOI: 10.1002/pen.20290

[25] Jin F-L., Park S-J.: Impact-strength improvement of epoxy resins reinforced with a biodegradable polymer. Materials Science and Engineering: A, **478**, 402–405 (2008).
DOI: 10.1016/j.msea.2007.05.053

[26] Tan S. G., Chow W. S.: Thermal properties of anhydride-cured bio-based epoxy blends. Journal of Thermal Analysis and Calorimetry, **101**, 1051–1058 (2010).
DOI: 10.1007/s10973-010-0751-7

[27] Thulasiraman V., Rakesh S., Sarojadevi M.: Synthesis and characterization of chlorinated soy oil based epoxy resin/glass fiber composites. Polymer Composites, **30**, 49–58 (2008).
DOI: 10.1002/pc.20532

[28] Lligadas G., Ronda J. C., Galià M., Cádiz V.: Development of novel phosphorus-containing epoxy resins from renewable resources. Journal of Polymer Science Part A: Polymer Chemistry, **44**, 6717–6727 (2006).
DOI: 10.1002/pola.21794

[29] Earls J. D., White J. E., López L. C., Lysenko Z., Dettloff M. L., Null M. J.: Amine-cured ω-epoxy fatty acid triglycerides: Fundamental structure–property relationships. Polymer, **48**, 712–719 (2007).
DOI: 10.1016/j.polymer.2006.11.060

[30] Pan X., Sengupta P., Webster D. C.: High biobased content epoxy–anhydride thermosets from epoxidized sucrose esters of fatty acids. Biomacromolecules, **12**, 2416–2428 (2011).
DOI: 10.1021/bm200549c

[31] Gerbase A. E., Petzhold C. L., Costa A. P. O.: Dynamic mechanical and thermal behavior of epoxy resins based on soybean oil. Journal of the American Oil Chemists' Society, **79**, 797–802 (2002).
DOI: 10.1007/s11746-002-0561-z

[32] La Scala J., Wool R. P.: Property analysis of triglyceride-based thermosets. Polymer, **46**, 61–69 (2005).
DOI: 10.1016/j.polymer.2004.11.002

[33] Meier M. A. R., Metzger J. O., Schubert U. S.: Plant oil renewable resources as green alternatives in polymer science. Chemical Society Reviews, **36**, 1788–1802 (2007).
DOI: 10.1039/B703294C

[34] Nicolau A., Mariath R. M., Martini E. A., dos Santos Martini D., Samios D.: The polymerization products of epoxidized oleic acid and epoxidized methyl oleate with cis-1,2-cyclohexanedicarboxylic anhydride and triethylamine as the initiator: Chemical structures, thermal and electrical properties. Materials Science and Engineering: C, **30**, 951–962 (2010).
DOI: 10.1016/j.msec.2010.04.014

[35] Zhu J., Chandrashekhara K., Flanigan V., Kapila S.: Curing and mechanical characterization of a soy-based epoxy resin system. Journal of Applied Polymer Science, **91**, 3513–3518 (2004).
DOI: 10.1002/app.13571

[36] Reiznautt Q. B., Garcia I. T. S., Samios D.: Oligoesters and polyesters produced by the curing of sunflower oil epoxidized biodiesel with cis-cyclohexane dicarboxylic anhydride: Synthesis and characterization. Materials Science and Engineering: C, **29**, 2302–2311 (2009).
DOI: 10.1016/j.msec.2009.05.021

[37] dos Santos Martini D., Braga B. A., Samios D.: On the curing of linseed oil epoxidized methyl esters with different cyclic dicarboxylic anhydrides. Polymer, **50**, 2919–2925 (2009).
DOI: 10.1016/j.polymer.2009.03.058

[38] Petrović Z. S., Guo A., Zhang W.: Structure and properties of polyurethanes based on halogenated and non-halogenated soy–polyols. Journal of Polymer Science Part A: Polymer, **38**, 4062–4069 (2000). DOI: 10.1002/1099-0518(20001115)38:22<4062::aid-pola60>3.0.co;2-l

[39] Pan X., Sengupta P., Webster D. C.: Novel biobased epoxy compounds: Epoxidized sucrose esters of fatty acids. Green Chemistry, **13**, 965–975 (2011). DOI: 10.1039/C0GC00882F

[40] Zong Z., Soucek M. D., Liu Y., Hu J.: Cationic photopolymerization of epoxynorbornane linseed oils: The effect of diluents. Journal of Polymer Science Part A: Polymer Chemistry, **41**, 3440–3456 (2003). DOI: 10.1002/pola.10942

[41] Zou K., Soucek M. D.: UV-curable cycloaliphatic epoxide based on modified linseed oil: Synthesis, characterization and kinetics. Macromolecular Chemistry and Physics, **206**, 967–975 (2005). DOI: 10.1002/macp.200400390

[42] Tan S. G., Chow W. S.: Thermal properties, curing characteristics and water absorption of soybean oil-based thermoset. Express Polymer Letters, **5**, 480–492 (2011). DOI: 10.3144/expresspolymlett.2011.47

[43] Petrović Z. S., Zhang W., Javni I.: Structure and properties of polyurethanes prepared from triglyceride polyols by ozonolysis. Biomacromolecules, **6**, 713–719 (2005). DOI: 10.1021/bm049451s

[44] Kiatsimkul P-P., Suppes G. J., Sutterlin W. R.: Production of new soy-based polyols by enzyme hydrolysis of bodied soybean oil. Industrial Crops and Products, **25**, 202–209 (2007). DOI: 10.1016/j.indcrop.2006.10.001

[45] Vázquez L., Akoh C. C.: Concentration of stearidonic acid in free fatty acid and fatty acid ethyl ester forms from modified soybean oil by winterization. Journal of the American Oil Chemists' Society, **88**, 1775–1785 (2011). DOI: 10.1007/s11746-011-1857-1

[46] Sharma V., Kundu P. P.: Condensation polymers from natural oils. Progress in Polymer Science, **33**, 1199–1215 (2008). DOI: 10.1016/j.progpolymsci.2008.07.004

[47] Chen J-S., Ober C. K., Poliks M. D., Zhang Y., Wiesner U., Cohen C.: Controlled degradation of epoxy networks: Analysis of crosslink density and glass transition temperature changes in thermally reworkable thermosets. Polymer, **45**, 1939–1950 (2004). DOI: 10.1016/j.polymer.2004.01.011

[48] Brown J. B.: Low-temperature crystallization of the fatty acids and glycerides. Chemical Reviews, **29**, 333–354 (1941). DOI: 10.1021/cr60093a009

[49] Brown J. B., Stoner G. G.: Studies on the chemistry of the fatty acids. I. The purification of linoleic acid by crystallization methods. Journal of the American Chemical Society, **59**, 3–6 (1937). DOI: 10.1021/ja01280a002

[50] Maerker G., Saggese E., Port W.: Glycidyl esters. II. Synthesis of esters of commercial and pure fatty acids. Journal of the American Oil Chemists' Society, **38**, 194–197 (1961). DOI: 10.1007/bf02633229

[51] Kester E. B., Gaiser C. J., Lazar M. E.: Glycidyl esters of aliphatic acids. The Journal of Organic Chemistry, **8**, 550–556 (1943). DOI: 10.1021/jo01194a010

[52] Altuna F. I., Espósito L. H., Ruseckaite R. A., Stefani P. M.: Thermal and mechanical properties of anhydride-cured epoxy resins with different contents of biobased epoxidized soybean oil. Journal of Applied Polymer Science, **120**, 789–798 (2011). DOI: 10.1002/app.33097

[53] Boquillon N., Fringant C.: Polymer networks derived from curing of epoxidised linseed oil: Influence of different catalysts and anhydride hardeners. Polymer, **41**, 8603–8613 (2000). DOI: 10.1016/s0032-3861(00)00256-1

[54] Ratna D.: Handbook of thermoset resins. Rapra, Shropshire (2009).

[55] Brandrup J., Immergut E. H., Grulke E. A., Abe A., Bloch D. R.: Polymer handbook. Wiley, New York (2005).

[56] Barton A. F. M.: Handbook of solubility parameters and other cohesion parameters. CRC Press, Boca Raton (1983).

[57] Van Krevelen D. W.: Properties of polymers. Elsevier, Amsterdam (1990).

[58] Jackson P. L., Huglin M. B., Cervenka A.: Use of inverse gas chromatography to quantify interactions in anhydride cured epoxy resins. Polymer International, **35**, 135–143 (1994). DOI: 10.1002/pi.1994.210350203

[59] Park S-J., Jin F-L., Lee J-R.: Thermal and mechanical properties of tetrafunctional epoxy resin toughened with epoxidized soybean oil. Materials Science and Engineering: A, **374**, 109–114 (2004). DOI: 10.1016/j.msea.2004.01.002

[60] Frischinger I., Dirlikov S.: Two-phase interpenetrating epoxy thermosets that contain epoxidized triglyceride oils. Part I. Phase separation. in 'Interpenetrating polymer networks' (Klempner D., Sperling L. H., Utracki L. A.) American Chemical Society, Washington, Vol 239, 517–538 (1994). DOI: 10.1021/ba-1994-0239.ch025

[61] Robeson L. M.: Polymer blends: A comprehensive review. Hanser, Cincinnati (2007).

[62] Ratna D., Banthia A. K.: Rubber toughened epoxy. Macromolecular Research, **12**, 11–21 (2004). DOI: 10.1007/bf03218989

[63] Harsch M., Karger-Kocsis J., Herzog F., Fejős M.: Effect of cure regime on internal strain and stress development in a filled epoxy resin assessed by fiber Bragg-grating optical strain and normal force measurements. Journal of Reinforced Plastics and Composites, **30**, 1417–1427 (2011).
DOI: 10.1177/0731684411413625

[64] Bell J. P.: Structure of a typical amine-cured epoxy resin. Journal of Polymer Science Part A-2: Polymer Physics, **8**, 417–436 (1970).
DOI: 10.1002/pol.1970.160080308

[65] Bellenger V., Morel E., Verdu J.: Solubility parameters of amine-crosslinked aromatic epoxies. Journal of Applied Polymer Science, **37**, 2563–2576 (1989).
DOI: 10.1002/app.1989.070370909

[66] Kwei T. K.: Swelling of highly crosslinked network structure. Journal of Polymer Science Part A: General Papers, **1**, 2977–2988 (1963).
DOI: 10.1002/pol.1963.100010918

[67] Mahendran A. R., Wuzella G., Kandelbauer A., Aust N.: Thermal cure kinetics of epoxidized linseed oil with anhydride hardener. Journal of Thermal Analysis and Calorimetry, **107**, 989–998 (2012).
DOI: 10.1007/s10973-011-1585-7

[68] Gao J., Li J., Benicewicz B. C., Zhao S., Hillborg H., Schadler L. S.: The mechanical properties of epoxy composites filled with rubbery copolymer grafted SiO_2. Polymers, **4**, 187–210 (2012).
DOI: 10.3390/polym4010187

[69] Kim J. R., Sharma S.: The development and comparison of bio-thermoset plastics from epoxidized plant oils. Industrial Crops and Products, **36**, 485–499 (2012).
DOI: 10.1016/j.indcrop.2011.10.036

[70] Miyagawa H., Mohanty A. K., Misra M., Drzal L. T.: Thermo-physical and impact properties of epoxy containing epoxidized linseed oil, 2. Macromolecular Materials and Engineering, **289**, 636–641 (2004).
DOI: 10.1002/mame.200400003

[71] Lu P.: Curing chemistry of epoxidized soybean oil and its application for structural composite materials, PhD Thesis, University of Missouri-Rolla, Rolla (2001).

[72] Liu Z., Doll K. M., Holser R. A.: Boron trifluoride catalyzed ring-opening polymerization of epoxidized soybean oil in liquid carbon dioxide. Green Chemistry, **11**, 1774–1789 (2009).
DOI: 10.1039/B915742P

[73] Liu Z., Erhan S. Z.: Ring-opening polymerization of epoxidized soybean oil. Journal of the American Oil Chemists' Society, **87**, 437–444 (2009).
DOI: 10.1007/s11746-009-1514-0

[74] Czub P.: Application of modified natural oils as reactive diluents for epoxy resins. Macromolecular Symposia, **242**, 60–64 (2006).
DOI: 10.1002/masy.200651010

[75] Park S-J., Jin F-L., Lee J-R.: Synthesis and thermal properties of epoxidized vegetable oil. Macromolecular Rapid Communications, **25**, 724–727 (2004).
DOI: 10.1002/marc.200300191

[76] Gelb L. L., Ault W. C., Palm W. E., Witnauer L. P., Port W. S.: Epoxy resins from fats. I. Epoxidized glycerides cured with phthalic anhydride. Journal of the American Oil Chemists' Society, **36**, 283–286 (1959).
DOI: 10.1007/bf02639997

[77] Tan S. G., Chow W. S.: Biobased epoxidized vegetable oils and its greener epoxy blends: A review. Polymer-Plastics Technology and Engineering, **49**, 1581–1590 (2010).
DOI: 10.1080/03602559.2010.512338

[78] Miyagawa H., Mohanty A. K., Misra M., Drzal L. T.: Thermo-physical and impact properties of epoxy containing epoxidized linseed oil, 1. Macromolecular Materials and Engineering, **289**, 629–635 (2004).
DOI: 10.1002/mame.200400004

[79] Tan S., Chow W. J.: Curing characteristics and thermal properties of epoxidized soybean oil based thermosetting resin. Journal of the American Oil Chemists' Society, **88**, 915–923 (2011).
DOI: 10.1007/s11746-010-1748-x

[80] Miyagawa H., Misra M., Drzal L. T., Mohanty A. K.: Biobased epoxy/layered silicate nanocomposites: Thermophysical properties and fracture behavior evaluation. Journal of Polymers and the Environment, **13**, 87–96 (2005).
DOI: 10.1007/s10924-005-2940-1

[81] Nicolau A., Samios D., Piatnick C. M. S., Reiznautt Q. B., Martini D. D., Chagas A. L.: On the polymerisation of the epoxidised biodiesel: The importance of the epoxy rings position, the process and the products. European Polymer Journal, **48**, 1266–1278 (2012).
DOI: 10.1016/j.eurpolymj.2012.04.013

[82] Varley R. J., Tian W.: Toughening of an epoxy anhydride resin system using an epoxidized hyperbranched polymer. Polymer International, **53**, 69–77 (2004).
DOI: 10.1002/pi.1324

[83] Mark H. F.: Encyclopedia of polymer science and technology. Wiley-Interscience, New York (2004).

eXPRESS Polymer Letters Vol.7, No.3 (2013) 293–303
Available online at www.expresspolymlett.com
DOI: 10.3144/expresspolymlett.2013.26

Enhancement of interfacial fracture toughness of carbon/epoxy composite adhesive joints by in-mold surface preparation

Y. Hikosaka[1], *R. Matsuzaki*[2*], *A. Todoroki*[1], *Y. Mizutani*[1]

[1]Department of Mechanical Sciences and Engineering, Tokyo Institute of Technology, 2-12-1-I1-58, O-okayama, Meguro, 152-8552 Tokyo, Japan
[2]Department of Mechanical Engineering, Tokyo University of Science, 2641 Yamazaki, Noda, 278-8510 Chiba, Japan

Received 16 September 2012; accepted in revised form 19 November 2012

Abstract. To reduce secondary processing such as sanding or chemical etching in the manufacture of composite structures, we present an in-mold surface preparation process using imprint lithography on carbon/epoxy composite adhesive joints. In the proposed in-mold process, microstructures are designed and fabricated on the surface of the mold to form composites. Through the formation of composites on the mold at an appropriate temperature and pressure, the shapes of the microstructures are imprinted onto the surface of the composite. Because molding and surface preparation can be performed simultaneously, the time and costs required are reduced compared to conventional surface preparations. In this paper, concavo-convex microstructures were fabricated on the surface of carbon/epoxy composites using in-mold surface preparation, which improved the apparent mode I fracture toughness of the composite/adhesive interface. From double-cantilever-beam tests, we confirmed that as the aspect ratio of the concavo-convex microstructures increased, the steady-state fracture toughness increased by up to 113% compared to structures without in-mold surface preparation, and the fracture mode changed from interfacial failure to complex cohesive adhesive failure.

Keywords: *polymer composites, processing technologies, adhesion, in-mold surface preparation, imprint lithography*

1. Introduction

The use of composite materials such as carbon-fiber reinforced plastics (CFRPs) within the automotive industry is increasing. In these mass-production industries, composite structures need to be efficiently manufactured [1]. The efficiency with which composite structures can be produced depends on the molding process and secondary fabrication processes such as trimming or surface preparation. Short-cycle resin transfer molding (RTM), which enables the formation of CFRPs in only 10 min, has been developed for the mass production of CFRP parts [2]. This short-cycle RTM was made possible by the development of rapid-cure resin and the rapid-impregnation method.

Secondary fabrication processes that involve conventional surface preparations such as sanding, sand blasting, plasma treatment, or chemical etching, are too time consuming to be applicable to mass production, especially for the production of large-scale structures. Furthermore, workers who are not properly protected may be exposed to carbon particulates suspended in the air or to the harmful chemicals used in surface-preparation processes [3]. To improve the production of CFRP structures, it is essential to reduce the number of secondary fabrication process.

*Corresponding author, e-mail: rmatsuza@rs.tus.ac.jp

Thus, we have proposed an in-mold surface preparation process using imprint lithography to produce bonded butt joints [4]. Imprint lithography was first proposed as nanoimprint lithography (NIL) by Chou and coworkers [5–6]. In this process, nanometer-scale structures on a mold are pressed onto melted polymeric material at appropriate temperature and pressure and the shape of nanostructures is transferred to the surface of the polymer. Because the nanostructures can be easily fabricated at low cost and with high throughput and resolution, the process has been applied in the semiconductor device industry to, for example, produce nanometer-scale metal–oxide–semiconductor field-effect transistors [7], a nanofluidic chip for DNA stretching [8], and optofluidics for environmental monitoring applications [9]. In our previous study [4], we performed the in-mold surface preparation of composite materials with imprint lithography using a silicon wafer as a mold; the surface of the wafer was photo-lithographically fabricated with the designed microstructures. This imprint technique can be used to imprint the shape of microstructures onto the surface and obtain an adherent surface for adhesive joining without the need for harmful sanding or sand blasting. Because the formation of composites and surface preparation can be performed simultaneously, this technique is faster and less expensive than conventional surface treatments. We fabricated pyramidal microstructures using in-mold surface preparation and experimentally determined the effect of the process on the tensile bonding strength of butt joints. The tensile strength of butt joints was found to be 67% higher than that of untreated joints. Although it has been reported that interfacial properties such as interfacial strength and fracture toughness are highly dependent on the surface topography of adherends, the effect of the shape and size of the microstructures created by in-mold surface preparation on the joint strength has not been studied [10–19]. Moreover, the resistance to crack propagation at the imprinted interface has not been investigated, although the fracture of bonded joints is likely to be caused by crack initiation and propagation at this interface.

Therefore, the present study investigated the effect of the shape of imprinted microstructures on the steady-state mode I fracture toughness of the CFRP/adhesive interface, with the goal of controlling the interfacial properties of composites by appropriately designing and fabricating microstructures on the mold surface. The concavo-convex microstructures were fabricated on the CFRP surface and the effect of the shape of the microstructures on the mode I fracture toughness was investigated using double-cantilever-beam (DCB) tests. Crack propagation behavior was also investigated with in situ microscopic observations.

2. In-mold surface preparation using imprint lithography

2.1. Concavo-convex microstructures

The driving forces of two-dimensional (2D) crack propagation are divided into mode I forces, which open a crack perpendicular to the crack surface, and mode II forces, which open the crack parallel to the surface. Generally, the fracture toughness is a measure of not only the energy required for surface generation but also the energy required for plastic deformation or to overcome friction during crack growth. The latter energy is called dissipation energy, and the dissipation energy of mode II is usually higher than that of mode I [20]. From the above observation, a concavo-convex shape, as shown in Figure 1, was selected for microstructures to improve the apparent mode I fracture toughness G_{IA} of an adhesive joint; G_{IA} indicates the resistance to macroscopic crack propagation when the macroscopic mode I load is applied to the CFRP/adhesive interface. In this calculation of the apparent fracture toughness, the concavo-convex microstructures are assumed to be a flat interface. It is also noted that this G_{IA} contains a microscopic mode II component as well as a microscopic mode I component. Here, the shape of concavo-convex microstructures is characterized by the aspect ratio given by Equation (1):

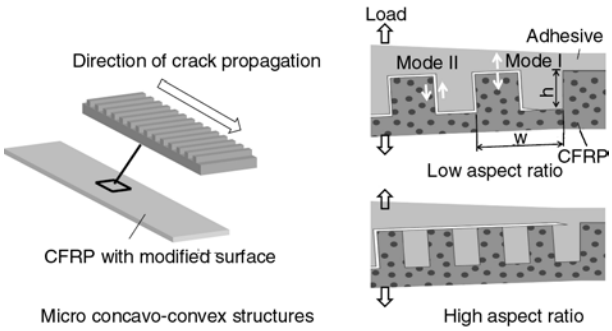

Figure 1. Schematic of concavo-convex microstructures and the fracture mode transition as the aspect ratio A is changed

$$A = \frac{h}{w} \tag{1}$$

where w is the summation of the widths of one convexity and one concavity and h is the height (see Figure 1). Note that $A = 0$ indicates a flat surface without concavo-convex microstructures.

Because the fracture toughness of cohesive failure is usually higher than that of interfacial failure [16], a crack may propagate along the interface of concave-convex microstructures. In this fracture mode, the actual length of microscopic cracks increases near concave-convex microstructures and mode II interfacial failure also occurs at the lateral faces of the microstructures. Because the mode II fracture toughness is usually higher than that of mode I in practical adhesion, higher energy is required for crack propagation. Thus, the crack resistance may increase as a result. As the aspect ratio of the concavo-convex microstructures becomes high enough, as shown in Figure 1, cohesive failure inside the adhesive or CFRP may occur, accompanied by interfacial failure. The fracture toughness of this fracture mode is not affected by the interfacial property but is influenced by the fracture toughness of the adhesive or of CFRP; thus, this mode is preferable for the realization of stable bonding. Because the ratio of the mode II fracture region increases in proportion to the aspect ratio of the concavo-convex microstructures, we evaluated the fracture toughness by changing this ratio.

2.2. Process of in-mold surface preparation

Concavo-convex microstructures were fabricated on the CFRP surface by in-mold surface preparation. This surface preparation follows the NIL procedure, which is a pattern-transferring technique in which microstructures of a mold are pressed into low-viscosity plastics at high temperature and patterns are transferred by demolding at low temperature. The technique was introduced during the curing of composites. Figure 2 shows a schematic of the application process to the adhesion layer between the CFRP panel and the stiffener. The steps in this process are as follows:

(1) Concavo-convex microstructures were fabricated on an aluminum plate using a milling machine. After coating the mold surface with releasing agent (ChemTrend, Chemlease #70), carbon/epoxy prepregs (Mitsubishi rayon, Pyrofil #380) were stacked on the mold. The stacking sequence was $[90/\pm45/0]_S$ in this study, with the concave and convex directions set to 90°; thus, the fiber direction in the top layer must be identical to the convex direction.

(2) Prepregs were cured in two steps over the glass transition temperature under a pressure of 0.6 MPa (85°C for 2 h and 135°C for 3.5 h), which allowed, the melted matrix resin to flow into the microstructures of the mold.

(3) Microstructures were transferred to the CFRP by demolding at room temperature.

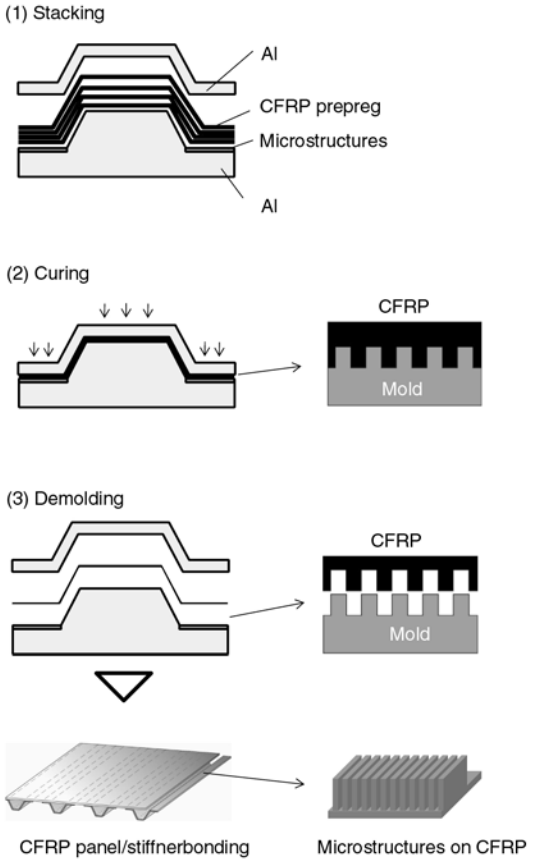

Figure 2. Process of in-mold surface preparation and application to the adhesive surface of a carbon-fiber reinforced plastic (CFRP) panel and stiffener

Figure 3 shows a schematic and a photograph of the mold. In the present study, microstructures of several sizes were fabricated on an aluminum plate. This enabled us to simultaneously fabricate CFRP laminates with microstructures of several aspect ratios, which increased the efficiency with which specimens were prepared for the experiments described later.

Figure 4 shows images of the surface of the imprinted CFRP taken with a scanning electron microscope (SEM; Keyence, VE-8800). In this study, five micro-

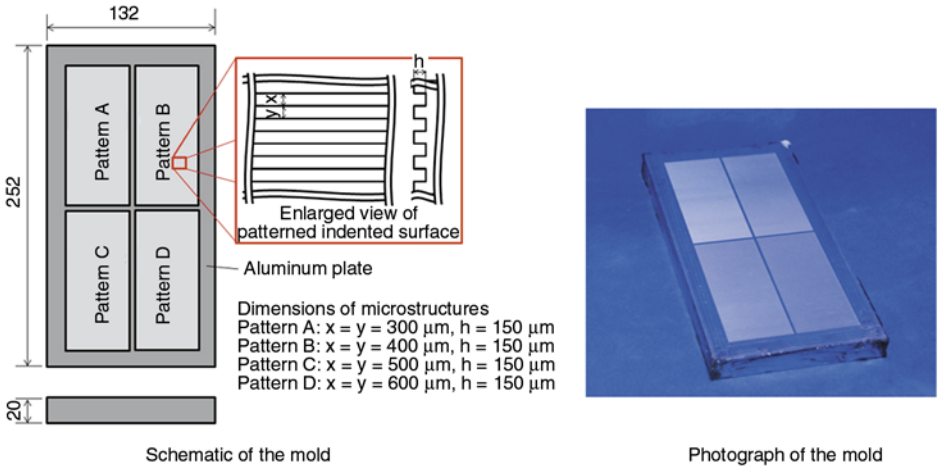

Figure 3. Schematic and photograph of the mold with microstructures

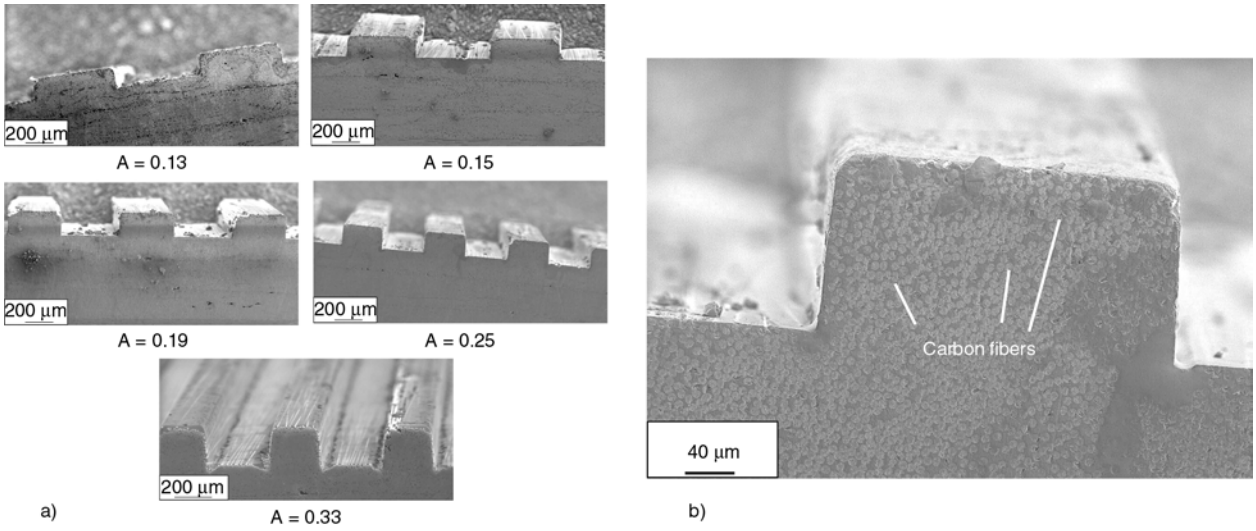

Figure 4. Scanning electron microscope images of microstructures on the surface of CFRPs treated by in-mold surface preparation: (a) images of the microstructures on CFRPs; (b) image of the enlarged view of a microstructure (A = 0.25)

structure shapes were fabricated on the CFRP using aspect ratios (A) of 0.13, 0.15, 0.19, 0.25, and 0.33. At aspect ratios ranging from 0.13 to 0.25, the height was set at a constant value of 150 μm as the width was changed to 600, 500, 400, and 300 μm; for A = 0.33, the height was 200 μm and the width was 300 μm because the milling machine can create a line no narrower than 300 μm. From the images in Figure 4, we confirmed that all of the microstructure shapes were successfully transferred to the CFRP surface. The convex microstructures were observed to contain a number of carbon fibers, and thus behave as composites at this scale.

3. Experimental procedures

3.1. DCB specimen

We conducted DCB tests to investigate the resistance to crack propagation along the CFRP/adhesive interface under macroscopic mode I loading. The DCB testing and data processing follow Japan Industrial Standards (JIS) K 7086, the testing method used to evaluate the interlaminar fracture toughness of CFRPs [21]. Figure 5 shows the DCB specimen configuration. After cutting the imprinted CFRP $[90/\pm45/0]_S$ into specimens 100 mm in length and 15 mm in width, the CFRP was cleaned off with a surface-active agent (Kao, Kitchen Haiter). Note that the specimen size is somewhat smaller than the size prescribed in the JIS protocol, due to limitations in fabricating the imprinted area. The proposed in-mold surface preparation was applied to one adherend, and the surface of the other adherend was treated using emery paper #240. In the range of the tested aspect ratio, we confirmed the crack propagates between the adhesive and in-mold prepared surface. The fracture toughness of the adherend treated with emery paper and that of the adherend treated using the proposed method are compared in

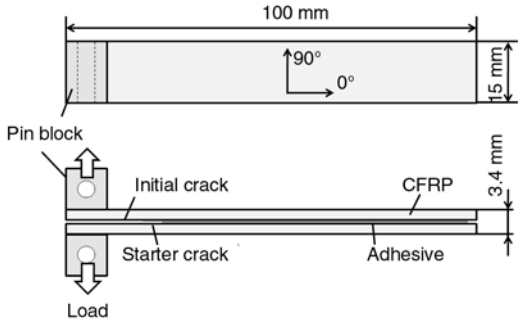

Figure 5. Configuration of a double-cantilever-beam (DCB) specimen

Section 4.2. Two CFRP adherends were bonded together using an epoxy adhesive (3M, DP-105) under pressure (about 0.01 MPa) using two aluminum plates as well as a plummet for 48 h at room temperature, with Teflon sheets (0.1 mm thickness) inserted between two adherends at both edges to introduce an initial crack and to control the thickness of the adhesive layer. Thus, the thickness of the adhesive layer was 0.1 mm, and the thickness of the fabricated DCB specimen was about 3.4 mm. After bonding, the excessive adhesive flowing out of the specimen was removed using emery paper. Before tests were conducted, a starter crack was fabricated by inserting a cutter knife. To evaluate the effect of the shape of the microstructures on the resistance to crack propagation and crack-propagation behavior, six kinds of adherends including a flat surface were prepared: A = 0, 0.13, 0.15, 0.19, 0.25, and 0.33. For each aspect ratio, three specimens were tested.

3.2. DCB tests for mode I fracture toughness

DCB tests were performed using a tensile testing machine (Shimadzu, AG-I) under crack opening displacement (COD) control at 0.2 mm/min. The COD is defined as the relative displacement between two attached pin blocks. During DCB tests, load, crack length, and COD as a function of time were recorded. The crack-propagation behavior at the CFRP/adhesive interface was observed using a digital microscope (Scholar, M3), and the crack length was measured with a measuring microscope (Pikaseiko, PRM-2). After the crack had propagated sufficiently (forming a crack about 25 mm long), the specimen was fully unloaded and the permanent offset displacement, δ_{offset}, was measured to check the quantity of plastic deformation. Our procedure to calculate fracture toughness is discussed in the next section.

4. Results and discussion

4.1. Evaluation of crack-propagation resistance

Because the proposed surface preparation produces a concavo-convex bonding interface, the crack-propagation resistance varies microscopically depending on the crack position within the concavo-convex shape. However, the objective of this study was not to obtain the precise crack-propagation resistance on a microscopic scale but to evaluate the macroscopic crack-propagation resistance, as a practical indicator of the effect of using the proposed surface preparation instead of conventional treatments. Therefore, we first investigated the method used to examine this resistance.

Figure 6 shows representative load-COD curves of the DCB tests for various aspect ratios ranging from 0 to 0.33. For all specimens, the load increases linearly up to the critical value to propagate the crack; the load then decreases smoothly as the crack length increases, although concavo-convex microstructures exist along the crack path. The observed δ_{offset} was within the 10% of the maximum COD suggested in JIS, implying that no permanent deformation of the adherend had occurred. It is normal for small final offsets to be observed because of the presence of the deformed adhesive slightly propping open the crack [22]. Note that the low gradient of the initial slope of A = 0.33 is the result of the slightly longer initial crack length fabricated manually by the cutter knife, which increases compliance. It is noted that we did not implement any specific control process for fabricating a constant and fine starter crack for simplicity. Thus, we use the crack propagating resistance when the crack stably propagates for some length in instead of using the initial crack propagating resistance for evaluation.

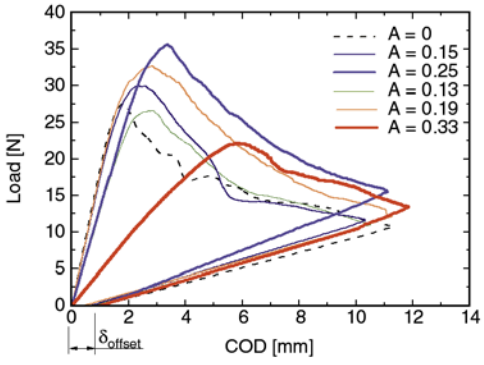

Figure 6. Representative load-crack opening displacement curves of DCB tests for various aspect ratios

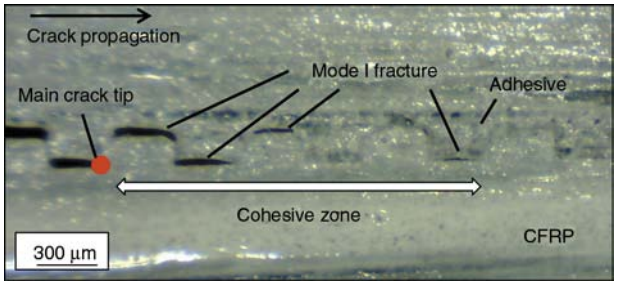

Figure 7. Microscopic image of cohesive zone ahead of the main crack tip during DCB tests

Figure 7 shows the microscopic image around the crack tip obtained during DCB tests of the $A = 0.25$ specimen, and shows the formation of multiple microscopic cracks ahead of the macroscopic main crack tip (the red circle in Figure 7), which penetrated from the left edge. We refer to this zone of multiple micro-cracks, ahead of the main crack, as the cohesive zone in this study; in this region, a cohesive force exists in the closure direction of crack surfaces [23, 24]. In this cohesive zone, mode I fracture occurred at the horizontal interfaces, whereas the lateral interfaces remained bonded. This was attributed to the fact that the fracture toughness of mode I is lower than that of mode II. This crack-propagation behavior was observed for all specimens, with the exception of the flat specimen, $A = 0$. It is also noted that the crack does not propagate along a straight interface rather than the concavo-convex interface because the apparent fracture toughness of the $A = 0.25$ surface was lower than that treated using emery paper #240 (as mentioned in Section 4.2).

When the size of the concavo-convex microstructure is sufficiently larger than that of the cohesive zone, the crack-propagation resistance may vary depending on the crack-tip position, as shown in Figure 8a. However, if multiple concavo-convex microstructures are included in the cohesive zone, as in the present study, energy dissipates more uniformly owing to the presence of the multiple microscopic cracks that allow the propagation of cracks that are independent of the main crack position in the concavo-convex microstructures, and the crack-propagation resistance has a more uniform value (Figure 8b). In the DCB experiments, the load decreased smoothly after crack propagation and variation in microscopic load due to the presence of the microstructures, such as stick-and-slip behavior, did not occur. Therefore, the uniform crack-propagation resistance of the concavo-convex microstructures was evaluated using the 'apparent fracture toughness' by assuming a flat interface. The apparent fracture toughness corresponds to the total energy dissipation including the cohesive zone, divided by the macroscopic crack length.

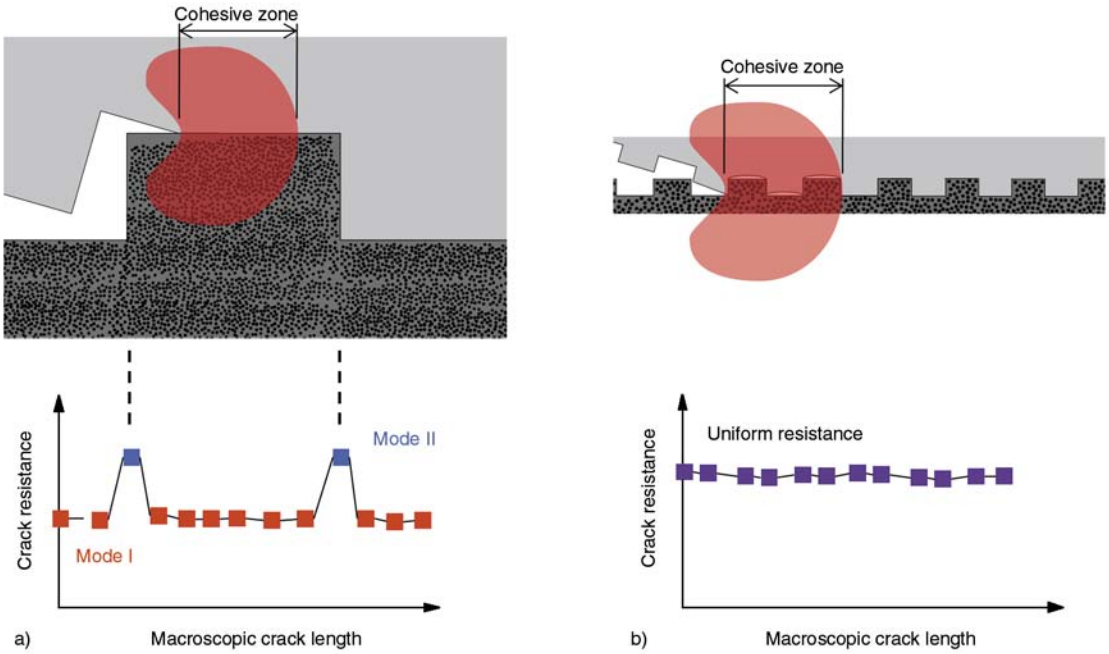

Figure 8. Schematics of cohesive zone ahead of the main crack tip and effects of crack-tip position on crack resistance: (a) large-scale structures (on the order of millimeters); (b) microstructures (on the order of micrometers)

The apparent mode I fracture toughness G_{IA} was calculated by Equation (2) in the same manner as JIS K 7086 [21]:

$$G_{IA} = \frac{3}{2(2H)}\left(\frac{P}{B}\right)^2 \frac{(B\lambda)^{\frac{2}{3}}}{\alpha_1} \quad (2)$$

where $2H$ and B are the thickness and width of the specimen, respectively; P is the applied load; and λ is the compliance of the specimen, calculated according to Eqution (3):

$$\lambda = \frac{\delta}{P} \quad (3)$$

where δ is COD. α_1 is a coefficient associated with the flexural rigidity of the adherend, which is obtained by least-squares approximation from the following Equation (4):

$$\frac{a}{2H} = \alpha_1 (BH)^{\frac{1}{3}} + \alpha_0 \quad (4)$$

where a is the macroscopic clack length, which corresponds to the distance between the crack tip and loading point in the longitudinal direction of the specimen. It should be noted that because the permanent offset displacement δoffset for all specimens shown in Figure 6 was less than 10% of the maximum COD, the effects of plastic deformation can be ignored [21].

4.2. Apparent fracture toughness and crack propagation behavior

Figure 9 shows a representative R curve indicating the apparent mode I fracture toughness G_{IA} as a function of the crack length. Although G_{IA} was unstable during the initial stage of crack propagation, it became constant as crack propagation progressed. The initial instability was caused by the unstable configuration of the starter crack fabricated by a cutter knife. The dashed line shows the steady-state fracture toughness, which was obtained by averaging the five points.

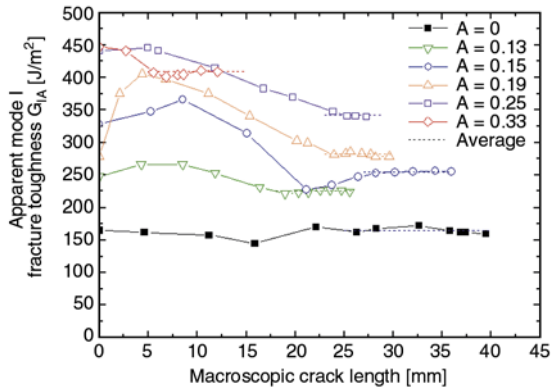

Figure 9. Representative relationships between the apparent mode I fracture toughness G_{IA} and crack length for various aspect ratios

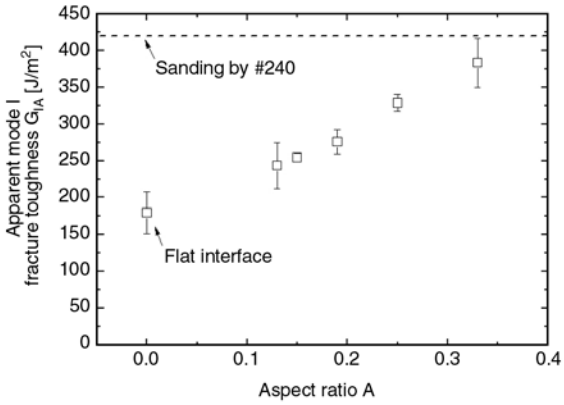

Figure 10. Apparent mode I fracture toughness G_{IA} as a function of A. The dashed line indicates G_{IA} of a specimen treated by conventional sanding treatment

Figure 10 shows the steady-state G_{IA} as a function of the aspect ratio A. It is noted that the G_{IA} is apparent macroscopic mode I fracture toughness including the effect of the presence of a microscopic mode II component. It can be seen from Figure 10 that the G_{IA} after in-mold surface preparation was enhanced compared to that of specimens with a flat interface. Furthermore, G_{IA} became higher as the aspect ratio A increased and improved by up to 113% at A = 0.33 compared to samples without in-mold surface preparation. The dashed line shows the mode I fracture toughness of the composite bonded joint treated by a conventional sanding surface preparation using #240 emery paper [25]. Table 1 lists the average and standard deviation of G_{IA} of in-mold preparations (A = 0.33) and sanding preparations (#240). Although the average G_{IA} of the in-mold preparations is somewhat lower (91%) than that of the sanded preparation, the in-mold preparation achieves almost the same effect as sanding

Table 1. Apparent mode I fracture toughness G_{IA} of composite bonded joints treated by in-mold surface preparation and by conventional sanding treatment

	In-mold surface preparation (A = 0.33)	Sanding by #240
G_{IA} [J/m^2]	383	419
SD [J/m^2]	33	49
$G_{IA}/G_{IA\,(A=0)}$	2.13	2.33

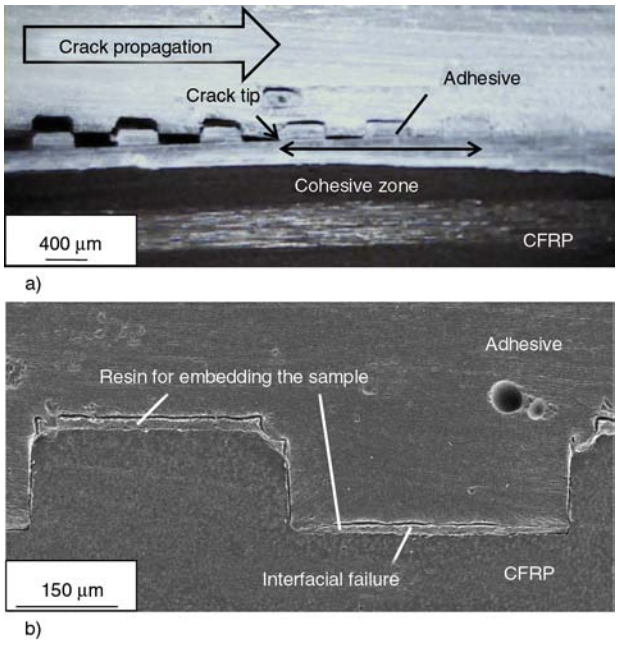

Figure 11. Microscopic images of CFRP/adhesive interfaces (A = 0.19): (a) digital microscope image during the DCB tests; (b) field-emission scanning electron microscope image after the DCB tests

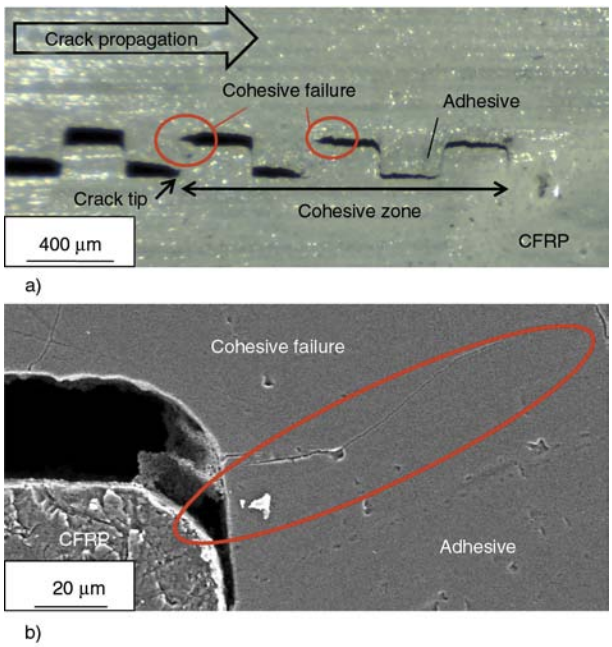

Figure 12. Microscopic images of CFRP/adhesive interfaces (A = 0.25): (a) digital microscope image during the DCB tests; (b) FE-SEM image after the DCB tests

(91%), but without the need for adverse secondary processes, which enables fast and cost-effective mass production.

Figures 11a and 11b show microscopic images of the CFRP/adhesive interface with A = 0.19, obtained using a digital microscope (Scholar, M3) during DCB tests and with a field-emission SEM (FE–SEM; Hitachi, s4500) after the DCB tests, respectively. The microscopic images show that the crack propagates along the interface of the concavo-convex microstructures whereas no crack was observed within either the adhesive or the CFRP (no cohesive failure). The specimens with A<0.19 show the same interfacial failure mode along the concavo-convex interface. This fracture behavior implies that as the aspect ratio A increases (up to A = 0.19), the mode II interfacial failure area per unit length in a specimen's longitudinal direction increases; this is attributed to the increase in the apparent fracture toughness.

Figures 12 and 13 show microscopic images of the failure interface in the A = 0.25 and 0.33 specimens, respectively. As shown in Figure 12, cohesive failure of the adhesive was observed near the corners of microstructures at the aspect ratio A = 0.25, in addition to interfacial failure. A comparison of Figure 13 with Figure 12 shows that cohesive failure

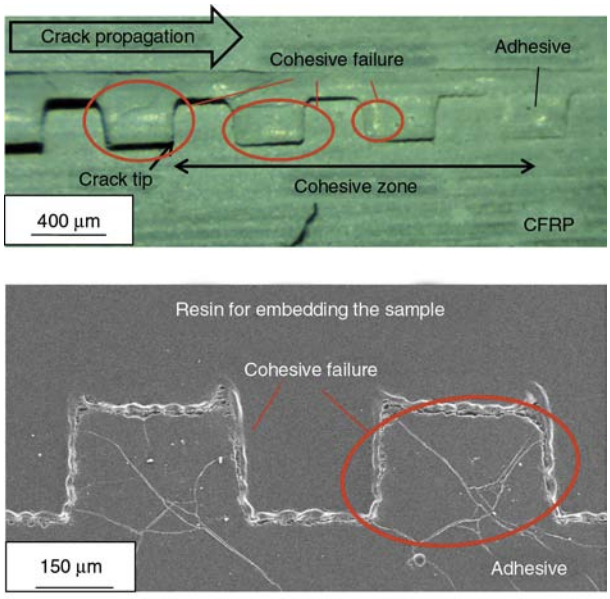

Figure 13. Microscopic images of CFRP/adhesive interfaces (A = 0.33): (a) digital microscope image during the DCB tests; (b) FE-SEM image after the DCB tests

was more complex at A = 0.33. This agrees qualitatively with the expectation, shown in Figure 1, that interfacial failure is dominant at a low aspect ratio, whereas cohesive failure occurs and enlarges as A increases, although the cohesive fracture mode is more complex. This is attributed to the complex stress distribution at the convex corner, and the rel-

ative difference in the fracture toughness between the cohesive failure of adhesives and the interface failure.

In the range of A = 0–0.19, the fracture mode, which is basically interfacial, is accompanied by the formation of cracks in the cohesive zone or microscopic crack creation involving multiple concavo-convex microstructures ahead of the main crack tip. In this fracture mode, energy is consumed independent of the microscopic crack-tip position within the concavo-convex microstructure during crack propagation; thus, G_{IA}, which is the average energy consumption per unit crack area, is expressed as shown by Equation (5):

$$G_{IA} = \frac{wG_{IC} + 2hG_{IIC}}{w} = G_{IC} + 2G_{IIC}A \qquad (5)$$

where G_{IC} and G_{IIC} represent the pure mode I and mode II fracture toughness, respectively. This equation indicates that the increase in G_{IA} is caused by two factors: the presence of higher mode II fracture toughness (G_{IIC}) and an increase in the actual crack length or the aspect ratio (A). Thus, G_{IA} increases in proportion to the increase in the aspect ratio A, where the proportionality factor corresponds to $2G_{IIC}$.

Figure 14 shows the experimentally obtained G_{IA} and estimated G_{IA} calculated by Equation (5). The values of G_{IC} and G_{IIC} in Equation (5) are 179.6±28.17 and 513.8±69.06 J/m^2, respectively, which were obtained by preliminary DCB and end-notched-fracture (ENF) tests of the flat interface (A = 0) specimens. The ENF tests were conducted by following JIS K 7086 [21]. The crack propagation in a single ENF test is unstable; thus, the span length was changed after unloading and the ENF tests were repeated to obtain mode II R curves.

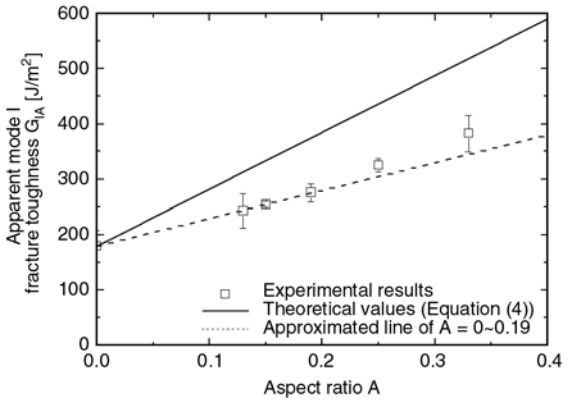

Figure 14. Comparison of estimated and experimental results of the apparent mode I fracture toughness G_{IA} as a function of aspect ratio

The dashed line in Figure 4 indicates the approximated line of experimental G_{IA} values of the interfacial fracture cases from A = 0 to 0.19. In the range from A = 0 to 0.19, the experimental results confirm a linear increase as A increases, as estimated in Equation (5), although the proportionality factor in the experimental results is lower than that of the estimation. This may be because Equation (5) does not take into account the effect of the stress concentration at the corner of the microstructure. The presence of this stress concentration enhances crack propagation, thus lowering the fracture toughness in the experiments compared to the value estimated in Equation (5).

Figure 14 also shows that the G_{IA} values of the cohesive failure modes of A = 0.25 and 0.33 are somewhat higher than the approximated line of the interfacial fracture mode. The higher G_{IA} is attributed to the higher energy dissipation due to the presence of cohesive failure, in addition to the complete interfacial failure of the microscopic regions of mode I and II. It is expected that in the case of cohesive failure accompanied by the partial interfacial failure of only the microscopic mode I region (such as in the case of a high aspect ratio, as shown in Figure 1), the energy required is less than needed for interfacial failure; thus, G_{IA} may be lower than the approximated dashed line. However, because the crack propagation was determined by a microscopic stress field and not by total energy dissipation, the cohesive failure mode, above the dashed line, occurred. In future research, a crack-propagation simulation using the finite-element method and a quantitative investigation of the fracture mode transition should be done, as well as investigations of the mode II and mixed-mode loading conditions, and the influence of thermal residual stresses on the fracture behavior.

5. Conclusions

In-mold surface preparation using imprint lithography was proposed for polymer composite materials and applied to the adhesive joints of CFRPs. Because this method allows surface treatments to be done as composite materials are forming, it reduces time and costs compared to those required in conventional techniques. Concavo-convex microstructures fabricated on the surface of CFRPs enhanced the

resistance to mode I crack propagation at the CFRP/adhesive interface and induced microscopic mode II interfacial failure and cohesive failure, which require high energies for crack propagation. DCB tests for assessing mode I fracture toughness confirmed that the steady-state apparent fracture toughness G_{IA} became higher as the aspect ratio of the concavo-convex microstructures increased, and was 113% higher than that without in-mold surface preparation, which was nearly the same as that achieved by sanding treatment. Thus, replacing the conventional treatments with the proposed method can eliminate the need for adverse secondary processes, enabling fast and cost-effective mass-production. Observations of interfaces during DCB tests revealed that the improvement of G_{IA} was caused by the increase in the microscopic actual crack length and microscopic mode II fracture area per unit length on the lateral side of the concavo-convex microstructure, as well as a fracture-mode transition from interfacial to cohesive failure.

References

[1] Suzuki T., Takahashi J.: LCA of lightweight vehicles by using CFRP for mass produced vehicles. in 'Proceedings of 15th International Conference on Composite Materials, Durban, South Africa' p.4 (2005).

[2] Yamasaki M., Taketa I., Yamaguchi K., Wadahara E., Kamae T., Iwasawa S., Sekido T., Kitano A.: ALSTECC program: Characterization of a short cycle RTM for mass production. in 'Proceedings of 16th International Conference on Composite Materials, Kyoto, Japan' p.7 (2007).

[3] Boatman E. S., Covert D., Kalman D., Luchtel D., Omenn G. S.: Physical, morphological, and chemical studies of dusts derived from the machining of composite-epoxy materials. Environmental Research, **45**, 242–255 (1988).
DOI: 10.1016/S0013-9351(88)80050-1

[4] Matsuzaki R., Suzuki T.: Surface modification by nanoimprint lithography for improvement of the joint strength of composites. Journal of Solid Mechanics and Materials Engineering, **4**, 963–973 (2010).
DOI: 10.1299/jmmp.4.963

[5] Chou S., Krauss P., Renstrom P.: Imprint of sub-25 nm vias and trenches in polymers. Applied Physics Letters, **67**, 3114–3116 (1995).
DOI: 10.1063/1.114851

[6] Chou S. Y., Krauss P. R., Renstrom P. J.: Imprint lithography with 25-nanometer resolution. Science, **272**, 85–87 (1996).
DOI: 10.1126/science.272.5258.85

[7] Schmitt H., Amon B., Beuer S., Petersen S., Rommel M., Bauer A. J., Ryssel H.: UV nanoimprint lithography process optimization for electron device manufacturing on nanosized scale. Microelectronic Engineering, **86**, 636–638 (2009).
DOI: 10.1016/j.mee.2008.11.017

[8] Abad E., Merino S., Retolaza A., Juarros A.: Design and fabrication using nanoimprint lithography of a nanofluidic device for DNA stretching applications. Microelectronic Engineering, **85**, 818–821 (2008).
DOI: 10.1016/j.mee.2007.12.048

[9] Yang R., Lu B-R., Xue J., Shen Z-K., Xu Z-C., Huq E., Qu X-P., Chen Y., Liu R.: Nanoimprint lithography for optic fluidics with phase gratings for environmental monitoring application. Microelectronic Engineering, **87**, 824–826 (2010).
DOI: 10.1016/j.mee.2009.11.030

[10] Kim J., Kim H. S., Lee D. G.: Investigation of optimal surface treatments for carbon/epoxy composite adhesive joints. Journal of Adhesion Science and Technology, **17**, 329–352 (2003).
DOI: 10.1163/156856103762864651

[11] Shahid M., Hashim S.: Effect of surface roughness on the strength of cleavage joints. International Journal of Adhesion and Adhesives, **22**, 235–244 (2002).
DOI: 10.1016/S0143-7496(01)00059-8

[12] Cho T. M., Choo Y. S., Lee M. J., Oh H. C., Lee B. C., Park T. H., Shin Y. S.: Effect of surface roughness on the adhesive strength of the heat-resistant adhesive RTV88. Journal of Adhesion Science and Technology, **23**, 1875–1882 (2009).
DOI: 10.1163/016942409X12508517390671

[13] Prolongo S., Rosario G., Ureña A.: Study of the effect of substrate roughness on adhesive joints by SEM image analysis. Journal of Adhesion Science and Technology, **20**, 457–470 (2006).
DOI: 10.1163/156856106777144345

[14] Zhang S., Panat R., Hsia K.: Influence of surface morphology on the adhesion strength of epoxy–aluminum interfaces. Journal of Adhesion Science and Technology, **17**, 1685–1711 (2003).
DOI: 10.1163/156856103322396749

[15] Zhang Y., Spinks G. M.: An atomic force microscopy study of the effect of surface roughness on the fracture energy of adhesively bonded aluminium. Journal of Adhesion Science and Technology, **11**, 207–223 (1997).
DOI: 10.1163/156856197X00318

[16] Kim W-S., Yun I-H., Lee J-J., Jung H-T.: Evaluation of mechanical interlock effect on adhesion strength of polymer–metal interfaces using micro-patterned surface topography. International Journal of Adhesion and Adhesive, **30**, 408–417 (2010).
DOI: 10.1016/j.ijadhadh.2010.05.004

[17] Janarthanan V., Garrett P. D., Stein R. S., Srinivasarao M.: Adhesion enhancement in immiscible polymer bilayer using oriented macroscopic roughness. Polymer, **38**, 105–111 (1997).
DOI: 10.1016/S0032-3861(96)00447-8

[18] Rider A. N., Arnott D. R.: The influence of adherend topography on the fracture toughness of aluminium-epoxy adhesive joints in humid environments. The Journal of Adhesion, **75**, 203–228 (2001).
DOI: 10.1080/00218460108029601

[19] Zavattieri P. D., Hector L. G., Bower A. F.: Determination of the effective mode-I toughness of a sinusoidal interface between two elastic solids. International Journal of Fracture, **145**, 167–180 (2007).
DOI: 10.1007/s10704-007-9109-y

[20] Volinsky A. A., Moody N. R., Gerberich W. W.: Interfacial toughness measurements for thin films on substrates. Acta Materialia, **50**, 441–466 (2002).
DOI: 10.1016/S1359-6454(01)00354-8

[21] JIS K 7086: Testing methods for interlaminar fracture toughness of carbon fibre reinforced plastics (2011).

[22] Blackman B. R. K., Kinloch A. J., Paraschi M., Teo W. S.: Measuring the mode I adhesive fracture energy, G_{IC}, of structural adhesive joints: The results of an international round-robin. International Journal of Adhesion and Adhesives, **23**, 293–305 (2003).
DOI: 10.1016/S0143-7496(03)00047-2

[23] Evans A. G., Hutchinson J. W.: Effects of non-planarity on the mixed mode fracture resistance of bimaterial interfaces. Acta Metallurgica, **37**, 909–916 (1989).
DOI: 10.1016/0001-6160(89)90017-5

[24] Bradley W., Cohen R.: Matrix deformation and fracture in graphite-reinforced epoxies. in 'Delamination and debonding of materials' (ed.: Johnson W. S.) ASTM, Philadephia, 389–410 (1985).

[25] Miyairi H.: Basis and application of structural adhesion. CMC Publishing, Tokyo (2006).

eXPRESS Polymer Letters Vol.7, No.3 (2013) 304–318
Available online at www.expresspolymlett.com
DOI: 10.3144/expresspolymlett.2013.27

Sheets of branched poly(lactic acid) obtained by one step reactive extrusion calendering process: Melt rheology analysis

J. Cailloux[1], O. O. Santana[1], E. Franco-Urquiza[1], J. J. Bou[2], F. Carrasco[3], J. Gámez-Pérez[4], M. L. Maspoch[1]*

[1]Centre Català del Plàstic (CCP) – Universitat Politècnica de Catalunya (UPC), C/ Colom, 114, 08222 Terrassa, Spain
[2]Department of Chemical Engineering – Universitat Politècnica de Catalunya (UPC), Pavelló G, planta 1, Avenida Diagonal,647, 08028 Barcelona, Spain
[3]Department of Chemical Engineering – Universitat de Girona (UdG), Campus Montilivi s/n, 17071 Girona, Spain
[4]Department of Polymers and Advanced Materials – Universitat Jaume I, Avenida de Vicent Sos Baynat s/n, 12071 Castelló de la Plana, Spain

Received 4 September 2012; accepted in revised form 28 November 2012

Abstract. One-step reactive extrusion-calendering process (REX-Calendering) was used in order to obtain sheets of 1mm from two PD,L-LA extrusion grades modified with a styrene-acrylic multifunctional oligomeric agent. In a preliminary internal mixer study, torque versus time was monitored in order to determine chain extender ratios and reaction time. Once all parameters were optimized, reactive extrusion experiments were performed.
Independently of the processing method employed, under the same processing conditions, PD,L-LA with the lower D enantiomer molar content revealed a higher reactivity towards the reactive agent, induced by its higher thermal sensitivity. REX-Calendering process seemed to minimize the degradations reactions during processing, although a competition between degradation and chain extension/branching reactions took place in both processes. Finally, the rheological characterization revealed a higher degree of modification in the melt rheological behaviour for REX-Calendered samples.

Keywords: *rheology, poly(lactic acid), chain extender, reactive extrusion, molecular weight distribution*

1. Introduction

Poly(D,L-Lactide) (PD,L-LA) is well known to be a biodegradable and biocompatible polymer available from renewable resources. In the beginning, it was mainly used for medical applications due to its high fabrication costs but now PD,L-LA polymers have finally found a commercial application in single use disposal items due to its low price compared with other biodegradable polymers. However, its brittle nature reduces its use to very limited applications and its poor melt strength limits specific processes such as film blowing or foaming [1].

As well as many aliphatic polyesters, PD,L-LA is subject to some thermal degradations and instabilities above its melting temperature, especially during processing. Radical and non-radical reactions are proposed to explain the various and complex mechanisms that could occur during processing, leading to a reduction of the molecular weight and viscosity. As a result, a general decrease of the material properties is expected [2].
Several authors [3, 4] reported that the residual water or moisture content inside the polymer matrix activates hydrolysis reactions (Figure 1a) implying the

*Corresponding author, e-mail: orlando.santana@upc.edu

split-up of the ester linkage into alcohol and acid carboxylic groups. Doi *et al*. [5] as well as Yu *et al*. [6] argued that thermal and hydrolysis reactions for biocopolymers could be generated by random chain scission reactions of the ester groups following a mathematical model depending on its own composition.

Coupled with these two last mechanisms, intra- (Figure 1c) and intermolecular (Figure 1d) transesterification reactions could also cause a drop in molecular weight at longer reaction times [7, 8]. In fact, backbiting effect (zip-like depolymerization, see Figure 1b) leads to the formation of cyclic oligomers (lactide) and lactic acid which is catalyzed by the presence of monomers, oligomers or hydroxyl groups. Pyrolysis mechanisms should also be considered but at high temperatures (>300ºC) where cis-elimination (Figure 1e) gives rise to the formation of carboxylic acid groups and a polymer chain containing acryloyl groups [9].

The extrusion process can take advantage of these degradation reaction products when combined with reactive agents, promotes polymerization (chain extension), grafting, branching and functionalization [10]. On one side, reactive extrusion is an attractive way to minimize the degradation effects during processing and to enlarge its processing window. On the other side, Corre *et al*. [11] as well as Pilla *et al*. [12] reported that chain architecture modification by chain branching enhances PLA melt properties. Chain branching degree depends on the functionality of the reactive agent and generally leads to an increase in molecular weight.

A new aspect that arises in this communication, in comparison with previous works [11, 12] on this subject, was the production of structural modified PD,L-LA sheets through a one-step reactive extrusion-calendering process (REX-Calendering) in a pilot plant. The main goal is to obtain sheets that could be used directly in the fabrication of thermoformed packaging and the evaluations of their final performances (melt rheology, thermal, mechanical and fracture behaviour).

The present communication shows the scaling up from an internal mixer study to a one step reactive extrusion-calendering process of two PD,L-LA extrusion grades, modified by a styrene-acrylic multifunctional oligomeric agent (SAmfE). The assessment of possible changes in the molecular weight and melt rheology is the aim of this publication. A

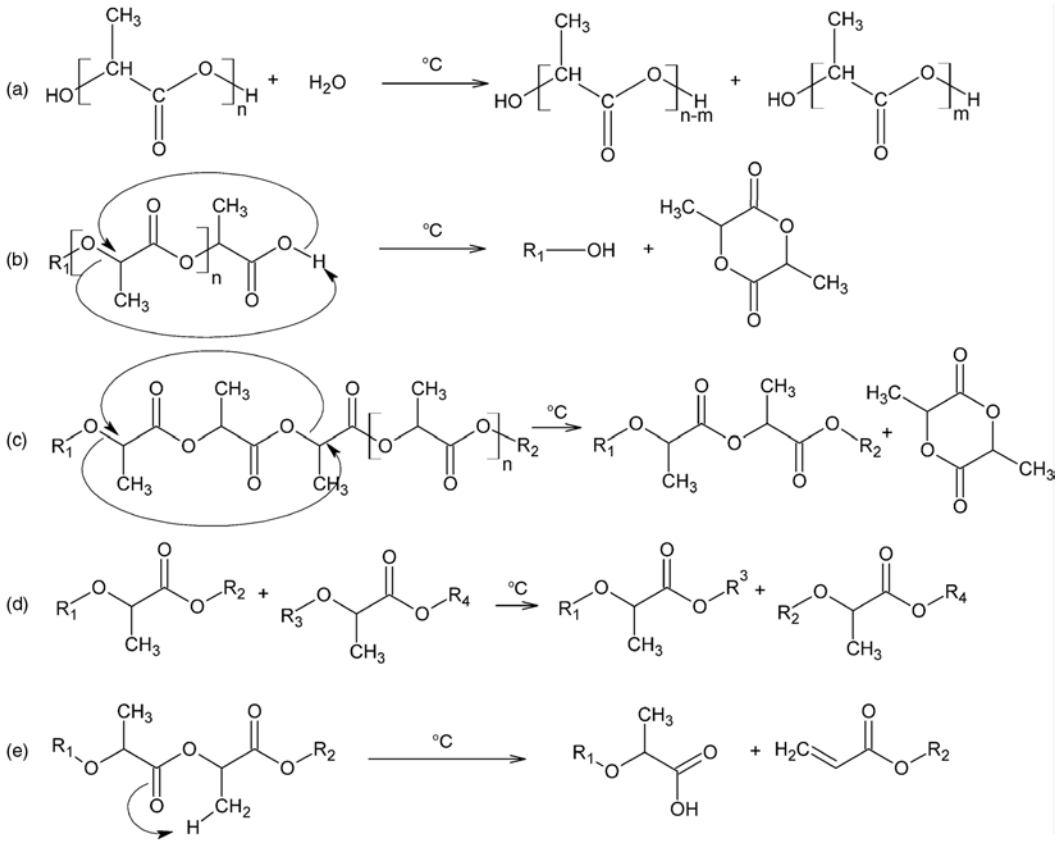

Figure 1. Reactions of degradation of PD,L-LA: (a) hydrolysis, (b) intramolecular transesterification (backbiting), (c) intramolecular transesterification, (d) intermolecular transesterification, (e) pyrolitic *cis*-elimination

one-step REX-Calendering process using PD,L-LA and SAmfE has not yet been described in literature to the best of our knowledge.

2. Experimental

2.1. Materials

Two PD,L-LA extrusion grades supplied by NatureWorks® (Arendonk, Belgium) were used in this study whose characteristics are described in Table 1 [13, 14].

A styrene-acrylic multi-functional-epoxide oligomeric agent (SAmfE) was used as reactive agent, supplied by BASF® (Ludwigshafen, Germany) (Joncryl-ADR-4300F) in flake form with a molecular weight of 5443 g·mol^{-1}, an epoxy equivalent weight of 433 g·mol^{-1} and T_g = 56°C. The food compliance was delivered by the European Union for its use in food packaging. Figure 2 shows its generic structure [15].

2.2. Processing

2.2.1. Lab-scale mixing: internal mixer

Both grades of PD,L-LA pellets were dried overnight at 55°C under vacuum prior to use in order to remove any excess moisture. SAmfE was stored overnight under vacuum. Melt blending of PD,L-LA and SAmfE was carried out in an internal mixer (Brabender Plastic-Corder W50EHT, Duisburg, Germany) with a mixing chamber volume of 55 cm^3, at 180°C and with a screw rotation speed of 50 rpm. A continuous flow of N_2 with a pressure of 3.5 bars was introduced into the mixing chamber in order to minimize degradation. SAmfE was added after the total fusion of PD,L-LA (3 min.).

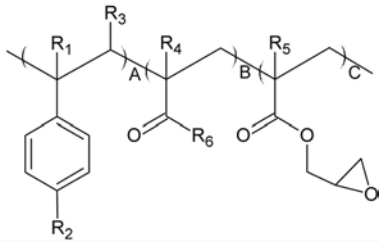

Figure 2. Structure of Joncryl-ADR-4300F used. R_1–R_5 are H, CH_3, a higher alkyl group, or combinations of them; R_6 is an alkyl group, and A, B are each between 1 and 20 and C between 1 and 12.

In a first step, for each preparation, torque vs. mixing time was monitored for a prolonged time in order to follow the evolution of the reaction. An optimum reaction time of 13 min was deduced from these mixing experiments, as it will be explained in Section 3.1.1. Fresh blends were equally processed applying this optimum reaction time of 13 min. After the reaction the material was extracted from the mixing chamber and cooled to room temperature. The obtained material was ground and vacuum-dried overnight at 55°C. Plates with a thickness of 1 mm were prepared by compression molding (40 bars) at 200°C for 10 minutes in a IQAP LAP PL-15 hot platen press.

2.2.2. Pilot plan scale: one step reactive extrusion-calendering

REX-Calendering process was performed in a co-rotating twin screw extruder 25 mm (L/D = 36), (KNETER 25X24D, COLLIN, Ebersberg, Germany). Prior to extrusion, PD,L-LA pellets were dried at 80°C for 3 hours in a PIOVAN (DSN506HE, Venice, Italy) hopper-dryer (dew point = –40°C) and kept during all the extrusion process under the same conditions. The SAmfE was powdered using a mortar and pestle and then stored under vacuum. The screw speed was 40 rpm, the residence time was 4 min and the extruder was operated by starve feeding. The following temperature profile was used: 150°C (feeding zone), 170°C (melting zone) and 175°C (metering zone and die). Both polymer and SAmfE were simultaneously introduced in the hopper of the feeding zone under a nitrogen blanket (2.5 bars) after that the production line was started and stabilized with raw PD,L-LA material. The feeding rate of the SAmfE was adjusted to the polymer feeding rate in such way that a nominal dosage of 0.5% weight/weight of SAmfE was obtained.

Table 1. Technical specifications for both PD,L-LA grades used

PD,L-LA grade	Sample I.D.	D enantiomer molar content [%]	M_n [kg·mol^{-1}]	M_w [kg·mol^{-1}]	MFI [g/10 min] (210°C/2.16 kg)	T_{mp}/T_{me}* [°C]	X_c* [%]
Ingeo 4032D	PLA-2	2	90	181	6.4± 0.3	167/173	40
Ingeo 2002D	PLA-4	4.25	99	187	5.8± 0.2	152/158	35

*T_{mp} (maximum melting signal temperature), T_{me} (end melting signal temperature) and X_C (crystallinity degree) were determined for raw materials by DSC from the first heating cycle at 10°C·min^{-1}, for which ΔH_m^0 = 93.6 J·g^{-1}.

Table 2. Nomenclature used for all processed samples in the study

Grade	Mixing process	Sample I.D.	Amount of SAmfE added [%w/w]
Ingeo 4032D	Internal mixer	PLA-2 "neat"	0
		PLA-2+0.5J	0.5
		PLA-2+1J	1
	REX-Calendering	PLA-2 extr.	0
		PLA-2-REX	0.5
Ingeo 2002D	Internal Mixer	PLA-4 "neat"	0
		PLA-4+0.5J	0.5
		PLA-4+1J	1
	REX-Calendering	PLA-4 extr.	0
		PLA-4-REX	0.5

Furthermore, vacuum was applied in the metering zone to remove any volatiles formed during the reaction. Sheets with 100 mm nominal width and a nominal thickness of 1 mm were calendered (Techline CR72T, COLLIN, Ebersberg, Germany). The chill roll temperature was set to 50°C. Using the above described processing parameters, about 40 m of calendered sheet were obtained.

Samples prior to SAmfE addition (referred to as PLA-2 extr. and PLA-4 extr.) and also from the stabilized regime as it will be explain in Section 3.1.2. (regime 2 at about 30 min) were analyzed (referred to as PLA-2-REX and PLA-4-REX).

All prepared samples are specified in Table 2; samples were distinguished by their different *D* enantiomer molar content, the amount of added SAmfE and the type of mixing process.

2.3. Characterization techniques

2.3.1. Size exclusion chromatography (SEC)

Average molecular weights (M_n and M_w) and the polydispersity index (PDI) were determined using a Hitachi mono-detector chromatograph with a separation column of PLHFIP gel (Polymer Laboratories, Santa Clara, CA, USA) running at room temperature. Mobile phase was hexafluoroisopropanol (HFIP) containing 6,8 g·L^{-1} of sodium trifluoroacetate to prevent polyelectrolyte effect. 100 µL were injected and the concentration of each sample was 0,2 w/v%. Calibration was performed with PMMA samples (Easycal kit, Polymer Laboratories, Santa Clara, CA, USA).

2.3.2. Rheological dynamic analysis (RDA)

An oscillatory rheometer (AR-G2, TA Instrument, New Castle, DE, USA) equipped with parallel-plate geometry of 25 mm diameter with a gap of 1 mm was used. Tests were conducted under controlled deformation conditions at 0,2% (LVR) at 172, 180 and 200°C. Prior to use, samples were dried at 55°C for 12 h under vacuum and kept during tests under nitrogen flow to minimize oxidation and to maintain a dry environment. Dynamic frequency sweeps were carried out over an angular frequency (ω) range of 628.3–0.06283 rad·s^{-1}.

In order to ensure sufficient data on the terminal region, creep experiments were performed at 180°C under a constant stress of 19.56 Pa. The creep data were converted into the relaxation spectrum $H(\lambda)$ using the NLREG method. Subsequently, the storage and loss modulus $G'(\omega)$ and $G''(\omega)$ were calculated by two Fredhom integral equations [16, 17].

Master curves were referenced at 180°C and were constructed from the combination of time-temperature superposition (TTS) and creep tests. The TTS principle was verified, plotting the phase angle delta versus the absolute value of the complex modulus [18].

The rheological parameters were analyzed using the 'modified Carreau-Yasuda equation' (c.f. Equation (1)) in order to take into account the several distinctly separated relaxation processes in the viscosity functions due to the possible presence of long chain branching (LCB) [19]:

$$|\eta^*(\omega)| = \eta_0 \prod_{i=1}^{m} [1 + (\tau_i \omega)^{\alpha_i}]^{\frac{\nu_i - 1}{\alpha_i}} \quad (1)$$

where η_0 represents the zero-shear viscosity [Pa·s] and m the number of curvatures in the viscosity function. τ_i and α_i represent characteristic relaxation times [s] and the width of each transition region between each different curvature. Finally, ν_i is the respective power law index of the latter ones. Equation (1) results in the conventional Carreau-Yasuda model for m =1.

3. Results and discussion

Reactive extrusion of polyesters and epoxies as reactive agent has been extensively studied and the reactions are well established. Both polyester end groups (i.e. carboxyl and hydroxyl groups) can react with epoxy functional groups via ring-opening reactions, creating covalent bonds with hydroxyl groups [20]. However, a higher reactivity of epoxy towards the carboxyl groups compared to hydroxyl groups was reported in the literature [21]. This is due to the

strong polarization of the hydroxyl groups of carboxylic acid [22].

Since a polyfunctional SAmfE was used in this work (functionality $f_n \leq 12$) and based on previous works dealing with reactions between polyesters and epoxies, a variety of different polymer topologies may be obtained, as shown in Figure 3. In a first step, PD,L-LA carboxyl groups open SAmfE

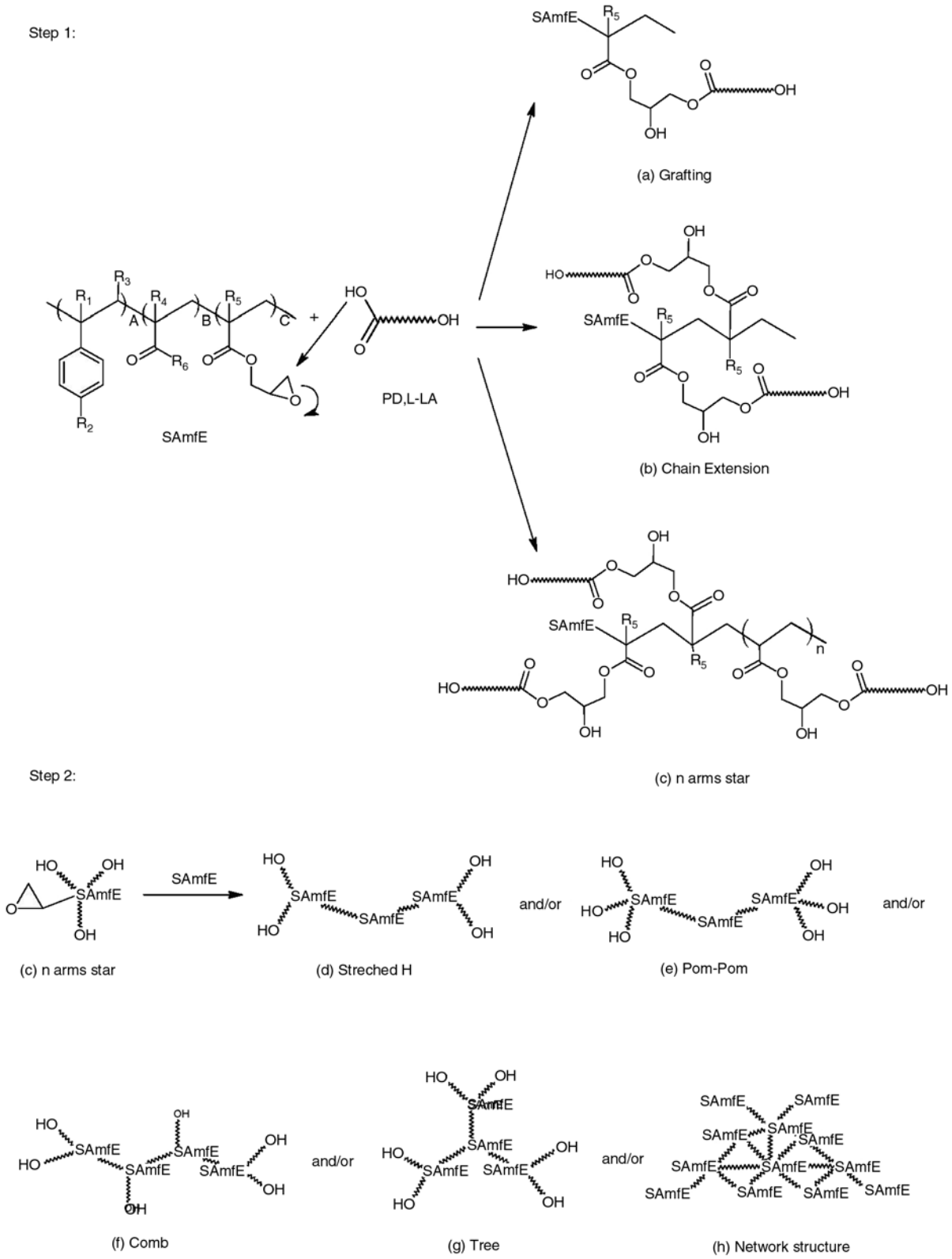

Figure 3. Sketch of the three possible reactions (a, b, c) occurring between PD,L-LA and SAmfE agent, followed by the possible topology structures, (d, e, f, g, h) created for longer reaction times

epoxy rings which results in (Figure 3a) grafting reactions followed by (Figure 3b) chain extension reactions and finally (Figure 3c) *n* arms star formation. In a second step, for longer reaction times, the SAmfE product may further react due to its high reactivity and therefore lead to (Figure 3d) stretched *H*, (Figure 3e) pom-pom, (Figure 3f) comb or (Figure 3g) tree type structures. Finally, an excess of SAmfE may generate a (Figure 3h) network structure.

3.1. Reactive modification process monitoring

3.1.1. Lab-scale mixing: internal mixer

As a first step, the effect of SAmfE addition on both PD,L-LA grades viscosity was evaluated in an internal mixing process as shown in Figure 4. The torque versus time was monitored over a prolonged time (35 minutes) in order to follow the evolution of the reaction.

Although not shown in Figure 4, the bulk temperature increased from 180 to 200°C during mixing process for all samples except PLA-2+1J. This is due to the mechanical shearing and the effect of the exothermal nature of the reaction.

According to Figure 4, the torque of PLA-2 and PLA-4 "neat" samples decreased monotonously over time. This decrease was more pronounced for PLA-2 "neat" samples than PLA-4 ones. This may be explained by the combination of two or more degradation mechanisms, namely backbiting and thermal degradation occurring during mixing process. On one hand PLA-2 presents a higher content of terminal functional groups (lower M_n) than PLA-4 (c.f. Table 1), which may act as a catalyst of backbiting degradation during processing. And on the other hand, as already observed by Bigg [23] for semi-crystalline polyesters, the thermal degradation depends on the width of the processing windows. PLA-4 presents a broader processing window (200–T_{me} = 42°C) than PLA-2 (= 27°C) according to their respective end melting signal temperature (c.f. Table 1) which will decrease the local shear field applied to the material during mixing and therefore the thermal degradation. A higher proportion of terminal functional groups (hydroxyl as well as carboxyl groups) was therefore produced for PLA-2 than PLA-4 during processing.

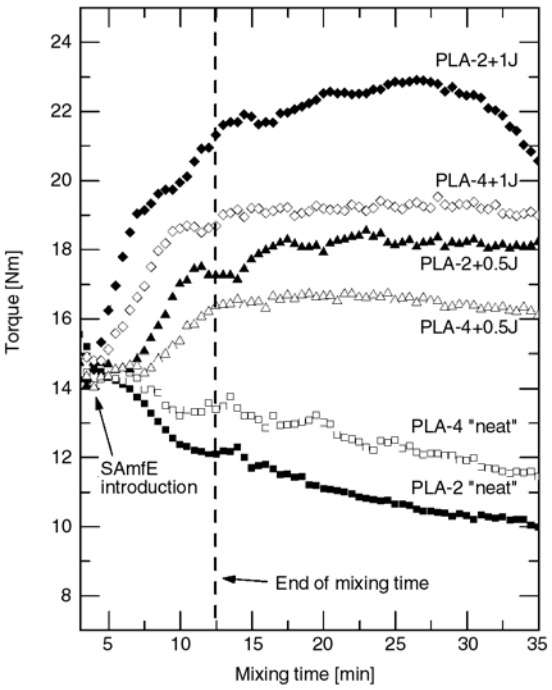

Figure 4. Torque versus mixing time for the samples processed by internal mixing process

In contrast, when both PD,L-LA grades were mixed with SAmfE agent, a strong torque increase was observed. This increase was in all cases higher for PLA-2 than PLA-4 samples. This may be due to the higher amount of PD,L-LA terminal functional groups in PLA-2 samples which results in a higher reactivity towards SAmfE agent. As can be seen in Figure 4, some torque fluctuations can be observed between 10 and 15 minutes for PLA-2+0.5J and PLA-4+1J samples. This might be a consequence of the stick and split behaviour on the wall of the internal mixer due to a possible increase of the melt elasticity.

The torque of PLA-2+1J sample did not reach stabilization over time but increased continuously, reaching a maximum around 28 minutes and then decreasing. Due to the high content of SAmfE and the apparent higher reactivity of PLA-2 a remarkable increase in viscosity was observed. Crosslinking reactions might have taken place together with branching reactions, giving rise to network structure formation (c.f. Figure 3h). At some point (28 min) the combination of high bulk temperature (≈215°C) and a high shear could initiate some degradation processes, resulting in a torque decrease as the network structure may be broken.

An optimum reaction time under these conditions was considered as the point when the torque stabilized, avoiding an excessive reaction time to prevent the aforementioned secondary reactions. Considering these results, an optimum mixing time of 13 min was chosen which corresponds to the first

torque stabilization (plateau on torque trace (c.f. Figure 4)). Fresh blends using this chosen processing time of 13 min were produced. After melt blending, the materials were compression molded into thin sheets, the latter were used for further RDA and SEC characterization.

3.1.2. Pilot plant scale: one step reactive extrusion-calendering

Based on the internal mixer study and to minimize the risk of gelation due to the possible crosslinking reactions and low final product quality, the comparison between both PD,L-LA grades during the REX-calendering process was only carried out with a nominal SAmfE content of 0.5 w/w%.

As a first step, frequency sweep tests at 190°C (exit temperature of the film) were carried out in order to determine the sheet length that showed the same modification degree. For these tests, the complex viscosity at 0.08 rad/s was used as the monitoring parameter and was determined in 15 points along the sheet length. Therefore, a profile of modification along the extruded sheet, expressed as extrusion time was plotted and represented in Figure 5.

As can be seen in Figure 5, three different regimes were observed. The first regime corresponds to the time needed to reach the reactive entities saturation in the dosing zone of the extruder. In both cases this time was longer than in the previous internal mixer preparation (20 min versus 13 min). This situation could be expected if the dynamic nature (continuous flow) of the extrusion process is considered. It is well established in the industry that, the stabilization of a production line requires a specific time in order to reach a stable regime. For the processing conditions employed in this work, this was the case for REX-Calendered samples. In fact, a specific time was needed to reach the saturation of the reactive species involved such as carboxyl groups and epoxies. In the case of the internal mixer, it must be remembered that the mixing process works by batch in with no continuous 'discharge' of the bulk mixed is done contrary to the extrusion process.

In the second regime, this saturation condition have been reached and all specimens possess a similar viscosity, indicating that a similar degree of modification (chain extension and/or branching) is obtained. The third regime shows a viscosity decrease because SAmfE dosage was stopped.

It should be noted that the stabilization was reached after ~20 min for both PD,L-LA grades. Furthermore, a higher viscosity was reached in the case of PLA-2 compared to PLA-4 as was also observed in the internal mixer study.

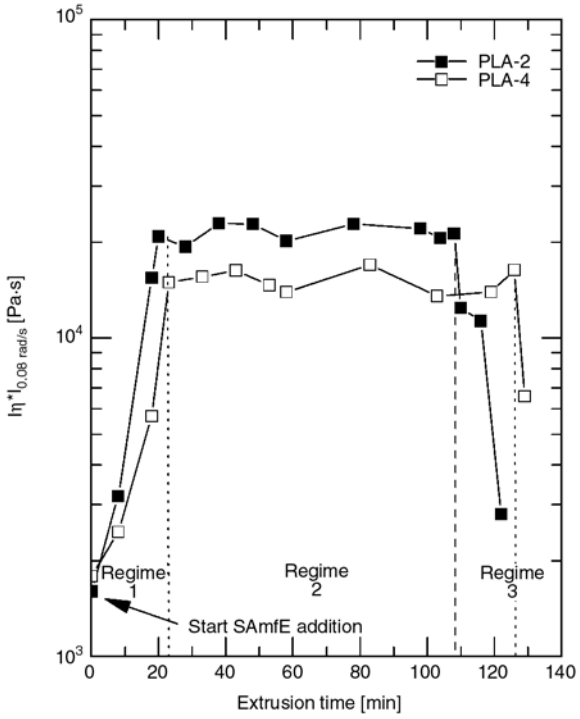

Figure 5. Complex viscosity (at 0,08 rad/s) versus extrusion time at 190°C for REX-Calendering samples

3.2. Molecular weight distribution (MWD) analysis

SEC tests were performed on all of the samples in order to determine the difference in the molecular weight distribution due to the reaction of both PD,L-LA grades with SAmfE agent. Figure 6 shows the molecular weight distribution curves obtained for PLA-2 samples for both processing methods: (a) internal mixer samples and (b) REX-Calendered samples in which each curve was normalized by the maximum dW/dlog$M$ of the "neat" and extr. grade, respectively. Similar curves were obtained for PLA-4 samples.

According to SEC tests, unmodified PLA-2 "neat" (c.f. Figure 6a) samples displayed a monomodal distribution which changed to a bi- and three-modal one with increasing SAmfE content. This was associated to the presence of two or three different hydrodynamic volumes, respectively, which could be a consequence of significantly different chain topologies. Substantially, a similar tendency could be seen for PLA-4 samples processed in the internal mixer, also exhibiting bi- and trimodal MWD.

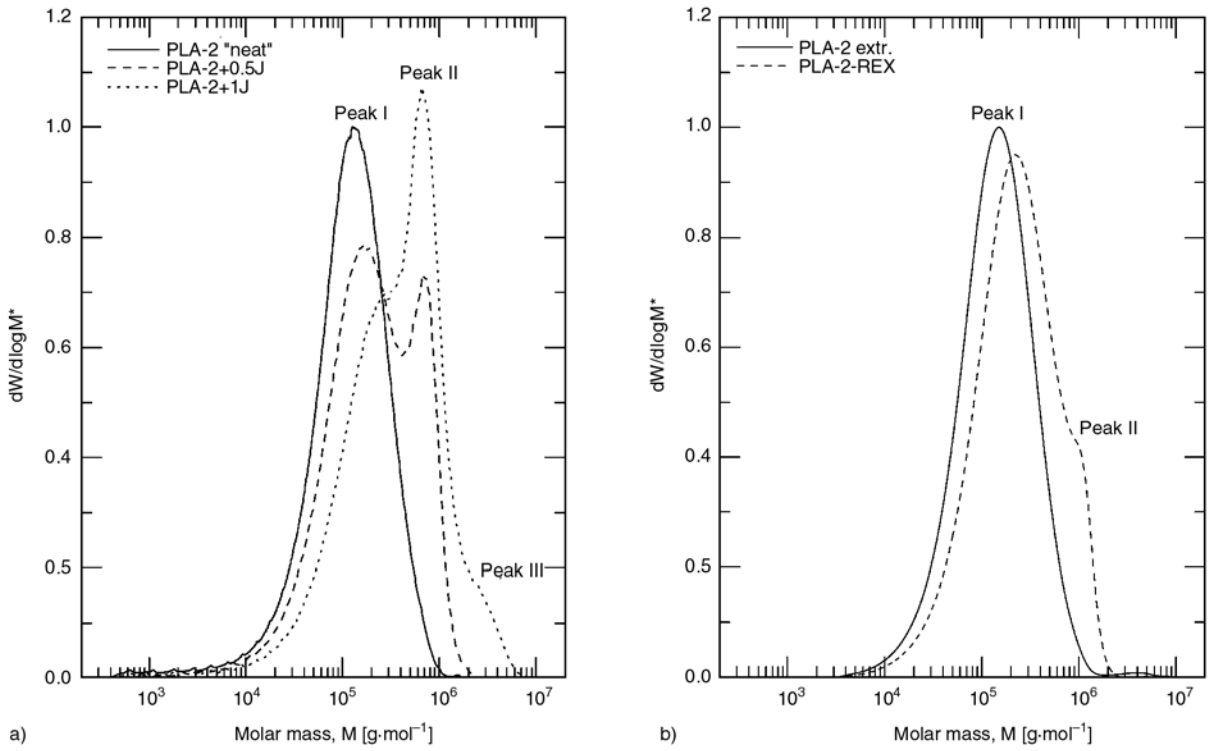

Figure 6. Molecular weight distribution for (a) internal mixer and (b) REX-Calendering PLA-2 samples. * Normalized by the maximum of the "neat" and extr. grade, respectively.

As can be seen in Figure 6b, a similar behaviour in the molecular weight distribution is noticeable for REX-Calendered samples. When SAmfE is added, a less evident bimodal distribution in these latter samples compared to internal mixer samples may be observed. Possibly, a less branched topology of the chains was generated due to a shorter reaction time. Therefore the differences in hydrodynamic volume were less pronounced in REX-Calendered samples and these less branched populations probably eluted together with the linear populations.

Due to the linear topology of unmodified PLA samples, the first peak at low molecular weight for all modified samples was attributed to a linear population and the second peak (at higher molecular weight) to a branched chain population of the polymer. Special attention should be paid to the samples PLA-2+1J and PLA-4+1J processed in internal mixer. These samples reveal a third peak (Peak III) at very high molecular weight which may be attributed to the presence of highly branched populations or even to network structures.

It is well known that classical SEC technique (monodetector) is not a suitable method to accurately determine the molecular weight of branched samples due to the fact that hydrodynamic volumes are greatly affected by the molecular topology. Preparative SEC experiments [24] and/or multi-detector technique may be a more appropriate technique to study modified samples but this analysis would be beyond the scope of this work. However, qualitative information about the complex molecular weight distribution can be extracted from classical SEC data in order to reveal a branching effect. Therefore, a deconvolution was applied to each size exclusion chromatogram in order to do a detailed analysis and results are presented in Table 3.

According to Table 3, a drop in M_w for unmodified PLA-2 and PLA-4 ("neat" and extr. ones) samples compared to raw, unprocessed materials was detected (c.f. Table 1). This is due to the action of different degradation mechanisms during processing. This decrease seems to be higher for PLA-2 sample processed in the internal mixer (PLA-2 "neat"). It appears that the mixing conditions in the internal mixer generated more degradation than in continuous extrusion process.

For both mixing process, when 0,5 w/w% SAmfE was added, M_w as well as the PDI of peak I increased, remaining the dominant fraction in all cases (higher relative area of the deconvolution). It could be a consequence of possible chain extensions coupled with co-elution problems of different chain topology structures.

Table 3. Numerical analysis of the molecular weight distribution for samples prepared by internal mixing and REX-Calendering process

Mixing process	Sample I.D.		M_n [g·mol^{-1}]	M_w [g·mol^{-1}]	PDI	Area [%]
Internal Mixer	PLA-2 "neat"	global	71 184	154 729	2.2	–
	PLA-2+0.5J	global	101 675	282 476	2.8	–
		Peak I*	88 222	196 768	2.2	57.3
		Peak II*	706 160	763 589	1.1	42.7
	PLA-2+1J	global	116 349	513 191	4.4	–
		Peak I*	86 147	283 157	3.3	41.1
		Peak II*	663 154	743 794	1.1	33.7
		Peak III*	1 735 205	2 351 076	1.4	25.2
REX-Calendering	PLA-2 extr.	global	84 207	179 441	2.1	–
	PLA-2-REX	global	119 533	297 307	2.5	–
		Peak I*	112 851	246 077	2.2	71
		Peak II*	990 320	1 058 111	1.1	29
Internal Mixer	PLA-4 "neat"	global	82 283	182 560	2.2	–
	PLA-4+0.5J	global	104 356	348 515	3.3	–
		Peak I*	95 021	253 967	2.7	60.4
		Peak II*	1 123 368	1 221 521	1.1	39.6
	PLA-4+1J	global	100 650	331 452	3.3	–
		Peak I*	87 428	242 884	2.8	57.5
		Peak II*	708 973	782 740	1.1	35.6
		Peak III*	1 806 505	1 923 430	1.1	6.9
REX-Calendering	PLA-4 extr.	global	98 087	181 815	1.8	–
	PLA-4-REX	global	118 650	246 789	2.1	–
		Peak I*	111 992	205 125	1.8	78.4
		Peak II*	794 821	842 948	1.1	21.6

*Results obtained from the deconvolution analysis.

Slight differences between both mixing processes may be observed when comparing the relative areas of peaks I and II. As can be seen in Table 3, for internal mixer samples, the relative area proportion attributed to chain branched topology (Peak II) is always higher compared to the REX-Calendered samples. This may be expected if the higher degree of degradation in internal mixer processing is considered. In fact, the formation of a higher concentration of carboxyl groups promoted an increase in coupling or branching reactions in the presence of the SAmfE agent and therefore a higher branching degree.

Regarding the internal mixer preparation, when the SAmfE content was doubled (from 0.5 w/w% to 1 w/w%), the respective areas of peak II and III increased at the expense of peak I, indicating an increase of this 'new' chain topology content which was attributed to long chain branching and/or more complex topology structures (comb, tree or network structure). For PLA-2+1J sample, the summation of peak II and III relative areas exceeds the peak I area. Possibly a network structure coupled with long chain branching was generated due to the pronounced modification degree reached in this system. Evidence of this last assumption was obtained by visual inspection and solubility tests which showed the existence of gel structures.

3.3. Rheological characterization

Rheological master curves referenced at 180°C for internal mixer as well as REX-Calendered samples are shown in Figure 7. Each sample exhibits a Newtonian plateau at low angular frequencies (except PLA-2+1J sample) and is shear thinned at high frequencies in its respective viscosity functions $|\eta^*(\omega)|$ as can be seen in Figure 7.

Special attention was paid for the analysis of PLA-2+1J samples prepared by internal mixing process (c.f. Figure 7a). A clear shoulder in the viscosity functions $|\eta^*(\omega)|$ is observed at low angular frequencies. This is a common behaviour for heterogeneous systems. In fact, at least one of the different phases has different relaxation times such as emulsions, immiscible polymer blends or polymer/inorganic filler composites. In all these cases, the Palierne's model [25] has been found to successfully predict the linear viscoelastic behavior. In this model, the viscoelasticity of both phases as well as

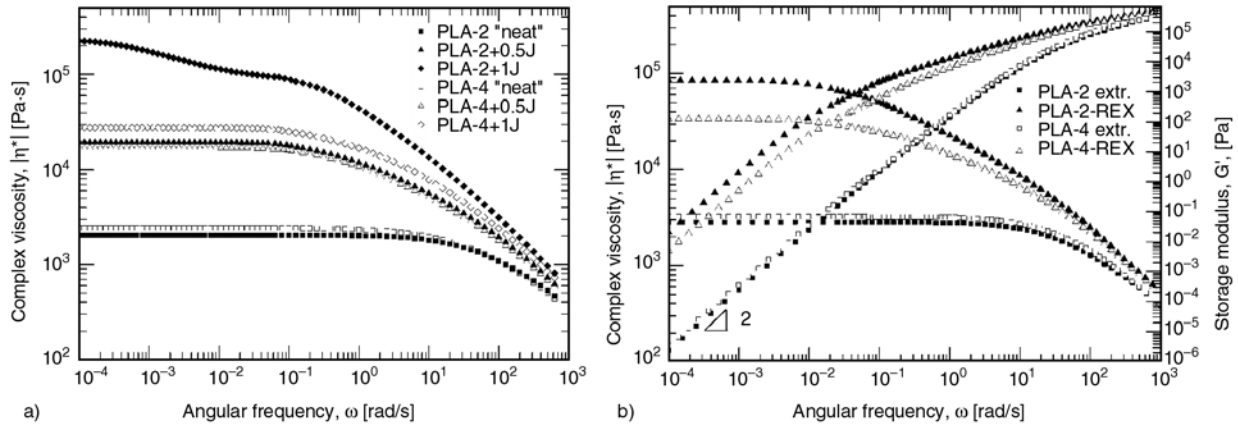

Figure 7. Rheological master curves at 180ºC for samples prepared by (a) internal mixer and (b) REX-Calendering process

the hydrodynamic interactions, the droplet size, the size distribution and finally the interfacial tension between both phases are considered. However, this kind of analysis is beyond the scope of the present work.

The rheological behaviour of branched/partially crosslinked structures, such as the sample PLA-2+1J, may be predicted using their corresponding SEC data. In fact, the majority presence of populations with significant different molecular topology (such as populations corresponding to Peak II and Peak III in Figure 6a) has quite distinct relaxation time compared to the linear population and commonly a shoulder is observed in its viscosity function at low angular frequencies.

As can be seen in Figure 7a and 7b for modified samples, the shear-thinning region of the viscosity function seems to present several curvatures. This latter observation leads to an insufficient accuracy to obtain a correct fitting of the viscosity function with the Carreau-Yasuda model. Stadler and Münstedt [19] reported a similar behaviour in their studies, based on metallocene-catalyzed PE. The presence of long-chain branching brings a complexity in the relaxation processes, leading to the existence of additional curvatures in $|\eta^*(\omega)|$. As a result, the viscosity function may be categorized into three different types considering the shape of the double logarithmic derivative $d\log|\eta^*|/d\log\omega$ versus $\log\omega$ curve. A 'modified Carreau-Yasuda model' (c.f. Equation (1)) was therefore used in order to consider the several distinctly separated relaxation processes in the viscosity function to obtain a proper fitting of this latter one [19].

The double logarithmic derivative of the viscosity functions versus $\log\omega$ is showed in Figure 8a for internal mixer samples and 8b for REX-Calendered samples.

As can be seen in Figure 8 for all unmodified PLA samples, the double logarithmic slope $d\log|\eta^*|/d\log\omega$ versus $\log\omega$ decreases monotonously which is the common behaviour for linear polymers. In contrast, all modified samples, excepting PLA-2+1J, show a shoulder in the double logarithmic derivative which

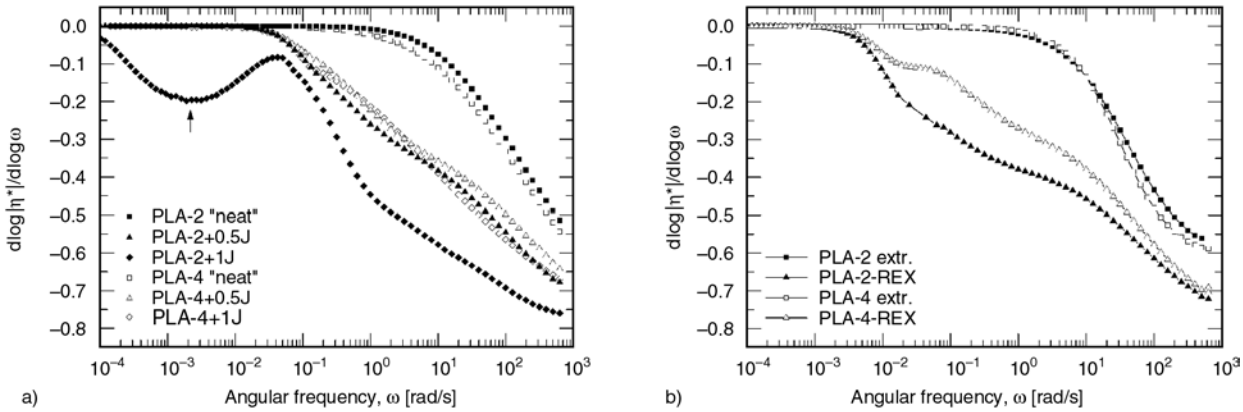

Figure 8. Double logarithmic derivative of the viscosity function versus angular frequency (ω) for samples prepared by (a) internal mixing and (b) REX-Calendering process

Table 4. Rheological parameters at 180°C for the samples prepared by internal mixing process

Parameters	PLA-2 "neat"	PLA-2+0.5J	PLA-2+1J	PLA-4 "neat"	PLA-4+0.5J	PLA-4+1J
η_0 [kPa·s]	2.05±0.01	19.4±0.2	233±5	2.44±0.01	17.1±0.2	27.7±0.2
τ_1 [s]	0.019±0.001	6.4±0.6	25±10	0.016±0.001	6.4±0.6	14.56±0.5
α_1	0.91±0.01	1.5±0.1	3±2	0.72±0.01	1.5±0.1	2.68±0.3
v_1	0.43±0.01	0.75±0.02	0.8±0.1	0.42±0.01	0.76±0.02	0.865±0.007
τ_2 [s]	–	0.04±0.03	–	–	0.05±0.03	0.17±0.02
α_2	–	0.8±0.1	–	–	0.84±0.09	0.81±0.03
v_2	–	0.59±0.03	–	–	0.61±0.03	0.49±0.01
R^2	0.9989	0.9981	0.3502	0.9983	0.9983	0.9985

Table 5. Rheological parameters at 180°C for the samples prepared by REX-Calendering process

Parameters	PLA-2 extr.	PLA-2-REX	PLA-4 extr.	PLA-4-REX
η_0 [kPa·s]	2.837±0.005	86.0±0.6	3.232±0.009	34.1±0.3
τ_1 [s]	0.025±0.001	45.3±0.2	0.027±0.001	50.09±0.2
α_1	0.92±0.01	1.4±0.3	0.92±0.02	1.2±0.01
v_1	0.39±0.01	0.644±0.002	0.38±0.01	0.841±0.006
τ_2 [s]	–	0.035±0.003	–	0.158±0.003
α_2	–	0.79±0.07	–	0.71±0.05
v_2	–	0.66±0.02	–	0.62±0.01
R^2	0.9984	0.9976	0.9986	0.9983

is reflected in the viscosity functions by two different curvatures in the pseudoplastic zone. PLA-2+1J sample presents a minimum in the double logarithmic slope (indicated by an arrow) which may be the effect of its very high molecular mass M_w (c.f. Table 3) or a very high degree of branching explained by the high content of reactive agent introduced during reactions (c.f. Figure 4). As previously discussed by Stadler and Münstedt [19], the modified Carreau-Yasuda model proposed is not able to fit this minimum and the validity of this model for highly branched polymers is questioned. Even though, and just for comparative study the modified Carreau-Yasuda model was fitted. Tables 4 shows the rheological parameters for PLA-2+1J samples.

Some differences between both mixing processes may be observed when comparing the shape of the double logarithmic derivative versus $\log\omega$. As can be seen in Figure 8a and 8b, the decrease in the double logarithmic derivative for modified REX-Calendered samples are initiated at substantially lower angular frequencies compared to modified internal mixer samples. Thus, the molecular modifications induced by REX-Calendering process seem to have a greater impact on the molecular dynamics during flow, increasing relaxation processes.

Rheological parameters for internal mixing process and REX-Calendering process are presented in Tables 4 and 5, respectively.

According to Tables 4 and 5, the results suggest that the zero-shear viscosity as well as characteristic times (τ_i) increase with increasing SAmfE content. The transition region (α_1) between the Newtonian region and the first curvature is broadened together with the apparition of a second curvature. This behaviour reflects the presence of additional relaxation modes due to a possible presence of long chain branching topology generated during reactions [19].

PLA-2 and PLA-4 extr. samples present a somewhat higher zero shear viscosity compared to "neat" internal mixer samples according to Tables 4 and 5. These results suggest that a higher level of degradation was developed during internal mixing preparation due to the higher thermo-mechanical exposition time (13 min.) compared to the REX-Calendered sample (4 min. of residence time), as also observed in SEC characterization.

While the viscosity of the modified samples processed by REX-Calendering was increased at low angular frequencies ω (i.e. low shear rates), the difference was not as pronounced for values of shear rates near the usual extrusion ($\approx$200 s^{-1}) due to the increase of their shear-thinning character (decreased power law index) and the convergence to the same point. This leads to a desirable benefit on the industrial level as their processability is maintained without relevant changes in extrusion conditions.

The results obtained up to that point suggest that the scaling up of the processing conditions from the internal mixing process to the one-step REX-Calendering process was correctly obtained. Since a one-step processing technique is of interest, samples produced during internal mixing will not be analyzed and only REX-Calendered samples will be considered for further analyses.

Information regarding the melt elasticity can be found by considering the storage modulus (G') [26]. As shown in Figure 7b, at high angular frequencies, G' values tend to converge to a similar point, somewhat higher in the case of the modified samples compared to the unmodified ones. As already observed by Han and Jhon [27], the molecular weight distribution is the governing parameter at high frequency while the influence of the chain structure is minimal. This was also expected for the materials under study and verified by SEC analysis. More specifically, a slight increase in polydispersity index and the appearance of bimodal distributions can be observed (c.f. Table 3).

According to the linear viscoelasticity predictions, the slope of $\log G'$ vs. $\mathrm{Log}\,\omega$ is equal to 2 in the terminal regime [28]. PLA-2 extr. and PLA-4 extr. samples present the typical behaviour of linear polymers with the presence of a terminal regime at relatively high frequencies which indicates a fast relaxation process of the chains. However for modified samples, the terminal zone of the storage modulus is broadened and the transition is shifted to lower frequencies, indicating a longer relaxation process of a better cohesive network formation [29]. As already observed by Liu *et al*. [30], this change of behaviour demonstrates the existence of randomly branched LCB in modified samples. Furthermore, G' shows higher values in the case of the modified samples, indicating an increase in the melt elasticity. This latter increase is more pronounced in the sample PLA-2-REX.

Although randomly branched LCB was generated in the modified samples, the exact composition and chain topology is not known. It is believed to be a mix of several components, each one with a different chain topology such as long-chain, star, *H* or comb-shaped branched structures [31]. Typical spectroscopic methods do not work either in order to determine these structures due to erroneous results quantities. Otherwise, the combination of linear viscoelasticity and rheology may be a useful way to determine these structures. The phase angle δ instead of modulus ($G'(\omega)$ and $G''(\omega)$) or viscosity ($|\eta^*(\omega)|$) was taken into account to predict the exact topology due to its comparably higher sensitivity to chain structures.

According to the theory of Trinkle and Friedrich [32], the Reduced van Gurp-Palmen-plot (RvGP) is a more transparent way to show the correlation between rheological data with long chain branching features. This plot is a powerful way to characterize the polymer chain structure from small amplitude oscillatory shear experiments, independently of the polymer used, the characteristic elementary relaxation time τ_0 or the temperature and tacticity.

As can be seen in Figure 9, both unmodified PLA samples (extr. ones) exhibit the typical behaviour of a linear polymer with a curve reaching a phase angle of 90° for low $|G^*|/G_n^0$ ratios. This corresponds to the lower frequencies oscillatory range of the respective master curve, indicating a viscous behaviour [33].

Trinkle *et al*. [31] reported that changes in the curve behavior (phase angle δ lowered or curve flattened) was mainly due to the effect of long chain branching and complex topologies created. According to the RvGP curves of star-polymers (poly(ethane-*alt*-propene)) proposed by Trinkle *et al*. [31] as well as the study of Lohse *et al*. [33] for well-defined polymer structures, the RvGP data at hand suggests the formation of asymmetric tree-arm star-branched polymers. PLA-2-REX seems to present longer arm lengths than PLA-4-REX due to the more pronounced bump at 60º [31].

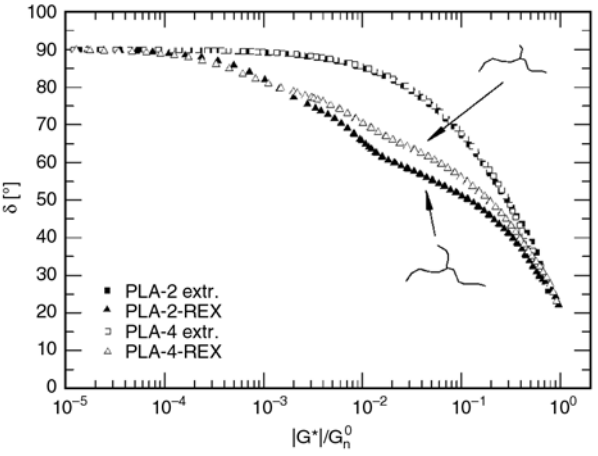

Figure 9. Reduce Van Grup Palmen plot (RvGP) for REX-Calendered samples. The two different tree arm star polymers are sketched to show the possible conformation.

As stated by the simulation performed by Liu *et al* [30] for PLA modified by a Dicumyl peroxide (DCP) samples and the similarity with Figure 8 for the storage modulus shape as well as Figure 9 for the delta shape, small amounts of asymmetric tree-arm star-branched polymers and linear chains in the modified samples may be expected.

Based on a technique developed by Honerkamp and Weese [16], the weighted relaxation spectrum $\lambda H(\lambda)$ was calculated from the linear relaxation spectrum $H(\lambda)$. It reflects the chain relaxation time distributions for REX-Calendered samples. Those are related to different kinds of chain movements dictated by their topologies.

As can be seen in Figure 10, both unmodified PLA samples (extr. ones) samples exhibit a short-time peak which is attributed to the reptation mechanism. It is the main relaxation process for linear polymers, which is the escape of chains by translation diffusion process along a tube.

Moreover, Figure 10 shows the presence of two and three main relaxation peaks, respectively for PLA-4-REX and PLA-2-REX samples. As a consequence, the melt response times increased for these samples. This is possibly due to asymmetric tree-arm star-branched polymer chains generated during the extrusion process. Furthermore, the reptation mechanism is not inhibited due to the large proportion of remaining linear chains. However, it is superseded by primitive path fluctuations and constraint release relaxations which are cumulative effects of the diffusion of the ends of the arms back toward the central star junction [28]. The need to retract an entangled branch is necessary for the backbone relaxation giving rise to an important increase of relaxation times. Wood-Adams and Costeux [34] also observed a bi-modal distribution in the weight relaxation spectrum for long chain branched PE, as well as Dorgan *et al*. [35] for star PLA samples.

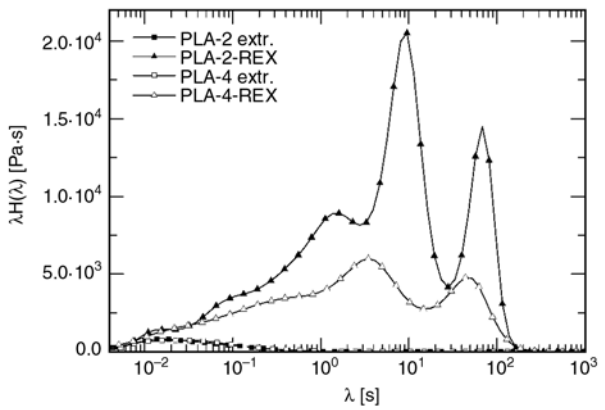

Figure 10. Weighted relaxation spectra ($H(\lambda)$) for REX-Calendered samples at 180ºC

For PLA-2-REX samples, relaxation times are always slightly larger due to longer arm lengths compared to PLA-4-REX. The area under the curve, which is related to the zero-shear viscosity and to the increase of molecular weight, confirms the results previously obtained.

4. Conclusions

For both reactive process employed in this work, results suggest a competition between polymer degradation and chain extension as well as chain branching reactions during processing. Internal mixer studies reveal a higher thermal sensitivity of PLA-2 during processing due to its narrower processing window and higher concentration of terminal functional groups compared to PLA-4. However, independently of the mixing process and the processing conditions employed, as a consequence of this more pronounced degradation, PLA-2 presents a higher reactivity towards the SAmfE agent during processing.

SEC together with RDA results suggest a minimized degradation of the polymer in the REX-Calendering process. Considering these assumptions, the rheological characterization reveals a higher modifications degree of the melt rheological behaviour for REX-Calendered samples compared to internal mixer ones.

Even though size exclusion chromatography presents some limitations with branched polymers due to co-elution problems, an increase in the molecular weight was detectable for all modified samples. Regarding the molecular weight distribution, some differences could be appreciated between internal mixer and REX-Calendered samples. In fact, for these latter samples, the bi-modal distribution is less pronounced compared to internal mixer samples, indicating a more homogeneous structure in samples processed by REX-Calendering.

The presence of several curvatures in the shear-thinning region of the rheological experiments suggests long chain branching in all modified samples. Differences in the double logarithmic derivative shape versus $\log \omega$ between internal mixer and REX-Calendered samples suggest that the molecular modifications induced by the latter processing mode

increase the relaxation processes due to a better cohesive structure.

Regarding REX-Calendered samples, the terminal zone of G' is broadened and shifted to lower frequencies which indicates that the melt elasticity of these samples is increased. In fact, the presence of possible asymmetric tree-arm star-branched polymers considerably increases the chain relaxation time.

Acknowledgements

The authors would like to thank the MICINN (Spain), the projects financial support MAT2010-19721-C02-01, MAT2010-19721-C02-02 and finally BASF® for kindly supplying chain extender.

References

[1] Fukushima K., Fina A., Geobaldo F., Venturello A., Camino G.: Properties of poly(lactic acid) nanocomposites based on montmorillonite, sepiolite and zirconium phosphonate. Express Polymer Letters, **6**, 914–926 (2012).
DOI: 10.3144/expresspolymlett.2012.97

[2] Carrasco F., Gámez-Pérez J., Santana O. O., Maspoch M. L.: Processing of poly(lactic acid)/organomontmorillonite nanocomposites: Microstructure, thermal stability and kinetics of the thermal decomposition. Chemical Engineering Journal, **178**, 451–460 (2011).
DOI: 10.1016/j.cej.2011.10.036

[3] Wang Y., Steinhoff B., Brinkmann C., Alig I.: In-line monitoring of the thermal degradation of poly(L-lactic acid) during melt extrusion by UV–vis spectroscopy. Polymer, **495**, 1257–1265 (2008).
DOI: 10.1016/j.polymer.2008.01.010

[4] Bhat G. S., Gulgunje P., Desai K.: Development of structure and properties during thermal calendering of polylactic acid (PLA) fiber webs. Express Polymer Letters, **1**, 49–56 (2007).
DOI: 10.3144/expresspolymlett.2008.7

[5] Doi Y., Kanesawa Y., Kunioka M., Saito T.: Biodegradation of microbial copolyesters: Poly(3-hydroxybutyrate-co-3-hydroxyvalerate) and poly(3-hydroxybutyrate-co-4-hydroxybutyrate). Macromolecules, **1**, 26–31 (1990).
DOI: 10.1021/ma00203a006

[6] Yu H., Huang N., Wang C., Tang Z.: Modeling of poly(L-lactide) thermal degradation: Theoretical prediction of molecular weight and polydispersity index. Journal of Applied Polymer Science, **11**, 2557–2562 (2003).
DOI: 10.1002/App.12093

[7] Zhang X., Wyss U. P., Pichora D., Goosen M. F. A.: An investigation of the synthesis and thermal stability of poly(DL-lactide)). Polymer Bulletin, **6**, 623–629 (1992).
DOI: 10.1007/BF00297431

[8] Signori F., Coltelli M-B., Bronco S.: Thermal degradation of poly(lactic acid) (PLA) and poly(butylene adipate-*co*-terephthalate) (PBAT) and their blends upon melt processing. Polymer Degradation and Stability, **94**, 74–82 (2009).
DOI: 10.1016/j.polymdegradstab.2008.10.004

[9] Nishida H., Mori T., Hoshihara S., Fan Y., Shirai Y., Endo T.: Effect of tin on poly(L-lactic acid) pyrolysis. Polymer Degradation and Stability, **81**, 515–523 (2003).
DOI: 10.1016/S0141-3910(03)00152-6

[10] Raquez J-M., Narayan R., Dubois P.: Recent advances in reactive extrusion processing of biodegradable polymer-based compositions. Macromolecular Materials and Engineering, **293**, 447–470 (2008).
DOI: 10.1002/mame.200700395

[11] Corre Y-M., Duchet J., Reignier J., Maazouz A.: Melt strengthening of poly (lactic acid) through reactive extrusion with epoxy-functionalized chains. Rheologica Acta, **50**, 613–629 (2011).
DOI: 10.1007/s00397-011-0538-1

[12] Pilla S., Kim S. G., Auer G. K., Gong S., Park C. B.: Microcellular extrusion-foaming of polylactide with chain-extender. Polymer Engineering and Science, **49**, 1653–1660 (2009).
DOI: 10.1002/pen.21385

[13] NatureWorks: PLA polymer 2002D. Technical Papers (2011).

[14] NatureWorks: PLA polymer 4032D. Technical Papers (2011).

[15] BASF: Joncryl ADR-4300. Technical Papers (2011).

[16] Honerkamp J., Weese J.: A nonlinear regularization method for the calculation of relaxation spectra. Rheologica Acta, **32**, 65–73 (1993).
DOI: 10.1007/BF00396678

[17] Hansen S.: Estimation of the relaxation spectrum from dynamic experiments using Bayesian analysis and a new regularization constraint. Rheologica Acta, **47**, 169–178 (2008).
DOI: 10.1007/s00397-007-0225-4

[18] van Gurp M., Palmen J.: Time-temperature superposition for polymeric blends. in 'Proceedings of the XIIth International Congress on Rheology, Quebec, Canada', 134–135 (1996).

[19] Stadler F. J., Münstedt H.: Numerical description of shear viscosity functions of long-chain branched metallocene-catalyzed polyethylenes. Journal of Non-Newtonian Fluid Mechanics, **153**, 203 (2008).
DOI: 10.1016/j.jnnfm.2008.05.001

[20] Incarnato L., Scarfato P., Di Maio L., Acierno D.: Structure and rheology of recycled PET modified by reactive extrusion. Polymer, **41**, 6825–6831 (2000).
DOI: 10.1016/S0032-3861(00)00032-X

[21] Nguyen Q. T., Japon S., Luciani A., Leterrier Y., Månson J-A. E.: Molecular characterization and rheological properties of modified poly(ethylene terephthalate) obtained by reactive extrusion. Polymer Engineering and Science, **8**, 1299–1309 (2001).
DOI: 10.1002/pen.10830

[22] Bikiaris D. N., Karayannidis G. P.: Chain extension of polyesters PET and PBT with two new diimidodiepoxides. II. Journal of Polymer Science Part A: Polymer Chemistry, **34**, 1337–1342 (1996).
DOI: 10.1002/(SICI)1099-0518(199605)34:7<1337::AID-POLA22>3.0.CO;2-9

[23] Bigg D. M.: Polylactide copolymers: Effect of copolymer ratio and end capping on their properties. Advances in Polymer Technology, **24**, 69–82 (2005).
DOI: 10.1002/Adv.20032

[24] Zhang L., Zhou J., Yang G., Chen J.: Preparative fractionation of polysaccharides by columns packed with regenerated cellulose gels. Journal of Chromatography A, **816**, 131–136 (1998).
DOI: 10.1016/S0021-9673(98)00475-0

[25] Palierne J. F.: Linear rheology of viscoelastic emulsions with interfacial tension. Rheologica Acta, **3**, 204–214 (1990).
DOI: 10.1007/Bf01331356

[26] Park H. E., Dealy J., Münstedt H.: Influence of long-chain branching on time-pressure and time-temperature shift factors for polystyrene and polyethylene. Rheologica Acta, **46**, 153–159 (2006).
DOI: 10.1007/s00397-006-0116-0

[27] Han C. D., Jhon M. S.: Correlations of the first normal stress difference with shear stress and of the storage modulus with loss modulus for homopolymers. Journal of Applied Polymer Science, **32**, 3809–3840 (1986).
DOI: 10.1002/app.1986.070320302

[28] Dealy J. M., Larson R. G.: Structure and rheology of molten polymers. Hanser, Munich (2006).

[29] Nam G. J., Yoo J. H., Lee J. W.: Effect of long-chain branches of polypropylene on rheological properties and foam-extrusion performances. Journal of Applied Polymer Science, **96**, 1793–1800 (2005).
DOI: 10.1002/app.21619

[30] Liu J., Lou L., Yu W., Liao R., Li R., Zhou C.: Long chain branching polylactide: Structures and properties. Polymer, **51**, 5186–5197 (2010).
DOI: 10.1016/j.polymer.2010.09.002

[31] Trinkle S., Walter P., Friedrich C.: Van Gurp-Palmen plot II – Classification of long chain branched polymers by their topology. Rheologica Acta, **41**, 103–113 (2002).
DOI: 10.1007/s003970200010

[32] Trinkle S., Friedrich C.: Van Gurp-Palmen-plot: A way to characterize polydispersity of linear polymers. Rheologica Acta, **40**, 322–328 (2001).
DOI: 10.1007/s003970000137

[33] Lohse D. J., Milner S. T., Fetters L. J., Xenidou M., Hadjichristidis N., Mendelson R. A., García-Franco C. A., Lyon M. K.: Well-defined, model long chain branched polyethylene. 2. Melt rheological behavior. Macromolecules, **35**, 3066–3075 (2002).
DOI: 10.1021/Ma0117559

[34] Wood-Adams P., Costeux S.: Thermorheological behavior of polyethylene: Effects of microstructure and long chain branching. Macromolecules, **34**, 6281–6290 (2001).
DOI: 10.1021/ma0017034

[35] Dorgan J. R., Williams J. S., Lewis D. N.: Melt rheology of poly(lactic acid): Entanglement and chain architecture effects. Journal of Rheology, **43**, 1141–1155 (1999).
DOI: 10.1122/1.551041